

University of Alabama in Huntsville

LOUIS

Theses

UAH Electronic Theses and Dissertations

2020

MCNP design of radiation shielding for pulsed fusion propulsion

David Jason Hewitt

Follow this and additional works at: <https://louis.uah.edu/uah-theses>

Recommended Citation

Hewitt, David Jason, "MCNP design of radiation shielding for pulsed fusion propulsion" (2020). *Theses*. 340.

<https://louis.uah.edu/uah-theses/340>

This Thesis is brought to you for free and open access by the UAH Electronic Theses and Dissertations at LOUIS. It has been accepted for inclusion in Theses by an authorized administrator of LOUIS.

**MCNP DESIGN OF RADIATION SHIELDING FOR PULSED FUSION
PROPULSION**

by

DAVID JASON HEWITT

A Thesis

**Submitted in partial fulfillment of the requirements
For the degree of Master of Science Aerospace Systems Engineering
in
The Department of Mechanical and Aerospace Engineering
of
The School of Graduate Studies
of
The University of Alabama in Huntsville**

HUNTSVILLE, ALABAMA

2020

In presenting this thesis in partial fulfillment of the requirements for a master's degree from The University of Alabama in Huntsville, I agree that the Library of this University shall make it freely available for inspection. I further agree that permission for extensive copying for scholarly purposes may be granted by my advisor or, in his/her absence, by the Chair of the Department or the Dean of the School of Graduate Studies. It is also understood that due recognition shall be given to me and to The University of Alabama in Huntsville in any scholarly use which may be made of any material in this thesis.



(student signature)

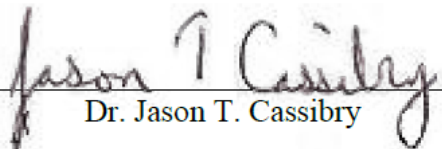

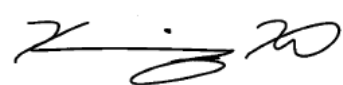
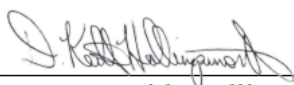
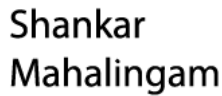

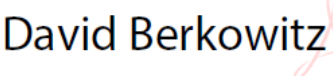
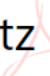
4/16/2020

(date)

THESIS APPROVAL FORM

Submitted by David J. Hewitt in partial fulfillment of the requirements for the degree of Master of Science in Aerospace Systems Engineering and accepted on behalf of the Faculty of the School of Graduate Studies by the thesis committee.

We, the undersigned members of the Graduate Faculty of the University of Alabama in Huntsville, certify that we have advised and/or supervised the candidate on the work described in this thesis. We further certify that we have reviewed the thesis manuscript and approve it in partial fulfillment of the requirements of the degree of Master of Science in Aerospace Systems Engineering.

 Dr. Jason T. Cassibry	4/16/2020 (Date)	Committee Chair
 Dr. William J. Emrich Jr.	4/16/2020 (Date)	Committee Member
 Dr. K. Gabriel Xu	4/16/20 (Date)	Committee Member
 Dr. Keith Hollingsworth	04/17/2020 (Date)	Department Chair
 Dr. Shankar Mahalingam	 Digitally signed by Shankar Mahalingam DN: cn=Shankar Mahalingam, o=College of Engineering, ou=Dean, email=sm0026@uah.edu, c=US Date: 2020.04.23 10:33:06 -05'00' (Date)	College Dean
 Dr. David Berkowitz	 Digitally signed by David Berkowitz DN: cn=David Berkowitz, o=University of Alabama in Huntsville, ou=Graduate Dean, email=berkowsd@uah.edu, c=US Date: 2020.04.23 10:51:39 -05'00' (Date)	Graduate Dean

ABSTRACT

The School of Graduate Studies
The University of Alabama in Huntsville

Degree Master of Science College/Dept. Engineering/Mechanical and Aerospace Engineering

Name of Candidate David J. Hewitt

Title MCNP Design of Radiation Shielding for Pulsed Fusion Propulsion

Pulsed fusion, fission and fission-fusion hybrid systems are currently being studied for advanced propulsion to enable rapid interplanetary space travel. A testbed for evaluating these technologies at the University of Alabama in Huntsville, called Charger-1, utilizes a form of Magneto-Inertial Fusion to implode small plasma loads with z-pinch that will produce thrust when coupled with a magnetic nozzle. Like all forms of nuclear propulsion, this experiment will also be able to produce significant amounts of ionizing radiation in the form of high energy neutrons and photons that need mitigation to protect personnel and equipment. The laboratory housing this testbed has existing shielding that is in need of verification to ensure safe operation; design standards for radiation protection use conservative approximations more than precision in their guidelines leading to large factors of safety in the final product. Used with a ground facility this is more than adequate, but for spaceflight applications more precision is needed to optimize shielding for maximum protection with minimum mass. The shielding for the laboratory is analyzed with Monte Carlo simulations in the MCNP radiation transport code. Techniques developed from this effort are then applied to a design concept for shielding a hypothetical spacecraft using pulsed fusion propulsion. Through the use of MCNP, the protected area of the Charger-1 facility is predicted to receive a worst case dose per pulse of 6.8×10^{-8} Sieverts. This is 0.068% of the dose received from a single chest X-ray.

Abstract Approval: Committee Chair Jason T. Cusick 4/16/2020
(Date)

Department Chair J. Keith Hallinger 04/17/2020
(Date)

Graduate Dean David Berkowitz
Digitally signed by David Berkowitz
DN: cn=David Berkowitz, o=University of
Alabama in Huntsville, ou=Graduate Dean,
email=berkowsd@uah.edu, c=US
Date: 2020.04.23 10:52:01 -05'00'
(Date)

ACKNOWLEDGEMENTS

When I first set out on this thesis in the spring semester of 2014, I had no idea what kind of road I would end up traveling nor did I know how long this adventure would take for me to bring it to a satisfactory conclusion. The process of learning and self-discovery that entailed all aspects of developing this work always ended up being much more difficult for every new step to accomplish than initially envisioned. Attempting a Master's Thesis in an already challenging academic discipline with a subject outside my initial area of expertise would have been a rigorous undertaking even as a full time student. It was made all the more challenging by the fact that I was simultaneously employed as an engineer working in the industry full time with all of the responsibilities and schedules entailed. An artist will suffer for their masterpiece, and in the world of science and engineering said masterpiece would not be possible without the foundations of all prior art preceding. To paraphrase Isaac Newton, I stood on the shoulders of giants to accomplish what I was able to do.

If it were not for the help of my advisor Dr. Jason Cassibry to push me through difficult times while poking at my assumptions and insufficient initial results, this would not have happened. Timely rescue and peer review of my analysis methods from Dr. Kevin Schillo, all while he toiled on his dissertation, allowed me to make great leaps in my own process and progress to help close out my final approach. My employer Dynetics, Inc. contributed greatly with their educational assistance program when it was available, having great patience with me as the semesters stretched on and timelines slipped away. My colleagues Dr. Jim Parsons, Joseph Huwaldt, Adrian Gimenez and Dr. Mark Smith all helped me in my quest to become a better analyst and researcher while providing timely

tips and advice from their own wellspring of experience. Their insights and knowledge with software packages similar to what I was attempting to learn and master allowed for my own growth and plateaus of learning to be crossed.

More thanks go to my good friend Dr. Yohon Lo for lending me textbooks that got him through his nuclear engineering program, one of which that became a very heavily cited source in this thesis. I guess, after six years, I can finally give them back to him. I also owe a great degree of gratitude to my DragonCon Space Track family, every time I was able to take the time to be a part of those great panels I met amazing people that were able to tell me their own stories of triumph and tragedy. The same goes for the good folks involved with the Tennessee Valley Interstellar Workshop where I was able to rub elbows with many great forward thinkers of our time and get insights from many perspectives. If I were not able to let it all out and express my creativity in other ways, it would have been impossible to finish. My brothers in music, Brandon Whitworth, Ken Barnes and Andrew Dubbel were my conduits of inspiration to go with a different flow allowing problems to be solved when not thinking about them while playing in our band Foot Pound Force.

So many other people contributed to this process being fellow travelers in studies or just being someone to vent to while using their spaces to work. Mike Lenox, Chris Wade, Kayla Gomez, Mary Robinson, Jesse Smith, Domenic Cave, Jared Claxon and John McCammon all contributed greatly to my sanity and to my progress towards the finish line. Finally, I would like to express some of my deepest gratitude to my wife Emily for putting up with this for as long as she has.

April 16, 2020

TABLE OF CONTENTS

MCNP DESIGN OF RADIATION SHIELDING FOR PULSED FUSION

PROPULSION
ABSTRACT.....	iii
ACKNOWLEDGEMENTS	v
LIST OF FIGURES	x
LIST OF SYMBOLS	xvi
Chapter 1. INTRODUCTION.....	1
1.1 Motivation.....	2
1.2 Nuclear Fusion for Spacecraft Propulsion	11
1.2.1 Fundamentals of Thermonuclear Fusion	12
1.2.2 Fusion Confinement Methods.....	20
1.2.3 Challenges of Propulsion Applications.....	25
1.2.4 Z-Pinch Propulsion Overview.....	36
1.2.5 Monte Carlo Methods for Analysis of Radiation Environments	48
1.3 Survey of Literature and Related Work	49
1.4 Objectives of this thesis.....	51
1.5 Summary of the Approach	52
Chapter 2. PROTECTION FROM IONIZING RADIATION.....	54
2.1 Ionizing Radiation.....	54
2.2 Radiation Fields and Sources	55
2.2.1 Fluence and Net Flow	56
2.2.2 Radiation Current.....	58
2.2.3 Radiation Field Directional Properties.....	59
2.2.4 Characterization of Radiation Sources.....	59
2.2.5 Neutron Sources.....	60
2.2.6 Gamma Ray Sources.....	63
2.2.7 X-Ray Sources	65

2.3	Interactions of Particles.....	68
2.3.1	Interaction Coefficient.....	68
2.3.2	Microscopic Cross Section.....	70
2.3.3	Neutron Interaction Mechanisms.....	70
2.3.4	Photon Interaction Mechanisms.....	74
2.3.5	Deterministic Transport Theory.....	80
2.4	Ionizing Radiation Dose.....	81
2.4.1	Conversion of Fluence to Dose.....	81
2.4.2	Absorbed Dose.....	83
2.4.3	Kerma.....	83
2.4.4	Exposure.....	84
2.4.5	Local Dose Equivalent Quantities.....	85
2.4.6	Photon Kerma, Absorbed Dose and Exposure.....	89
2.4.7	Neutron Kerma and Absorbed Dose.....	90
2.4.8	Phantom-Related Dosimetric Quantities.....	91
2.4.9	Dose Coefficients for Anthropomorphic Phantoms.....	95
2.4.10	Equivalent Dose.....	96
2.4.11	Effective Dose.....	96
2.5	Biological Effects of Radiation Dose.....	98
2.5.1	Dose Limits.....	101
2.5.2	Dosimetry.....	104
2.6	Radiation Shielding Analysis and Design.....	105
2.6.1	Basic Methods in Radiation Attenuation Calculations.....	105
2.6.2	Shielding Materials.....	110
2.6.3	Regulations and Standards for Shielding Design.....	112
Chapter 3. MONTE CARLO METHODS FOR SHIELD DESIGN.....		114
3.1	Introduction to MCNP.....	114
3.1.1	MCNP Input File Structure.....	115
3.1.2	Model Geometry.....	116
3.1.3	Data Cards.....	117
3.1.4	Variance.....	122

3.1.5	Accuracy vs Precision.....	130
3.2	Dosimetry in MCNP.....	135
3.2.1	Dosimetry with the F4 Tally	135
3.2.2	Dosimetry with the F6 Tally	137
3.3	Test Cases.....	139
3.3.1	Photon Verification Problem	139
3.3.2	Neutron Verification Problem.....	140
Chapter 4.	MODELING AND SIMULATION	142
4.1	Charger-1 Facility	142
4.1.1	Early Iterations and Lessons Learned	144
4.1.2	ChargerLab50 Configuration	151
4.1.3	ChargerLab50 Null Case.....	156
4.2	Z-Pinch Spacecraft	157
4.2.1	ZShip3 Configuration	159
Chapter 5.	PRESENTATION OF DATA	162
5.1	Analysis of Output Files.....	162
5.1.1	Attenuation Determination from Output.....	163
5.2	ChargerLab50 Results	165
5.3	Pulsed Fusion Spacecraft Shielding (ZShip3) Results.....	171
Chapter 6.	DISCUSSION AND CONCLUSIONS	178
6.1	Discussion of Results	178
6.2	Safety Recommendations for Charger-1	179
6.3	Lessons Learned.....	180
6.4	A Path Forward on Analysis	181
REFERENCES.....		186
APPENDIX A: Photon Verification Problem		198
APPENDIX B: Neutron Verification problem.....		214
APPENDIX C: Example Input Decks.....		243

LIST OF FIGURES

Figure 1.1. Comparison of IMLEO and transit times for Mars roundtrip [2].....	10
Figure 1.2. Reactivity of controlled fusion reactions [15]	16
Figure 1.3. Lawson criterion of controlled fusion reactions [15]	17
Figure 1.4. Triple product of controlled fusion reactions [15]	18
Figure 1.5. Parameter Space for MFE, MIF and ICF [2].....	34
Figure 1.6. Conceptual Crewed Spacecraft Using Z-Pinch Pulsed Fusion [40].....	35
Figure 1.7. Stages of the Z-Pinch Cycle [42].....	38
Figure 1.8. Optimal Z-Pinch Engine Concept [42].....	40
Figure 1.9. Reactions in the Z-Pinch Fusion Ignition Chamber [42].....	40
Figure 1.10. Pulsed Fission Fusion hybrid target geometry with outer lithium cone [25]	41
Figure 1.11. UAH Propulsion Research Center Charger-1 Testbed.....	44
Figure 1.12: Wire diode configurations to be tested [2]	46
Figure 2.1 Spherical polar coordinate system to specify the unit direction vector Ω [67]	56
Figure 2.2: Element of volume ΔV in the form of a sphere with radiation penetrating cross sectional area ΔA in (a) and traveling via paths through the sphere in (b) [67].....	57
Figure 2.3: Element of area in a surface where particles cross the area from the other side [67].....	58
Figure 2.4. The various processes of high energy photon interaction with matter [74] ..	74
Figure 2.5. Diagram of the classic coherent scattering process [75]	76

Figure 2.6. Diagram of Compton Scattering [75]	77
Figure 2.7. The photoelectric process [75]	78
Figure 2.8. Diagram of the pair production process [75].....	79
Figure 2.9: Relationship between the protection quantities and operational quantities for use in radiological protection [82]	97
Figure 2.10. Point isotropic source in a vacuum (a), attenuated with a slab shield (b), and attenuated by a spherical shield (c) [67].	107
Figure 3.1. The types of tallies available in MCNP [94].....	121
Figure 3.2. Interpretation of the relative error R [94]	125
Figure 4.1. Charger-1 Facility as viewed from satellite imagery with a representative of Charger-1 superimposed on the roof.....	143
Figure 4.2. Representation of the complex geometry of early ChargerLab configurations	149
Figure 4.3. Zoomed Visual Editor detail of typical early ChargerLab configurations ..	150
Figure 4.4. ChargerLab50 Visual Editor layout.....	152
Figure 4.5. Screenshot of material cards for ChargerLab50 input deck	153
Figure 4.6. Screenshot of the cards for defining the particle source in ChargerLab50 .	154
Figure 4.7. Screenshot of the importance settings in ChargerLab50.....	155
Figure 4.8. Screenshot of Forced Collisions settings for ChargerLab50.....	155
Figure 4.9. Basic dimensions of conceptual z-pinch powered spacecraft [42].....	157
Figure 4.10. ZShip3 Visual Editor layout.....	160
Figure 4.11. ZShip3 Visual Editor zoom on multilayer shield with Cell numbers and material descriptions	161

Figure A.1. NTR-based spacecraft diagram [91].....	198
Figure A.2. Gamma ray mass attenuation coefficients [91]	201
Figure A.3. Fission gamma ray energy distribution [91].....	203
Figure A.4. Dose to the astronaut as a function of burn time	205
Figure A.5. Initial configuration of Emrich13-1 model.....	208
Figure A.6. Zoom in on reactor side of Emrich13-1 model.....	209
Figure A.7. Particle flux to astronaut as a function of burn time.....	212
Figure B.1. Screenshot of Mathematica tool results in NASA study [42].....	216
Figure B.2. Screenshot of Mathematica tool with inputs set to match Figure B.1	218
Figure B.3. Illustration of measurement intervals determining attenuation at points through the shield	223
Figure B.4. Neutron attenuation through multilayer shield upper and lower bounds....	230
Figure B.5. Neutron attenuation detail on Shield 1 - Shield 2- Shield 3 interface region	230
Figure B.6. Mathematica tool closest match to MCNP curves.....	232
Figure B.7. Zoom in on the Shield 1 - Shield 2 - Shield 3 region on the Mathematica tool	233
Figure B.8. Upper and lower bound neutron attenuation curves from second cut	235
Figure B.9. Shield interface region neutron attenuation from second cut	235
Figure B.10. Revised Mathematica tool closest match to MCNP curves.....	238
Figure B.11. Zoom in on the Shield 1 - Shield 2 - Shield 3 region on the revised Mathematica tool	239

LIST OF TABLES

Table 1.1. Comparison of IMLEO and propulsion systems on Mars roundtrip	9
Table 1.2. Light Element Fusion Fuel Cycles [14]	15
Table 2.1. General effects from an acute whole body dose [68, 79]	100
Table 2.2. NCRP recommendations for exposure limits [67, 84]	102
Table 3.1. MCNP Input File Structure [65]	115
Table 3.2. Mode Card set for particle transport combinations with MCNP5 [65]	118
Table 5.1. NPS and Runtimes for ChargerLab50 Datasets	165
Table 5.2. Particle Statistics for ChargerLab50	165
Table 5.3. Determination of fluence at 1 meter from the source	166
Table 5.4. Determination of fluence at location in front of concrete wall	166
Table 5.5. Determination of fluence for null case at location behind shield	167
Table 5.6. Mean tally scores for ChargerLab50Null at 1 billion particle histories	167
Table 5.7. Mean tally scores for ChargerLab50 at 3 billion particle histories	168
Table 5.8. Concrete attenuation as determined from the stack up of tally tolerance	168
Table 5.9. Dose rate range for tallies in ChargerLab50	169
Table 5.10. Total dose per pulse range for tallies in ChargerLab50	170
Table 5.11. Total ambient equivalent dose per pulse range for ChargerLab50	170
Table 5.12. Total ambient equivalent dose per pulse for ChargerLab50	171
Table 5.13. NPS particle history and Runtimes for ZShip3 Datasets	172
Table 5.14. Particle Statistics for ZShip3	172
Table 5.15. Determination of fluence at 1 meter from the source	173

Table 5.16. Determination of fluence for null case at location behind shield	173
Table 5.17. Mean tally scores for the ZShip3Null condition at 1 billion particle histories	173
Table 5.18. Mean tally scores for the ZShip3 condition at 2 billion particle histories ..	174
Table 5.19. Multilayer shield attenuation as determined from the stack up of tally tolerance	174
Table 5.20. Dose rate range for tallies in ZShip3	175
Table 5.21. Total dose per pulse range for tallies in ZShip3	175
Table 5.22. Total ambient equivalent dose per pulse range for ZShip3	176
Table 5.23. Total ambient equivalent dose per pulse for ZShip3	176
Table A.1. Burn time with simulation input and output conditions.....	213
Table B.1. Configuration and dimensions for each shield layer.....	217
Table B.2. Shield1 configuration.....	221
Table B.3. Shield12 configuration.....	221
Table B.4. Shield123 configuration.....	221
Table B.5. Neutron flux tallies at Surfaces 4 and 5 in the Shield1_500 configuration .	224
Table B.6. Photon flux tallies at Surfaces 4 and 5 in the Shield1_500 configuration ...	225
Table B.7. Neutron flux tallies at Surfaces 4 and 6 in the Shield12_750 configuration	225
Table B.8. Photon flux tallies at Surfaces 4 and 6 in the Shield12_750 configuration .	226
Table B.9. Neutron flux tallies at Surfaces 4 and 7 in the Shield123_500 configuration	226
Table B.10. Photon flux tallies at Surfaces 4 and 7 in the Shield123_500 configuration	227

Table B.11. Tally values for Shield1_500_a_20181106a.....	228
Table B.12. Relative attenuations found from median tally values	228
Table B.13. Upper and lower bounds for tally values in Shield1_500_a_20181106a ..	229
Table B.14. Upper and lower bounds of attenuation Shield1_500_a_20181106a	229
Table B.15. Data points gathered from MCNP simulations for Appendix B	240

LIST OF SYMBOLS

SYMBOL	DEFINITION
Δv	Change in Velocity
I_{sp}	Specific Impulse
g_c	Acceleration Due to Gravity
MR	Mass Ratio
m_s	Mass of Vehicle Structure
m_{pl}	Mass of Payload
m_p	Mass of Propellant
v_{eq}	Equivalent Exhaust Velocity
λ_p	Payload Mass Fraction (Moekel)
T_t	Trip Time (Moekel)
R	Distance Between Earth and Destination (Moekel)
N	Number of Stages (Moekel)
k	Ratio of Tank to Propellant Mass (Moekel)
γ	Ratio of Propulsion System to Initial Mass of Nth Stage
α	Propulsion System Specific Mass
β	Mission Type Multiplication Factor
$m_{0,1}$	Initial Mass in Low Earth Orbit
σ	Microscopic Reaction Cross Section
$\langle\sigma v\rangle$	Nuclear Fusion Reactivity
n	Nuclear Fusion Reactant Number Density
V	Fuel Volume
τ_E	Confinement Time
k_B	Boltzmann constant
E_F	Fusion Energy
T	Temperature
β_S	Ratio of Plasma Pressure to Magnetic Field Pressure
Ω	Unit Direction Vector
Φ	Fluence
N_p	Number of Particles
ΔA	Cross Sectional Area of Sphere
s_i	Path Length Segment
ΔV	Volume of Sphere
ϕ	Flux

J_n	Net Flow
ΔM_p	Total Number of Particles Crossing Sphere Area
\mathbf{r}	Point Function Position in Radiation Field
E	Particle Energy
θ	Polar Angle
ψ	Azimuth Angle
S_p	Point Source
μ	Photon Interaction Coefficient (Photon Macroscopic Cross Section)
Σ	Neutron Macroscopic Cross Section
D	Absorbed Dose
$H_{I,d}$	Deep Dose Equivalent
$H_{I,s}$	Shallow Dose Equivalent
$H^*(d)$	Ambient Dose Equivalent
$H'(d, \boldsymbol{\Omega})$	Directional Dose Equivalent
H_T	Tissue Equivalent Dose
E_D	Effective Dose

CHAPTER 1. INTRODUCTION

The objectives of this thesis are as wide ranging as the different methods of thermonuclear fusion available to use for advanced propulsion. This first chapter is an introduction to basic concepts of propulsion as related to interplanetary travel and how missions to other planets could be greatly enhanced through the use of fusion propulsion. There is a brief summary of the different techniques available to achieve fusion ignition as well as the top candidates for applying this to propulsion systems. The Charger-1 pulsed power testbed is described along with some of the fusion experiments scheduled to be performed by this apparatus. A hypothetical spacecraft using a pulsed fusion propulsion system similar to the testbed is also described; pulsed fusion propulsion systems produce ionizing radiation and the main objective of this work is to analyze existing shielding in the Charger-1 facility with the Monte Carlo code known as MCNP. Techniques developed from this analysis will then be applied to a lightweight multilayer radiation shield for the aforementioned hypothetical spacecraft.

The second chapter is a deep dive into the basics of ionizing radiation from the physics involved with photon and neutron interactions, to definitions of radiation dose as well as laying out standards for protection against radiation. The third chapter describes the basics of Monte Carlo analysis of high energy particles using MCNP and details techniques used in this research. The fourth chapter describes the problem setup and the model descriptions for analysis of both the facility shielding and the spacecraft shielding. The fifth chapter contains a summary of the analysis performed for the facility and the

spacecraft, and finally the sixth chapter presents the results and conclusions from this effort.

1.1 Motivation

Throughout human history, great feats of accomplishment have always been due to hard work, creativity and learning from the triumphs and mistakes of previous attempts at greatness. In the history of exploration, every significant milestone reached was much more difficult than the one before and at great expense in resources and ingenuity. At every new frontier there are new gulfs of opportunity filled with treacherous paths to cross them. Humanity is now at the shore of a new ocean known as the Solar System, our ingenuity has allowed us to be able to conquer the gravity well of our home planet and take the first tentative steps outward. Our robotic emissaries are sent on the currents of orbital mechanics to visit the far off shores of interplanetary space, and with these same abilities we are able to send a few of our own to drift about in our cosmic neighborhood. Our abilities are limited though by the great distances and velocities needed, for we are at a new step function threshold to be able to send people out further.

The coin of the realm in interplanetary space is measured in meters per second, for anything to be gained or lost will all be determined by the ability to change that velocity increment. That increment, known as “delta vee”, or Δv , is the measure of difficulty of going to orbit, and subsequently to higher orbits and escape to visit places like the Moon, Mars, Ceres, and Neptune. We are at the mercy of the currents of Δv , for our only way to achieve these changes is through the means of chemical or electric propulsion. Probes are sent outward on a great burst from chemical propulsion, achieving the velocity change very quickly and consuming large amounts of propellant or the same increment is taken slowly

by expelling ions or electrons over a long period of time in electric propulsion. For the most part, once a mission has been sent on its way there is little opportunity for new large Δv without the use of the tricks of gravity, orbital mechanics and the timetables of low energy Hohmann transfer orbit trajectories.

If we continue the analogy of being on the shore of a new ocean and use it to convey the scale of the history of our early explorations as compared to what could be in our future in the stars, we could come to this conclusion: The current state of the art in traversing interplanetary space is akin to Paleolithic tribes plying canoes through Ice Age estuaries and hugging shorelines in search of resources to live off of. Instead of using paddles, our canoes are steered and pushed by jets of hot gas coming from rocket engines. The available Δv is highly dependent on the efficiency of the propulsion system in converting available propellant mass into thrust; this efficiency is commonly known as the specific impulse, or I_{sp} , and is defined as the thrust per unit mass flow rate [1]. Using specific impulse, the following can be derived as an expression of available Δv for a given I_{sp} :

$$\Delta v = g_c I_{sp} \ln MR \quad (1)$$

where the term g_c is the acceleration due to gravity and MR is known as the mass ratio, which is defined as

$$MR \equiv \frac{m_i}{m_f} = \frac{m_s + m_{pl} + m_p}{m_s + m_{pl}} \quad (2)$$

The mass ratio is an accounting of the inert masses of the vehicle structure (m_s) and the payload (m_{pl}) as well as the propellant mass (m_p) before the burn divided by the inert mass once the propellant is depleted. The individual masses are useful for various

means and several ratios and expressions have been developed for usage in mission analysis. One of the most important of these is the payload mass fraction, and the need for useful payload in mission design drives all of the propulsion design decisions. One notable use of this is in designing for launch from the surface of the Earth where the mass ratios in the rocket equation quickly drive a multistage design solution. This is just as important in interplanetary missions.

Another way of expressing the availability of Δv from propulsive means is in the form of the ideal rocket equation that relates equivalent exhaust velocity, v_{eq} , in the place of specific impulse and gravitational acceleration [1].

$$\Delta v = v_{eq} \ln MR \quad (3)$$

The rocket equation clearly shows that the higher the exhaust velocity (and specific impulse), the higher the Δv . There are inherent tradeoffs in the rocket equation that are driven by the physics of propulsion. Generally speaking, the higher the exhaust velocity the lower the thrust imparted by the propulsion system. Thrust performance typically suffering at the expense of exhaust velocity is due to fact that more energy per unit mass is needed to accelerate gases for propulsion [2]. The tyranny of the rocket equation lies in the amount of energy available in the propellant mass fraction, as it resides in the logarithmic portion of the equation.

Chemical propulsion systems expel propellant mass rapidly and at relatively low exhaust velocities whereas electric systems have very high exhaust velocities but very low mass flow rates. This also means that chemical propulsion needs a higher propellant mass than electric propulsion for a given Δv , and conversely less payload mass is made available for the actual mission. Electric propulsion can grant more payload mass and mission range,

but due to its low thrust nature, transit times are very long and it is limited by available power. Chemical propulsion performance is dependent on the amount of enthalpy that can be added to a gas, either by combustion or catalytic reaction of the propellant(s). Electric propulsion adds energy through the acceleration of ionized gases via electrothermal and electromagnetic body forces.

Limitations from current means of propulsion constrain ambitions for deep space exploration. The combustion of chemicals for propulsion depends on the release of chemical binding energies, which is limited to about 10 MJ per kg of propellant. This roughly translates into a maximum exhaust velocity on the order of 10^4 m/s. Electric propulsion has exhaust velocities as high as 10^5 m/s, in the case of ion thrusters, and some concepts may produce higher thrust than is typically seen but that depends on available energy [2]. All of the missions currently flying with electric propulsion are powered by solar energy, newer concepts that have higher performance would need to have a higher energy source in the form of nuclear power.

Nuclear propulsion is not a new concept; there are technologies that were developed in the 1960s to utilize a fission reactor to heat propellant in the form of hydrogen to be used in a high thrust and high I_{sp} fashion. This technique is known as Nuclear Thermal Propulsion (NTP), it was tested extensively 5 decades ago in the Nuclear Engine for Rocket Vehicle Applications (NERVA) program funded by NASA and the Department of Energy (DOE) [3]. This technology shows much promise and after years of stagnation, funding is slowly returning to this application to further its development and Technology Readiness Level (TRL). With enough commitment, this technology could be developed for flight in

relative short order and would have great impact on in-space applications for robotic and human-piloted missions.

NTP is but an intermediate step in the development of in-space propulsion, it is a logical first step in nuclear applications for it will enable more advanced methods by being developed. Fission reactors in space could be used for powering a spacecraft as well, and this power could be used to enable electric propulsion with even greater potential than what is currently in use with solar power. Subsystems developed for these applications would enable the development of an even more powerful source for propulsion, thermonuclear fusion. In-space propulsion as constrained to derivatives of the rocket equation can be divided into two types, Type I and Type II, as derived by Moekel [4]. Type I approximates impulsive systems in which burn time is small compared to the coast time, examples of this would be in chemical and Nuclear Thermal Propulsion. Type II categorizes systems where burn time is comparable to the coast time; electric and fusion systems fall into this category.

When discussing nuclear propulsion, specific impulse becomes a less useful term for relating to efficiency of the system. A term based on power density takes its place; known as the propulsion system specific mass it is denoted by α and is an expression relating the amount of power available per unit mass [5]. Nuclear electric propulsion (NEP) is on the order of 100 W/kg, which is actually less effective than solar electric propulsion in some ways where this value can climb as high as 3 kW/kg. This is due to the mass of the nuclear powered vehicle as compared to a solar-powered vehicle, electricity generated from a nuclear reactor is about 30% efficient and limited by the Carnot cycle efficiency. Excess heat generated by this process needs to be rejected via large radiators

that consume a large portion of spacecraft mass [6]. Solar electric propulsion (SEP) has a mass advantage until the mission is carried out far enough away from the sun that the drop off in solar energy as an inverse square of the distance from the sun makes it ineffective. The lowest end fusion propulsion performance is on the order of 1 kW/kg, but has thrust profiles on the order of kilonewtons versus the millinewtons provided by electric propulsion. Fusion propulsion could get as efficient as 10 kW/kg given sufficiently advanced technologies, however this is all still a dream since 1 kW/kg fusion has yet to be demonstrated.

A good indicator of the effectiveness of a propulsion system in an interplanetary mission is the Initial Mass in Low Earth Orbit (IMLEO) as a function of the trip time. For example, the most recent NASA study for a round trip human Mars mission pegged the IMLEO for a chemical propulsion system at 486 metric tons. This would be a multi stage affair with tankage and engines being jettisoned in route and a risky aerocapture method being used to brake the spacecraft into Mars orbit; without aerocapture, the Δv from the maneuver would need to come from propellant which would make the IMLEO significantly higher [7]. The optimum transit time to and from Mars would be determined by the relative positions of the planets at the time of the mission milestones. General studies were conducted by Cassibry, et al, which compared these different performance metrics for a Mars round trip [2]. The two stage chemical propulsion system in this study makes the trip in just over three years at the IMLEO determined by the NASA study. A spacecraft with the same IMLEO powered by 1 kW/kg fusion could make the round trip to Mars and back in around 5 months [2, 8].

The important mission sizing parameters used to determine the IMLEO were based on the work of Moekel in his derivations for the performance of Type I and Type II rockets. A simple exercise comparing the IMLEO of different propulsion systems can be done using equations derived by Moekel relating to the payload mass fraction of both of his types of rockets. This parameter, known as λ , can be determined from the following equations

$$\begin{aligned} \text{Type I} \quad \lambda_p &= \left[\frac{1+k}{10^{\frac{3\beta R}{7Nv_{eq}T_t}} - k - \gamma} \right]^N \\ \text{Type II} \quad \lambda_p &= \left[1 - \left(\frac{2}{3} T_t \right)^{-3/2} \beta R \sqrt{\alpha/(2N)} \right]^{2N} \end{aligned} \quad (4)$$

with T_t being the trip time, R being the distance between the Earth and destination, N being the number of stages, k being the ratio of tank to propellant mass, γ being the ratio of propulsion system to initial mass of Nth stage, v_{eq} being the equivalent exhaust velocity, α being the aforementioned propulsion system specific mass, and β being the mission type multiplication factor [4].

Consider a round-trip mission to Mars, a distance R of 0.5 AU, with a payload mass of 100 metric tons, with a trip time T_t of 1.5 years. Using the relations of Equation 4, we can make a first order comparison of how much IMLEO would be needed to make the round-trip in the time given for a chemical propulsion system, an NTR system, a NEP system of 100 W/kg, a fusion propulsion system of 1 kW/kg, and a fusion propulsion system of 10 kW/kg. The IMLEO, given as $m_{0,1}$, is found via

$$m_{0,1} = \frac{m_{pl}}{\lambda_p} \quad (5)$$

where m_{pl} is the payload mass [4].

Moeckel makes several simplifying assumptions in his equations, the ratios k and γ can be subjective in mission planning for such advanced systems as are the assumptions behind β in determining trip time multipliers for rendezvous versus flyby versus roundtrip. More exhaustive astrodynamics analysis with patched conic trajectories would yield more accurate results, but the mathematics involved with the propulsive profiles of Type II systems in relation to orbital mechanics can get quite exhaustive for initial mission sizing. Using conservative application of these factors, the following table was generated comparing the different systems on an 18 month roundtrip mission to Mars and back for a 100 mT payload.

Table 1.1. Comparison of IMLEO and propulsion systems on Mars roundtrip

Propulsion Type	λ_p	IMLEO (mT)	Number of SLS Block 1B Launches
Chemical	0.0126	7940	61
NTR	0.1122	891	7
NEP, 100 W/kg	0.2731	366	3
Fusion, 1 kW/kg	0.7209	139	1.07
Fusion, 10kW/kg	0.9068	110	0.85

The results in Table 1.1 demonstrate that it is possible to send a 100 mT payload to Mars and back in 18 months with all of the propulsion systems, but mass penalties fall out rapidly for the conventional systems. If this kind of mission were attempted, the chemical rocket version of it would need 61 launches of the Space Launch System (SLS) to be assembled; this comes with the caveat of using the SLS Block 1B configuration, the most powerful currently in development capable of launching 130 mT into LEO. This profile is far too aggressive for optimized missions using chemical propulsion (as demonstrated

earlier with the NASA Mars study), and the economics never converge with so many launches needed. In contrast, a 10 kW/kg fusion system could be launched with 1 Block 1B SLS for this mission. Moeckel's equations run out to their natural course build a useful parameter space for mission sizing, as is shown in Figure 1.1 with the variability of mission time added to the analysis summarized in Table 1.1.

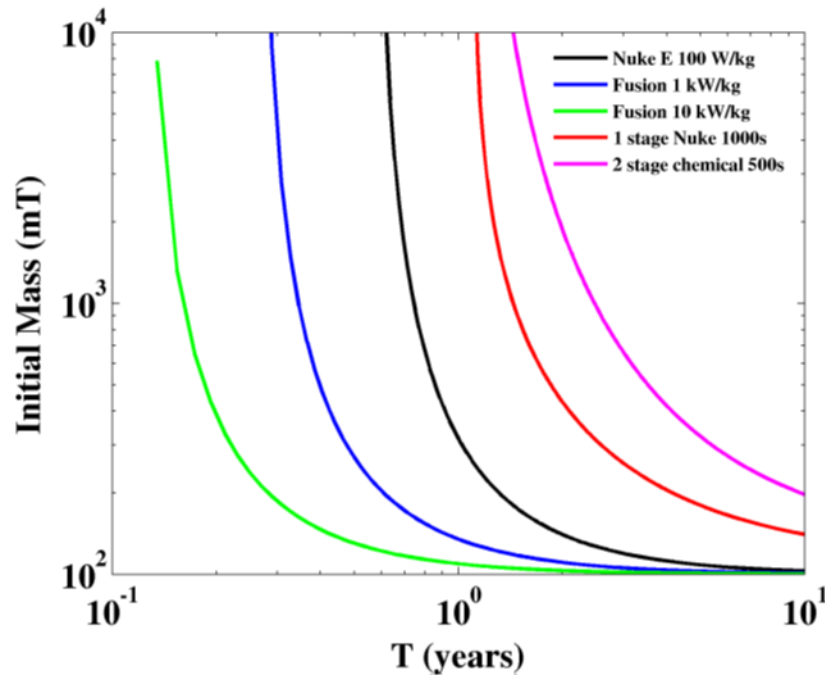


Figure 1.1. Comparison of IMLEO and transit times for Mars roundtrip [2]

Interplanetary space is vast and full of hazards to human health, therefore cutting trip times would reduce exposure to these risks. The less time spent in transit means less exposure to Galactic Cosmic Radiation (GCR), high energy particles from solar storms, micrometeorites as well as the effects of microgravity on frail human physiologies. All options for nuclear propulsion are appealing for cutting transit times, but fusion is king in that performance space. The utility of having this kind of interplanetary capability opens up the solar system for much more rapid human and robotic exploration than previously

possible. There is great potential for fusion propulsion and with it contains many different ways that physics predicts that it could be accomplished, it is worth exploring some of those concepts and the science behind them.

1.2 Nuclear Fusion for Spacecraft Propulsion

Thermonuclear fusion is an intensive process requiring conditions that are barely imaginable for achievement. Fusion occurs when light elements are forced together to fuse into heavier elements and as a result large amounts of energy are released. This occurs naturally in stars where isotopes of hydrogen are compressed together in gravitational confinement in the form of superheated gas ionized into plasmas, and the resulting implosion creates new and heavier isotopes of helium with an outburst of energy. This is a self-sustaining reaction as there is excess energy to keep the soup of plasma heated to a high enough energy state to overcome the resistance of nuclear forces. Stars burn their fuel for timespans from hundreds of millions to billions of years depending on the mass of the star. The heaviest stars burn through their fuels much more quickly than lighter stars and end their lives in spectacular fashions when the elements created become too heavy for sustainable energy production.

A key forcing parameter in the enabling of thermonuclear fusion is the confinement and compression of the plasma fuels. In a star, the burn rate is a function of its mass for the greater the mass the greater the compression due to gravitational forces. Due to the immense volume of a star in combination with gravitational compression, the probability of collision between fuel atoms is so high that fusion will occur at around 15 million K. In order to produce fusion artificially, the mass and volume of a star is obviously not available for compression and confinement so to increase probability of collision the plasma

temperature needs to be increased to at least 150 million K [9]. This energy addition can be in a controlled manner with a reactor or in an uncontrolled manner as with a nuclear weapon.

Though the required temperature range for thermonuclear fusion starts on the order of 10^8 K, the reaction products are born with energies much higher in the MeV range. These products are difficult to thermalize in short distances, and this leads to large reactor sizes. Neutrons produced in these reactions have a flux roughly an order of magnitude greater than fission reactors, exacerbating an environment that is already very unfriendly to materials [10]. Since there has yet to be a reactor concept to demonstrate breakeven where energy output exceeds input, it is difficult to visualize a reactor concept that could be used for propulsion. There are several candidates for this, and it would be helpful to discuss the varied concepts and methods. Before the discussions on the different concepts for reactors, it will be helpful to first review the basics of fusion.

1.2.1 Fundamentals of Thermonuclear Fusion

Thermonuclear fusion has been achievable for over 80 years, and since the detonation of the first hydrogen bomb in 1952, energy production from fusion has always remained “30 years away...”. Despite all of the best efforts of research and technology, artificially induced thermonuclear fusion has never achieved ignition, the point at which fusion becomes self-sustaining. Since the physics behind sustained ignition are not well understood, many methods have been proposed that exploit a variety of plasma properties to attempt to achieve it and there is still an open question as to the best approach for energy production.

Fusion was first achieved experimentally with particle accelerator experiments in the 1930s, and these experiments paved the way for many fundamentals in fusion energy production. During World War II and the race to nuclear weapons capability won by the Manhattan Project, scientists realized that fusion could be initiated in hydrogen fuels from the conditions created by nuclear fission weapons. By the end of the 1940s, primitive electromagnetic magnetic devices were confining and compressing plasmas into fusion and the groundwork was laid for an explosion of ideas for ways to create fusion reactions. These experiments and the theoretical underpinnings derived from them led to a few basic understandings about the necessary conditions for fusion.

In order for two nuclei to fuse, they must first overcome the repulsive force of the Coulomb Barrier, and once this is crossed the Strong Nuclear Force takes over and causes the nuclei to be attracted to each other. In hydrogen isotopes, the minimum potential energy to overcome the Coulomb repulsion is 360 keV [11]. A significant factor in determining whether nuclei are able to fuse or not is the reaction cross section, σ , which is a measure of the probability of a fusion reaction given the relative velocity of the reactant nuclei. The reactants will generally have a distribution of velocities, and it is useful to include an average over the distributions of product of cross section and velocity. This is called the reactivity, denoted by $\langle\sigma v\rangle$ it increases from virtually zero at room temperature to significant magnitudes at temperatures in the range of 10 to 100 keV. From this term, the reaction rate can be found for two reactant species given a volume of fuel and it is given as

$$\frac{dN}{dt} = n_1 n_2 \langle\sigma v\rangle_{12} V \quad (6)$$

with n_1 and n_2 being the reactant number densities and V being the fuel volume [12].

Artificially induced fusion has been the most easily accomplished with the lightest elements, and Table 1.2 shows the different reactions most commonly available from isotopes of hydrogen, helium, lithium, and boron. These happen to be common reactions in the cores of some main sequence stars as well because ignition conditions for these elements are the simplest. The hydrogen isotopes deuterium (D) and tritium (T) are the most common fusion reactants in the universe. Energy producing reactions happen with heavier elements, but the higher ignition energies require more stellar mass. The carbon, nitrogen and oxygen cycles of high mass stars are beyond the reach of practicality for energy production from artificial fusion due to much higher confinement requirement [13].

The fusion reactions create new particles in addition to the new elements produced that have much higher energy states than the reactants. The most common products are alpha particles (helium-4 nuclei), neutrons, protons and high energy photons. The desire in a fusion reactor is to contain the energies produced in the reactions in particles that can be magnetically controlled, for they can remain contained and add heat to sustain the reactions. Alpha particles and protons are well suited for this task, but not all reactions are easily done that produce these particles. Often times the reaction products are neutral particles like neutrons and the results of Bremsstrahlung radiation, which cannot be contained and their energy is lost to the outside world unable to be harnessed to help the process.

Table 1.2. Light Element Fusion Fuel Cycles [14]

Reaction	Fusion Fuel Cycles, MeV	Ignition Temperature, °C
1a	$D + D \rightarrow T (1.01) + p (3.02)$ 50%	300×10^6
1b	$D + D \rightarrow {}^3\text{He} (0.82) + n (2.45)$ 50%	
2	$D + T \rightarrow {}^4\text{He} (3.5) + n (14.1)$	50×10^6
3	$D + {}^3\text{He} \rightarrow {}^4\text{He} (3.6) + p (14.7)$	500×10^6
4	$T + T \rightarrow {}^4\text{He} + 2n + 11.3$	
5a	${}^3\text{He} + T \rightarrow {}^4\text{He} + p + n + 12.1$ 51%	
5b	${}^3\text{He} + T \rightarrow {}^4\text{He} (4.8) + D (9.5)$ 43%	
5c	${}^3\text{He} + T \rightarrow {}^3\text{He} (2.4) + p (11.9)$ 6%	
6	$p + {}^6\text{Li} \rightarrow {}^4\text{He} (1.7) + {}^3\text{He} (2.3)$	
7a	$p + {}^7\text{Li} \rightarrow 2{}^4\text{He} + 17.3$ ~20%	
7b	$p + {}^7\text{Li} \rightarrow {}^3\text{Be} + n - 1.6$ ~80%	
8	$D + {}^6\text{Li} \rightarrow 2{}^4\text{He} + 22.374$	
9	$p + {}^{11}\text{B} \rightarrow 3{}^4\text{He} + 8.7$	
10	$n + {}^6\text{Li} \rightarrow T + {}^4\text{He} + 4.8$	
11	$n + {}^7\text{Li} \rightarrow T + {}^4\text{He} - 2.5$	

The reactivity of the different reactions changes as a function of temperature, and it can be shown that some reactions have easier thresholds than others. Figure 1.2 shows this reactivity range for Reactions 1, 2, 3 and 9 from Table 1.2. The plots in this figure show that the deuterium-tritium reaction ends up with the highest reactivity at the lowest temperature, and this correlates well with the ignition temperature shown in Table 1.2. The D-T reaction may be ideal for initiation of ignition and burn, but for spacecraft the copious neutrons produced creates a problem that needs to be shielded from.

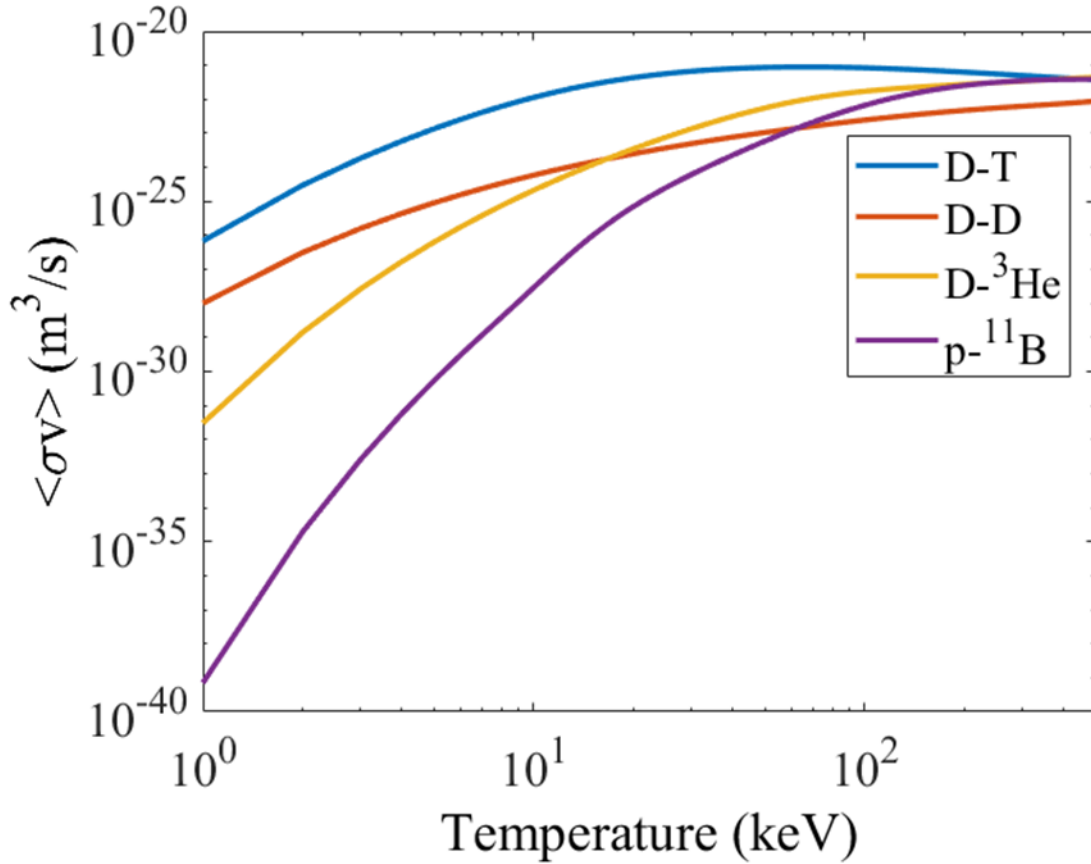


Figure 1.2. Reactivity of controlled fusion reactions [15]

Fusion reactor design is driven by criteria to determine viability based upon a reactor's ability to achieve thermonuclear ignition as well as the conditions required to achieve ignition. The two most important of these criteria are the Lawson criterion and the triple product. A reactor has to contend with power losses when generating the conditions necessary for the reaction, and these losses affect the viability of the reactor. These power losses affect the ability for the plasma to reach the state necessary for ignition, which is essentially the amount of heat to the plasma needed to maintain fusion conditions against the power losses. These power losses come from radiation, conduction, and transport across magnetic field lines. Magnetically confined plasmas have a factor known as the energy confinement time which is the time that the diffusive energy losses equal the total

energy of the plasma. Most radiation losses are driven by Bremsstrahlung, which will be discussed in greater detail in Chapter 2 [12, 14, 15].

The Lawson criterion is a breakeven point where fusion heating is greater than all of the losses and is expressed by

$$n\tau_E \geq \frac{12k_B T}{E_F \langle\sigma v\rangle} \quad (7)$$

where n is number density, τ_E is the confinement time, k_B is the Boltzmann constant, E_F is the fusion energy and T is the temperature.

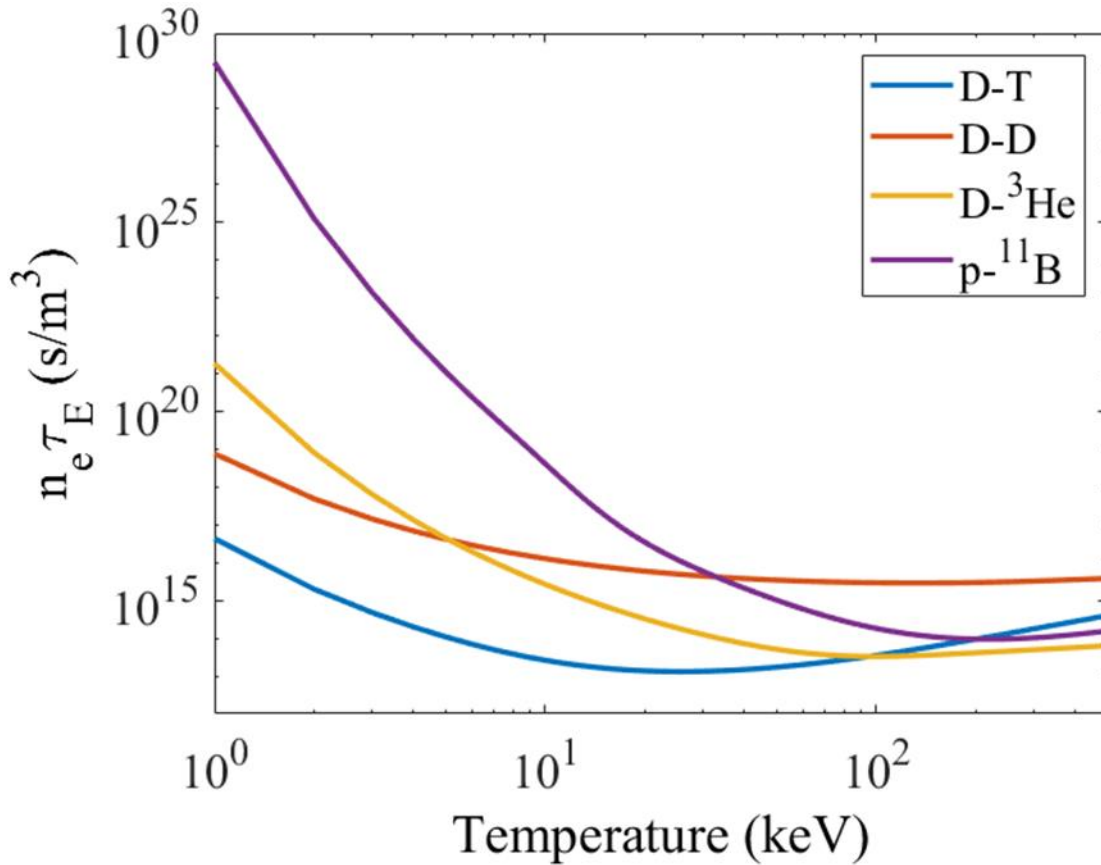


Figure 1.3. Lawson criterion of controlled fusion reactions [15]

Shown graphically, the D-T reaction minimizes its Lawson criterion at the lowest temperature of the reactions due the high cross section shown in Figure 1.3. When coupled

with the triple product criterion, the D-T reaction becomes even more useful for fusion research. The triple product criterion is the combination of the product of plasma density, confinement time and temperature for fusion and is expressed as

$$n\tau_E T \geq \frac{12k_B}{E_F} \frac{T^2}{\langle\sigma v\rangle} \quad (8)$$

If the triple product on the left hand side is greater than the value on the right hand side of this inequality, the energy generated by the reactor will be greater than the energy necessary to maintain the plasma in the desired conditions for fusion. This particular criterion has yet to be achieved by any reactor. Figure 1.4 has a graphical representation of the triple product for the reactions shown in Figure 1.3.

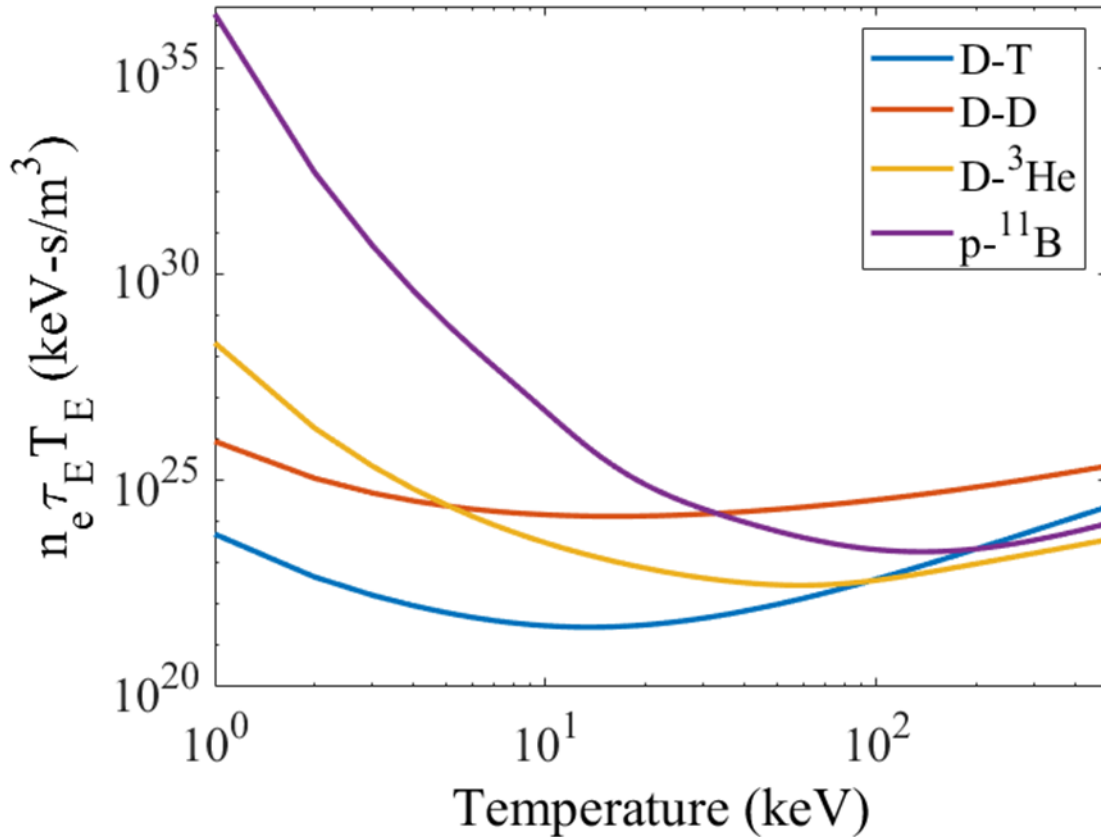


Figure 1.4. Triple product of controlled fusion reactions [15]

When observing the curve for the D-T reaction, it shows that the triple product is much lower at lower temperatures than the other reactions. Though the D-T reaction has a triple point of 14 MeV, which converts to a relatively chilly temperature of 162.47 million Kelvin, its utility in a sustained fusion reaction by itself is made more difficult due to the neutron that is born from the reaction. Shown from Reaction 2 in Table 1.2, a 4.3 MeV alpha particle is also created and can be retained for self-heating but this is a great deal less energy than the 14.1 MeV lost to the neutron that cannot be harnessed. Ignition is easier than other fuels, but sustainment is more difficult.

For all the benefits of the least difficult ignition conditions, at this point it is also still quite cost prohibitive to perform fusion research with these two fuels. A hydrogen atom in its most basic state consists of one proton and one electron, the addition of a neutron to the nucleus creates deuterium. This exists in nature in relative abundance, one out of every 6420 hydrogen atoms in the Earth's oceans is deuterium and when isolated it is commonly known as "heavy water" [16]. Tritium, on the other hand has two neutrons in the nucleus and is unstable with a half-life of 12.32 years decaying into helium-3 and a neutron [17].

Tritium is produced most commonly via the bombardment of lithium-6 with neutrons in a fission reactor, which yields helium-4 as well as 4.8 MeV of exothermic energy. This is Reaction 10 in Table 1.2, and a less common one is Reaction 11 that is endothermic with lithium-7. There are several other methods that yield less tritium, another common but less frequently extracted way of production is in heavy water moderated reactors. The heavy water acts as a neutron moderator and the tritium that is created needs to be cleaned from the moderator after several years of use to reduce the risk

of tritium water contaminating the environment [18]. Despite this production, there is not enough available for significant fusion research activity. Therefore most research is conducted with the more difficult to ignite D-D combination. Other fuel combinations that are possible and have utility for fusion propulsion will be discussed in upcoming sections including D-³He and D-⁶Li (Reaction 8).

1.2.2 Fusion Confinement Methods

Decades of research into nuclear fusion for terrestrial power production has yielded a spectrum of methods to confine the superhot plasmas necessary for fusion. The most common methods that have been studied are sorted into the categories of Magnetic Confinement Fusion (MCF), Inertial Confinement Fusion (ICF), Magneto-Inertial Fusion (MIF), Inertial Confinement Fusion (ICF), and Inertial Electrostatic Confinement Fusion (IEC). In the following section, each of these methods will be examined in more detail and propulsion concepts will be discussed as they relate to their fusion methods.

1.2.2.1 Magnetic Confinement Fusion (MCF)

MCF confines a low density plasma with a strong magnetic field, usually in a volume that is hundreds of cubic meters in size and the plasma is run in a continuous steady state operation (on the order of multiple seconds) to increase the likelihood of initiating a fusion reaction [19]. The plasma carries the majority of the energy and since it is an ionized gas, the magnetic fields work very well to confine the ions inside the reaction area while minimizing thermal losses. The most used MCF device is known as the tokamak, which confines the plasma inside of a toroidal magnetic field. There are several derivatives of the tokamak which distinguish themselves with different geometries of the magnetic field generated; the spheromak, the Reversed Field Pinch (RFP), and the stellarator are the

primary examples of this [2]. All of these methods had common use until breakthroughs in the late 1960s made the tokamak the preferred MCF choice.

The trend for tokamaks has seen a large increase in reactor size over the decades, with the flagship of the current generation being the stadium-sized International Thermonuclear Experimental Reactor (ITER) under construction in southern France. A major reason for this increase in size is that the larger the reactor is, the more volume is available for the confined plasma to circulate at temperature and thereby increasing the likelihood of collisions. It is hoped that the large size of ITER will finally enable a tokamak to produce more energy than it consumes, but due to the international governmental nature of the project it will still be some time before it is finished and operational. Several parallel efforts are underway to figure out ways to reduce the size of MCF devices while retaining the advances in heating and confinement capabilities. Private investment has been creeping into the field and several startups are pursuing their own designs to more quickly enable fusion devices through the application of cutting edge technologies in problem areas. One example of this is in the superconducting coils that produce the magnetic fields, they need cooling down to 4.5 K with liquid helium in enormous cryostats that surround the whole reactor [20]. High temperature superconductors are being evaluated by some of the startup companies that would enable changing the working fluid of the cryostat to the much warmer and much less expensive liquid nitrogen; this would lead to much smaller cryostat hardware was well [21].

1.2.2.2 Inertial Confinement Fusion (ICF)

ICF utilizes a concentration of large energies with a spherically symmetric distribution of laser pulses or heavy ion beams to compress a small pellet of fusion fuel

into reaction. Fusion is initiated through the ablation and implosion of the pellet, which is really a hollow shell consisting of layers of hydrocarbons doped with additives in the outer layers and D-T ice on the inside. As the energy is delivered to the pellet, the ablator heats and expands while the inner shell is compressed due to the conservation of momentum. The outward motion of the ablator compresses the center of the target and increases the temperature of the D-T fuel until it ignites in a self-sustained burn of the fuel. This reaction occurs over a short timescale on the order of around 10^{-9} seconds [2, 19]. The most advanced facility for ICF is at the Lawrence Livermore National Laboratory (LLNL) National Ignition Facility (NIF), and it is used to direct 192 laser beams at the target while delivering 1.8 MJ of energy in a pulse [22].

1.2.2.3 Inertial Electrostatic Confinement Fusion (IEC)

IEC utilizes the phenomenon of ions being influenced by the existence of electrostatic fields, and it typically involves the use of a spherical electrostatic field produced by a grid or other means to radially confine ions. The ion energies are determined by the electrostatic potential well, therefore making a simple device in practice that is only limited by the power supply [23]. This has meant that hobbyists and hackers have long had the ability to build IEC devices and operate them in their own workshops with little or no funding. The principles that make fusion possible with IEC involve how charge distributes itself inside the geometry of the grid. The outer electrode acts as an anode to allow the ions to pass into the center through a spherical cathode designed to be transparent to the converging ions. The ions form a space charge when reaching the center, repelling each other and creating a virtual anode from the positive ion shell. Electrons emitted from the inner cathode pass through the virtual anode and create an inner shell of electrons as a

virtual cathode inside the virtual anode. Like nested dolls, this process repeats itself with higher electrical potential until conditions at the center meet the Lawson criterion for a fusion reaction. Even tabletop homemade devices can produce neutrons [19].

1.2.2.4 Magneto-Inertial Fusion (MIF)

MIF utilizes an inertially confined plasma inside of a magnetic field with the goal of minimizing thermal losses and enhancing the self-heating of the fuel by alpha particles. MIF is a hybrid approach to fusion confinement that takes place in between MCF and ICF in the density and time scale regimes. This confinement method reduces the aerial density threshold ρR for ignition which allows for lower implosion velocities or a higher gain for a given implosion, but it is highly dependent on the liner which must be energetic enough to compress the target to ignition while conserving magnetic flux. The liner must also be able to confine the target plasma for a long enough period to allow for the fusion yield to exceed the liner driver and target generation energies. MIF is actually quite mature as far as techniques go to induce fusion, it was used for the first magnetically controlled fusion experiments in the late 1940s before more powerful methods were tried [24]. The original MIF devices used solid liners and they are still in use, but major innovations in plasma liners over the past few decades have started to show promise in more efficient and reusable operation.

In solid liner MIF, a metal cylindrical shell is used to implode a simply connected magnetized plasma via the application of a large current on the order of $\sim 10^6$ A through the shell. The induced $\mathbf{j} \times \mathbf{B}$ Lorentz force compresses the liner into implosion with the contained plasma and the conditions for fusion are met. Solid liners, though mature in development, have issues that make them barely suitable for use in a reactor due to the

creation of debris that needs cleanup in between shots and their high manufacturing costs. Plasma liner driven MIF (PLMIF) addresses that problem by making a reusable liner but at the cost of needing higher implosion velocities and loss of hydrodynamic efficiency due the liner being thicker than the solid one. This has the benefit of situating the driver hardware far enough away from the fusion pulses that it will not be significantly damaged during operation [19].

1.2.2.5 Fission-Fusion Hybrids

Research on fission-fusion hybrid reactors has been ongoing mostly for military applications for decades, but energy researchers have largely stayed away since this technique is not as environmentally friendly as the other concepts. Ironically, the pursuit of more benign fusion fuels has led to the use of fuels with lower ignition temperatures but produce high energy neutron flux that is greater than what is seen in most fission reactions. Essentially, modern nuclear weapons are fission-fusion hybrids in the sense that a fissile trigger is sent into criticality and the resulting neutron, gamma and alpha flux provides enough heat for a liner made from fusion fuel (mostly deuterium and lithium) to ignite. Turning a high-yield weapon into something that is repeatable and on a much smaller scale is quite a challenge, but there are promising techniques that make use of small pellets of fissile material coated with fusion fuel inside of MIF devices that are in development. One major effort is in the research being done by Adams, et al, on the Pulsed Fission Fusion (PuFF) propulsion system that is described in detail in Section 1.2.4 [25].

1.2.3 Challenges of Propulsion Applications

Space propulsion from a fusion reactor has many challenges of its own to overcome. We are a very long way from having the capabilities as advertised by the potential outlined earlier. Science fiction applications aside, there are many ideas that are grounded in physics that could lead us down the road of one day having an “impulse engine” from *Star Trek*. A study was conducted by Schulze [26] for NASA that included a roundup and analysis of all of the ideas that had come at that point in time. Though this study was published 30 years ago, most of the concepts and evaluations are still valid.

The Schulze memo is an extensive survey of the state of art of fusion technology, his analysis delved into both DOE and NASA efforts examining the benefits and shortfalls of each promising fusion technique. One important conclusion that he arrived at was that if NASA were to be serious about pursuing fusion propulsion, they would need to uncouple their efforts from the DOE efforts at terrestrial power production. Since worldwide energy supply was and still is quite abundant in other forms, energy from fusion is a low priority and therefore a relatively low funded part of the DOE research and development portfolio. Also, the best candidates for terrestrial energy production have been trending towards the use of immense facilities that would be hard pressed to be converted into a lightweight option that could be launched into orbit. Advanced reactor designs not being pursued by the DOE were better choices for propulsion at the time of Schulze’s analysis [2, 26].

The history of the study of fusion propulsion is rich with imaginative concepts that have ranged from near-term practicality all the way to interstellar flight. Schulze made observations from his survey of this history that fell into categories that fit within the different fusion confinement methods. For MCF, he found that best practices so far in

terrestrial applications yielded general characteristics that apply to space propulsion. Minimum specific power of 1 kW/kg would be needed for practical solar system exploration and a step function for interstellar travel made the threshold for specific power to be 10 kW/kg. Minimum mass would be required, but that is difficult to achieve since the coils, supporting structure and shielding for the magnets would be quite heavy for a flight system. The system would also need to minimize recirculation power for the reactor and be designed to permit a simple conversion to direct thrust and electrical power. Finally, Schulze determined that sustainable fusion propulsion in space ought to be able to get fuel from places in space and that the preferred fuel combination would be the D-³He reaction due to the relatively high amounts of both known to be out there. The reactor should be able to burn this fuel, but research focus on this fuel cycle on Earth has been lacking since terrestrial sources of the Helium-3 isotope are extremely rare.

MCF methods evaluated for propulsion include the Field Reversed Configuration (FRC), tokamak, spherical torus, tandem mirror, Spheromak, Electric Field Bumpy Torus (EFBT), ELMO Bumpy Torus (EBT), stellarator, and the aforementioned RFP. The FRC is a machine with a high ratio of plasma pressure to magnetic field pressure, or β_S [11, 14, 12], and is a “compact toroid” that combines attractive features of both toroidal and linear systems. The closed inner field allows for good plasma confinement and the linear topology of external magnetic field lines would allow for a straightforward and relatively simple way to vent plasma for direct thrust. FRC continues to be studied with several institutions using devices that operate in this regime, but major advancements have been few and far between due to low funding levels.

The tokamak does not appear to be a good candidate for propulsion for a variety of reasons that have already been pointed out, but Schulze decided that the chief disadvantages for a flight tokamak are low β_S values, heavy mass, high complexity and a specific power of around 10^{-4} kW/kg. The tokamak had also been determined by the time of his study to not be able to efficiently burn his preferred D-³He fuel cycle. The Spherical Torus is an idealized tokamak envisioned for space applications that would use superconducting magnets to eliminate large recirculating power fraction and mass associated with more conventional conductors in terrestrial spherical torus designs. The performance would be maximized by the D-³He fuel cycle with a theoretical power density of 5.75 kW/kg and the coil design has the possibility of polarizing the fuel combination to suppress neutron generation. This has an extremely low TRL, but there have been advances in the last 30 years with this device, namely through the National Spherical Torus Experiment [2].

The Tandem Mirror is a linear reactor, capable in theory of a wide range of specific impulse and specific power greater than 1 kW/kg. There has been little interest in funding development of this type of magnetic mirror beyond experiments in the 1970s and 1980s, but efforts have continued in Russia at a low level since Schultze's study. There have been recent advances in critical technologies, namely high temperature superconductors, that has caused renewed interest in this method for terrestrial power and investment has been ongoing with Lockheed Martin Skunkworks to develop a compact reactor using a magnetic mirror [27]. Another aspect of the tandem mirror is that other critical technologies have been under development using ion cyclotron resonance heating, but at a much lower power level intended for electric propulsion with the Variable Specific Impulse Magnetoplasma

Rocket (VASIMR) that was invented by former astronaut Franklin Chang-Diaz in 1977. Development has been ongoing since then and a startup, Ad Astra Rocket Company, has been working to commercialize it. This electrothermal thruster could be a good propulsion candidate for NEP and it utilizes many key technologies also needed in fusion propulsion [28].

The Spheromak is a compact toroid, similar to the FRC but with β_S values at two to five times lower than what is necessary for FRC. The difference between the Spheromak and an FRC is that a Spheromak has an extra toroidal field and the field can run both with and against the spinning plasma direction [29]. A space version of the Spheromak has been studied, but no experimentation has been done. Small Spheromaks have been used as a source to heat up plasmas before injection into a larger tokamak and they have also been used as a verification technique for astrophysical simulations. The reason they have utility in astrophysics is due to magnetic helicity enabled by the field configuration, this phenomenon occurs in many forms with natural space plasmas.

The Electric Field Bumpy Torus (EFBT) was pursued by NASA Glenn Research Center (then Lewis) when it was studying space fusion. This reactor design operated in steady state and combined electric and magnetic fields to confine and heat the plasma. The bumpiness of the toroidal magnetic field is due to the configuration being a ring of magnetic mirrors connected in such a way that a continuous magnetic field is created with spots of high intensity where the mirrors are located [30]. This was terminated in 1978 when funding ran out, but a successor to this technology was initiated at around the same time at Oak Ridge National Laboratory called the ELMO (Electro Magnetic Orbit) Bumpy Torus (EBT). The EBT was also a steady state system with β_S values of up to 0.5 that

made use of ion cyclotron resonance heating to provide initial high-relativistic energy for the plasma [31, 32]. Both of these Bumpy Torus configurations encountered problems with inherent limitations due to transport loss as well as excessive plasma leakage, which in turn caused funding to disappear from this area by the late 1980s.

Other MCF devices that have been studied for terrestrial power include the previously mentioned stellarator and RFP. Neither seem to be scalable to use in a propulsion system, the stellarator operates at a steady state but is very massive with specific power on par with the tokamak. After decades of stagnation in advancement of the stellarator, it is undergoing renewed interest with advancement in technologies and plasma physics. These new advances in stellarator design have increased the quality and power of the magnetic fields generated that have led to improved performance over predecessor designs. New devices that have been built in the last 20 years include the Wendelstein 7-X in Germany [33], the Helically Symmetric Experiment (HSX) in the United States [34], and the Japanese Large Helical Device [35]. The RFP has a much lower magnetic field than what is needed for a tokamak, but currently these designs need large recirculating power fractions for operation which drives up the mass of the system [26].

ICF has been researched and tested with increasing power levels and complexities since the early 1970s, but there are many obstacles to overcome before it can be a viable energy source. The most advanced ICF device currently is the previously mentioned NIF, and it is the product of decades of DOE work that has largely been focused on learning ignition properties for nuclear weapons. This means that most of the details of the work done in this field has been highly classified. There have been unclassified efforts around the world, most notably in Japan, but none are as sophisticated as NIF. This technique has

an extremely low TRL for space applications and there are major issues that would need to be addressed if ICF were to be used in space.

Fuel selection so far on ICF has been with D–T reactions, and this is something that was a concern to Schulze but it has a lower energy threshold for laser ignition than D-³He. A high gain reactor would be absolutely necessary to overcome the energy cost of achieving ignition as well as to bring the specific power to a high enough level to overcome the large mass of the reactor. The NIF achieved a fuel energy gain (the ratio of energy released by the fuel to energy absorbed) of 1.2 to 1.9 in 2013, but this does not account for the amount of laser energy that was dumped into the system and lost through various inefficiencies to deliver the energy to the fuel. Due to those losses the total gain demonstrated is on the order of 0.01, far short of the gain of 1500 identified by Schulze as necessary for propulsion [26, 36]. Laser technology would need to be considerably advanced as well with drastic increases in power output and reductions in weight. Other issues to be addressed include a high power and lightweight source of startup energy for the lasers, demonstration of ignition, safety concerns, reliability, simplification of operations, verification through extensive testing and great advances in the capabilities of space radiators to reject heat.

Many other confinement concepts were evaluated by Schulze with varying degrees of feasibility including the LLNL Ring Accelerator Experiment (RACE) which physically compresses plasma and accelerates it with a magnetic coaxial gun, and the PLASMAK Magnetoplasmod which would suspend a spherical plasma inside a vacuum contained by another plasma. Aneutronic fusion is claimed to be possible with this ball-lightning like apparatus, but it remains in the realm of science fiction. Another concept investigated was

MIGMA, which would direct ions into collision like in a particle accelerator; four small reactors to test this concept were built in the 1970s and 1980s with some early successes but funding dropped off when technical difficulties made it less attractive than other devices. The concept known as Magnetically Insulated Inertial Confined Fusion (MICF) would combine features of MCF and ICF containing plasma inside of a metal shell while the plasma would generate a magnetic field to thermally isolate it from said shell. A laser would be used to create the plasma, and the plasma could be expanded out of a magnetic nozzle for propulsion. This was funded in Japan for a time in the 1980s with several papers written, but no experiments have been performed to date.

IEC fusion devices have also been studied extensively for propulsion applications, with one of the leading advocates being the late fusion pioneer Robert W. Bussard [37]. His Polywell magnetically contained IEC device gained considerable traction over the last 20 years of his life, and in that time he devoted much of his efforts to commercializing the device with his company EMC2 Corporation. One of the largest benefits to the Polywell design is that the inherent feature of its magnetic coil system eliminates the need for electrode screens that drive energy losses that plague most other IEC designs [19, 38, 39]. There has been funding from multiple sources for this technology in fits and starts over the years, and breakthroughs may yet come with this technology. Schulze found this technology to have much potential as well as that of Magnetic Dipole containment, which was pointed out to have the potential capability of specific powers ranging from 1 kW/kg to 10 kW/kg. This technique by contrast to IEC has not yet been experimentally demonstrated. Schulze briefly mentioned the MIF-based dense z-pinch fusion, but did not

go into many details to his detriment in some ways since this field has advanced considerably in the last 25 years.

Fusion propulsion is highly configuration sensitive, with most applications of fusion power generation being fundamentally incompatible with space propulsion requirements. Schulze had a favorite concept using the FRC but admitted that much had yet to be determined with regards to its feasibility. Mass is key for space applications, but there are other significant factors pointed out by Schulze that would need to be addressed. Magnetic nozzles appear to be the most efficient way to convert plasma energy into controllable thrust power, but much work is still needed to make them practical. Other critical problems to solve beyond the capability of breakeven power include: development of high magnetic fields for space reactor designs, low specific mass magnets and lightweight structures, plasma stability under the flight regime, efficient plasma confinement, minimal recirculation power, space start and restart power, ash removal, reactor flight control systems under net power operation, mass flow rate augmentation, and space fuel conservation in exhaust plasma [26].

A key difficulty to all of the possible ways to do fusion is that we do not understand all that is needed to make these systems space borne. Research and therefore data are lacking to be able to make meaningful conclusions. Reactor masses need to be determined to find performance potential, but mass cannot be determined until critical fusion plasma confinement experiments which produce net power have been accomplished. The whole field is in a recursive loop until more data is generated. A good way to look at this is to take the view that simplicity will be the key for propulsion and most of the methods for fusion are not simple. MCF and ICF require large infrastructure and great power reserves

making them very impractical for propulsion, and IEC needs more work to determine its feasibility. Work innovated on by Bussard with IEC made enough progress on a contract with the US Navy that the results ended up being classified making it difficult to comment on its level of sophistication [2].

When observing the different methods of fusion in a parameter space comparing plasma energy levels and density, MIF operates at a middle ground in terms of affordability and power requirements making it an ideal candidate for fusion propulsion; it has the potential for a low-cost and relatively lightweight reactor for fusion break-even [40]. The parameter space (as shown in Figure 1.5) plots regions of density and plasma energy where fusion occurs for Magnetic Fusion Energy (MFE), MIF and ICF. In this space, MFE represents all of the different magnetically confined steady state reactors being studied for propulsion. The advantages for MIF are twofold; first it has a relatively high density (roughly between sea level air and liquid) that allows for smaller reacting volumes as compared to MFE and its embedded magnetic field suppresses cross-field thermal conduction that leads to losses. Its second big advantage is that the implosions can be driven by electromagnetically accelerated liners which is more efficient than lasers and MFE methods [2, 41].

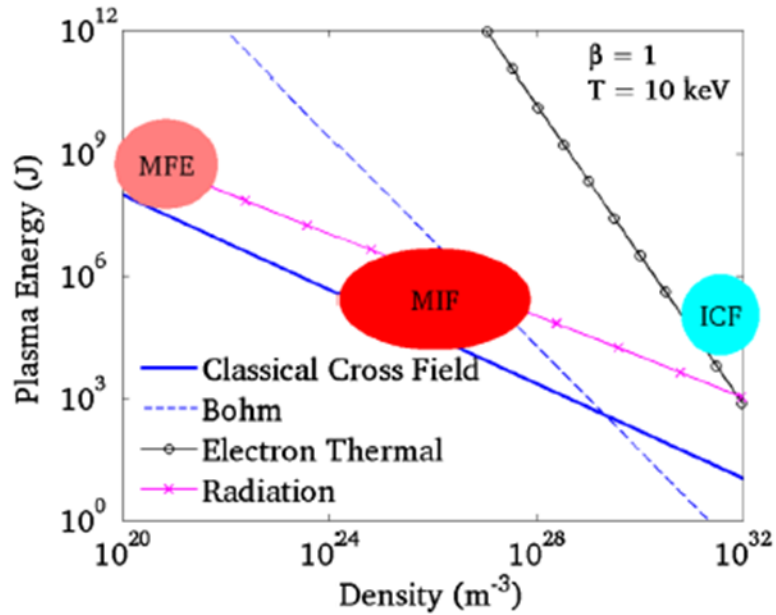


Figure 1.5. Parameter Space for MFE, MIF and ICF [2]

Starting in the late 1990s, a program was begun at NASA Marshall Space Flight Center (MSFC) to study the application of PJMIF to propulsion. Several iterations of these studies yielded a conclusion that a pulsed propulsion concept based on PJMIF could be the most feasible approach to a near-term application for propulsion. Elements of these studies led to efforts to evaluate pulsed z-pinch as the most near term method of MIF propulsion achievable. Pulsed power technology has emerged in the last 30 years that allows for favorable fusion yield that scales with the peak current and new plasma theories have led to ways of overcoming instabilities. A recent NASA MSFC study with several support contractors as well as the University of Alabama in Huntsville designed a crewed mission to Mars concept using pulsed z-pinch propulsion and other elements developed from previous studies at MSFC. This propulsion system is a central element to this thesis and an experiment is being commissioned to test concepts in z-pinch for propulsion [42].

The concept vehicle designed around the z-pinch propulsion system, shown in Figure 1.6, has heritage in an earlier study that used Magnetized Target Fusion (MTF) as an option for Human Exploration of the Outer Planets (HOPE) [43]. This study incorporated a systems engineering approach to build a spacecraft around the fusion propulsion system that identified all of the critical technologies needed to sustain MTF. These features were incorporated into the later z-pinch spacecraft including the usual habitation modules, propellant tanks, radiators and a fission reactor to power the spacecraft and kick start the propulsion system. Systems definition and design work also delved into what it might take to develop flight-weight systems such as the magnetic nozzle, power distribution systems, capacitor modules to power the z-pinch system, and a multilayer radiation shield.

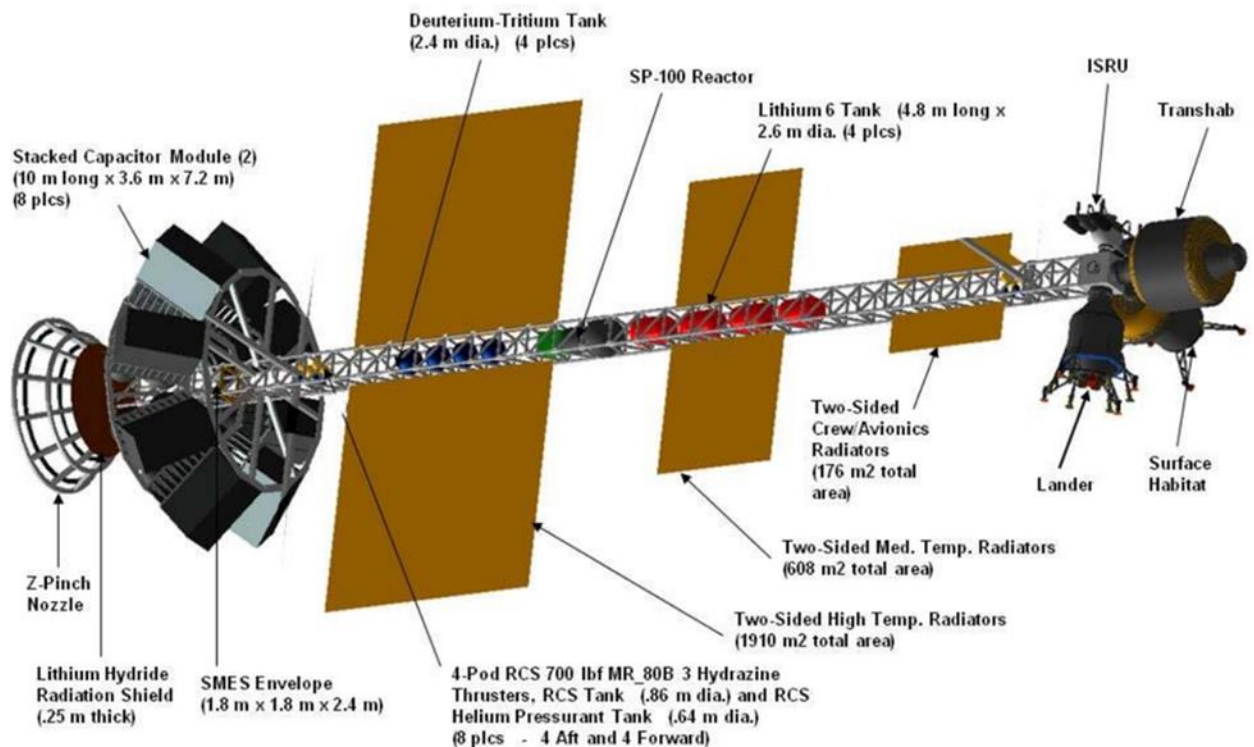


Figure 1.6. Conceptual Crewed Spacecraft Using Z-Pinch Pulsed Fusion [40]

1.2.4 Z-Pinch Propulsion Overview

The nature of MIF driven by z-pinch dense plasma is one of extremely large amounts of current driven through plasma on timescales of a couple hundred nanoseconds. If this ignition mechanism could be coupled to a sequential system and allowed to run through implosions at a rapid rate, the plasma could be exhausted into space via a magnetic nozzle and produce a respectable amount of thrust and considerable specific impulse. This would amount to being a pulsed propulsion system and could be quite achievable given the right amount of commitment to research and development. As a functioning flight system though, many hurdles remain to make that dream a reality and the fundamentals need to be understood through experimentation and test.

At this point it would help to explain some of the nomenclature, as z-pinch is an MIF technique but not all MIF techniques are z-pinch. A high current is sent through a conductive column, either a solid or a gas (as in the case of PLMIF), and the cathode is along the z-axis of this column. The “pinch” in the z-Pinch is due to the strong magnetic field that is generated by the mega-ampere scale current travelling along the length of the plasma; as the current increases and peaks, the magnetic field constricts causing radial implosions to occur in the plasma. The ionization and implosion cycle occurs in time-scales of microseconds and can be broken down into a number of steps that occur in the following order, assuming a PLMIF configuration:

1. Gas injection/pre-ionization
2. Compression/implosion
3. Stagnation/burn
4. Expansion/explosion

This cycle is very similar to the thermodynamic Otto cycle and is visually demonstrated in Figure 1.7. The first step above is similar to the valve intake process of an internal combustion engine, the second step is akin to the adiabatic compression stroke, the third step can be approximated as a constant volume heat addition step of the Otto cycle and the fourth step is like the adiabatic expansion and exhaust portion of the cycle. This analogy is not perfect, but it is a good fit to describe the process mechanically. Instead of spark plugs to provide the energy for the burn portion like in the Otto cycle, the spark generator in the z-pinch process is on the order of 10^3 to 10^6 joules in energy instead of the range of 10^{-3} to 10^{-2} joules in a spark plug [42].

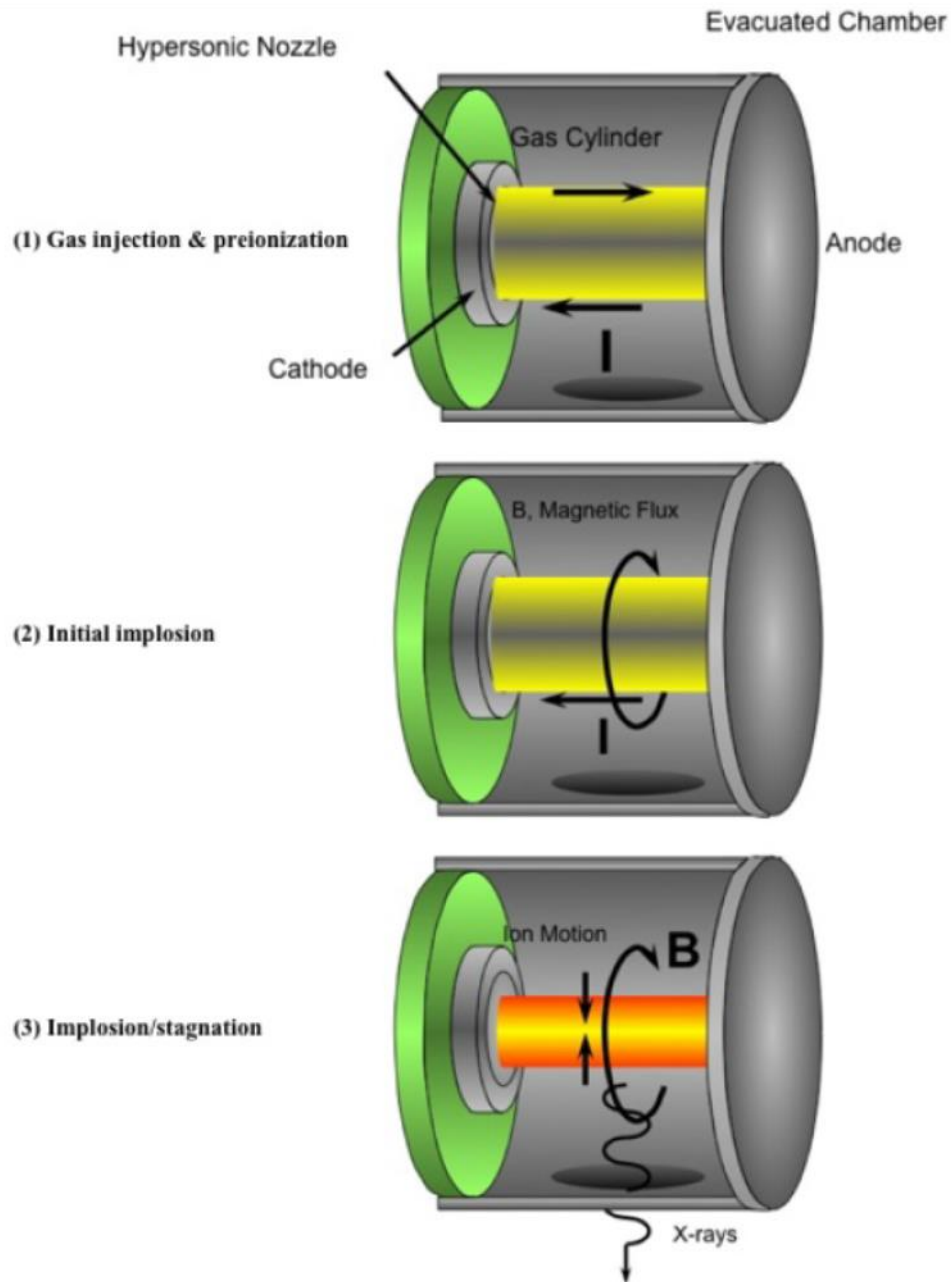


Figure 1.7. Stages of the Z-Pinch Cycle [42]

There have been several studies conducted by a variety of organizations on the application of z-pinch propulsion to spacecraft over the years, and since many fuel combinations are possible in this configuration there has been debate over what works best. Historically with z-pinch, there have been plasma instabilities that have stymied efforts at

making sustained reactions. Many experiments have been conducted to a varying degree of success in an attempt to utilize the plasma created to induce fusion on a timescale that is faster than one where instabilities start to develop. An example of this is the MagLIF experiment at Sandia National Laboratory, which uses a pulsed-power machine to implode a cylindrical liner onto a pre-heated and magnetized fuel and ultimately resulted in D-D and secondary D-T fusion reactions [44]. Other experiments that have been conducted include the Los Alamos National Laboratory (LANL) High Density Zeta Pinch (HDZP) [45] and the ZaP Flow at the University of Washington [46].

With the advent of more precision control in pulsed power as well as new modeling and simulation techniques and the lessons learned from the aforementioned experiments, the fundamentals to making propulsion possible have emerged [2, 47]. The potential for z-pinch stretches from concepts for interplanetary travel [42] all the way to interstellar with the Firefly Icarus concept [48]. The focus here will be on output from the NASA MSFC study that revolves around a piloted round-trip mission to Mars.

In an optimized configuration for propulsion like in the NASA study, the Z-pinch would be formed using annular nozzles injecting two different fuel mixtures into the reaction chamber. The innermost nozzle would contain a deuterium-tritium mixture and the outermost nozzle would contain a lithium-6/7 mixture, as shown in Figure 1.8. The chamber configuration would be focused in a conical manner so that the different fuel mixtures would meet at a specific point to act as a cathode allowing for the lithium-6/7 mixture to be the current return path back to the anode. The lithium-6/7 mixture also acts as a radiation shield to moderate neutrons from the D-T reaction; the lithium-6 reacts with neutrons to produce tritium adding additional fuel to the reaction and thus energy is boosted

[40]. The NASA study determined that this configuration would make a high performance engine with careful regulation of fuel mixture ratios and a pulse frequency of at least 10 Hz [8].

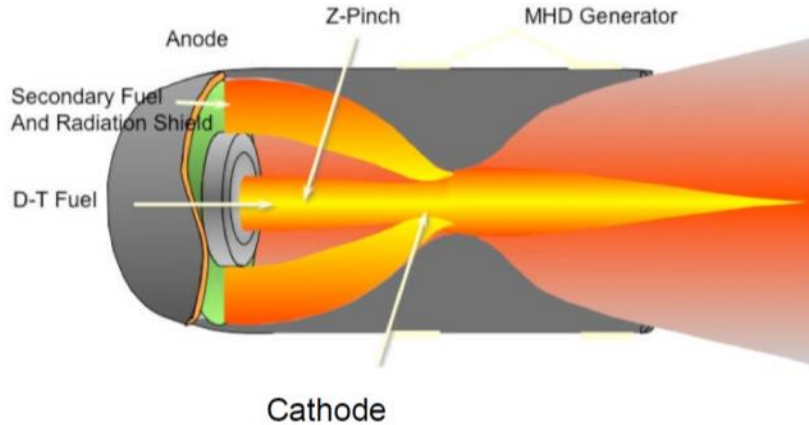


Figure 1.8. Optimal Z-Pinch Engine Concept [42]

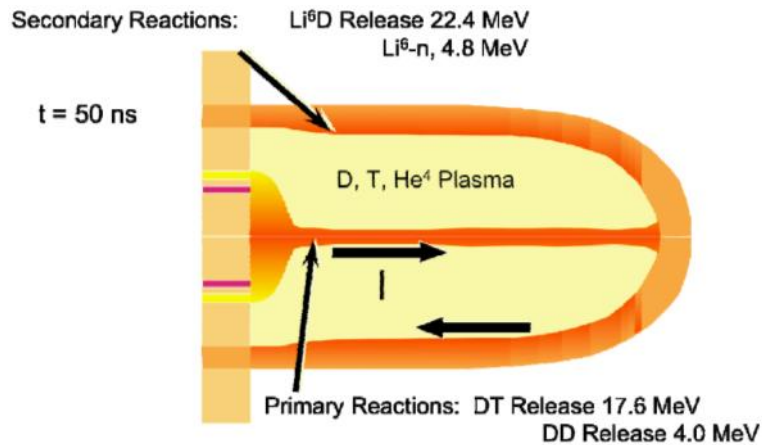


Figure 1.9. Reactions in the Z-Pinch Fusion Ignition Chamber [42]

An optimized system making full use of the potential for z-pinch/dense plasma focus propulsion will require several critical technologies working together that are still under development and immature. One such example is double-shell nozzles for injecting the concentric columns of the different plasma compositions necessary to create the

different fuel layers; this technology has been demonstrated for z-pinch devices before but more work is needed [49]. There are other potential configurations that could be equally viable or more easily achievable for this kind of propulsion system, especially when considering the amount of power needed to start and sustain such a reaction. One of these concepts is known as Pulsed Fission Fusion (PuFF) propulsion, and this method being studied as an alternate configuration in the design studies for the conceptual spacecraft shown in Figure 1.6. In addition to the fusion fuels described in the optimum configuration, the fusion reaction is aided by a fission target containing a small amount of uranium or another fissile material. A common feature between PuFF and the optimum fusion concept is in the use of an injectable lithium shell as a current return path as well as a neutron absorber.

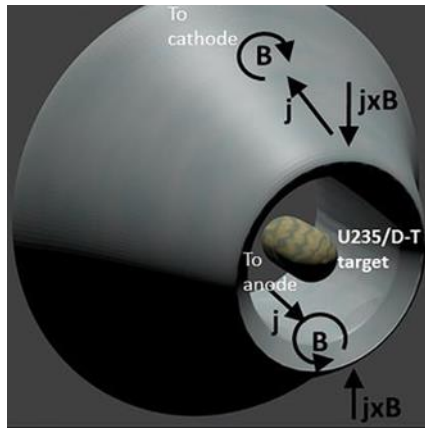


Figure 1.10. Pulsed Fission Fusion hybrid target geometry with outer lithium cone [25]

The PuFF reaction is accomplished via the z-pinch compression of a hybrid target of uranium and D-T to one-tenth of original size, reaching criticality for the fissile material. This criticality produces neutrons and heating from a spontaneous fission reaction, which in turn heats the D-T fuel creating conditions for fusion for the first stage of the reaction. The second stage of the reaction occurs as the fusion produces additional neutrons which

ignite more fission in the remaining fissile material. These additional fission reactions generate more heat and neutrons, boosting the fusion rate in a cascade cycle of fission to D-T fusion and back again until burnout from fuel exhaustion [25].

The plasma produced in this impulse would then expand outward against the magnetic nozzle, in the same fashion as the exhaust from the previously discussed pure fusion concept would. This magnetic nozzle directs the charged particles to generate thrust as well as capturing some of the plasma energy to recharge the system for another pulse. This single target impulse event would occur over several microseconds, with a pulse cycle upwards of 100 Hz. In order for a sustained thrust to be possible, the fuel injection system would need to be extremely reliable and repeatable. Pre-ionization of plasmas would be useful in this setup for injection at these extreme pulse rates but the PuFF targets would present some difficulty since ionization of uranium would be impractical. This spacecraft concept is also dependent on a series of stacked capacitor modules that can fire and recharge sequentially to deliver the necessary current for implosions. Recapture of some of the plasma energy to help recharge the capacitors for the next shot as well as a rapid recharge rate will be essential for this pulse rate to be achieved.

1.2.4.1 Charger-1 Facility

All of the challenges outlined for fusion propulsion can be overcome, but trade studies coupled with theoretical modeling and simulation can only go so far without data to anchor those models. Plasma instabilities are difficult to predict and magnetic nozzles are a very immature technology. There are several devices that can perform fusion via z-pinch, a major example being the Z-Machine at Sandia National Laboratories, but none are currently geared towards propulsion research and data generated by these devices remain

largely classified. A better understanding is needed of z-pinch characteristics in a propulsion configuration and a testbed for these propulsion concepts is under development for research and development in academia and industry. This testbed will have the added benefit of being able to produce results in an unclassified environment when needed, allowing for a focus on academic collaboration and publication.

This effort is led by the University of Alabama in Huntsville (UAH) Propulsion Research Center with its Charger-1 Pulsed Fusion Propulsion testbed [50]. This device, which is under construction in a laboratory on the US Army Redstone Arsenal, will be able to produce implosions of fuel sources for durations on the order of 100 nanoseconds once operational. The Charger-1 facility is being commissioned to study direct applications of Z-pinch techniques to propulsion systems. Fundamental physics in plasma interactions with magnetic fields, ignition, burn stability and other phenomena need to be better understood and models need to be anchored in this extreme condition. In order to bring everything together to make this experiment become a reality, UAH has formed a consortium for fusion propulsion research with partners that include NASA, the US Army, the US Defense Threat Reduction Agency (DTRA), the Y12 National Security Complex, the State of Alabama, the Boeing Company, and L3 Communications.

The Charger-1 facility will bring a unique capability to academic propulsion research, for most other z-pinch devices have been used in the realm of simulating nuclear weapons effects. It utilizes a Marx generator coupled to a transfer capacitor which transmits a pulse of energy through a magnetically insulated transfer line. This device is built from a power module called DM2, which was originally a development prototype for the Decade Radiation Test Facility (DRFT) located at US Air Force Arnold Engineering

and Development Center. In the DRFT, four modules identical to DM2 are coupled together with output diodes meeting at a single point to create imploding plasma loads and x-rays to simulate the radiation conditions of nuclear weapons effects in order to test military equipment in this environment. Once DM2 became available, the UAH fusion propulsion consortium was able to obtain it and move it to Redstone Arsenal in 2010. The slow process of converting this device into a propulsion testbed has been ongoing ever since.



Figure 1.11. UAH Propulsion Research Center Charger-1 Testbed

The DM2 is capable of storing 572 kJ worth of energy at a potential of ± 21.25 kV, and can discharge this energy in a pulse width of 47 nanoseconds at 30 times the current of a lightning bolt. This energy discharge can drive imploding plasma radiation loads for soft x-ray production in the range of 1 – 5 keV through a bremsstrahlung diode [51]. In the initial Charger-1 configuration, DM2 will transmit its pulse into a vacuum chamber with one wall being a cathode and the opposite wall being an anode. Completing this circuit will be an array of Lithium-6 wire coated with deuterium ($D-^6\text{Li}$), a configuration that allows for the most basic of fusion implosion loads to be studied. Upon introduction

of the discharge current, the wire array will vaporize forming a cylinder of conductive plasma. Magnetic flux will then compress the plasma into a focus point causing an implosion and brief ignition of the plasma. If the gas injection step in Figure 1.7 was started as the aforementioned wires, then the process shown would be very representative of the initial Charger-1 configuration.

This method is known as “gas puff”, and the main focus of this experiment will be an attempt to learn how to leverage and control instabilities that occur in the plasma during the gas puff. This research is more into the fundamentals of a technique that if mastered, could be used in the pulsed fusion propulsion system. There are multiple potential configurations for the D-⁶Li wire array diode that will be tested, and the collaboration with the Y12 complex allows for access to this wire through their proprietary manufacturing techniques. Before this can be tested, initial experiments are planned with aluminum and copper wires as surrogates in order to verify the z-pinch plasma creation process. The next step will involve the D-⁶Li wire diode configuration, and a final potential step would be liquid injection of this material. The goals for this will be the measurement of x-ray and neutron output, estimation of fusion energy output, code validation, optimization of diode design and scaling for break-even design.

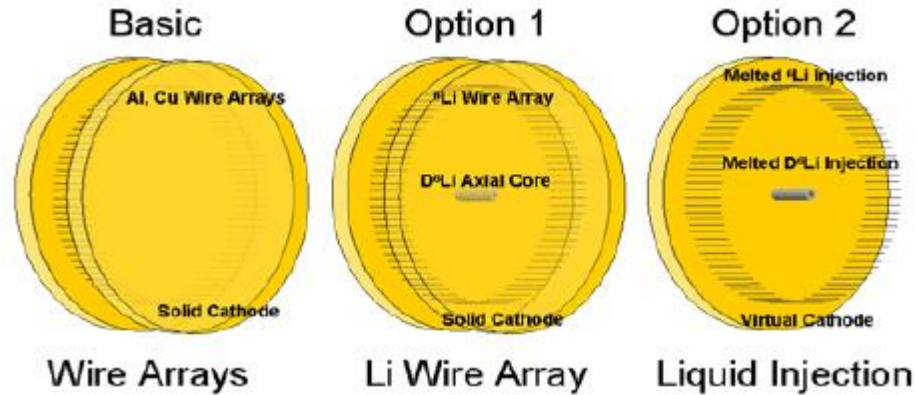


Figure 1.12: Wire diode configurations to be tested [2]

The Charger-1 testbed will grow beyond this basic configuration with the addition of a magnetic nozzle in an expansion from the initial vacuum chamber capability. This will allow for plasma flow to be more readily studied in a relevant configuration for propulsion. One goal envisioned in this expansion will be to evaluate the underlying impulse physics of hybrid PuFF targets. This leverages legacy nuclear experience with the potential for nearer term sustainable thermonuclear fusion and addressing of plasma stability issues. The availability of nuclear material will largely determine when this experiment could be conducted. Other potential applications include the study of conditions relevant to astrophysical phenomena such as the simulation of a solar Coronal Mass Ejection (CME) event, which is a significant factor in space weather that affects all spacecraft. There is also still much to be learned about the operation of magnetic nozzles, and the availability of plasma at these energy levels will present an opportunity to study magnetic seed field propagation, field line freezing and the subscale verification of space weather codes (much like the CME experiment) [52].

Regardless of the configuration, there is the potential for much higher energy ionizing radiation than is produced in the soft x-rays from basic imploding plasma loads.

These implosions will create ionizing radiation in the form of x-rays and neutrons that will need to be shielded against to protect personnel and equipment. Several design concepts have been put forward to address radiation protection for the Charger-1 facility, but modeling and simulation of the facility and radiation environment produced by the operation of the experiment has thus far been lacking. One of the focal points of this thesis will be in that modeling and simulation as it relates to the design of radiation protection and verifying that the concepts will indeed make the Charger-1 facility safe for operation.

1.2.4.2 Z-Pinch Spacecraft

The z-pinch spacecraft design concept shown in Figure 1.6 was the output of a thorough systems study at NASA MSFC by Polsgrove et al. that incorporates critical elements from the pulsed power machinery discussed in the previous section [40, 42]. The stacked capacitor modules are arranged in such a way that the pulse and recharge method could be optimized for a functional propulsion system. Other subsystems identified include propellant tanks, radiators, a fission reactor for startup power, crew habitation modules, a magnetic nozzle, and most importantly a multilayer radiation shield for crew and equipment protection. This shield is part of another focus of this thesis, and it is another item that will be subjected to modeling and simulation via the same techniques used for the Charger-1 facility. A major difference between the two is that the spacecraft shielding will need to be made of lightweight materials in order to be feasible for spaceflight, and this will be discussed in much greater detail in upcoming chapters.

1.2.5 Monte Carlo Methods for Analysis of Radiation Environments

As this thesis unfolds, it will quickly become apparent that there are many methods and standards in existence to size radiation shielding adequately for the protection of life and equipment against many different types of sources. There are also many ways to estimate the dose received depending on if the recipient of the dose is a living being or an inanimate object. In both general cases for shielding and dosimetry, most of the methods available rely on relatively simple equations and tables of data to obtain approximations that are usually adequate for most situations. In order to obtain accurate results, statistical tools are needed due to the behavior of high energy particle interactions and the most common tool for this is in the use of Monte Carlo simulations to develop probabilistic determinations of the various outcomes of particle interaction. The most common codes in use for this Monte Carlo process are FLUKA (FLUktuierende KAskade), GEANT4 (GEometry ANd Tracking) and MCNP (Monte Carlo Neutral Particle).

FLUKA was developed and is managed by the Italian INFN (Istituto Nazionale di Fisica Nucleare) and CERN (Conseil Européen pour la Recherche Nucléaire or in English: European Organization for Nuclear Research) [53]; GEANT4 is another product of CERN development [54]. MCNP was developed and is managed by the Los Alamos National Laboratory (LANL). Both FLUKA and MCNP were written in the Fortran language and are largely text-based, while GEANT4 is the first package of this type written in C++ giving it the ability to be largely graphically based. In all cases these codes utilize large data libraries with the properties of materials at wide varieties of energy levels as well as particle interactions. Each code has its strengths and weaknesses, but they are all powerful

in the hands of the right user. MCNP is the code of choice for all of the modeling and simulation work in this thesis.

1.3 Survey of Literature and Related Work

From the beginning of the research effort for this thesis, the first cuts at analysis were run using hand calculations from accepted standards for design of one type of shielded facility. This initial analysis was completed with only a bare understanding of the fundamentals of radiation dose and other mysteries that were hidden in the details of countless sources yet to be found. When MCNP was chosen as the analysis tool of choice to meet the objectives of this thesis, another learning curve had to be surmounted with this one steep enough and high enough that the air was very thin. The oxygen tank for this hill climber ended up being in the form of a few chosen documents that explained the basics of MCNP and Monte Carlo methods in general as well as snippets of code and hints of ways to solve the puzzles ahead.

An initial literature survey of Master's Theses and PhD Dissertations was performed in the relevant areas of shielding, dosimetry, radiation environments, spacecraft applications, and many others using MCNP as an analysis tool. Many of these documents yielded a treasure trove of information to educate a beginner user of MCNP, most of the lessons learned having been earned over multiple iterations and strategies for convergence and optimization. The most important ones that yielded insights were a group of four Theses and three Dissertations.

The theses by Chinaka [55], Lukhele [56], and Meyerian [57] as well as the dissertation by Davis [58] provided valuable insight and references to help with the theoretical underpinnings of the radiation environment, dosimetry basics, and the

fundamentals of Monte Carlo Simulations. The focus of Davis on shielding optimizations for the ITER reactor is particularly relevant to this thesis, it provides a rich resource for data on the fusion world as well as validation of Monte Carlo methods used for the much simpler analysis in this thesis. The thesis by Spackman [59], as well as the dissertations by Dickson [60] and Asbury [61] created a space to show how deep and thorough shielding studies involving MCNP and other coding techniques could go.

Kowash [62] showed in his thesis the potential for using MCNP to assist in the optimization of shielding design for spacecraft, but his focus was on setting up a path to optimization with MCNP as one cog in his machinery of code. The most insight that led to the approach this thesis ultimately used was gained from the work of Dugal [63] and later Khatchadourian [64] in their respective theses. Both of these focused on using MCNP to optimize shielding for medical neutron facilities, with Khatchadourian actually building upon and referencing Dugal's work for his research done seven years later. The most important takeaways for the research done and published by Dugal involved the use of spherical dose phantoms and the method of modifying the MCNP input with the proper flux-to-dose conversion factors. If it were not for the work of Dugal as well as the MCNP Primer by Shultis and Faw [65], the learning curve for MCNP would never have gone beyond the first set of foothills into the mountains.

Beyond literature surrounding MCNP in shielding, the textbook by Chilton, Shultis and Faw [66] as well as the chapter by Shultis in the handbook by [67] provided the best formal theory behind the principles of radiation shielding. The textbook by Emrich [68] as well as class notes from a class he teaches on fission propulsion at UAH provided everything needed for the code verification and test cases. The interactive nature of

Emrich's book being published as viewable on the Mathematica software package meant that a parametric calculator could be used to compare with MCNP code on otherwise difficult to solve neutron attenuation problems.

Various industrial standards by the International Council for Radiation Protection (ICRP) and the National Committee for Radiation Protection (NCRP) were handy references for shielding design on a variety of types of radiation sources. The equations in these standards make use of many attenuation assumptions that are tabulated as results from extensive Monte Carlo simulations in the past. The most important standard used in this thesis ended up being ICRP 74 [69], for it established the formal methodology behind the flux-to-dose conversion factors used in this thesis as well as Dugal's. Finally, the various user's manuals for the different versions of MCNP used in the many iterations for this thesis were extremely valuable for learning the fundamentals behind why some models would work and others would not. LANL also provided several technical papers expanding upon applications of MCNP to different aspects of radiation work.

1.4 Objectives of this thesis

The objectives of this thesis are wide-ranging, but in short, all involve analysis of radiation shielding concepts. The first goal is to create an MCNP model of the Charger-1 Pulsed Power Facility as it relates to the radiation source and existing infrastructure for protection of personnel. The simulation results from this model will tally the dose received in phantoms (spherical detectors composed of generic organic material) placed around the facility in areas behind the wall, in front of the wall and right next to the source. These results will be used to calculate attenuation of the existing concrete wall and intervening

air between the user and the radiation source in order to meet the objective of verifying that the Charger-1 facility will be safe for personnel.

The second objective of this thesis will be to apply the same techniques to the z-pinch spacecraft in Figure 1.6, which carries a lightweight multi-layer shield just forward of the magnetic nozzle of the propulsion system. This multilayer shield was studied in some detail for the paper by Polsgrove, et al., with attenuation curves being found through a parametric tool that also allowed for mass estimates to be derived for the shield. The addition of MCNP techniques to analyze shielding problems in spacecraft could lead to more accurate mass estimates for future studies of any spacecraft using a form of nuclear propulsion.

To assist in the objectives of this thesis, two code verification efforts will be used to validate the assumptions for studies on the facility as well as the spacecraft. MCNP is a powerful tool to simulate the effects of high energy neutral particles being introduced into an environment, but in order to verify the accuracy of the MCNP techniques, textbook problems in radiation shielding and attenuation will be used. One effort will focus on photon attenuation and the other will focus on neutron attenuation via the creation of MCNP models of the textbook problems.

1.5 Summary of the Approach

Up until this point, the context of the importance of fusion propulsion has been established and hints have been dropped about the hazards associated with the radiation produced by such a propulsion system. Now the thesis will dive into the details relevant to the objectives that were laid out in the previous section. In Chapter 2, the thesis

establishes the basics of the physics and the environment of ionizing radiation as well as the fundamentals of dosimetry. Chapter 2 also delves into the established standards for radiation protection and the fundamentals of the design of radiation shielding.

In Chapter 3, the basics of MCNP will be discussed in great detail with a particular focus on techniques relating to dosimetry from particle tallies and the error reduction methods used. Chapter 3 concludes with an overview of the models for test cases run for the verification problems. Chapter 4 will discuss the development of the models used in the MCNP analysis of the Charger-1 facility and the z-pinch spacecraft and lay out the grounds rules and assumptions for each model. Chapter 5 will present the results of the MCNP analysis for the Charger-1 facility and z-pinch spacecraft. Chapter 6 will be a discussion on the conclusions of this of this effort with an emphasis on lessons learned, applicability to future efforts, and a spectrum of items of concern for fusion propulsion researchers to be aware of with regards to ionizing radiation produced by their experiments.

The appendices of this thesis contain detailed accounts of all of the modeling and simulation efforts on the code verification test cases. The appendices focus on theoretical underpinnings of the verification problems as well as the methods used to arrive at satisfactory results to generate confidence in the MCNP techniques. As a benefit to future researchers, MCNP input decks from each major model iteration used in this analysis are also included in the appendices.

CHAPTER 2. PROTECTION FROM IONIZING RADIATION

2.1 Ionizing Radiation

Ionizing radiation is conceptualized as a broad range of particles that can strip electrons from atoms to form ion pairs and is divided into directly and indirectly ionizing categories. Directly ionizing radiation consists of fast moving charged particles with sufficient energy to ionize through many small interactions; examples of which include alpha and beta particles. Indirectly ionizing radiation consists of uncharged particles which transfer their energy to charged particles in relatively few interactions; these particles penetrate deep into matter and are the most difficult to shield. These particles when emitted go in all directions from their source and collectively, the particles and their trajectories in some region of space or unit of time are known as a radiation field [67].

High energy photons in the form of x-rays and gamma rays as well as neutrons are indirectly ionizing particles. High energy photon interactions can cause scattering of additional photons at lower energy levels until absorbed, this emission and absorption counts as additional secondary radiation. High energy neutrons can activate nuclei to decay and emit additional particles until thermal equilibrium is reached. During this process secondary radiation is produced through scattering of new photons and emission of lower energy neutrons.

Different particles have different properties at given energy levels and therefore have different interactions with matter. Alpha particles are high energy ionized helium nuclei that can be stopped by paper, but internal exposure can cause cell damage due to soft tissue interactions. Beta particles are high energy electrons that can be stopped by

aluminum foil, but at a high enough energy, interactions will induce x-ray scattering. This type of scattering is the primary mechanism for generation of high energy photons in x-ray tubes. Other charged particles include protons, deuterons, tritons, Helium-3, and heavy ions. These charged particles interact with atoms through electromagnetic force with energy loss being a direct result of the interaction between the electric field of a moving charge and that of the medium. This can result in ionization with the residual atom or molecule left in a disassociated state. Charged particles interact intensely with matter losing energy in short distances. High energy photons in either the x- or gamma ray spectra can penetrate deep into matter and cause secondary emissions of photons [55, 66].

The transport of high energy particles through various media and the interactions resulting from this transport is the fundamental process by which shielding is designed and analyzed. Two different quantities are defined for particle fluence and particle flow to characterize a radiation field and its boundary conditions. The particle fluence and flow are radiometric properties of a field, as opposed to the dosimetric properties which deal with the energy transferred by that field [67]. These concepts will be explored in much greater detail in the following sections.

2.2 Radiation Fields and Sources

Radiation fields are fundamentally a subatomic realm, but the details and timespans of individual particles are not as useful to a shielding analysts as are more macroscopic concepts developed to be able to create the bounds of the problem. First, a note on directions and solid angle conversions. Radiation field directional properties are described using spherical polar coordinates where the direction vector is a unit vector given in terms of Cartesian unit vectors **i**, **j**, and **k** by [66, 67]

$$\mathbf{\Omega} = iu + v + kw = i \sin \theta \cos \psi + j \sin \theta \sin \psi + k \cos \theta \quad (9)$$

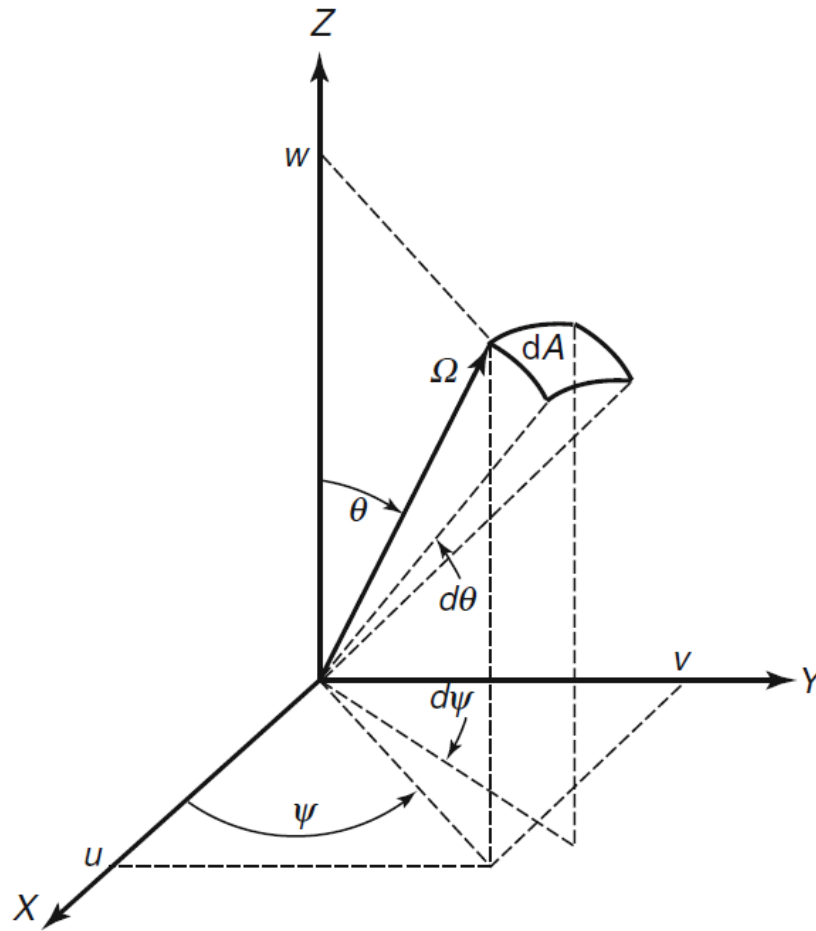


Figure 2.1 Spherical polar coordinate system to specify the unit direction vector $\mathbf{\Omega}$ [67]

2.2.1 Fluence and Net Flow

A fundamental for measuring a radiation field depends on the characterization of the number of particles that enter a specified volume. This characterization is accomplished by radiometric concept of fluence. Particle fluence at any point in a radiation field can be defined in terms of the number of particles ΔN_p that penetrate a hypothetical sphere of cross sectional area ΔA as illustrated in Figure 2.2a. The fluence is defined as

$$\Phi \equiv \lim_{\Delta A \rightarrow 0} \left[\frac{\Delta N_p}{\Delta A} \right] \quad (10)$$

Another useful definition for fluence is in sum of path length segments $\sum_i s_i$ within the ΔV volume of the sphere as illustrated in Figure 2.2b.

$$\Phi \equiv \lim_{\Delta A \rightarrow 0} \left[\frac{\sum_i s_i}{\Delta V} \right] \quad (11)$$

The difference quotients described in Equations 10 and 11 are useful conceptually, however a more accurate representation was developed by the ICRU [70]. This prescribed that fluence should be given in terms of differential quotients since ΔN_p is the expectation value of the number of particles entering the sphere [67]. The fluence rate, or flux, is the per unit time expression of the number of particles entering a sphere, or the sum of path length segments traversed within a sphere as shown in

$$\phi \equiv \frac{d\Phi}{dt} = \frac{d^2 N_p}{dA dt} \quad (12)$$

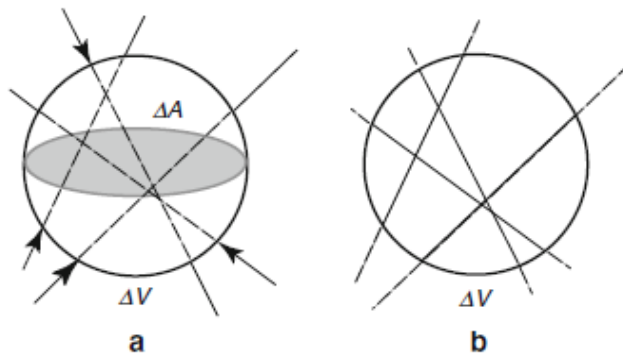


Figure 2.2: Element of volume ΔV in the form of a sphere with radiation penetrating cross sectional area ΔA in (a) and traveling via paths through the sphere in (b) [67]

2.2.2 Radiation Current

The radiation current is the net number of particles crossing a surface with a well-defined orientation over a specified time interval. The net number of particles flowing across a unit differential area on the surface in net particle flow are heading in a direction specified as positive. The surface, as shown in Figure 2.3, has one side characterized as the positive side and identified with a unit vector \mathbf{n} normal to area ΔA . The number of particles crossing ΔA from the negative to the positive side is ΔM_p^+ and the number from positive to negative is denoted by ΔM_p^- such that $\Delta M_p \equiv \Delta M_p^+ - \Delta M_p^-$. The net flow is given as

$$J_n \equiv \lim_{\Delta A \rightarrow 0} \frac{\Delta M_p}{\Delta A} = \frac{dM_p}{dA} \quad (13)$$

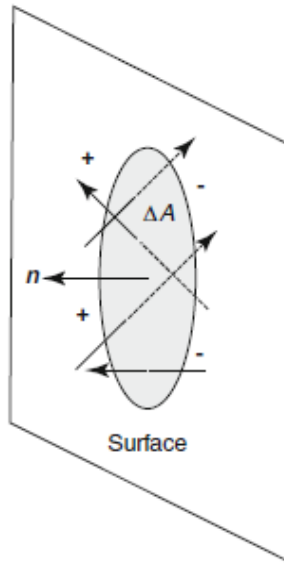


Figure 2.3: Element of area in a surface where particles cross the area from the other side

[67]

2.2.3 Radiation Field Directional Properties

The resulting fluence from computation is a point function of position \mathbf{r} , but any attempt at measurement of fluence will result in a large amount of uncertainty as well as ambiguity in identifying the actual “point” from which the radiation is being emitted. This error has much to do with the fact that the detector has finite volume in which to track the particles. Though particles are naturally implicit, and the argument \mathbf{r} in $\phi(\mathbf{r})$ is sometimes implicit, with no other arguments ϕ or $\phi(\mathbf{r})$ represent the total fluence regardless of particle energy or direction. To expand the concept of fluence to include the information on particle energy or direction, the use of distribution functions are necessary. For example, the fluence energy spectrum contained by the expression $\phi(\mathbf{r}, E)dE$ is the fluence energy spectrum of particles with energies between E and $E + dE$. Angular dependence of fluence adds the angular variable in the vector direction $\mathbf{\Omega}$ which is a function dependent on the polar and azimuthal angles, θ and ψ . The angular fluence at \mathbf{r} is represented by $\phi(\mathbf{r}, \mathbf{\Omega})d\Omega$; the joint energy and angular distribution is defined such that $\phi(\mathbf{r}, E, \mathbf{\Omega})dEd\Omega$ is the fluence of particles with energies in dE about E as well as with directions in $d\Omega$ about $\mathbf{\Omega}$ [66, 67].

2.2.4 Characterization of Radiation Sources

For most analysis, the most fundamental type of source is the point source for its inherent simplicity. Real sources can be approximated as point sources so long as the following assumptions can be met. First, the volume of the real source must be sufficiently small with dimensions much smaller than the dimensions of the attenuating medium between the source and the detector. Next, there needs to be negligible interaction of radiation with the matter in the source volume; this requirement can be relaxed if source

characteristics account for self-absorption and other interactions between source and particles [67].

A point source is normally characterized as dependent on energy, time, and direction. Some timespans for the delay in the change in a radiation field as a result in a change of a source are usually negligible, time is not treated as an independent variable. Most point sources have a general characterization in terms of energy and direction such that $S_p(E, \Omega)dEd\Omega$ is the number of particles emitted with energies in dE about E and in $d\Omega$ about Ω . The most conservative and simple of shielding analysis methods have the point source treated as isotropic so that the source characterization only requires $S_p(E)dE$ to be the number of particles emitted in dE about E per unit time. Isotropic sources include radioisotopes, fission sources, capture gamma rays and fusion sources; examples of non-isotropic sources include directional x-ray and proton beams [66, 67].

2.2.5 Neutron Sources

2.2.5.1 Fission Sources

There are many heavy nuclides that will emit neutrons either spontaneously as a byproduct of a fission event or from the absorption of a neutron from a nearby fission event. These fission neutrons may in turn produce secondary radiation sources from processes such as scattering; transmutation of stable isotopes into radioactive isotopes may also be a consequence of interaction with these neutrons.

Fission sources produce two types of neutrons, the vast majority being fast neutrons emitted within 10^{-7} seconds of the event. The delayed neutrons are less than 1% of the total fission neutrons and are produced by the neutron decay of fission products happening many minutes after the first fission event. The delayed neutrons have significantly less

energy than the fast (or prompt) neutrons and are therefore not usually accounted for in shielding analysis.

A large family of transuranic isotopes that have appreciable spontaneous fission probabilities can be used as compact sources of fission neutrons. The most studied of these isotopes are those instrumental in nuclear weapons and power applications such as ^{235}U with its energy dependence of the fission neutron spectrum having been extensively studied. All fissionable nuclides have their own unique distribution of prompt fission neutron energies going from zero to a maximum of about 0.7 MeV [67].

2.2.5.2 Photoneutrons

A photoneutron reaction, (γ, n) , can be caused by a gamma photon with energy high enough such that it overcomes the neutron-binding energy. This energy is at around 7 MeV in most nuclides and can be achieved in an electron accelerator where a target material is bombarded with energetic electrons resulting in intense bremsstrahlung with a distribution of energies up to that of the incident electrons [67]. This, incidentally, is the mechanism behind the x-ray tube that has become so ubiquitous to modern life.

Gamma photons in reactor shielding analysis have energies too low with most shielding materials having photoneutron thresholds too high for these to be concerning. Light elements have threshold energies low enough that (γ, n) can occur in reactor environments; photoneutron production in heavy water-moderated fission reactors can be very high due to the water composition. The fuels in fusion reactors are also subject to photoneutron production as are hydrogenous layers of shielding. Capture gamma photons due to neutron absorption have particularly high energies and may in turn cause a

significant high energy photoneutron production in surrounding materials [67]. This is handy for sustaining fusion reactions but not for sizing hydrogenous shielding.

2.2.5.3 Alpha Neutron

Neutron emission can be induced in some materials by the interaction of alpha particles in the (α, n) reaction; a large number of nuclides will emit neutrons when bombarded by alpha particles with sufficient energy to penetrate the Coulomb barrier to exceed the threshold energy. Light isotopes that have (α, n) reactions which are exothermic have particular interest due to the low threshold energy required to overcome the Coulomb barrier. This process is crucial for thermonuclear fusion reactions in particular, for the heating provided by the (α, n) reactions with the light elements in fusion can greatly enhance the reactivity due to this kind of neutron emission [9]. Alpha particles emitted by uranium and plutonium have energies in the 4 to 6 MeV range and can cause neutron production from (α, n) when in the presence of oxygen and fluorine [67,71]. Alpha particles can be directed at a target material to produce neutrons in portable sources, with targets made from beryllium and polonium being useful for neutron generators in early nuclear weapons [72].

2.2.5.4 Activation Neutrons

Another possible source for neutrons is when they are emitted by the decay of a few highly unstable nuclides. Fission reactions have delayed neutrons that are the result of decay from the fission products. This process is not restricted to the heavy isotope side of the periodic table, for there are nuclides such as ^{17}N which is produced in water modulated reactors which have rapid decay chains to emit neutrons. The emission of most

decay neutrons are within ± 0.2 MeV of the most probable energy in a spectrum of up to 2 MeV [67].

2.2.5.5 Fusion Neutrons

Thermonuclear fusion is accompanied by the release of energetic neutrons in the exothermic reaction which figure heavily into the requirements for shielding design. As established in Chapter 1, the threshold energy for fusion to occur is very high and the energies of the resulting neutrons can be much higher than that of the previously discussed neutron sources. The fusion process does not yield prompt gamma photons, but the interactions of the high energy particles resulting from fusion does produce photons. These will be of a lower energy than the fusion neutrons, so to a shielding analyst, a shield designed for the neutrons will be more than adequate for any resulting photons [67].

2.2.6 Gamma Ray Sources

2.2.6.1 Radioactive Sources

There are a multitude of isotopes that have spontaneous emission of photons, and these sources have been extensively characterized. There are many data sources available for these characterizations. In the professional world of radiation safety, the highest energy sources are heavily used in industrial radiography and have tightly governed controls on their use overseen by the Nuclear Regulatory Commission (NRC) [73]. Some isotopes emit photons at low enough energies to be useful and relatively safe for medical applications such as the injection of radioactive markers into a patient's bloodstream.

2.2.6.2 Prompt Fission Gamma Photons

Fission reactions release a generous amount of high energy photons, the prompt fission gamma photons are what is released in the first 50 nanoseconds after a fission event. Fission product gamma photons are emitted after the first products have been formed and both of these factor heavily into shielding design and the calculations for gamma heating in a reactor [67].

2.2.6.3 Gamma Photons from Fission Products

The products from fission leave behind a long lasting legacy of gamma ray activity produced by the decay of those products; the total energy of the gamma rays produced in the fission product chains at times greater than 50 nanoseconds after the fission is comparable to that of the prompt fission gamma photons. Around 75% of the total energy of the delayed gamma rays is released within the first thousand seconds of the fission event. When considering spent nuclear fuel, the gamma activity for several months or even years after it has been removed from a reactor is of great interest and the long lived fission products need to be considered when analyzing the shielding of the spent fuel storage containers [67].

2.2.6.4 Capture Gamma Photons

When neutron absorption creates a compound nucleus, it has an initial condition in a highly excited state with an energy equal to the kinetic energy of the incident neutron plus the neutron binding energy averaging out to about 7 MeV. This type of nucleus decays rapidly, mostly within 10^{-12} seconds and through mostly intermediate states producing several energetic photons. In shielding analysis, these type of photons are an undesirable secondary source of radiation in neutron shielding and must be accounted for [67].

2.2.6.5 Gamma Photons from Inelastic Neutron Scattering

When a neutron is inelastically scattered, the resulting excited nucleus formed decays to the ground state within 10^{-14} seconds with excitation energy being released as one or more photons. Conservation of energy and momentum in all scattering interactions imposes a limitation where that inelastic neutron scattering cannot occur without the incident neutron energy being greater than the energy required to excite the scattering nucleus to its lowest excited state. This type of scattering is a very important mechanism in the attenuation of fast neutrons with the resultant photons being at a lower energy state than the initial neutron [67].

2.2.6.6 Activation Gamma Photons

The absorption of a neutron in many materials produces a radionuclide with a half-life measuring from a tiny fraction of a second all the way to many years. The radiation produced by the decay of the activated nuclei can be a troublesome feature to many devices that produce neutron radiation. Structural components of reactor cores are especially susceptible to neutron activation, and most radionuclides encountered in medicine, industry and research were manufactured through this method. Most of these decay through a beta emission that leaves the daughter nucleus in an excited state that will decay quickly with the emission of one or more gamma photons [67].

2.2.7 X-Ray Sources

X-rays are emitted as a side effect to the interaction of charged particles and photons with matter; x-rays themselves are high energy photons just like gamma rays but differ in the fact that gamma rays are generated from effects in the atomic nucleus while x-rays originate from the electron shells. What is widely considered as x-rays can more accurately

be depicted as being secondary x-rays due to their generation from high energy particle interactions. Most x-ray sources in shielding applications are relatively low energy at levels generally less than 100 keV. This is true for most medical applications, but there are industrial uses for X-rays that can bring energies as high as 500 keV. Generally, X-rays with energies at less than or equal to 10 keV are known as “soft X-rays” while the X-rays at energies up to 500 keV are known as “hard X-rays”. The two main methods of secondary X-ray photon production include the rearrangement of atomic electron configurations leading to characteristic X-rays as well as the deflection of charged particles within a nuclear electric field resulting in bremsstrahlung [67].

2.2.7.1 Characteristic X-Rays

Electron arrangements seek the lowest potential in their nuclear shells, and if electrons are excited to higher energy levels or an inner electron is ionized, a complex series of transitions to vacancies in the lower shells occurs to return the atom to its unexcited state. As these electrons transition back to a lower energy state, they acquire higher binding energies; in each transition the difference in the change in binding energy is either emitted as a photon, called a characteristic X-ray, or given up to an outer electron and ejected from the atom which is known as an auger electron. Due to the discrete electron energy levels and transition probabilities varying with the Z number of the atom, characteristic x-rays are a unique signature for each element.

2.2.7.2 Bremsstrahlung

The kinetic energy of a charged particle is dissipated either through it colliding with electrons as it travels or by photon emission as it is deflected (and hence accelerated) by the electric fields of nuclei. This deflection of the charged particle produces X-ray photons

that are called bremsstrahlung, translating from German into “braking radiation”. Several charged particles can produce bremsstrahlung, but the most important particle for shielding concerns is the electron, for the impact of a near relativistic electron into a high-Z material can produce high energy bremsstrahlung emission. Electrons are the least massive of the charged particles and therefore produce the most significant bremsstrahlung; all other charged particles have masses much closer to the target material and cannot be accelerated as quickly as electrons. Bremsstrahlung from electrons plays heavily into X-ray tubes, betatrons and beta decay of nuclides. During beta decay, the beta particle is accelerated with a small amount of bremsstrahlung being emitted, small enough that it is a tiny fraction of the total beta decay energy [66, 67].

2.2.7.3 X-Ray Machines

Any device that produces high energy electrons can also produce X-ray photons due the bremsstrahlung effect. In a device where a high voltage is used to accelerate electrons into an appropriate target material, the bremsstrahlung yields a significant amount of X-rays. X-ray tubes are the most common form of this kind of device that would be used in industry, but another device that can be considered is an electron beam welder which operates in either a vacuum chamber or with an inert gas to provide strong and unoxidized weld joints. Electron beam welders need to have shielding incorporated as a result of the aforementioned effects of bremsstrahlung.

The energy spectrum of the resultant photons from this kind of interaction has a continuous bremsstrahlung component up to the maximum energy of the electron, which corresponds to the maximum voltage. Depending on the target material, if the voltage applied is high enough to cause ionization in the target material there will be characteristic

X-ray lines superimposed on the spectrum. These properties allow for filtering of x-ray beams for certain types of radiographic applications. In radiography, the ability to change the beam intensity or focus high photons along narrow characteristic X-ray bands allows for tunable penetration for certain materials and improvements of image quality [67].

2.3 Interactions of Particles

When radiation is emitted, it produces interactions depositing energy into the surrounding media; this is known as the dose. Nuclear interactions result from a bombarding particle and a target nuclei, the nature of interaction depends on the properties of the particle (i.e. charged, uncharged) and the energy level. At energies greater than 10 MeV, interaction may yield a compound nucleus which decays and emits secondary particles.

2.3.1 Interaction Coefficient

The interaction of a given type of radiation with matter is categorized with regards to the type of interaction and the properties of the matter with which the interaction takes place. The interaction could be through scattering of the incident radiation, a process by which deflection of particles occurs with an accompanying energy change. A scattering interaction may be elastic or inelastic depending on the types and energies of the particles involved. Other types of interactions are absorptive in nature, where if an incident radiation energy is transformed to excitation of the nucleus, a secondary particle may be emitted.

The interaction of radiation with matter is always statistical in nature, to demonstrate, let P denote probability that this particle interacts in some specified manner while travelling a distance Δx . It has been found that the quantity $\mu \equiv \lim_{\Delta x \rightarrow 0} \left(\frac{P}{\Delta x} \right)$ is a

property of the material for a given interaction with the limit process being interpreted like that of fluence in Section 2.2.1. In the limit of small path lengths, μ is seen to be the probability per unit path length that a particle will undergo a specified interaction. μ is constant for a given material and for a given type of interaction, therefore this implies that the probability of interaction per unit path length is independent of the path length traveled prior to the interaction. The interaction probability per unit path length is fundamental in describing how radiation interacts with matter, this concept is also known as the linear attenuation (or interaction) coefficient [66].

The nomenclature thus far has been in describing photon interactions where μ can be referred to as the macroscopic cross section, while the symbol Σ is used for the same purpose in neutron interactions. Since μ does not have the dimensions of a cross section, this is mostly avoided in analysis but sometimes needs to be used to interpret the analysis of some source materials [66, 68]. The linear interaction coefficient is especially useful like in Equation 12, where one can interpret flux density ϕ as the path length traveled by particles per unit volume per unit time. The product $\mu\phi$ is the number of interactions per unit volume per unit time, and division by the material density yields the interaction rate per unit mass $\left(\frac{\mu}{\rho}\right)\phi$.

The linear attenuation coefficient is not only a function of the energy of the particle, but is also a function of many other factors depending on the nature of the interaction. These additional factors include the energy of the particle after scattering, the energy of the recoil atom (or electron), the angles of deflection of the scattered radiation and recoil atom (or electron), and the angles of emission of secondary particles all measured from the initial direction of the incident particle.

2.3.2 Microscopic Cross Section

Of the quantities that determine μ , one of the most important is the density of the target atoms or electrons in the material. The linear interaction coefficient is proportional to the density N of the target atom or electron such that $\mu = \sigma N$, where σ is the microscopic cross section, a constant of proportionality independent of N . The microscopic cross section is the interaction probability per unit path length normalized to one target atom or electron per unit volume; this can also be considered as the effective area presented to radiation by one nucleus of the material. Common SI units for this area are cm^{-2} or barns (1 barn = 10^{-24} cm^{-2}). Cross section can be defined for each type of nuclear reaction and each type of nuclide and it generally varies with the energy of the incident particle [55].

2.3.3 Neutron Interaction Mechanisms

Neutrons can only interact with nuclear matter, but those interactions cause intense secondary effects. In other words, all neutrons lead to additional ionizing radiation. Total neutron cross section is the sum of the cross sections of possible neutron interactions and it indicates the probability that a neutron with a given area will interact in one way or another. This cross section is given by

$$\sigma_t(E) = \sigma_s(E) + \frac{\sigma_{(n,\gamma)}(E)}{\sqrt{E}} \quad (14)$$

where E is the given energy level, $\sigma_s(E)$ is the elastic scattering cross section and $\sigma_{(n,\gamma)}$ is the cross section for neutron and gamma reactions [55].

Neutrons interact with matter through elastic scattering, inelastic scattering, radiative capture reactions, charged particle threshold reactions and neutron producing reactions. All of these interactions transfer energy eventually moderating the neutrons to

the thermal regime thus slowing them down; slow neutrons are better than fast neutrons in radiation protection for they are less dangerous and easier to absorb. There are fundamental differences between the two scattering processes described for neutrons which will be described in greater detail in the next two sections. A shorthand way to differentiate between what happens in the two scattering methods is as follows

$$n + X \rightarrow \begin{cases} X + n & \text{elastic scattering} \\ X^* + n' & \text{inelastic scattering} \end{cases} \quad (15)$$

where n represents an incident and elastically scattered neutron, n' represents an inelastically scattered neutron, X denotes the scattering nucleus in a ground state, and X^* is the scattering nucleus in an excited state [55].

2.3.3.1 Elastic Scattering

Elastic scattering takes place through the formation of a compound nucleus and the re-emission of a new neutron that in turn brings the target neutron to a ground state. The scattering of the projectile neutron is accomplished through a localized force field and can emerge with either no loss in kinetic energy or the energy is lost by other direct and non-direct processes. With elastic scattering, the original kinetic energy of the neutron nuclear system is conserved. Neutron energies are lowered through scattering interactions as represented by the following equation

$$\sigma_s(E' \rightarrow E) = \sigma_s(E')p(E' \rightarrow E) \quad (16)$$

where $\sigma_s(E' \rightarrow E)$ is the transfer cross section, $\sigma_s(E')$ is the cross section of the interaction, and $p(E' \rightarrow E)$ is the net efficiency of the interaction.

Shielding for neutrons works best if there is a significant amount of hydrogen locked up in the shielding material, for hydrogen is very effective at reducing incident neutron energies through elastic scattering. Since the mass of a hydrogen atom is comparable to that of a neutron, an incident neutron can lose up to 50% of its energy per elastic scattering event with a hydrogen atom. The lower the mass of the nuclide encountered, the more efficient the resulting elastic scattering will be [55].

2.3.3.2 Inelastic Scattering

Inelastic scattering results from when an incident neutron excites the internal energy state of a target nucleus and the nucleus remains in an excited state after the emission of a lower energy neutron. The excited nucleus will then normally bleed off its excess energy by decaying through the emission of a gamma photon. Due to the energy transfer and reduction of energy by the emitted neutron, inelastic scattering reactions always have a threshold energy. Additionally, it is possible to excite multiple energy levels that can be excited simultaneously with increasing neutron energies [55].

2.3.3.3 Radiative Capture Reactions

Incoming neutrons are absorbed by nuclei, and some energy is lost in that transfer in the form of another neutron at a lower energy level and/or a gamma ray photon. Eventually, the neutrons radiated from these capture and scattering events will drop to an energy level where they will end up captured and absorbed in a nucleus through the process known as radiative capture. This concept was touched on in Section 2.2.5.2 where neutron capture occurs, and then a by-product will be the decay of a gamma photon. Generally,

the absorption cross-section for neutrons in these interactions varies inversely with the square root of the neutron energy [55].

2.3.3.4 Charged Particle Threshold Reactions

When neutrons are at high incident energies, the resulting excitation energies make threshold reactions possible. These are reactions with their cross-section at zero below the threshold energy. At this threshold and below, inelastic scattering then occurs due to the kinetic energy of the incident neutron being high enough to raise the target nucleus to an excited state. This will then overcome the binding energy to be re-emitted. Threshold reactions remove highly penetrating neutrons and replace them with charged particles which have a very short range in penetration of matter and are easily stopped [55].

2.3.3.5 Neutron Producing Reactions

As the chain of energy absorbing reactions lowers energy, neutrons are finally absorbed in a nucleus via a process known as radiative capture. Neutral particles are not effected by coulomb forces while near the positive target nucleus and are therefore captured more easily in neutron-nucleus interactions than compared to interactions with charged particles. Slower neutrons are captured easily, in general the absorption cross section for neutrons for radiative capture reactions varies inversely with the square root of the neutron energy. At low energies, the capture cross section of nuclei are usually high and much greater than their actual geometric cross sections. Neutron capture excites the nucleus resulting in the decay of a gamma photon [55].

2.3.4 Photon Interaction Mechanisms

Ionizing photons are electromagnetic radiation with properties of a wave or a particle, at high energies quantum properties are important therefore photons are regarded as particles in interactions. Gamma rays result from nuclear changes as well as sometimes from being the product of particle/antiparticle annihilation. X-rays primarily result from electrons changing orbits (Bremsstrahlung), internal conversion, and the photo-electric effect. Photons can penetrate deeply into matter, though not as deeply as neutrons can, and can interact with matter in twelve possible ways. Four of those ways are the most important to mechanisms that will be discussed here [55].

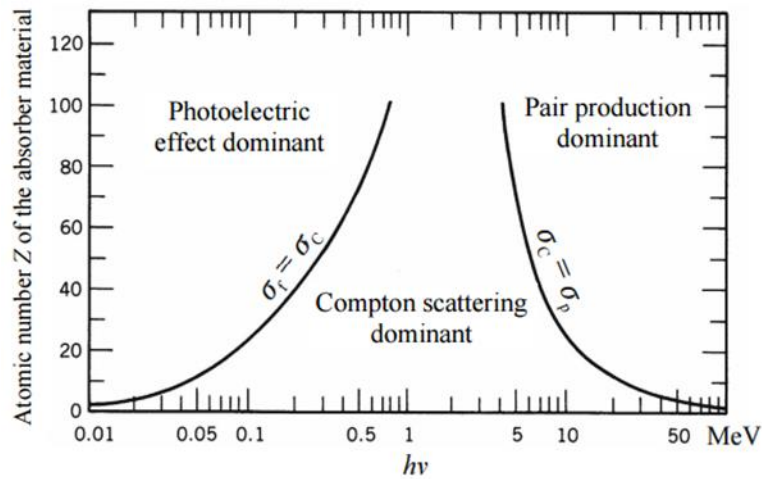


Figure 2.4. The various processes of high energy photon interaction with matter [74]

Depending on the energy of the incident photon as well as the atomic number of the interaction material, there are regions where different processes dominate. From low energy to high, the dominance gradually changes from photoelectric effect to Compton scattering and finally to pair production. The cross sections of these different interactions

of photons with matter have very detailed individual derivations, but can be summed up in the following equation

$$\sigma = \sigma_c + \sigma_f + \sigma_p \quad (17)$$

where σ_c is the cross section is for Compton Scattering, σ_f is the cross section for Photoelectric Absorption, and σ_p is the cross section for Pair Production [74].

2.3.4.1 Coherent Scattering

Coherent scattering results when incoming photons interact directly with electrons in an atomic shell. In this interaction, the photon is scattered coherently by the combined action of the atomic electrons which in turn are not ejected from the atom but aid in emission of a new and deflected photon. The recoil momentum in this interaction is absorbed by the atom as a whole and the photon loses negligible energy with very small deflection angles. Coherent scattering has a minimal effect on energy and direction of the deflected photon and is generally ignored in shielding analysis. Additionally, coherent scattering is valid for photons with an energy of 10 keV or below, therefore the energy is low enough to be negligible as far as shielding is concerned [55, 75].

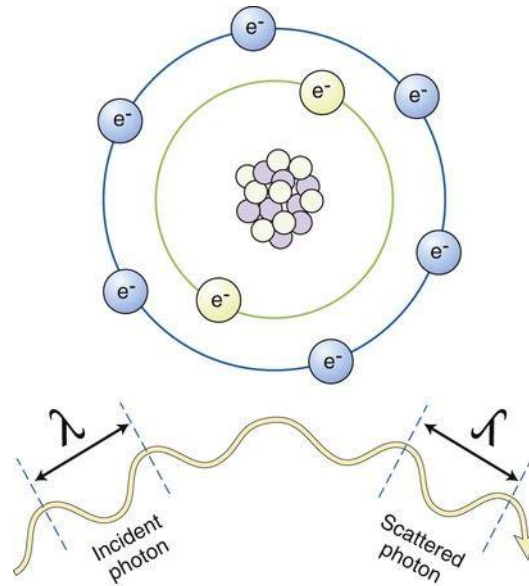


Figure 2.5. Diagram of the classic coherent scattering process [75]

2.3.4.2 Compton Scattering

Compton scattering is due to an incident photon interacting with an individual electron of an atom normally regarded as a free electron. This is incoherent scattering, and at energy levels where this is dominant, the bound electrons are assumed to interact as free particles. In Compton, a photon may transfer only a portion of its energy to the electron which may either be bound or free. The electron recoils in one direction while the photon is scattered from the collision at a different angle with lower energy. The Compton Effect is generally important for photons between 0.6 and 2.5 MeV, and total Compton scattering is proportional to the number of electrons an atom has. This is why the best shielding materials for photons are made from high-Z elements such as lead [55, 75].

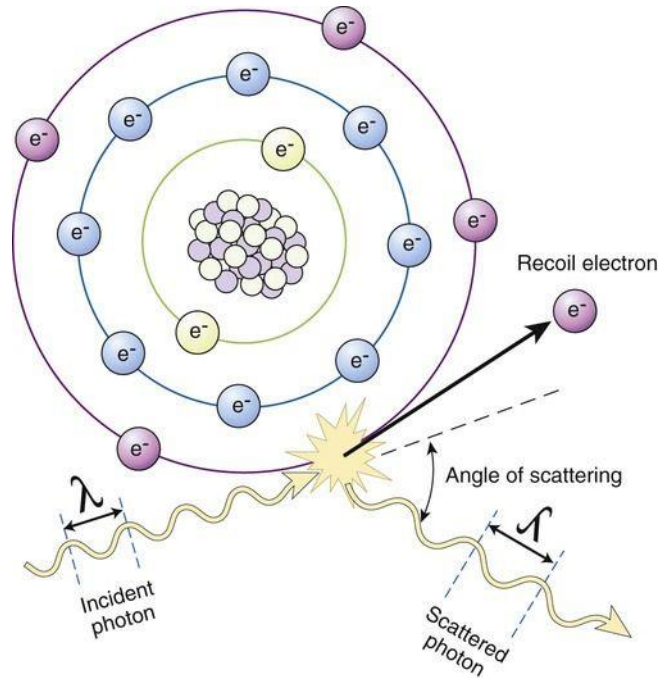


Figure 2.6. Diagram of Compton Scattering [75]

2.3.4.3 Photoelectric Absorption

In photoelectric absorption, the incident photon interacts with the meson fields of the atomic nuclei resulting in total absorption. The excess energy in the atom then causes the emission of an electron, known as a photo-electron, with negligible recoil energy. The majority of emitted photo-electrons come from the K-shell, and when the vacancy is filled by an outer electron either fluorescence characteristic x-rays or auger electrons are emitted. As incident photon energy drops below the energy of the K-shell, cross section drops discontinuously and these sudden changes are known as absorption edges. Photoelectric absorption is the dominant attenuation mechanism for photons with low energies, and over the energy range where it is dominant, high- Z materials work well as absorbers. In this process, photo-electrons are reabsorbed by other atoms which then emit more photo-

electrons of lower energies. This continues until the energy drops below the level for ionization [55].

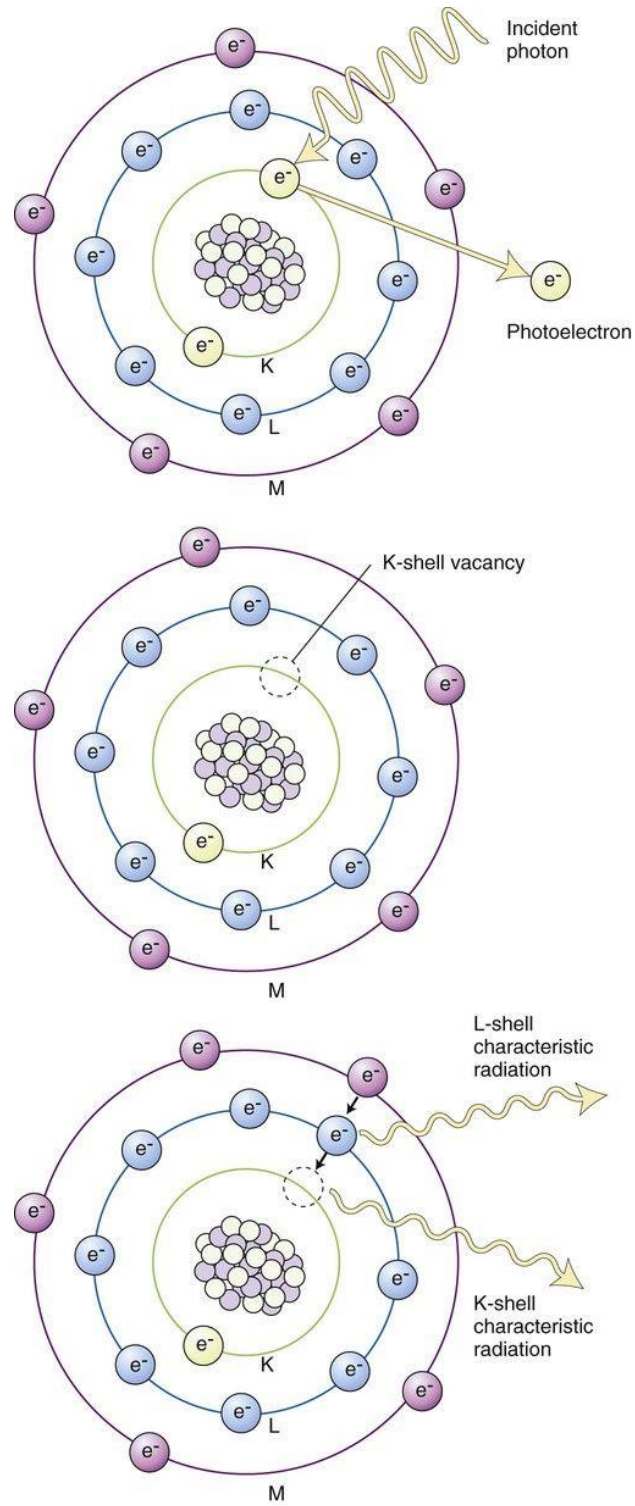


Figure 2.7. The photoelectric process [75]

2.3.4.4 Pair Production

Pair production occurs when the incident photon is absorbed and replaced with a positron-electron pair. The phenomenon is induced by the strong electric field in the vicinity of the nucleus and has a photon threshold energy of 1.02 MeV. Total atomic pair production cross section varies with atomic number Z , and the resulting annihilation of the electron-positron pair usually results in two photons moving in opposite directions at an energy level of 0.511 MeV [66].

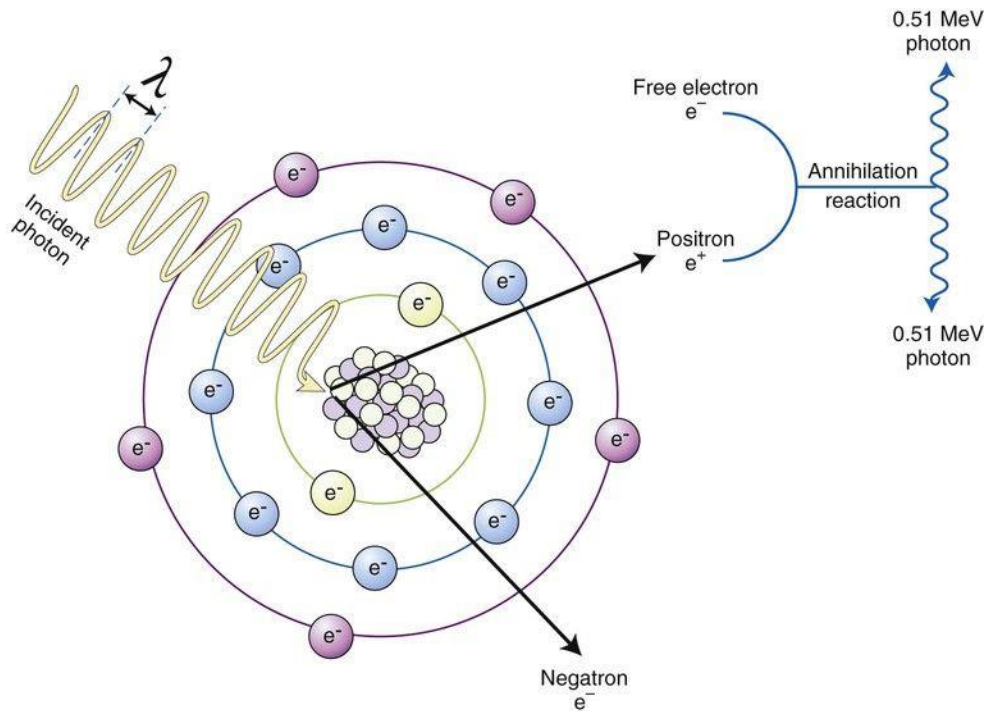


Figure 2.8. Diagram of the pair production process [75]

2.3.4.5 Linear Interaction Coefficients for Ionizing Photons

The linear interaction coefficient for photons is, in the limit of small distance, the probability per unit of distance travelled that the photon will undergo for any significant interaction. For any specified medium,

$$\mu(E) = ZN_e\sigma_C(E) + N\sigma_{ph}(E) + N\sigma_{pp}(E) \quad (18)$$

Where N is the atomic density and ZN is the electron density. A more common way of presenting this data is in the mass interaction coefficient

$$\frac{\mu}{\rho} = \frac{\mu_C}{\rho} + \frac{\mu_{ph}}{\rho} + \frac{\mu_{pp}}{\rho} \quad (19)$$

Where the following interaction coefficients μ_C represents Compton Scattering, μ_{ph} designates photoelectric scattering, and μ_{pp} is for pair production. Note that Rayleigh scattering as well as other minor effects are excluded from this definition. In Equation 19,

$$\frac{\mu_C}{\rho} = \frac{Z}{a} N_{Ae}\sigma_C(E) \quad (20)$$

$$\frac{\mu_{ph}}{\rho} = \frac{1}{a} N_A\sigma_{ph}(E) \quad (21)$$

$$\frac{\mu_{pp}}{\rho} = \frac{1}{a} N_A\sigma_{pp}(E) \quad (22)$$

Where N_A is Avogadro's Number [66]. For the shielding analyst, the mass interaction coefficient summarized in Equation 19 is a useful tool in first order shielding design against photons. The National Institutes of Standards and Technology (NIST) maintains extensive tables of this data [76].

2.3.5 Deterministic Transport Theory

The transport theory for neutral particles mentioned in the last few sections is based upon the linear form of the Boltzmann equation; this is shown as a balance of the different mechanisms by which particles can be added or subtracted to an arbitrary volume. This

linear and time-independent form of the Boltzmann transport equation is relevant for the neutral particle transport in a non-multiplying media [55].

2.4 Ionizing Radiation Dose

The radiation dose is the energy deposited through the interaction of radiation with matter, but it also must be quantified in relation to what has been covered thus far. The radiometric quantity known as fluence is not a useful determinant for radiation effects since it is not closely related to those effects. Energy fluence is a more useful correlator to radiation effect than is fluence by itself, this is due to the energy that is carried by a particle must have some kind of correlation to the damage it can do to a material like organic tissue. There are many mechanisms at play in how radiation effects matter, effects of which were covered in the previous section on interaction. Due to this variety of factors, basic dosimetric properties are divided between absorbed dose and equivalent dose for whatever material is being affected. The difference between the two is that absorbed dose is the energy deposited per unit mass in an absorbing medium, mainly tissue, and the damaging effect of the type of radiation absorbed is the equivalent dose. Additionally, there are many other more detailed and specialized dose types that are also in consideration depending on analysis needs [67].

2.4.1 Conversion of Fluence to Dose

For a radiation field with given properties, a dose conversion coefficient is used to provide a link between the fluence and the measure of radiation dose or a detector response. Two classes of conversion coefficients exist, one being the local coefficient which converts the energy spectrum of the fluence at a point, $\phi(\mathbf{r}, E)$ to the point value of the dose. This

value is the kerma, exposure, absorbed dose, or effective dose. The other class of dose conversion coefficients, commonly known as being phantom related, uses local fluences and dose coefficients inside geometric and anthropomorphic phantoms for the evaluation of average or effective doses of various types with regards to risk.

Operational dose quantities such as ambient dose are evaluated with geometric phantoms, this correlates with monitored occupational exposure. Anthropomorphic phantoms with their more complicated configurations are useful for with effective doses for planning and optimizing protection strategies as well as retroactively demonstrating compliance with dose limits for an existing design. Phantom related coefficients account for the relative sensitivities of the various organs and tissues to radiation as well as the relative biological effectiveness of various radiations [67, 77].

Within a given flux density ϕ , a detector with volume V_d and response function \mathcal{R} will have a response R of

$$R = \int_0^{\infty} dE \int_{4\pi} d\Omega \int_{V_d} dV \mathcal{R}(\mathbf{r}_d, E, \mathbf{\Omega}) \phi(\mathbf{r}_d, E, \mathbf{\Omega}) \quad (23)$$

where $\phi(\mathbf{r}_d, E, \mathbf{\Omega})$ is the fluence, and $\mathcal{R}(\mathbf{r}_d, E, \mathbf{\Omega})$ is the expected (or average) detector response caused by a particle of energy E traveling in direction $\mathbf{\Omega}$ at point \mathbf{r}_d per unit of path length traveled. $\mathcal{R}(\mathbf{r}_d, E, \mathbf{\Omega})$ is also considered to be the dose conversion coefficient in this general form of detector response. A more idealized case that is commonly used treats the detector as a point with an isotropic response such that

$$R(\mathbf{r}_0) = \int_0^{\infty} dE \mathcal{R}(E) \phi(\mathbf{r}_0, E). \quad (24)$$

Detector response as a concept includes simple isotropic detector types such as a flux-density detector where $\mathcal{R} = 1$, and an energy flux density detector where $\mathcal{R}(E) = E$. Other detectors that are used for shielding analysis are generally dosimetric in nature having response functions that are related to energy deposition per unit mass. There are many fluence to dose conversion factors available from a variety of sources covering a multitude of phantoms and conditions [66, 67].

2.4.2 Absorbed Dose

If a small incremental volume of material ΔV and mass Δm around a given point is exposed to a field of ionizing radiation imparting energy $\Delta\epsilon$ into the incremental volume, the absorbed dose D in the material is defined by

$$D \equiv \lim_{\Delta V \rightarrow 0} \frac{\Delta\epsilon}{\Delta m} \quad (25)$$

where the limit process limits statistical variability. The standard unit for absorbed dose is the gray (Gy) in which 1 Gy is equal to the energy imparted of 1 joule per kilogram; a common and much older unit known as the RAD is defined as 100 ergs per gram which makes 1 rad equal 0.01 Gy. Absorbed dose is treated as a point function from a macroscopic point of view and is quite useful in radiation protection for energy imparted per unit mass in tissue loosely correlates with radiation hazard [66, 67, 70].

2.4.3 Kerma

Absorbed dose is measurable, but calculations of it from incident radiation fluence and material properties can often be difficult. Such a calculation requires a full accounting of the energies for all secondary particles leaving the region of interest. The kerma, or kinetic energy of radiation produced per unit mass in matter, is a closely related

deterministic quantity used only with indirectly ionizing radiation. This is the sum of the kinetic energies of all the charged particles liberated by interactions of neutral particles in a specific material.

Kerma requires some knowledge of material properties in the incremental volume but it is more easily calculated than absorbed dose since it is only concerned with interactions with the primary beam while ignoring the transport of secondary particles. Unlike with absorbed dose, kerma is very difficult to measure directly nor is it related in principle to biological effects nor to the shield heating effects of absorbed dose. Ignoring those effects lends simplicity to first order shielding calculations therefore making kerma valuable to a shielding analyst. Kerma K is defined by

$$K \equiv \lim_{\Delta V \rightarrow 0} \frac{\Delta E_k}{\Delta m} \quad (26)$$

where the limit process ignores statistical variations, and ΔE_k is the energy transferred as kinetic energy of the secondary charged particles released by interaction with indirectly ionizing radiation within ΔV . The units for kerma are the same as absorbed dose, and due to the phenomenon of charged particle equilibrium, for certain conditions kerma can be treated as interchangeable with absorbed dose [66, 67].

2.4.4 Exposure

Exposure, with abbreviation X , is traditionally used to specify the radiation field of high energy photons. It is defined as the absolute value of the ion charge (of one sign) produced anywhere in air by the complete stoppage of all electrons (except those produced by bremsstrahlung) that are liberated by the interaction of the photon field in an incremental volume of air, per unit mass of air in that volume. It is similar to kerma, but the one

important difference lies in the energy being from ionization of air caused by secondary electrons rather than the further interaction of those secondary electrons with air. The unit for exposure in SI is expressed as coulombs per kilogram, and a much older unit in use known as the Roentgen (R) is defined precisely as 2.58×10^{-4} coulombs of separated charge (of either sign) per kilogram of air in the incremental volume home to primary photon interactions [66, 67].

Air kerma and exposure are closely related and can be converted due to the fact that a known proportion of the initial kinetic energy of secondary charged particles results in ionization of the air. This ionization results in the production of 33.85 ± 0.15 electron volts of kinetic energy per ion pair [78]. This factor combined with the air kerma results in the exposure, but this product must be slightly reduced to account for losses from some of the original energy of the electrons going into bremsstrahlung instead of ionization or excitation.

2.4.5 Local Dose Equivalent Quantities

2.4.5.1 Relative Biological Effectiveness

In the process of accounting for the behavior of biological material or organisms that are subjected to radiation, the variations in sensitivity of biological material to different types or energies of radiation need to be considered. To this end, the relative biological effectiveness (RBE) has been defined by radiobiologists for each type and energy of radiation as well as the varying biological effects resulting from exposure to the different radiation types. The RBE is standardized by being the ratio of the absorbed dose of a reference type of radiation inducing a certain kind and magnitude of biological effect to the absorbed dose of the radiation under consideration to produce the same kind and

magnitude of effect. Typically, the reference standard the RBE is measured against is the physical dose from 250-kVp X-Rays or the gamma ray dose from exposure to Cobalt-60. Under normal circumstances, RBE is determined experimentally while taking into account all factors that would affect biological response to radiation in addition to absorbed dose.

The ICRP has described the effectiveness of different types of radiation by a series of these RBE factors with the value of 1 for all radiations having low energy transfer and gamma radiations of all energies. The other values for RBE were selected to be a broad representation of the results observed in biological studies, most significantly those relating to cancers and hereditary effects. With the RBE factors, it is possible to define a more biological meaningful unit of radiation dose called the Sievert (Sv) in SI parlance and Roentgen Equivalent Man (REM) in more traditional units. This is represented by the equation with the form of

$$Sv = \sum_{i=1}^n RBE(i) \times Gy(i) = 100 \text{ REM} \quad (27)$$

where i is the index representing a radiation type for which a dose is to be calculated and n is the total number of radiation types for which a dose is to be calculated [67, 68].

2.4.5.2 Linear Energy Transfer

When a charged particle interacts with matter, it is slowed down and gives up kinetic energy through Coulombic interactions with local electrons bound to the material's component atoms and radiative energy loss through bremsstrahlung (for electrons only). The unrestricted linear energy transfer (LET or L_{∞}) is often denoted as $-dE/dx$ is the stopping power or expected energy loss per unit distance of travel by the charged particle.

The larger the LET of a charged particle, the more the ionization and biological damage caused per unit of travel distance through the absorbing medium [67].

2.4.5.3 Radiation Weighting Factor and Dose Equivalent

There are many variables that factor into RBE including the properties and nature of the radiation field, the type of biological material, specific biological response, the degree of the response, the dose, and the dose rate. This makes for a complex concept that is difficult to apply in the regular practices of radiation protection or in the implementation of standards and regulations. This led to the establishment in 1964 of a substitute quantity known as the quality factor Q for application to the local value of the absorbed dose to yield a quantity known as the dose equivalent H which is widely used as an appropriate measure of radiation risk when applied to operational dosimetry. Quality factor is also applied to the evaluation of doses related from geometric phantoms, an example of which being the ambient dose.

An important parameter in explaining the variations in biological effects of radiation of different types and energies is believed to be the spatial density of ionization and excitation along particle tracks; since density is proportional to LET, quality factor has been defined in terms of L_{∞} . Since tissue is mostly water with an average atomic number close to that of water, the quality factor was made a mathematical function of the unrestricted LET in water in 2007 by the ICRP. Quality factor is an evolving quantity having changed in its definition over the years as understanding of the fundamental processes at work has grown and changed [67].

$$Q(L_\infty) = \begin{cases} 1 & L_\infty < 10 \text{ keV}/\mu\text{m} \\ 0.32L_\infty - 2.2 & 10 \leq L_\infty \leq 100 \text{ keV}/\mu\text{m} \\ 300/\sqrt{L_\infty} & L_\infty > 100 \text{ keV}/\mu\text{m} \end{cases} \quad (28)$$

Quality factor is dependent on the nature of the energy deposition from whatever primary radiation is imposed, whether it be from charged or neutral particles. A determination must first be made on how absorbed dose is distributed among the particles which are losing energy at different LETs. Once this is set, the variability of Q with L_∞ can be accounted for and the average quality factor \bar{Q} can be determined. With indirectly ionizing radiation, quality factors can be ascribed with knowledge of the secondary charged particles released when the neutral particles interact with matter. Since secondary electrons released by gamma or X-rays are always assigned a quality factor of one, this same factor can be universally applied to all ionizing photons. Neutron interactions are much more complex and the following describes how average values are determined for those particles.

The radiation weighting factor, w_R , is a term closely related to the quality factor that was implemented by the ICRP in 1991 and modified in 2007 for use with the dose equivalent in tissues of the anthropomorphic phantom. Dose equivalent H is determined using this weighting factor and it also has the SI unit of Sievert described in Section 2.4.5.1 as related to RBE. Neutron weighting factors are computed using the 2007 formulation as shown below [67].

$$w_R = \begin{cases} 2.5 + 18.2\exp[-\ln^2(E)/6] & E < 1 \text{ MeV} \\ 5.0 + 17\exp[-\ln^2(2E)/6] & 1 \text{ MeV} \leq E \leq 50 \text{ MeV} \\ 2.5 + 3.25\exp[-\ln^2(0.04E)/6] & E > 50 \text{ MeV} \end{cases} \quad (29)$$

2.4.6 Photon Kerma, Absorbed Dose and Exposure

Another way to look at photon kerma involves properties of the material absorbing the radiation in a manner that leads to the following equation

$$K = \left(\frac{f(E)\mu(E)}{\rho} \right) E\phi(E) \quad (30)$$

where $\mu(E)$ is the total interaction coefficient (neglecting coherent scattering), $f(E)$ is the fraction of the energy transferred by the photons to secondary charged particles and ρ is the density of the interacting material. The quantity $f(E)\mu(E)$ is also known as the linear energy transfer coefficient μ_{tr} . Constraining energy E to units in MeV, fluence ϕ in units of cm^{-2} , the mass energy transfer coefficient $\mu_{tr}(E)/\rho$ in units of cm^2/g , and the conversion coefficient \mathcal{R}_K in units of Gy cm^2 ,

$$\mathcal{R}_K(E) = 1.602 \times 10^{-10} E \left(\frac{\mu_{tr}(E)}{\rho} \right) \quad (31)$$

where $\mu_{tr}(E)$ is averaged using the weight percentages for each element composing the medium of particle transport at the point of interest.

On the occasion that the secondary charged particles are able to produce a large amount of bremsstrahlung, the region of interest radiates a significant portion of the kinetic energy from the charged particles in the form of X-rays from the region of interest. The absorbed dose calculated from kerma can be prone to overestimation though even under the assumption of charged-particle equilibrium. Bremsstrahlung production is able to be accounted for by the substitution in Equation 31 of the mass energy absorption coefficient $\mu_{en}/\rho = [1 - G(E)]\mu_{tr}/\rho$ in which $G(E)$ becomes the fraction of the secondary

charged particle initial kinetic energy lost as X-rays. With the assumptions of charged-particle equilibrium and no local energy transfer from bremsstrahlung, this leads to

$$\mathcal{R}_D(E) = 1.602 \times 10^{-10} E \left(\frac{\mu_{en}(E)}{\rho} \right) \quad (32)$$

There are extensive tables for values of μ_{en}/ρ available on the internet categorized with regards to material and energy levels maintained by NIST and other organizations [76]. Exposure in units of roentgen with (μ_{en}/ρ) for air in units of cm^2/g , ϕ in cm^{-2} , and E in MeV can be found via [67]

$$X = 1.835 \times 10^{-8} E \left(\frac{\mu_{en}(E)}{\rho} \right)_{\text{air}} \phi \quad (33)$$

2.4.7 Neutron Kerma and Absorbed Dose

In neutron transport, charged particle equilibrium is for the most part valid in such a way that kerma becomes an outstanding approximation of the absorbed dose. To this end, the local dose conversion coefficient with units of Gy cm^2 is given by

$$\mathcal{R}_K(E) = 1.602 \times 10^{-10} E \sum_i \frac{N_i}{\rho} \sum_j \sigma_{ji}(E) \epsilon_{ji}(E) \quad (34)$$

where ρ is the material density given in g/cm^3 , N_i is the density of atomic species i with units of cm^{-3} , $\sigma_{ji}(E)$ is the cross-section in cm^2 for nuclear reaction j with atomic species i , and $\epsilon_{ji}(E)$ given in MeV is the energy transferred to the medium in that interaction.

2.4.8 Phantom-Related Dosimetric Quantities

2.4.8.1 Characterization of Ambient Radiation

There is a common problem that appears frequently in the design and implementation of radiation shielding and this is summed up in the following way. For a given reference point in a location that would be accessible to a human body, the fluences and fluxes of various radiation types in the radiation field have been characterized in terms of being computed in a free field. This assumption neglects the presence of a human body. Suppose that just a single radiation type is involved, for instance only photons or neutrons, and the energy spectrum $\phi(E)$ of the fluence is known at the reference point. A dose quantity R for a phantom representation of the human subject at that point can then be defined and calculated with a response function \mathcal{R} , or an appropriate conversion coefficient such that

$$R = \int_0^{\infty} \mathcal{R}(E)\phi(E) dE \quad (35)$$

creating a quantity similar to Equation 24. In this formula, \mathcal{R} is a phantom-related conversion coefficient and ϕ is the fluence energy spectrum independent of the presence of the phantom. The conversion coefficient is built upon the determination of the absorbed dose as well as accounting for phantom internal radiation transport that results from incident radiation with a specifically defined angular distribution, usually in the form of a parallel beam.

If both the angular and energy distributions of the fluence of ionizing radiation at a point in space is known, then operational and limiting dose quantities can be evaluated as radiation doses in phantoms exposed to a uniform radiation field derived from the actual

field at that point. In the expanded field, the phantom is irradiated across its entire surface by radiation with energy and angular distributions being the same as those in the actual field at the point of interest. If the phantom is irradiated by unidirectional radiation with an energy spectrum that is the same as the actual field at the point, it is exposed to an expanded and aligned field [67].

2.4.8.2 Dose Conversion Factors for Geometric Phantoms

One of the more commonly used geometric phantoms is known as the ICRU Sphere, at 30 cm in diameter, it is composed of a tissue-equivalent material with a composition by mass of 76.2% oxygen, 11.1% carbon, 10.1% hydrogen and 2.6% nitrogen. With a density of 1.0 g/cm³, the volume and mass is a good approximation for a human body and the geometry allows for a simple way to determine dose quantity, which may be the maximum dose within the phantom or the dose at an appropriate depth.

There are a multitude of dose conversion coefficients for a number of phantoms and irradiation conditions, and at certain points or regions within the phantom absorbed dose values are determined. These are often approximated kerma values, and these determinations contain contributions by all secondary-charged particles that are accounted for. For every type of charged particle of a given energy, the L_{∞} in water and Q are obtained; these values are then applied to the absorbed dose contribution from each particle to find the dose equivalent contribution at the location designated in the phantom. This information is applied to the absorbed dose contribution from each charged particle obtaining the dose equivalent contribution at the location of interest within the phantom. The maximum dose value is then obtained with the examination of the absorbed dose and dose equivalent distributions resulting from the charged particles, sometimes at a relevant

location such as at 10 mm in depth. The dose conversion coefficient resulting from this is the value of either the absorbed dose or dose equivalent divided by the incident beam's fluence [67].

2.4.8.3 Dose Equivalent Indices

2.4.8.3.1 Deep Dose Equivalent Index

This dose quantity assumes that the radiation field has the same fluence and energy distribution as what is found at a specified reference point, but with the phantom exposed to an expanded broad parallel beam. This dose, signified by $H_{I,d}$, is the maximum dose equivalent within the ICRU sphere's 14 cm radius central core. This dose quantity is difficult to use if the incident radiation is polyenergetic or consisting of both neutrons and photons. For every type of radiation or variety of energy level, there is a different depth of maximum dose making this quantity non-additive [67].

2.4.8.3.2 Shallow Dose Equivalent Index

This dose quantity, $H_{I,s}$, is nearly identical to the deep dose equivalent index but with a key difference. This being that the maximum dose equivalent value resides between 0.007 and 0.010 cm in depth from the outer surface of the ICRU sphere. This corresponds to the depths of radiosensitive cells of the skin [67].

2.4.8.3.3 Ambient Dose Equivalent

This dose equivalent, $H^*(d)$, is a useful quantity for operational limits against established dose standards. The assumption with this quantity is the same as that of the deep dose equivalent for the radiation field with an expanded broad parallel beam striking the phantom having the same fluence and energy distribution as the field at a reference

point. The expanded and aligned field deposits energy to be evaluated at a depth of d on a radius vector in the opposite direction from the beam. This quantity as calculated is associated with the measured personal dose equivalent $H_p(d)$, a quantity found in soft tissue below a specified point in the body at a depth d . Personal dosimetry in operational situations using radiation monitoring badges and/or pocket dosimeters strongly correlates to this dose equivalent. The standard depths for evaluation are 0.07 mm for the skin and 3 mm for the lens of the eye for weakly penetrating radiation, and for strongly penetrating radiation 10 mm is the evaluation depth [67, 79].

2.4.8.3.4 Directional Dose Equivalent

This dose quantity, $H'(d, \Omega)$, assumes that the angular and energy distributions of the fluence at a reference point apply themselves across the entire surface of the phantom. The same depths as the ambient dose equivalent are evaluated with the directional dose equivalent. In order for angular distribution Ω to be specified, a reference system of coordinates in which directions are expressed is required. If the field is unidirectional, $H'(d, \Omega)$ can instead be written as $H'(d)$ and it becomes equivalent to $H^*(d)$ [67].

2.4.8.3.5 Spherical Phantom Irradiation Geometries

A multitude of conversion coefficients for both photons and neutrons have been calculated and tabulated for radiation protection and operational limits by the ICRP [77]. Included in these data sets are coefficients relevant to deep and shallow indices as well as directional dose equivalents at depths of 0.07, 3 and 10 mm. The following irradiation geometries are included:

- a. PAR, a single plane parallel beam
- b. OPP, two opposed plane parallel beams

- c. ROT, a rotating plane parallel beam
- d. ISO, an isotropic radiation field

A single plane parallel beam is the most conservative of these irradiation geometries, and in this assumption the conversion coefficients for $H_{I,d}$ and $H^*(d)$ at 10 mm are nearly identical for photons. In the case of neutrons, these differ only at low energies with the deep dose equivalent index being more conservative due to its greater value [67].

2.4.9 Dose Coefficients for Anthropomorphic Phantoms

With the use of anthropomorphic phantoms, it becomes possible to determine doses to individual organs and tissues. The individual doses averaged together with weight factors related to radiosensitivity to organs and tissue can be summed up to become the effective dose equivalent, or more simply put, the effective dose. There are varying ways to apply an anthropomorphic phantom to this determination, most commonly either by an adult gender neutral single phantom or through both male and female adult phantoms. This drills deeper with an additional array of phantoms available representing humans, male and female, ranging from newborn to adult [80]. Dose quantities developed from these phantoms are used for radiation protection purposes in occupational and public health, as well as in internal dosimetry related to nuclear medicine procedures. The dose quantities are applicable at levels well below annual limits across an average of large and diverse populations; careful judgments must be made when using these quantities for health assessments on individuals since effects will vary from person to person [67].

Anthropomorphic phantoms are mathematical constructs that describe the organs and tissues in a human body that allow for numerical simulations and calculations to be performed on radiation transport in the human body. Conversion coefficients are found

through calculations with the main assumption being that the phantom is exposed to monoenergetic radiation in a fixed geometric orientation. Of these orientations, the most conservative one is anteroposterior (AP) having irradiation from the front to back with the beam orthogonal to the long axis of the body. Other geometries include postanterior (PA), lateral (LAT), rotational (ROT), and isotropic (ISO); these orientations have applications dependent on specific assumptions with ROT being the most complex since it models someone walking with a changing orientation respective to that of the beam. Dose conversion coefficients based on these methods are published in tables provided by the ICRP, and these are updated periodically as methods and data evolve [67, 81].

2.4.10 Equivalent Dose

Absorbed doses of equal value may not have the same biological effects depending on the type of radiation absorbed. Equivalent dose H_T in tissue or organ T is given by

$$H_T = \sum_R w_R D_{T,R} \quad (36)$$

where $D_{T,R}$ is the average absorbed dose in tissue or organ T by ionizing radiation of type R , and w_R is the radiation weighting factor which is used to equate the biological effects of different radiation types. Since w_R is dimensionless, the unit for equivalent dose is the same as for absorbed dose in J/kg with the special designation in Sv. Values for w_R are found in Equation 29 for neutrons, and are unity for photons [79].

2.4.11 Effective Dose

Effective dose, E_D , is the summation of organ or tissue doses to those parts irradiated if more than one tissue type is involved. The tissue weighing factor, w_T , is used

to equate the effects of radiation on different organ or tissue types. The values of all of the tissue weighting factors combined add up to one [55, 66, 79].

$$E_D = \sum w_T H_T = \sum w_T \left[\sum_R w_R D_{T,R} \right] \quad (37)$$

There are many sources for tissue weighting factors to be used in dosage calculations as provided by organizations such as the ICRP and NCRP. These factors are usually dependent on the geometry of the dose phantom used in the evaluation. Organs and tissues considered in these weighting factors include the gonads, bone marrow, lungs, breasts, thyroid, bone surfaces, colon, stomach, bladder, liver, esophagus, skin, salivary glands and the brain. Even though the eye is very sensitive to ionizing radiation, the ICRP has never evaluated it with regards to effective dose instead regulating safe dose to the eye operationally as a lower quantity than every other organ.

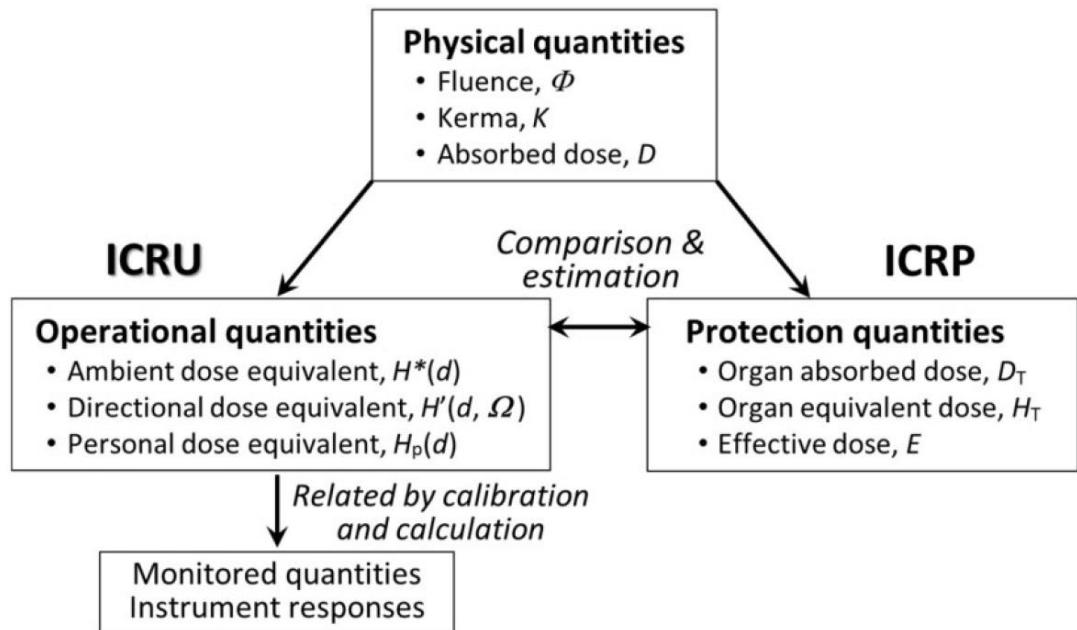


Figure 2.9: Relationship between the protection quantities and operational quantities for use in radiological protection [82]

2.5 Biological Effects of Radiation Dose

When biological tissue is exposed to a radiation field, the interactions with ambient atoms produce chemical free radicals causing cell bio-molecular oxidation-reduction reactions. There are many potential outcomes to such reactions depending on the severity and duration of the dose, but determining detrimental effects on living cells can be difficult to determine from these reactions. When organic compounds are ionized, electrons shared between individual atoms are ejected and the compounds fall apart from the breaking of their chemical bonds. In a living cell, radiation will sometimes strike a critical molecule of a cell such as in a chromosome. The genetic information for the cell to function and reproduce is contained in the chromosome, and damage to such often results in the destruction of the cell. Sometimes the repair mechanisms of the cell can fix the cellular damage as well as damage to the chromosome, but minor errors in genetic repair can lead to the development of cancer or other more minor genetic or hereditary effects [67, 68].

There are many variables determining how harmful radiation effects are to living tissue, the type of radiation as well as the energy level, dose rate, and exposure time will present a variety of outcomes. Another factor that determines the severity of the effects of a radiation dose is on the type of tissue involved in the exposure. Tissues and organs with the greatest sensitivity to radiation include the lymph nodes, bone marrow, gastrointestinal tract, the reproductive system and the eyes. The skin, the lungs and the liver all exhibit medium sensitivity while the least sensitive tissues are the muscles and bones [68].

The different types of ionizing radiation have variable effects on biological material, each needing to be considered for the effects of their interactions. Alpha particles are highly ionizing but have a very short range in tissues, to the point that the surface of

the skin can be sufficient to stop this radiation. If alpha particles are absorbed internally, the greatest tissue damage will occur due to the secondary interactions. Beta particles are moderately ionizing also having a short range in tissues, with stoppage occurring after a slight penetration of the skin. Like with alpha particles, internal dosage of beta radiation also causes great damage due to secondary interactions. Gamma rays, X-rays, and neutrons are all moderately ionizing and deeply penetrating, and due deep tissue exposure, external dose is important to consider [68].

The effects and hazards of radiation dose on humans can be broken up into two major categories, hereditary effects and somatic effects. Hereditary effects manifest themselves in genetic damage not detrimental to the exposed individual, but in succeeding generations hereditary illness may result. Somatic effects on the individual exposed are classified further by the nature (i.e. acute or chronic) and the time scale of the radiation exposure. The effects of exposure of a human to ionizing radiation depend on the exposure and the duration; acute exposures are life threatening that lead to deterministic effects that require medical treatment [67].

Deterministic effects are often of an acute nature, usually the result of the death or malformation of somatic cells following radiation exposure and only at a high dose threshold. Severity, but not probability of occurrence, of these effects, depends on the total dose absorbed. Deterministic effects usually manifest after an extremely high dosage exposure over a short period of time. Examples include rapid fatality through acute radiation syndrome, radiation burns, chronic radiation syndrome, and radiation induced thyroiditis. The severity depends on the dose [66].

Physiological effects due to acute exposures have been catalogued due to a small number of incidents that resulted in a high dose of radiation received to one or more individuals. Table 2.1 is a compilation of studies from mostly the acute exposure on survivors from the nuclear weapon attacks on Hiroshima and Nagasaki, Japan at the end of World War II as well as from the 1986 Chernobyl accident in the former Soviet Union. This relatively small dataset shows the correlation of dose received with the various physiological effects that could occur as a result of this exposure [68].

Table 2.1. General effects from an acute whole body dose [68, 79]

Dose (mSv)	Effect	Lethality (Without Treatment)
0 to 25	None detectable through routine blood tests	0%
25 to 100	Slight changes in blood, nausea	0%
100 to 200	Nausea and vomiting, moderate blood changes	< 5%
200 to 300	Nausea and vomiting, hair loss, severe blood changes	< 50%
300 to 600	Nausea and vomiting, severe blood changes, gastrointestinal damage, hemorrhaging	50 – 99%
600 to 1000	Nausea and vomiting, severe gastrointestinal damage, severe hemorrhaging	99 – 100%

In contrast to acute exposure, repeated chronic exposure to a low dose leads to stochastic effects that are also known as “Occupational Exposure”, where the dose influences subsequent ill effects in a probabilistic sense. With stochastic effects only probability of illness, but not its severity, is dependent on the radiation exposure. Cancers with delayed onset or other heritable effects involving the development of cancer may occur in either mature somatic cells or through the mutation of reproductive cells as a result of this exposure. Across a population, the effects of low level radiation exposures can be estimated, but effects to individuals can only be described probabilistically [66, 67].

Many studies have been performed over the years to statistically compile the effects of chronic radiation exposures; a number of different models have emerged from these

studies that attempt to estimate health effects of low doses based upon data extrapolated from observations of the health effects resulting from high radiation doses. In the case of these models, the specific health effect studied is the probability of the occurrence of cancer. There has been intense debate over the details of these models in this same time period and so far, none of these models have been conclusively shown to be correct. There are several families of these models ranging from various linear models that assume cancer risk being proportional to dose and that there is no dose below which there is no increased cancer risk. This threshold dose is debated and some models include it with varying degrees of intensity, including one that operates on the assumption that small doses can be beneficial [68].

2.5.1 Dose Limits

There are many organizations that have issued public guidelines for the limits on radiation dose; in addition to recommendations from the ICRP and the NCRP, the US Nuclear Regulatory Commission (NRC) also issues guidelines. The evolution of radiation protection standards in concert with the growth in understanding of statistical effects has led to the acceptance of risk-related dose limits based upon probabilistic assessment of radiation hazards. The ICRP [83] introduced a conservative limit for occupational whole-body dose to 50 mSv per year based upon these initial assessments of risk. After further development, the NCRP [84] went on to recommend a more thorough set of limitations on dose based upon risk analysis that continues to serve as the basis for the radiation protection standards of the United States [67]. This recommendation is summarized in Table 2.2. As the science and understanding of dose continues to evolve, the ICRP and NCRP both revisit these standards every five to ten years to see if any new recommendations need to be made.

Table 2.2. NCRP recommendations for exposure limits [67, 84]

Type of Dose	mSv	REM
<i>Occupational exposures (annual):</i>		
1. Limit for stochastic effects	50	5
2. Limit for nonstochastic effects:		
a. Lens of the eye	150	15
b. All other organs	500	50
3. Guidance: cumulative exposure age(years) x	10	1
<i>Public exposures (annual):</i>		
1. Continuous or frequency exposure	1	0.1
2. Infrequent exposure	5	0.5
3. Remedial action levels	5	0.5
4. Lens of the eyes, skin and extremities	50	5
<i>Embryo-fetus exposure:</i>		
1. Effective-dose equivalent	5	0.5
2. Dose-equivalent limit in a month	0.5	0.05
<i>Negligible individual risk level (annual):</i>		
1. Effective-dose equivalent per source or practice	0.01	0.001

2.5.1.1 Dose Limits for Astronauts

A primary concern of this thesis is radiation produced by a hypothetical nuclear fusion propulsion system and the protection of personnel from this radiation. Limits on ground facilities are readily contained in the previous section, and it should be reasonable to assume that the Charger-1 facility be restricted to the 1 mSv per year limitation on public exposure as a design goal as shown in Table 2.2. This is a reasonable goal when considering the advantages of being on the ground, but spaceflight criteria by necessity are less stringent. Since a secondary goal of this thesis is to perform analysis on shielding for

a hypothetical spacecraft with a fusion propulsion system, it would be reasonable to establish an expectation for the dose to any on board astronauts.

The radiation environment for a spacecraft is complex with many sources of energetic particles both charged and uncharged to potentially wreak havoc on materials, both organic and inorganic. The space environment is filled with charged particles from the solar wind that cause secondary interactions, as well as the random high energy Galactic Cosmic Radiation (GCR) particle that can wreak havoc with its high energy. GCR particles originate from outside the solar system and are generally composed of the nuclei of atoms that have been completely ionized and travelling at nearly the speed of light. These particles were most likely accelerated by magnetic fields of supernova remnants in the past few million years. Due to these hazards, there is a strong argument that the space environment can be just as harmful if not more so to an astronaut as a nuclear propulsion system would be.

The hazards of the space environment has driven NASA to adopt a limit of 500 mSv per year for their astronauts. This limitation is for blood forming organ exposure, eyes and skin are allowed to have even higher exposures of 2000 and 3000 mSv, per year respectively. Astronauts are restricted to a total lifetime dose ranging from 1000 to 4000 mSv depending on the age and gender of the subject. In general, older people are allowed higher lifetime doses than younger people while men are allowed higher doses than women. The career dose equivalent is based upon a maximum 3% lifetime excess risk of cancer mortality, while the risks from this dose are dependent on the gender and age at the start of exposure. The bias towards higher exposure with age is based upon the assumption that a younger person should be exposed to less radiation since they have more of a life to

live; this also increases the risk of the development of future health problems from radiation exposure with the longer potential timeline [85].

2.5.1.2 ALARA

The principles of radiation safety effectively revolve around the simple fact that exposure ionizing radiation needs to be reduced to ALARA, or As Low as Reasonably Achievable. The most important factor to consider is the dose, but the dose is not only affected by energy level but exposure time and distance from the source as well. The key is to minimize exposure time and maximize distance from the source. If one or both of those variables are not available, then shielding is the most logical and effective method of bringing exposure to ALARA levels.

2.5.2 Dosimetry

There are several methods available for the measurement of operational dose through the use of instruments with the ability to measure both total dose as well as dose rate. The most common devices are survey meters for the measurement of dose rate that range from the relatively simple Geiger-Mueller counter to the more complex ion chamber devices. Depending on operational restrictions and available shielding, many radiation workers are required to wear dosimeters in their everyday use. Nuclear power plant workers, radiographers that use isotopes for imaging, and radiographers using portable X-ray tube heads for imaging are all required to wear dosimeter badges on the chest for monthly whole body total dose, as well as pocket dosimeters to measure daily total dose and electronic alarming rate meters that are set to sound an alarm when a dangerous dose rate is detected. All of these are measures to maintain ALARA conditions; the NRC [73] governs the policies and procedures in the US for radiation workers and their dosimetry.

Medical workers with regular exposure to radiological devices and isotopes are also required to use dosimeter badges for whole body total dose.

Most organizations appoint an independent Radiation Safety Officer (RSO) to be responsible for maintaining the monitoring of radiation workers as well as the annual inspection of radiation generating devices and shielding. Monitoring badges, either in the form of TLDs (Thermo Luminescence Device) [86] or Optically Stimulated Luminescence (OSL) [87] technologies, are sent in monthly to monitoring organizations for reading the dose on the badge as compared to a control badge and the dose from this badge is added to the cumulative dose database for each worker. If a worker gets an unsafe exposure rate that exceeds monthly limits, they can be removed from the program until their monthly reset comes around [73].

2.6 Radiation Shielding Analysis and Design

2.6.1 Basic Methods in Radiation Attenuation Calculations

This section contains a basic overview of the most common simplified methods used for the estimation of dose under special source and geometric conditions. These methods are applicable to circumstances where a source and receiver have a direct path and uncollided radiation contributes significantly to the dose. Generally, radiation sources have a spatial distribution at the point of measurement, but this distribution can be modeled as a set of contiguous small sources with each being treated as a point source. For each point source, the uncollided dose can be calculated using an uncollided point kernel. The total uncollided dose can then be found via integration over the source volume. Correction factors are available for application to the uncollided point kernel, these yield the point kernel for combined uncollided and collided radiation. The correction factor for

monoenergetic gamma rays is known as the buildup factor; polyenergetic X-rays use an attenuation factor to jointly account for both the collided and uncollided radiation. A total dose point kernel is also used to estimate the dose from uncollided and collided fast polyenergetic neutrons in hydrogenous media [67].

2.6.1.1 The Point-Kernel Concept

Uncollided radiation is a primary factor of determination of fluence or dose at a point of interest when it has flowed directly from the source without any interaction with the surrounding medium. If, for example, only air separates a detector from an ionizing radiation source, the interactions with air or any solid objects in the intervening space are often negligible and the detector interacts almost entirely with uncollided radiation straight from the source. Secondary radiation due to scattering and other processes has minimal impact to the overall dose in this case. Methods for estimating dose from uncollided radiation are derived from its basic properties as presented in this section [67].

2.6.1.1.1 Exponential Attenuation

Recall from Section 2.3.4.5 that the linear interaction coefficient $\mu(E)$ for indirectly ionizing radiations, in the limit of small distances, is the probability per unit distance of travel that a particle of energy E experiences an interaction such as scattering or absorption. This definition allows for the probability of a particle travelling a distance x without interaction to be given by

$$P(x) = e^{-\mu x} \quad (38)$$

Knowing this relation, the half-value thickness x_2 required for the reduction of the uncollided radiation to one-half its initial value is found to be $x_2 = \ln 2/\mu$. The tenth value

thickness x_{10} , which is the distance that uncollided radiation must travel to be reduced to one-tenth of its initial value, can also be found to be $x_{10} = \ln 10/\mu$. The concepts of half and tenth-value thickness are widely used in radiation protection and radiography in areas more broad than just with uncollided radiation; often they are used to describe the attenuation of the total radiation dose. A particle streams from its point of birth to the point at which it makes its first interaction at an average distance of λ_{mfp} , known as the mean-free path length it can be easily shown that $\lambda_{\text{mfp}} = 1/\mu$ [67].

2.6.1.1.2 Uncollided Dose from a Monoenergetic Point Source

Uncollided radiation produced by isotropic point sources result in dose ways that vary with the conditions. The following subsections contain a few basic expressions of this dose as derived from specific situations as shown in Figure 2.10.

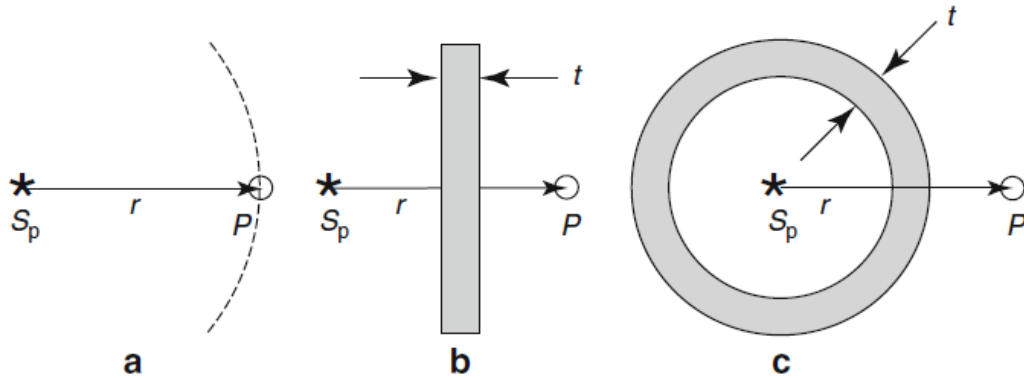


Figure 2.10. Point isotropic source in a vacuum (a), attenuated with a slab shield (b), and attenuated by a spherical shield (c) [67].

2.6.1.1.2.1 Point Source in a Vacuum

A point isotropic source emitting S_p particles into an infinite vacuum is shown in Figure 2.10a. Particle motion radiates entirely outward without interaction, and with

source isotropy, a spherical shell of radius r from the source has the same number of particles crossing it for each unit area. This particle density per unit area is represented by $S_p/(4\pi r^2)$. From the definition of fluence it follows that at a distance r from the source, the fluence ϕ^0 of uncollided particles is

$$\phi^0(r) = \frac{S_p}{4\pi r^2} \quad (39)$$

If the source particles all have the same energy E , the point detector response at distance r from the source can be found by multiplication of the uncollided fluence and the appropriate dose conversion coefficient \mathcal{R} . This normally is dependent on the particle energy, specifically,

$$D^0(r) = \frac{S_p \mathcal{R}(E)}{4\pi r^2} \quad (40)$$

Something that becomes quickly apparent is the fact that fluence and dose decrease as $1/r^2$ with increase in distance from the source. This universal relation in physics as applied to the decrease in dose with increase in distance is often known as geometric attenuation [67].

2.6.1.1.2.2 Point Source in a Homogenous Attenuating Medium

If the same monoenergetic point source is immersed in an infinite homogenous medium with total interaction coefficient μ , the source particles also stream outward but some interact before they reach the edge of the imaginary sphere of radius r . Those that collide with the medium do not contribute to the uncollided fluence. The source particles that travel at least a distance r without interaction are represented by $S_p e^{-\mu r}$, making the uncollided dose

$$D^0(r) = \frac{S_p \mathcal{R}(E)}{4\pi r^2} e^{-\mu(E)r} \quad (41)$$

In order to differentiate the geometric attenuation $1/r^2$ term, the $e^{-\mu r}$ term is known as the material attenuation [67].

2.6.1.1.2.3 Point Source with a Shield

If the only attenuating material between the detector and the source is a slab of material with attenuation coefficient μ and thickness t as shown in Figure 2.10b, the probability that a source particle reaches the detector without interaction is $e^{-\mu t}$. The uncollided dose becomes

$$D^0(r) = \frac{S_p \mathcal{R}(E)}{4\pi r^2} e^{-\mu(E)t} \quad (42)$$

This result is also true if the attenuating medium has any shape so long as a ray drawn from the sources passes through the attenuating material with a thickness of t . An example of this is in the spherical shell of Figure 2.10c [67].

If the shield is made from multiple layers of different materials that force the uncollided particle to penetrate a series of thickness t_i of materials with attenuation coefficients μ_i before reaching the detector, the uncollided dose becomes

$$D^0(r) = \frac{S_p \mathcal{R}(E)}{4\pi r^2} e^{-\sum_i \mu_i(E)t_i} \quad (43)$$

The total number of mean-free-path lengths of attenuating material that an uncollided particle must pass through without interaction is $\sum_i \mu_i(E)t_i$, and the probability that a source particle traverses this number of mean-free-path lengths without interaction is $e^{-\sum_i \mu_i(E)t_i}$ [67].

2.6.2 Shielding Materials

Metals are very effective at shielding against photons due to high melting points, large neutron cross sections for scattering and capture, stability under irradiation, suitable thermal conductivity, and are relatively cheap and easy to fabricate. High-Z materials like lead are the most effective at attenuating and absorbing photons, but other metals can be used. Concrete is an effective shield against photons and neutrons, if allowed to be thick and heavy enough. Concrete's effectiveness against neutrons is due to its containing water molecules; the heavier elements in concrete work to slow neutrons by inelastic scattering and then hydrogen slows them even more. The slow loss of hydrogen atoms eventually causes concrete to lose its effectivity against neutrons as well as its structural strength. Given enough distance from the source and thickness, other materials can be effective at attenuating radiation such as soil and even air.

Neutrons are much more disruptive at high energies than photons, so when considering the best practices for designing and developing shielding against them, several items must be considered. First, incoming neutrons must be slowed down, for slower neutrons are easier to absorb. High-Z materials are useful in moderating fast neutrons through inelastic scattering and an isotope such as iron can be used to remove neutrons through threshold reactions. Iron is also useful for scattering neutrons through large angles. Hydrogen is used to effectively slow neutrons below the 4 MeV threshold, and the production of energetic ionizing photons and radioactive neutron activation byproducts can be suppressed by mixing a slow neutron absorber such as boron carbide in the neutron hydrogenous layers of the shield [55].

Materials such as paraffin wax, polyethylene and water are best suited for this use, and commercial grade polyethylene doped with boron carbide is available on the market. Drawbacks to the hydrogen containing materials also need to be taken into account in shielding design. Cross section falls as energy is increased, scattering angle is forward peaked, energetic capture gamma rays are emitted, and these materials can be damaged by high energy cross sections of neutrons and lose integrity. Additionally, wax has structural issues to consider and anything containing water can leak as well as corrode.

2.6.2.1 Spacecraft Shield Materials

When considering radiation shielding on spacecraft, there are constraints due to the nature of the design and the intended operating environment. Since mass is always a concern for spacecraft, the standard design practice with respect to shielding has been one of triage. Astronauts on board the International Space Station (ISS) are exposed to a higher degree of radiation than the general public on the ground, and it was never a practical concern for the development of shielding for the entire crew cabin. The most protection available to ISS crew members generally consists of specially made sleep cabins lined with a similar material to the aprons used by patients in medical x-ray situations. Otherwise, additional protection could be available in storage areas where water bags are kept [88].

Most spacecraft are designed to handle a moderately ionizing environment, for there is no escaping the charged particles, gamma rays, X-rays and cosmic rays. A general approach on spacecraft systems is to design electronics with moderate radiation protection in mind; radiation hardened assemblies with the most critical components shielded in the constant trade-off between weight and protection. NASA, the European Space Agency (ESA) and other organizations have developed standards for radiation hardening on

spacecraft with reliability and low mass design in mind [89]. Spacecraft with exposure to extreme fluence such as the Juno mission orbiting Jupiter have a two-pronged approach: first, the orbit is highly elliptical with closest approach on the order of a few hours to minimize exposure time. Second, all of the spacecraft electronics are kept inside a hardened radiation vault. On the Juno mission, this vault is a titanium box with 1 centimeter thick walls weighing in at about 200 kg. This extreme measure, as far as spacecraft go, is designed to keep exposure 800 times lower than the 200,000 Gy of exposure anticipated over the mission lifetime [90].

Advanced spacecraft designs such as ones powered by nuclear reactors have higher mass margins in their design, and the approach at this point has been to design shadow shields to be placed adjacent to the reactor/engine that are of a minimal diameter to be able to project a cone of shadow over the critical areas of the spacecraft, such as a crew cabin. Optimization is still highly dependent on mass, and the approach that has evolved makes use of multilayer shielding consisting of materials optimized for different properties. One such design is evaluated in this thesis and consists of three layers: a hydrogenous material such as lithium hydride to slow the fast neutrons and most of the photons, a boron carbide neutron absorber to stop the remaining neutrons, and finally a tungsten layer to stop secondary photons and remaining neutrons. This is discussed in greater detail in upcoming chapters of this thesis [68].

2.6.3 Regulations and Standards for Shielding Design

There are several established international standards for the design of shielding against ionizing radiation depending on the application and source. These standards have been developed through decades of rigorous testing and simulation and make use of tables

developed from this experience for rapid sizing guidelines in hand calculations for a shielding designer to use with a degree of safety factor included. The most effective shielding materials are going to be subject to their application and feasibility, but in general all shielding materials are chosen for their ability to prevent the transport of high energy particles. The industry built around radiation protection uses standard materials and applies the simplest approximations such as half-value layer thicknesses to the design of most shielding applications.

Standards for radiation protection that have been developed exhibit a great degree of commonality due to the physics involved. Most are directly traceable to the reports and standards issued by the ICRP, ICRU, and NCRP. The United States Code of Federal Regulations has radiation protection standards set as the ultimate legal requirements for radiation protection; each state has its own board of radiation protection that regulates industrial and medical occupations with all legal traceability to federal laws [73]. The nuclear power industry, the medical imaging communities, and the high energy physics communities have the most mature and specific standards written for radiation protection. The American National Standards Institute (ANSI), the American Society of Mechanical Engineers (ASME), and the Institute for Electronics and Electrical Engineers (IEEE) have the most extensive industry standards available [67].

CHAPTER 3. MONTE CARLO METHODS FOR SHIELD DESIGN

3.1 Introduction to MCNP

Using the established standards and materials, a rough order of magnitude design for shielding on the Charger-1 facility as well as a hypothetical spacecraft shield can be developed through simple hand calculations. However, any additional optimization can only occur through statistical means. Most hand calculations can only occur after much simplification in the source assumptions, and the only the approximations that can be found in photon problems are accurate. Neutron problems are nearly impossible to solve analytically, therefore numerical methods must be used [91].

Since particles behave in so many different ways in radiation transport, the most effective way to model their behaviors in interaction with various shielding materials is through Monte Carlo simulation. Monte Carlo is considered a well-honed method of solving complicated problems, and in this case MCNP is the tool that is used. MCNP is a code that has been used for over 50 years and has been managed all this time by Los Alamos National Laboratory. It has a vast database of materials to call upon as well as conversion coefficients and other abilities to model relevant radiation environments and materials to interact with.

In particle transport, the principles used in the Monte Carlo method are simple and follow established laws of physics. A radiation particle has many paths that it can take in its lifetime and is simulated from emission to death by absorption or escape from the problem boundaries. The various interactions that may occur during a particle's lifetime are randomly sampled and simulated, and the outcomes are tallied for statistical purposes. Particle histories are generated by pseudo-random numbers, and each particle history has

random numbers generated to sample the probability distributions for multiple outcomes and variables [4].

3.1.1 MCNP Input File Structure

The MCNP input file is arranged in a format that traces back to the early days of electronic computation, which also is concurrent with the age of MCNP itself. This file is arranged into four major blocks, three of which are crucial to the operation of the MCNP computation. Within these functional blocks are cards, each equivalent to an executable line, and all of these cards are stacked for input. Together this is known colloquially as an input deck, and this syntax is a carry-over from the pioneering days of punch card inputs in computing where an input was literally a deck of cards.

Depending on the intended function of a card, syntax and column delimitation figures importantly with improper use causing fatal errors before the code can even be executed. Each card is limited to 80 columns for functionality with comments being exempt from columnar counting. Column spacing also figures prominently depending on the intended function and location of the card. Many sources of error for a beginning MCNP user start with improper use of this format.

Table 3.1. MCNP Input File Structure [65]

Message Block (Optional)
Blank Line Delimiter (Optional)
One Line Problem Title Card
Cell Cards [Block 1]
Blank Line Delimiter
Surface Cards[Block 2]
Blank Line Delimiter
Data Cards [Block 3]
Blank Line Delimiter (Optional)

3.1.2 Model Geometry

3.1.2.1 Cell Cards

Cell cards are found in the first block and derived from surfaces in the 2nd block. When setting up a problem, one defines the surfaces before the cells. In this block, the user applies intersection, union and complement between the surfaces bounding the volume (or cell) and contains user defined materials. The inputs for the cell card are structured as follows: Cell Number, Material#/Void, Density, and Union/Intersection of Surfaces. The cell number and material number are both arbitrarily selected by the user, and if a cell is void the material number is always zero. The density is input with a negative number designating grams/cm³ and a positive entry designates atom density in 10²⁴ atoms/cm³; if the cell is void there is no entry for density. The union and intersection of surfaces are designated with a space between surface numbers indicating an intersection and a colon indicating a union [65].

3.1.2.2 Surface Cards

Since any geometrical configuration consists of surfaces in different positions in three dimensional space, MCNP is made to treat problems in terms of regions or volumes bounded by first and second degree surfaces. The user defines shape and position represented functionally by $f(x, y, z) = 0$; shapes can also be defined by equations, points, and/or macrobodies. The format of a surface card defined by equations is as follows: Surface Number, Mnemonic, and List. The Surface Number is selected arbitrarily by the user and cannot exceed five digits. The Mnemonic indicates surface of the shape while the list becomes the numerical coefficients of the surface equation. The surface card defined by points contains the format bounded by Surface Number, Mnemonic, and Card Entries.

Card Entries specify coordinates of the three points that define the plane. Macrobody is an alternative method for surface definition that can be mixed with standard cells and surfaces. MCNP decomposes a macrobody internally into surface equations and the facets are assigned identifying numbers according to a predetermined sequence. The facets can be used for tallying, tally segmentation, other cell definitions, sources, and many more applications that delve deeply into the MCNP User's Manual [65, 92, 93].

3.1.3 Data Cards

This block contains almost all of the information and specifications relevant to the execution of the input file beyond the geometry of the model. This includes material specifications, cross section specifications, radiation sources, tallies, variance reduction, how results are to be scored, and the level of detail for the physics of particle information as well as other parameters. The most important data cards are outlined below.

3.1.3.1 Radiation Source Cards

The source and type of radiation particles transported in an MCNP problem are specified by the SDEF command. This card has many parameters used to define the characteristics of the sources in the problem including size, shape, position, and energy. The input file should only have one SDEF card. The Mode Card sets the different particle transport combinations, and depending on the version of MCNP some particle combinations include charged particles like alphas. Table 3.2 lists the most commonly used combinations.

Table 3.2. Mode Card set for particle transport combinations with MCNP5 [65]

Abbreviation	Combination
N	Neutron only
NP	Neutron and neutron induced photon
NPE	Neutron, neutron induced photon, and electron
P	Photon only
PE	Photon and electron
E	Electron only

MCNP comes bundled with full support for three different releases of the program: MCNP5, MCNP6, and MCNPX. Each version has its own highly optimized area of specialty and it is possible to create more refined models and results by running the same assumptions in the different versions. For the most part, MCNP5 was used in the development of this thesis as it had the best basic support documentation enabling a beginning user to get started. Once such utility discovered in MCNP6 was the use of the fission criticality source card known as KCODE which specifies a criticality source in order to determine the k_{eff} eigenvalue for a given fissile system. KCODE allows for a predetermined number of iterative cycles to be run in order to narrow down k_{eff} from initial guesses all the way to a converged value for criticality. If this value converges for a given fission neutron source geometry, the output file will print a prediction for the total number of neutrons produced upon arriving at criticality. This also takes advantage of MCNP6 having the additional capability to track alpha particles that does not appear in the other versions. MCNP6 has a different setup and references cross-section libraries better optimized for nuclear fission types of problems than MCNP5 [65, 92, 93, 94].

3.1.3.2 Material Specification Card

The Mm Card specifies the isotopic composition and cross section for all the cards containing material m, where m refers to the Material Number on the cell card. Material can be specified by its atom fraction or mass fraction and specification of materials filling the various cells entail

- a. Defining the unique material number
- b. The elemental (or isotopic) composition
- c. The cross-sectional compilations to be used.

The density of the material, as discussed in Section 3.1.2.1, is specified in the cell definition card. MCNP contains a vast library of material compositions correlated with nuclear and energy data across a vast spectrum of studies and sources. Additionally, there are material formulations that have special compatibility for particles specified in the mode card. For example, a photon-only problem can execute on material properties specific to tables of data analyzed only for photon interactions; materials optimized for neutron problems may not necessarily work on photon problems and fatal errors will occur [65, 92, 93].

3.1.3.3 Physics Card

The PHYS card is used to specify energy cutoffs and the physics treatments to be used for photons, neutrons and electrons. For photon problems, the physics card provides for the following settings and assumptions: energy above which simple physics is to be used; whether or not to include bremsstrahlung; whether or not to include electron transport in a PE problem; whether or not to include coherent scattering; if photonuclear interactions are either used in an analog manner, not used at all, or used with a bias; whether or not to

use Doppler broadening from the speed of electrons. Neutron problems include assumptions of the following: energy above which neutron data is not placed in memory (default is very large); energy below which neutrons are treated for analog capture and above which implicit capture is used; the averaged cross sections above the resolved cross section region are used or if by default, probability tables that describe a myriad of levels and widths of the unresolved resonances are used; if prompt plus delayed neutrons are included or the setting is an either prompt or delayed neutrons. These assumptions directly affect the computational times depending on other settings and parameters of the model [65].

3.1.3.4 Cutoff Card

The cutoff card will terminate the run when a certain number of particle histories have been run or desired computing time has been exceeded. There are two cutoff cards, NPS determines the number of particles to stop the run after exceeding and the CTME card will stop the run at a specified time in minutes. If both are specified, the first cutoff will cause program termination. Depending on the desired outcome of the problem combined with the scale of the size of the problem, high NPS or CTME settings usually deliver the most accurate results since they will lead to a larger sample size to reduce statistical error. In the forthcoming chapters discussing results of simulations, NPS is used frequently as a stand-in to designate the total number of particle histories run in a simulation [65].

3.1.3.5 Tally Card

The tally card is used to specify what type of information the user wants to gain from the Monte Carlo Calculation. Tallies include current across a surface, flux at a point, flux in a volume, flux through a surface, and energy deposition. The user will request this

function by specifying tally type (numbered 1-8), particle type (N, P, E), as well as a choice of seven basic neutron tally types, 6 basic photon tally types, and 4 basic electron tally types. Tallies are discussed in much greater detail in upcoming sections as pertaining to the analysis done in this thesis, and needless to say there are a multitude of ways to obtain what is needed from a problem [65].

Mnemonic	Tally Type	particles <i>pl</i>	Fn Units	*Fn Units
F1: <i>pl</i>	surface current	N or P or N,P or E	#	MeV
F2: <i>pl</i>	average surface flux	N or P or N,P or E	#/cm ²	MeV/cm ²
F4: <i>pl</i>	average flux in a cell	N or P or N,P or E	#/cm ²	MeV/cm ²
FMESH4: <i>pl</i>	track-length tally over 3D mesh	N or P or E	#/cm ²	MeV/cm ²
F5a: <i>pl</i>	flux at a point or ring	N or P	#/cm ²	MeV/cm ²
FIP5: <i>pl</i>	pin-hole flux image	N or P	#/cm ²	MeV/cm ²
FIR5: <i>pl</i>	planar radiograph flux image	N or P	#/cm ²	MeV/cm ²
FIC5: <i>pl</i>	cylindrical radiograph flux image	N or P	#/cm ²	MeV/cm ²
F6: <i>pl</i>	energy deposition	N or P or N,P	MeV/g	jerks/g
F7: <i>pl</i>	fission energy deposition in a cell	N	MeV/g	jerks/g
F8: <i>pl</i>	pulse height distribution in a cell	P or E or P,E	pulses	MeV

Figure 3.1. The types of tallies available in MCNP [94]

3.1.3.6 Dose Data Card

Tallies can be modified by dose data cards which bring in the input of dose conversion coefficients. These modifications become pointwise response functions specific to the desired data point in the tally. MCNP contains a few default tables for this, and it is flexible enough to allow manual input of a large variety of dose conversion coefficients for the various phantom dose conditions discussed in Section 2.4.8. These data cards are also dependent on the type of tally used as well as the mode of the problem [65].

3.1.3.7 Variance Reduction Cards

A challenge in using MCNP is to minimize computing expense to obtain a tally estimate with acceptable relative error. Direct simulation (analog MCNP) many times

requires far too many histories for acceptable results with computer time available. There are many techniques used to reduce the relative error (or variance) of a tally for a fixed computing time. There are two basic approaches to reduce the computational effort of a problem: simplification of the MCNP model through truncation of geometry and physics as well as the use of non-analog simulations. The non-analog simulations modify the process by making events more or less probable than they actually occur. Three general methods are used including population control, modified sampling and partially-deterministic calculations. There are many cards available to play in this game of variance reduction and many of the techniques these cards employ are outlined in the next section [65].

3.1.4 Variance

3.1.4.1 Tally Variance

A significant part of the Monte Carlo tally is the uncertainty associated with the result. The quality of the result is determined by the number of histories run and other factors that provide insight into the statistical behavior of the tallies. Particle histories produce a range of scores depending on the tally used and the variance reduction techniques deployed. In a Monte Carlo simulation, the i th history contributes a score x_i to the tally. If a particle never reaches the tally region, then $x_i = 0$; if it reaches the tally without interaction, then x_i is often very large. The mean score (or expected value) of x is given by:

$$\langle x \rangle = \int_0^{\infty} xp(x) dx \quad (44)$$

where $p(x)dx$ is the probability of any history contributing a score between x and $x + dx$. The term $p(x)$ is a probability distribution function (PDF). If $p(x)$ is not known a priori, MCNP approximates $\langle x \rangle$ by the average \bar{x} of the scores of N particles,

$$\bar{x} \equiv \frac{1}{N} \sum_{i=1}^N x_i \quad (45)$$

As $N \rightarrow \infty$, the strong law of large numbers guarantees that $\bar{x} \rightarrow \langle x \rangle$, provided $\langle x \rangle$ is finite. The variation in different scores x_i is measured by the standard deviation of the histories, which for large N

$$S^2 \equiv \frac{1}{N-1} \sum_{i=1}^N (x_i - \bar{x})^2 \simeq \overline{x^2} - \bar{x}^2 \quad (46)$$

where

$$\overline{x^2} = \frac{1}{N} \sum_{i=1}^N x_i^2 \quad (47)$$

The estimated variance of the average \bar{x}

$$S_{\bar{x}}^2 = \frac{1}{N} S^2 \quad (48)$$

The central limit theorem states that if the simulation is repeated a large number of times, the variation of the mean \bar{x} from each simulation will be distributed normally about the true mean $\langle x \rangle$ and have a variance $S_{\bar{x}}^2$, this uncertainty (or variance) is what is to be reduced in MCNP simulations. A goal for this approach is to estimate \bar{x} with the least uncertainty or minimum standard deviation $S_{\bar{x}}$ [65].

3.1.4.2 Relative Error

In any variance reduction method, the simulation is changed so that $p(x)$ is concentrated about its mean $\langle x \rangle$. This concentration makes the variance of the mean $S_{\bar{x}}^2$ less than the analog PDF. Relative error is the fractional 1 sigma estimated uncertainty in the tally mean, and is the ratio of the standard deviation of the tally mean to the tally mean.

$$R \equiv \frac{S_{\bar{x}}}{\bar{x}} \quad (49)$$

The value of R is determined by the history scoring efficiency q , which is the fraction of histories producing non-zero x_i 's, as well as the dispersion in non-zero scores. This is a very important statistic, but it alone cannot decide the acceptability of the tally result. MCNP breaks relative error into two components

$$R^2 = R_{eff}^2 + R_{int}^2 \quad (50)$$

where R_{eff} is the spread in relative error caused by scoring inefficiency and R_{int} is the intrinsic spread of the non-zero history scoring events.

If every source particle contributes to the tally ($q = 1$), then $R_{eff} = 0$; as more and more particles produce zero score, R_{eff} increases. R_{int} measures uncertainty produced by the spread of non-zero scoring events, and if some particles produce zero scores while the remainder produce the same score, $R_{int} = 0$. As the scoring particles have increasingly different scores, R_{int} increases. The purpose of variance reduction techniques is to increase the scoring efficiency, hence reducing R_{eff} while decreasing the spread of non-zero scores [94].

Range of R	Quality of Tally
> 0.5	Meaningless
0.2 to 0.5	Factor of a few
< 0.1	Reliable (except for point/ring detectors)
< 0.05	Reliable even for point/ring detectors

Figure 3.2. Interpretation of the relative error R [94]

3.1.4.3 Figure of Merit

MCNP requires long calculation times especially for thick shielding, this results in significant attenuation of radiation with much fewer particles going through a thick shield. This makes it difficult for effective sampling of source variables, the challenge is to minimize computing expense needed to arrive at a result that is within accepted statistical criteria. Efficiency is evaluated with Figure of Merit and reducing uncertainty can be done by many ways, one way is to have longer computing time. Generally a square law relationship exists between the error and the number of observations and the usual way out is through variance reduction. Figure of Merit, FOM , is calculated by the following relation

$$FOM = \frac{1}{R^2 T} \quad (51)$$

Where T is the run time, which is proportional to N , the number of histories run. Since run time varies with computer, the same simulation performed on different machines produces different figures of merit. Since $R^2 \sim 1/N$, FOM should remain relatively constant. For different variance reduction techniques, the one with the largest FOM is preferred [65].

3.1.4.4 Truncation Techniques

There are a multitude of techniques available in MCNP to reduce the computational time for a problem to run. Truncation techniques exist to reduce time per particle history by simplifying geometry and simplifying the physics used to generate the random walk for each particle. Care must be taken since any simplification of geometry or physics introduces bias into the tally; a very precise (low variance or relative error) estimate can be achieved, but it may not be very accurate. Multiple runs with different approximations must be made to assess the importance of any simplification, but MCNP can give no warning about errors caused by geometry simplifications. At best a warning may occur in the output file for an error in a physics simplification. Methods can be employed in the code to aid in this simplification that include the use of Energy, Time, Weight Cutoff, and Physics cards.

3.1.4.5 Non-Analog Techniques

Non-analog techniques can be used in cases where thick shielding attenuates particles through scattering and/or absorption. This results in changes in particle energy and direction and in very small particle counts outside the shield requiring large numbers of histories. This in turn requires long run times for statistically reliable results. Particles are assigned statistical weights in non-analog techniques, weight is reduced through physical events such as collision and absorption. A particle is tracked until elimination or it reaches number of particles that have been set in the calculation. Several techniques are available to artificially bring more particles to tally region such as Source Biasing, Splitting, Russian Roulette, and Implicit Absorption [65].

Difficult and often impractical data is generated in non-analog techniques, the original problem can be distorted in such a way that uncertainty in the solution is reduced (importance sampling) or by making allowances for various causes of variation in data (regression). Uncertainty can be measured in terms of variance, methods of variance reduction do not introduce bias into estimation. Results can be made more precise without sacrificing reliability and techniques adjust the natural sampling procedures to focus on “important particles”. In this case, particles are given statistical weight to compensate using the following relation.

$$w_{biased}pdf_{biased} = w_{unbiased}pdf_{unbiased} \quad (52)$$

where pdf is probability distribution and w is particle weight.

In some cases, integer splitting (where the sum of the split branch weights always equal 1) is used and the above equation is modified to become

$$n \times w_{biased}pdf_{biased} = w_{unbiased}pdf_{unbiased} \quad (53)$$

where $pdf_{biased} = pdf_{unbiased}$ and the physical process is changed rather than the probability.

3.1.4.6 Variance Reduction Techniques

MCNP offers a variety of variance reduction techniques. These include propulsion control methods, modified sampling methods and partially deterministic methods. Population control methods artificially increase or decrease the number of particles in regions that are important or unimportant to the tally score. These include geometry splitting and Russian roulette (IMP card), energy splitting/roulette (ESPLT card), weight cutoff (CUT and PWT cards), and weight windows (WWE, WWN, WWG, and WWGE

cards). Modified sampling methods artificially increase the likelihood of events that increase the probability of a particle reaching a tally region. These include exponential transform (EXT and VECT cards), implicit capture (PHYS card), forced collisions (FCL card), bremsstrahlung biasing (BBREM), source direction and energy biasing (SDEF, SP, SB and SI cards), and neutron-induced photon production biasing (PWT and 2-31 cards).

Partially deterministic methods replace the random walk process by a deterministic process to move particles from one region to another. These include point and ring detectors (F5a card), DXRAN spheres (DXT and DXC cards), and correlated sampling (PD and 2-143 cards) [65]. Out of the above methods presented, the most commonly used ones are discussed in greater detail below.

3.1.4.6.1 Geometry Splitting

Geometry splitting is one technique that is actively being used in the simulations for this thesis, specifically with importances that are assigned to each cell of the problem. Generally, cells near the tally region should have a greater importance than cells farther away. Each cell i is assigned importance I_i , if a particle of weight w_0 passes from a cell of importance I_i to a cell with higher importance $I_j (I_i < I_j)$, the particle is split into $\nu = I_i/I_j$, identical particles of weight w_0/ν . If a particle of weight w_0 passes from a cell of importance I_i to a cell with lower importance $I_k (I_i > I_k)$, Russian roulette is applied, killing the particle with a probability of $1 - (I_k/I_i)$. In each splitting, the weight of the remaining particle is adjusted to keep the tally unbiased and cell importances are adjusted so as to keep the population of particles relatively constant [65, 92, 93].

3.1.4.6.2 Weight Windows

Weight windows adjust the weight of the particles as they change energy and move through the problem geometry. In each cell, a lower weight bound and an upper bound are specified for particles entering a cell or if created in a cell. If a particle weight is above the upper bound, the particle is split such that all split particles are within the weight window. If a particle weight is below the upper bound, Russian roulette increases particle weight until it lies within the window or is killed. In most problems, weight windows is preferred over importance biasing [65].

3.1.4.6.3 Exponential Transform

Exponential transform artificially changes the distance to the next collision. Particles can be moved preferentially towards the tally region and inhibited from moving away. The path length between collisions is stretched in a preferred direction by adjusting the total cross section as $\sum_t(1 - p\mu)$ with p being the stretching parameter and μ being the cosine of the angle between the particle direction and the preferred direction [65].

3.1.4.6.4 Energy Splitting/Russian Roulette

For some problems, only particles with a certain range of energies are of interest. The ESPLT command for a particle in this range can be used to split it into daughter particles of the same type. For particles outside this range of interest, Russian roulette eliminates some of them. Russian roulette is mostly used to kill a particle when it reaches a region of space far from the tally region being unlikely with further random walk simulation to return to that region [65].

3.1.4.6.5 Forced Collisions

Forced collisions increases sampling of collisions in specified cells, generally those near a DXTRAN sphere of a point/ring detector; this splits particles into collided and uncollided parts. The collided part is forced to interact within the current cell while the uncollided part exits the cell without collision. The weight windows game is not played at surfaces bounding a cell in which forced collisions are specified [65]. This technique figures prominently in the simulations conducted for this thesis, arriving at its use was a hard-earned lesson that came after many iterations and it helped clear the path to the first meaningful solutions in the thesis process.

3.1.4.6.6 Source Biasing

Source biasing was another technique that was discovered early on in iterations, for the distances involved in the calculations made detection of particles from point sources very difficult. This is one of the easiest non-analog techniques to implement, any SDEF variable can be biased in MCNP and in many ways. For example, source particles can be started with enhanced weights, preferred energies, and in regions closer to the detector. A very useful source biasing technique is to start particles in preferred directions, generally toward tally regions [65].

3.1.5 Accuracy vs Precision

MCNP makes it possible to produce tally results that are extremely precise but not very accurate. Precision is the uncertainty in the tally mean, \bar{x} , caused by statistical fluctuations in individual scores, x_i , of simulated histories which is measured by tally variance. Accuracy is a measure of how close the tally mean is to the true physical quantity being estimated and systematic error is the difference between true value and expectation

value of the simulation. Many factors affect accuracy, in the MCNP code inaccuracies are introduced by the use of physics models, mathematical models, uncertainties in nuclear/atomic data and coding error. The MCNP model can be affected by improper modeling of source energy and angular distributions, poor representation of actual geometry as opposed to MCNP model geometry, errors in material compositions and plain user errors.

Factors affecting precision include forward versus adjoint calculations; for problems with spatially extended sources and small tally regions, an adjoint simulation often produces more precise results with few histories compared to a forward simulation. Tally type also affects precision, point detectors, for example, are often less precise than surface detectors in a scattering medium. Variance reduction also affects precision as well as the number of histories, for the more histories that are run, the better will be the precision of the tallies. MCNP produces statistics to assess the precision of the result, and initial focus should always be on the ten statistical indices calculated by MCNP.

3.1.5.1 MCNP Produced Statistics

MCNP produces a wealth of information to assess the precision of the result. The output file has so much information that it can be overwhelming to the novice user. The initial focus for any simulation should be on the ten statistical indices calculated by MCNP. Some of the more important ones are detailed below.

3.1.5.1.1 Variance of the Variance

The estimation of relative error is important to indicate the precision of the tally mean. To determine the accuracy of the relative error, MCNP estimates the relative variance of R , a variance of the variance (VOV) which is found via

$$VOV = \frac{S^2(S_{\bar{x}}^2)}{S_{\bar{x}}^2} = \frac{\sum_{i=1}^N (x_i - \bar{x})^4}{[\sum_{i=1}^N (x_i - \bar{x})^2]^2} - \frac{1}{N} \quad (54)$$

where $S^2(S_{\bar{x}}^2)$ is the variance of $S_{\bar{x}}^2$. The *VOV* involves the third and fourth moments of the tally distribution $f(x)$, this is much more sensitive to fluctuations in large history scores than R for it is based on only the first and second moments [65].

3.1.5.1.2 Tally Probability Distribution Function

The tally probability distribution function (PDF) is constructed by MCNP to help assess the quality of the confidence interval estimates for the tally mean. Examining the high-end tail of this distribution is important to problems involving infrequent events with very high score. There are three possible outcomes for such problems:

1. Statistically meaningful confidence intervals are produced
2. A rare event with large scores is sampled causing the mean and R to increase with a corresponding significant decrease in FOM . This is easily detected by observing behavior of R and FOM in the Tally Fluctuation Chart (TFC) produced at the end of the MCNP output.
3. The tally mean is substantially underestimated despite the problem appearing to be converged from statistical tests. This is due to inadequate sampling of large scoring histories and detecting this situation is difficult. This is why MCNP performs extensive analysis of the high tally tail of the PDF.

The Central Limit Theorem (CLT) guarantees the tally mean will appear to be sampled from a normal distribution with standard deviation σ/N if N is sufficiently large. Confidence intervals in MCNP for the tally are based upon this assumption, but the question remains, how large must N be? In order for this to hold, the first two moments of

the tally PDF $f(x)$, $E(x) = \int_0^{\infty} xf(x)dx$ and $E(x^2) = \int_0^{\infty} x^2f(x)dx$ must exist. The existence of these first two moments is dependent on $f(x)$ having a finite upper tally cutoff, or on x decreasing faster than $1/x^3$.

MCNP uses the 200 highest scoring histories to estimate the slope of the high tally tail for the PDF by fitting a generalized Pareto function to the high tally events. This Pareto function is found via

$$f_p(x) = \frac{1}{a(1 + kx/a)^{1+(1/k)}} \quad (55)$$

with the slope being

$$SLOPE = 1 + \frac{1}{k} \quad (56)$$

On the output plot of the PDF, the Pareto fit is shown by a string of the letter “s”, and the tally mean is shown by a string of the letter “m”. For this to apply, the *SLOPE* must equal 3. If too few histories are run to generate an estimate, *SLOPE* is reported as zero. If the PDF falls off faster than $1/x^{10}$, the slope is set to a “perfect” value of 10 [65].

3.1.5.1.3 Confidence Intervals

MCNP estimates the confidence interval for the tally from the relative error. Since the estimated mean and the estimated uncertainty in the mean are correlated, the midpoint of the confidence interval needs to shift slightly from the mean. The amount of this midpoint shift is proportional to the third central moment and should decrease as $1/N$. This refinement is calculated by MCNP as the simulation progresses [65].

3.1.5.1.4 Tally Estimates

Sometimes a conservative tally estimate is needed, in case rare high-tally events have not been completely considered. In the output file, MCNP shows what would happen if the mean, relative error, variance of variance, et cetera of the next history $N + 1$ were the same as the largest scoring history in the simulation of N histories. If large changes occur with this estimate, it is wise to be suspicious of the results for the simulation may be flawed [65].

3.1.5.1.5 The Ten Statistical Tests

The most important measure in MCNP for reliability of results check is contained in the 10 statistical tests performed on each tally. Tally Mean, \bar{x} , must exhibit, for last half of problem, only random fluctuations as N increases and no up or down trends are allowed. Relative Error, R , must be less than 10% of 1σ error (5% for point and ring detectors), must decrease monotonically with N for last half of problem, and must decrease as $1/\sqrt{N}$ for last half of problem. The Variance of the Variance, VOV , must decrease monotonically with N for last half of problem, must decrease as $1/\sqrt{N}$ for the last half of problem and the magnitude must be less than 0.1 for all tallies. The FOM must remain statistically constant for the last half of problem, and it must exhibit no monotonic up or down trends for that segment as well. Finally, the slope determined from largest scoring events must be less than 3 for the tally PDF, $f(x)$. If a tally passes all of these statistical tests, the simulation is considered to be as complete as it can be made [65].

3.2 Dosimetry in MCNP

Of the many ways to collect tally data, the dose determination in the models for this thesis was found to be most effective using the F4 and F6 tallies. During the literature surveys, the thesis by Dugal became the guiding focus for the best method on dosimetry using these tallies [63]. Using the MCNP dose functions outlined in Section 3.1.3.6, it is possible to input dose conversion coefficients like those covered in Section 2.4.8.2 to turn tally quantities into meaningful numbers to compare against. The following subsections outline underlying theory for finding dose in the F4 and F6 tallies.

3.2.1 Dosimetry with the F4 Tally

The F4 tally is the average flux in a cell with units of particles/cm². Suppose a particle of weight W and energy E creates a track-length segment T within a cell of volume V . This segment makes a score contribution of $W T/V$ to the flux (or fluence) in the cell. These contributions are summed and reported as the full F4 tally in the MCNP output. If $\Phi(\mathbf{r}, E, \Omega)$ were the energy and angular distribution of the fluence as a function of position with Φ being the fluence, \mathbf{r} being the particle position vector, and Ω being the direction vector, then the F4 tally would measure [65]

$$\text{F4} = \frac{1}{V} \int_V dV \int_E dE \int_{4\pi} d\Omega \Phi(\mathbf{r}, E, \Omega) \quad (57)$$

Ambient dose equivalent can be found using the F4 tally with the photon and neutron fluence methods. The photon fluence tally calculates the photon fluence differential energy averaged over the volume of the cell and is represented by the term $\left(\frac{d\bar{\Phi}'_\gamma}{dE_\gamma}\right)$. The neutron fluence tally calculates the neutron fluence differential energy

averaged over the volume of the cell and is represented by $\left(\frac{d\Phi'_n}{dE_n}\right)$. These are essentially the raw output from the F4 tally when integrated with respect to the energy differentials. Combining these with a conversion coefficient allows for these outputs to be reported in units of dose equivalence. There are a multitude of conversion coefficients to choose from, and the focus here will be on conversion coefficients necessary to calculate ambient dose equivalent at a depth of 10 mm.

Ambient dose equivalent, covered in Section 2.4.8.3.3, has a few important conditions to be met in order to be valid. The first assumption is in the use of the ICRU Sphere, and the second one is in the use of the expanded and aligned field which is a derived radiation field calculated from a reference point in a real radiation field. For this to be the case, the fluence at the reference point is first made to be unidirectional by rotating each of the fluence components such that they are in one direction. Next this unidirectional fluence is expanded throughout the derived radiation field such that the fluence has the same value throughout the derived radiation field's volume [94].

The ambient dose equivalent, $H^*(d)$, is defined at a point in a radiation field as the dose equivalent that would be produced by the corresponding expanded and aligned field, in the ICRU sphere at a depth d on the radius opposing the direction of the aligned field. 10 millimeters depth is the recommended variable for use with the strongly penetrating radiation that is being simulated. For a known depth and radiation type, energy-dependent conversion coefficients can be evaluated that relate the fluence at a point to the ambient dose equivalent calculated at that point. In the case of this thesis, the dose conversion factors used were from ICRP Publication 74 [69]. After these conversion factors are applied, the ambient dose equivalent is in units of Sieverts/particle [66].

Total ambient dose equivalent at 10 mm depth is found by combining the F4:n and F4:p outputs with their appropriate flux-to-dose conversion factors and is shown in the following equation.

$$H^*(10) \doteq \int_0^\infty \left(\frac{d\bar{\Phi}'_\gamma}{dE_\gamma} \right) \left(\frac{H_\gamma^*(10)}{\bar{\Phi}'_\gamma} \right) dE_\gamma + \int_0^\infty \left(\frac{d\bar{\Phi}'_n}{dE_n} \right) \left(\frac{H_n^*(10)}{\bar{\Phi}'_n} \right) dE_n \quad (58)$$

where $\left(\frac{H_\gamma^*(10)}{\bar{\Phi}'_\gamma} \right)$ represents the photon fluence to ambient dose equivalent conversion coefficient at a 10mm depth, and $\left(\frac{H_n^*(10)}{\bar{\Phi}'_n} \right)$ represents the neutron fluence to ambient dose equivalent conversion coefficient at a 10mm depth [63].

3.2.2 Dosimetry with the F6 Tally

The F6 tally is the energy deposition averaged over a cell with units of MeV/gram. Suppose a particle creates a track length segment across a cell where the segment makes a score contribution of $WT\sigma_t(E)H(E)\rho_a/m$ to the cell. $\sigma_t(E)$ is the microscopic total cross section in barns as a function of energy, $H(E)$ is the heating number as a function of energy in MeV/collision, ρ_a is the atom density in atoms/barn-cm, and m is the cell mass. The F6 tally would then measure [94]

$$F6 = \frac{\rho_a}{m} \int_E dE \int_V dV \int_{4\pi} d\Omega \sigma_t(E) H(E) \Phi(\mathbf{r}, E, \boldsymbol{\Omega}) \quad (59)$$

Another way to examine the F6 tally is in terms of neutron and photon kerma. The heating can be broken down in the neutron side as follows

$$F6:n = H_n \doteq \int_0^\infty \left(\frac{d\bar{K}'_n}{dE_n} \right) Q_n(E_n) dE_n \quad (60)$$

The neutron quality factor as a function of energy, $Q_n(E_n)$, is used to account for the higher relative biological effectiveness of neutron kerma over the relative biological effectiveness of dose from electrons. The neutron kerma tally calculates a modified neutron kerma differential in energy averaged over the volume of a cell, $\left(\frac{d\bar{K}'_n}{dE_n}\right)$ where E_n is the neutron energy and $d\bar{K}'_n$ is the modified neutron kerma averaged over the volume of a cell in the interval between E_n and $E_n + dE_n$.

The tally is modified from using a pure neutron kerma tally in that provisions are made so that kerma cannot be double-counted. This is a necessary change if one wants to approximate dose by kerma. Double counting could arise from many possible outcomes, an example being secondary particles created when an uncharged particle creates an charged particle and that particle's energy is considered to be locally deposited. The charged particle, not having deposited all of its energy, goes on to create an uncharged particle which then produces a charged particle with energy assumed to be locally deposited again. This could lead to kerma being counted twice and lead to dose overestimates. MCNP prevents double counting by restricting the tally of kerma from an uncharged particle to only being counted if the uncharged particle has no parent particle that was counted as kerma. The modified neutron kerma is assumed to be completely deposited locally [63].

The photon kerma side of the F6 tally can be further explained by the following equation

$$\text{F6: p} = H \doteq \int_0^{\infty} \left(\frac{d\bar{K}'_{\gamma}}{dE_{\gamma}} \right) dE_{\gamma} + \frac{E_{kill,\gamma}}{m} \quad (61)$$

where $\left(\frac{d\bar{K}'_{\gamma}}{dE_{\gamma}}\right)$ is the modified photon differential in energy averaged over the cell, and $E_{kill,\gamma}$ is the total energy of the photons killed within the cell which is in turn divided by the mass of the cell, m . $E_{kill,\gamma}$ is a term that needs to be estimated since it is not directly available in MCNP. Combining Equations 60 and 61 gives a summation of all of the heating across the cell with regards to neutron and photon kerma [63].

3.3 Test Cases

In light of the issues identified earlier in this chapter regarding accuracy and precision with models and simulations in MCNP, the application of verification and validation becomes important. All of the models created for the Charger-1 facility as well as the z-pinch powered spacecraft lack an anchor in operational reality. In order to validate the process, the models need to have a basis for comparison with solved problems. To this end, it was decided to model examples with solutions published in a textbook. The verification process was split into two problems with one focusing on photon simulations and the other focusing on neutron simulations. Both problems were derived from the work of Emrich [68].

3.3.1 Photon Verification Problem

In order to validate the methods going forward with regards to photon calculations, a textbook problem was chosen that used relatively simple methods to arrive at conclusions. This problem created a hypothetical crewed spacecraft with an NTR propulsion system using liquid hydrogen as propellant; this spacecraft would not have shielding to save mass and instead rely on attenuation from the column of liquid hydrogen

in between the reactor and the crew module. The one of the goals of this analysis would be to create a time-dependent astronaut dose curve in synch with the depletion of the propellant as it is used in the NTR [68].

This problem was replicated using MCNP to model attenuation through the hydrogen, and since MCNP cannot be run through a variable situation like the dropping of propellant levels, the attenuation curve was painstakingly created through individual runs for each time step of depletion. This process proved to be very challenging and time consuming but many lessons were learned in the process that improved the ability to use MCNP. This repetition was practice for refining methods to run MCNP simulations since the learning curve for MCNP is quite steep and difficult. Ultimately, the attenuation curve was replicated and details for this exercise are presented in Appendix A.

3.3.2 Neutron Verification Problem

As has been discussed earlier, analysis of neutrons is not as straightforward as it is for photons. With so many types of interactions and secondary effects to consider, hand calculations do not give accurate results. That being said, there are several approximations that have been derived to consider the effects of neutrons in attenuation. The electronic version of Emrich's textbook is viewable in the Mathematica software package, and it takes advantage of the functions of that program to have several calculators embedded in the text in the various chapters of the book. One of these calculators is set up to approximate attenuation through a multilayer shield, built with three layers of variable thickness and different materials it is able to plot attenuation curves for neutrons and gamma rays through the different layers.

Building upon the work of Adams, et al in the 2011 study on Z-pinch propulsion, a spacecraft multilayer shield was modeled in MCNP for the efforts of this thesis [42]. The results from that paper were presented as an output from Emrich's Mathematica calculator. For the sake of consistency, the shield configuration in that paper was set as the shield configuration studied in this thesis. This is detailed in the next chapter for studying the spacecraft configuration. For the purposes of neutron verification, this configuration was replicated in the Mathematica tool and new attenuation curves were generated. A series of MCNP runs were executed with detection set up step-wise throughout the thickness of each shield to find attenuation at the point of interest to be able to generate a curve. This effort was time consuming and challenging but was made much less difficult by the lessons learned from the many iterations in the photon verification task. The neutron verification effort is presented in great detail in Appendix B.

CHAPTER 4. MODELING AND SIMULATION

4.1 Charger-1 Facility

The facility housing Charger-1 is a building of great length, sharing space with Charger-1 is a light gas gun managed by the UAH Aerophysics Research Center taking up a significant portion of the nearly 1200 ft of length. By contrast, Charger-1 resides in the northwest corner of the facility taking up close to 150 ft of the length and 5000 ft² at the end of the building. The building itself is of basic steel construction dating from the 1960s with structural members and sheet metal cladding on a concrete foundation. The main lab space is in the cavernous length where the light gas gun is used to perform research on hypervelocity projectile impacts in vacuum conditions. This gun is close to 900 ft in length and it is the reason for the original construction of the facility. The control room for the gun is located near the midpoint of the building adjacent to office space; this room is reinforced with 2 foot thick concrete walls to protect the occupants in the case of a catastrophic failure of the gun. This will also be the control room for Charger-1, and it is located 500 feet from where the radiation source will be [50].

Within the footprint as shown in Figure 4.1, the facility layout includes support equipment for Charger-1. The Marx Generator on Charger-1 needs transformer oil for operation, this oil is stored in a tank just outside the building. The Trigger Capacitor and Transfer Line need deionized water for operation and this is manufactured through a deionization system that is inside the building. Charger-1 itself occupies a small corner of the facility and is in a spot with pre-existing barriers for radiation protection for outsiders. Along the north and west sides of the building, there is an earthen berm that is as tall as the

building allowing for protection to the residential area a half mile to the west of the facility. The berm was built up for the gun portion of the facility but soil of that amount will provide significant radiation protection as well. The radiation output for Charger-1 will be concentrated in the area nearest to the northwest corner of the building.

The next few sections detail the buildup of the MCNP model of this facility and a note needs to be made on units going forward. Up until this point in this chapter, all dimensions of the facility have been presented in feet and inches but since MCNP operates in metric units, all further mentions will be consistent with metric conventions.

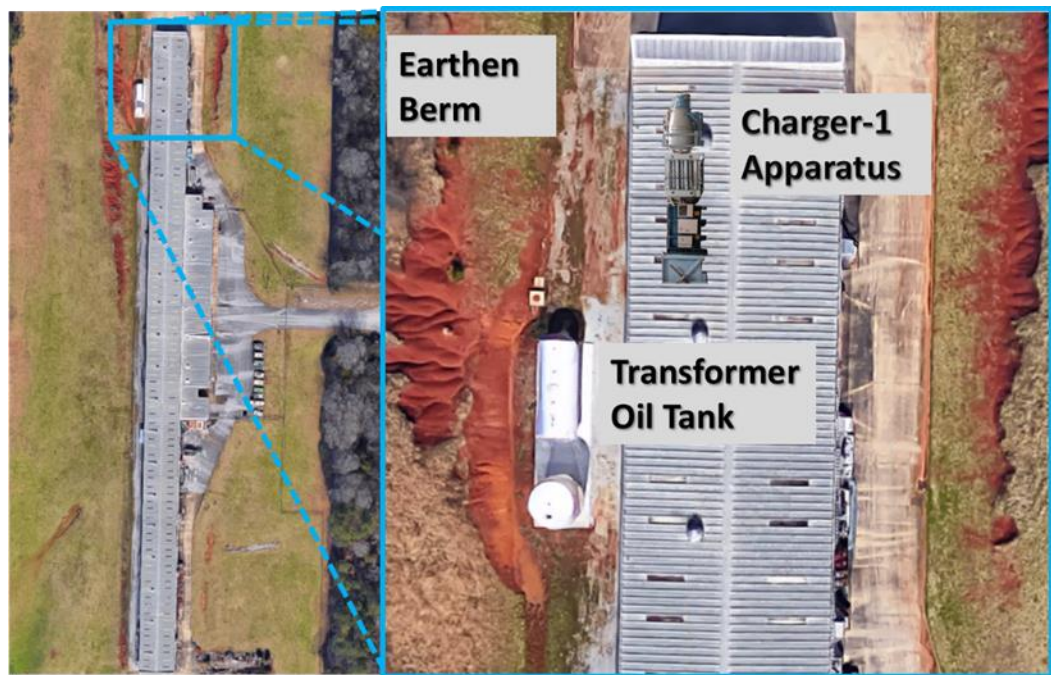


Figure 4.1. Charger-1 Facility as viewed from satellite imagery with a representative of Charger-1 superimposed on the roof

4.1.1 Early Iterations and Lessons Learned

The learning curve of MCNP is a very steep one that can only be climbed through the repeated execution of input decks. The evolution of the model through iterations started with assumptions that as a beginning user, could not have foreseen the folly of precisely trying to replicate the facility in the model. The process to first develop model geometry and input conditions that would even run as a simulation was in of itself a long one. Initially, it was difficult to even get the syntax of the cells and surfaces correct which then led to fatal errors that needed to be diagnosed and learned from. Ultimately, a complex series self-learning adventures with MCNP over the course of several semesters led to more efficient runs through trial and error.

One tool that quickly became useful in the early development of MCNP models was the MCNPX Visual Editor. This proved to be powerful for learning the proper syntax and subtle ways of proper input for Cell and Surface cards that allow for the input deck to be able to compile. It also proved to be as troublesome as useful due to frequent crashes in response to improper input syntax, but these crashes helped close the loop learning on proper geometry techniques. The Visual Editor is set up with a database of default material compositions commonly used in nuclear and other radiological industries, and this allows for a quick input of detailed material compositions without consultation of a user's manual. This was ultimately used to help shape the configuration for every simulation that was run in this thesis effort [95].

The first attempts to capture the Charger-1 facility included details like concrete floors, walls, underlying soil, air, and even simulated reactor vessels. Initially, the model control volume was a large sphere on the order of 17,000 cm in diameter. Poor

understanding of the mechanics of MCNP as related to the transport of particles through every cell combined with the large distances and model complexity led to early iterations being very cumbersome and wasteful in terms of computing resources. One of the earliest lessons learned was that increasing NPS particle cutoff numbers led to better statistical convergence at the tallies. However, when applied to a facility model, the long distance between the source and most of the tally regions as well as the attenuation from the control room concrete wall led to NPS cutoffs in the billions of particles. These runs would take most of a day to execute and tallies would end up with high relative errors and poor performance in the ten statistical tests despite the high number of initial particles.

Extremely low particle counts from the earliest runs led to experimentation with artificially biasing the particles toward the tally regions. The first change was from the default source assumption of a point isotropic source radiating in all directions to a disc source with particles going in one direction. This source biasing assumption helped with complicated geometries, but the distances to the tally regions were still a difficult problem to overcome. Much experimentation was also done in attempts to model more complex sources to attempt to replicate the plasma geometry of the z-pinch as shown in Figure 1.8 and Figure 1.9. This led to multiple sources overlapping with broad spectrums of energies input to stretch the available capabilities of the SDEF card. This more complicated source was not able to be run as a unidirectional disc and therefore led to high relative errors in the tallies.

The quest to improve particle counts at tallies also led to the trial and error optimization of the settings of importances for use as another method of biasing particle

flow towards the detectors. This setting, detailed in Section 3.1.4.6.1, is a form of geometry splitting that allows MCNP to prioritize the counting of particles being transported through certain cells over other ones. Again, due to great distances, this trick is necessary to enable the tallies to collect enough data to pass all of their statistical tests. If done correctly, the setting of importances will be able to reduce computation time significantly. In the case of this problem, the highest importances are associated with the detector cells; the vacuum outside the problem boundary is set to zero in order to kill the particles.

The trial and error process also led to the implementation of forced collisions, covered in Section 3.1.4.6.5, this non-analog technique proved quite effective in driving tally convergence with their statistical tests. Forced collisions (FCL card) allows for certain cells in the model to be biased towards particle collisions while other cells are exempted from this bias. This technique can be toggled between focusing on entering and colliding particles entering the cell as well as just the entering particles [94]. Most of the utility of the forced collisions technique was largely discovered during the modeling and simulation efforts for the photon verification test cases. Once this was applied, computation times were cut 30% and full statistical convergence was arrived at in tallies where this was not the case before this technique was applied.

The facility modeling went through several iterations, with the 24th iteration being the first one to start giving consistent results using a disc source. Several more iterations were done with varying success, one attempt was even made to model a very complex facility geometry that included walls, the roof, as well as the transformer oil tanks and the earthen berm outside. This was quickly abandoned when it became apparent that the computational resources were not available to run to almost any results in a reasonable

amount of time. By the 30th iteration, the facility model lost its walls and outside details and the focus was on the concrete floor, a concrete shield wall and a metal reactor vessel containing the complicated z-pinch plasma mentioned earlier. This was an attempt to model the neutron, photon and electron interactions with two sources nested within one another to simulate D-T fusion as well as D-Li6 fusion.

The MCNP learning curve is like a mountain range where each summit surpassed reveals another higher and steeper set of peaks beyond; the territory in between filled with deep canyons and raging rivers of snowmelt. Every breakthrough in executing inputs to drive statistically significant results was accompanied by large setbacks and painful repetition. The nomenclature for the facility modeling used the ChargerLab moniker in the development of the facility simulations. By ChargerLab30, it was not yet clear that the complex geometries were the main factor for tediously long computation times. The addition of FCL biasing finally cleared a path for results containing lower relative errors, but the results in the ICRU sphere behind the concrete wall were still yielding relative errors of 0.3, down from the 0.5 before the addition of FCL. ChargerLab30 executed a run of 500 million particle histories in 1,234 minutes before FCL allowed for the execution of a billion particle run in 1,224 minutes.

In the process of becoming more proficient at MCNP, several side quests were executed as well. The initial runs in the spring of 2017 yielded lessons that were applied in runs during the summer and fall of 2017. By the spring of 2018, the state of the art was the ChargerLab30 family of configurations accompanied at the same time by the intense photon verification effort that consumed most of that semester. By the summer of 2018, deep investigations were played out in new configurations. ChargerLab35 was a photon-

only problem applying lessons learned from the test cases, this problem yielded the first results behind the wall with acceptable relative errors in the 0.01 range. Those results were viewed as incomplete since neutron interactions were not accounted for, but it executed ten million particle histories in only 25 minutes.

Another rabbit hole was dug in an effort to capture the lessons learned from the MCNP efforts of Schillo on his dissertation [15]. This led to a deep effort to learn criticality codes in MCNP6 with the KCODE card. The use of KCODE made it possible to create a model of a PuFF source, in this case a 1 cm diameter sphere of Highly Enriched Uranium (HEU) surrounded by a Lithium shell. There were several iterations of the ChargerLab configuration as an attempt was made to optimize criticality calculations. The results of this ended up being neutron production rates that were too small to drive convergence in the distant tally regions.

Due to the extremely low amount of particles penetrating the shield in this condition as well as the low number reaching the ICRU sphere in front of the shield, the focus on KCODE tapered off by ChargerLab45. It also was around this time that the first efforts were done to run test cases in neutron verification as well as the first attempts to run models of the z-pinch powered spacecraft. A trend had emerged in the summer of 2018 iterations showing that simplification of model geometry was starting to lead to better results in shorter computation times. During the emergence of this process to reduce complexity, a computer crash occurred which led to the loss of raw input and output files from months of previous work that wiped out the progress being made on the model evolution. The iterations had been narrowing down results that were showing trends towards better relative

errors on tally values, but since the raw inputs were now missing, a new opportunity emerged to vastly improve results through more simplification of geometry.

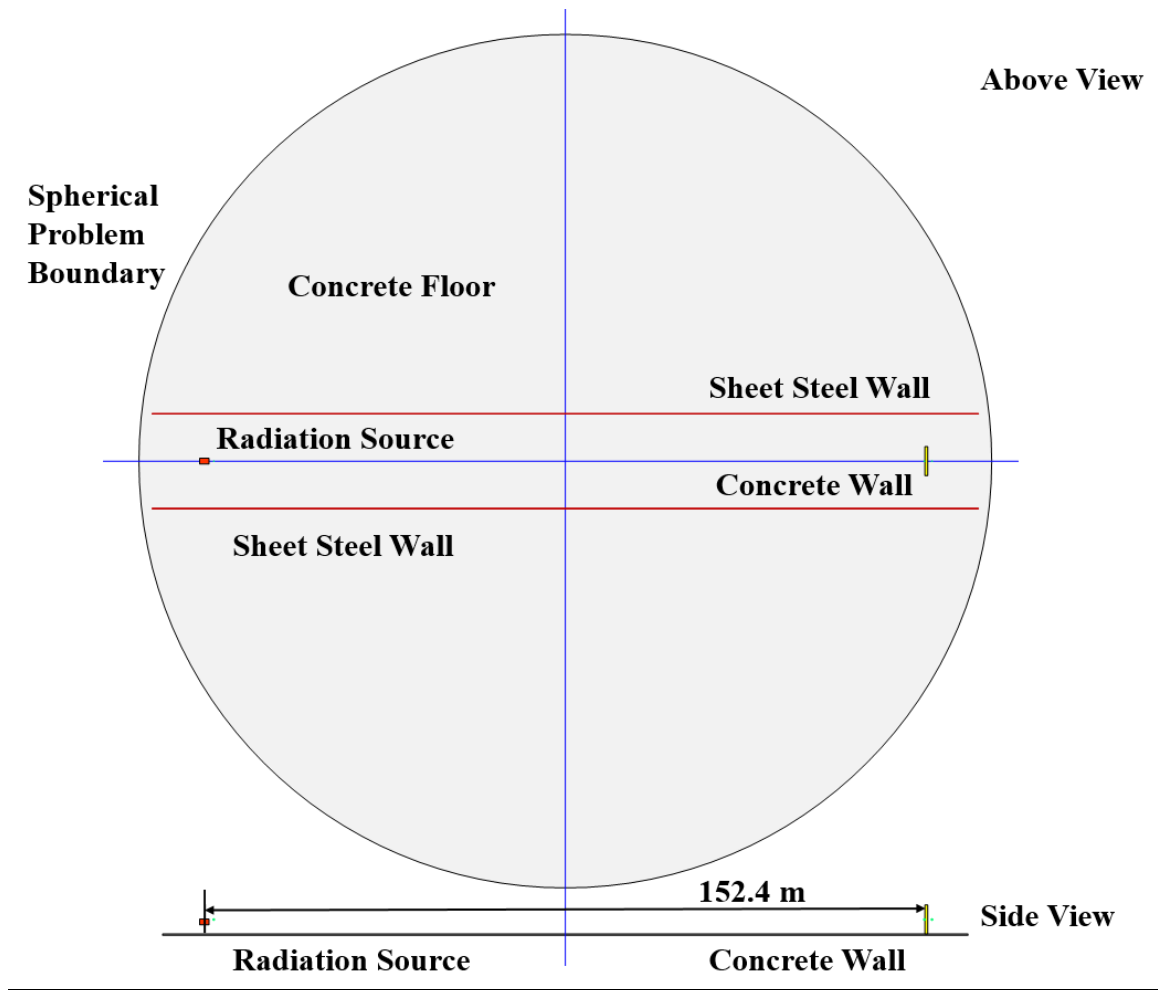


Figure 4.2. Representation of the complex geometry of early ChargerLab configurations

New models were created from scratch that incorporated lessons learned up until that point with ChargerLab47 being among the first to treat the problem as a simple slab shield inside a narrow cylindrical control volume with only the source, the ICRU spheres, a section of the concrete shield wall, and air intervening. Before this configuration, facility models were much larger in volume with immense spherical problem boundaries containing unneeded details such as a concrete floor, the soil underlying the floor as well

as metal walls surrounding the facility. Represented in the big picture by Figure 4.2 and in a zoomed detail with Figure 4.3, this was simplified into what is shown in the next section.

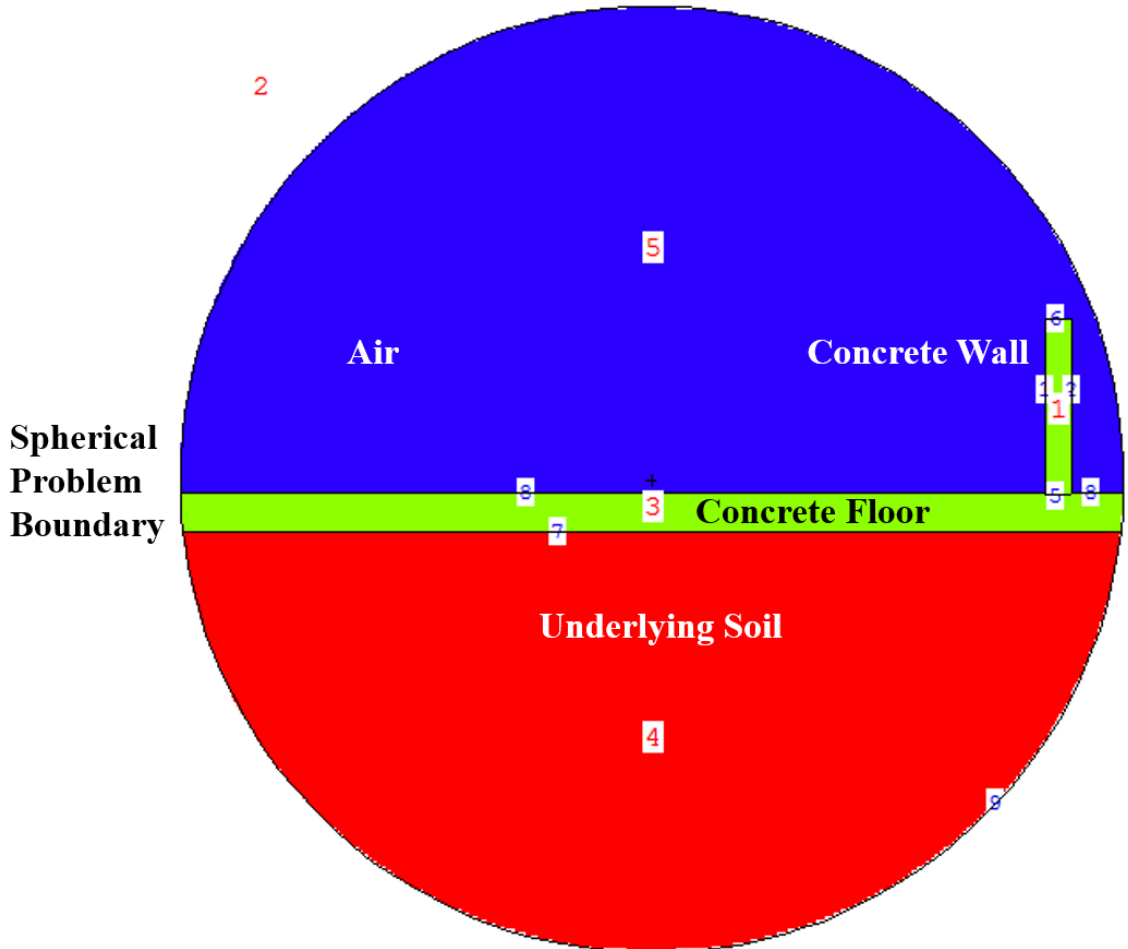


Figure 4.3. Zoomed Visual Editor detail of typical early ChargerLab configurations

The ChargerLab47 iteration was the first one to make use of ICRP 74 flux-to-dose conversion coefficients as well and the first time data runs were accomplished on a full model as well as a model with a null condition. The null condition chosen was the substitution of the concrete wall with open air, this allowed the attenuation of the concrete to be considered by comparing the concrete condition to the null condition. ChargerLab47 was also the last major attempt to optimize the source for criticality with KCODE; relative

error was reduced considerably but still was at unacceptable levels. The fall 2018 efforts yielded very rapid progress after geometry simplification drove lower computational times. This, in parallel with the neutron verification effort proceeding in earnest, was able to compile lessons learned into ChargerLab50, the configuration that wound up producing the results analyzed in this thesis. Details of this iteration are presented in the next section.

4.1.2 ChargerLab50 Configuration

4.1.2.1 ChargerLab50 Model Geometry

The ChargerLab50 configuration represents a comfortable optimization balancing simplicity and fidelity while aiming for efficiency. This 50th iteration has captured the most basic aspects of the facility problem and sets up the pertinent features of the shield wall and intervening air as a slab shield analysis. The model consists of 9 Surface Cards and 7 Cells, the boundary condition for this is a cylindrical cell with a radius of 1.96 m and a length of 153.5 m. Outside of this cell is vacuum, and inside of this cell is where the particle transport for the simulation is constrained. Any particle that leaves the control volume is killed and no longer tracked by the simulation. Figure 4.4 shows a representation of the model configuration as shown in the MCNPX Visual Editor. The vacuum outside the problem boundary is Cell 7; Cell 6 contains the rest of the problem encompassing the concrete wall (Cell 3), the small spherical fusion plasma source (Cell 1), and the three ICRU spheres (Cells 2, 4, and 5).

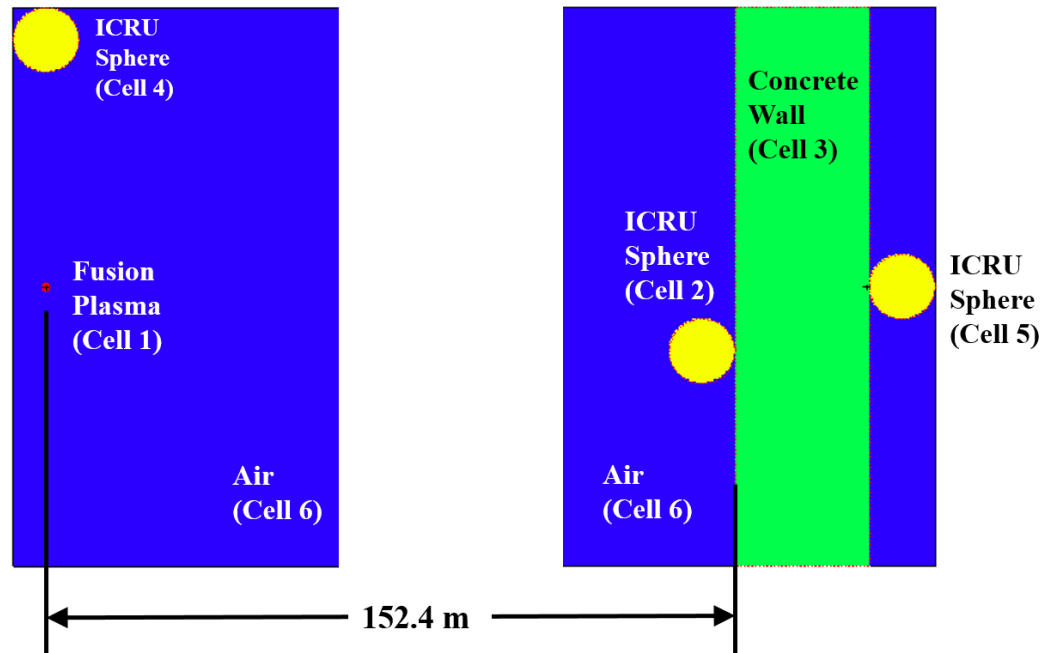


Figure 4.4. ChargerLab50 Visual Editor layout

The ICRU spheres are set up in strategic locations throughout the model, with the most intense location being that of Cell 4 which is 1 meter from the radiation source. This measurement is important as a way to normalize measurements for attenuation due to distance. The measurement of the source is taken at 1 meter for the sake of convenience in the inverse square relations, in the case of this sphere the measurement point is at 1 mm inside the surface. This measurement is a driver for the radius of the control volume so that the ICRU sphere is completely inside it. Cell 2 is used for dose measurements in front of the control room wall with the only attenuation being from air and 152.4 meter distance from the source. Cell 5 is used for dose measurements inside the control room, against the wall with 62.5 cm of concrete attenuating the radiation detected by Cell 2.

4.1.2.2 ChargerLab50 Material Cards

```

c *****
c Concrete, density = 2.35g/cm^3
m1  1001.70c  -0.005558  $concrete (ordinary with ENDF-VI)
      8016.70c  -0.498076  11023.70c  -0.017101  12024.70c  -0.001999
      12025.70c  -0.000264  12026.70c  -0.000302  13027.70c  -0.045746
      14028.70c  -0.289486  14029.70c  -0.015181  14030.70c  -0.010425
      16032.70c  -0.001216  16033.70c  -1e-005  16034.70c  -5.7e-005
      19039.70c  -0.01788  19040.70c  -2e-006  19041.70c  -0.001357
      20040.70c  -0.08019  20042.70c  -0.000562  20043.70c  -0.00012
      20044.70c  -0.00188  20046.70c  -4e-006  20048.70c  -0.000186
      26054.70c  -0.000707  26056.70c  -0.01139  26057.70c  -0.000265
      26058.70c  -3.6e-005
c *****
c ICRU Soft Tissue, Four Component, density = 1.00 g/cm^3
m2  1001.70c  -0.101172  $tissue,  6000.70c  -0.111000
      7014.70c  -0.026000  8016.70c  -0.761828
c *****
c ICRP Air, density = 1.20484E-3 g/cm^3
m3  7014.70c  -0.755636  $air (US S. Atm at sea level)
      8016.70c  -0.231475  18000.35c  -0.012889
c *****
c D-T, D-D Plasma density = 1e-6 g/cm^3
m4  1002.70c  -0.250000  $Deuterium Tritium
      1003.70c  -0.250000  2003.70c  -0.250000  2004.70c  -0.250000
c *****

```

Figure 4.5. Screenshot of material cards for ChargerLab50 input deck

The material cards (shown above) were derived from the built-in database in the MCNPX Visual Editor as well as from formulations found in users manuals. The concrete formulation in this model is an ordinary blend using isotope properties from the ENDF-VI database, this forms the basis for conservative estimating on radiation transport. The material used for the cell containing the radiation source is a custom blend of deuterium, tritium, and helium standing in as a surrogate for a fusion plasma set at the very low density of a microgram per centimeter cubed. The ICRU soft tissue formulation is of the four component variety filling the ICRU spheres while the air is a standard ICRP variety assumed to be United States standard atmosphere at sea level.

4.1.2.3 ChargerLab50 Source Definition

```
c --- Point Isotropic Source, 14.1 MeV Neutrons
c   Particles in all directions
c
SDEF POS=0 -7620 0 CEL=1 PAR=1 ERG=d1
SP1 -4 -14.1 -1
phys:p 100 0 0 0 0
phys:n 100 50
NPS 3000000000
```

Figure 4.6. Screenshot of the cards for defining the particle source in ChargerLab50

This problem uses the assumption of a point isotropic source emitting 14.1 MeV neutrons in all directions originating from Cell 1. The problem operates in Mode N P with the primary particle tracked being neutrons (PAR=1) while allowing secondary photons to be tracked as they are produced through the neutron interactions. The neutron energy distribution is defined in the source probability card SP1 as being a Gaussian fusion spectrum with the primary fusion being the D-T reaction at 14.1 MeV. Physics simplifications (phys:p and phys:n) constrain the source with the photon assumption being that 100 MeV is the energy ceiling before simple physics is used, Bremsstrahlung is included, coherent scattering is included, photonuclear interactions are not used, and Doppler broadening from the speed of bound electrons is used. The neutron physics simplification constrains 100 MeV as the ceiling above which neutron data is not placed in memory and neutrons below 50 MeV are treated by analog capture. Finally, this problem is constrained by the NPS cutoff of 3 billion particle histories [92, 93].

4.1.2.4 Geometry Splitting

```
c Importance
c      1  2  3  4  5  6  7
IMP:n  1  8  4  5  9  3  0  $1 - 7
c
IMP:p  1  8  4  5  9  3  0  $1 - 7
c
```

Figure 4.7. Screenshot of the importance settings in ChargerLab50

The importances in this problem are set up with a scale of most to least important in particle transport with the heaviest bias assigned to the Cell 5 ICRU sphere behind the wall in the control room. The 8 is assigned to the ICRU sphere in front of the wall while attenuating mediums such as air (3) and concrete (4) have lower priorities since there is so much more of it than the ICRU spheres. Cell 7 is set at zero as a way to have a cutoff, for this setting tells MCNP to kill tracking of a particle if it enters the vacuum of that cell since it has crossed the problem boundary. This bias strategy is to ensure that the most distant cells have a higher sensitivity and the cells with the most attenuating material have a higher sensitivity. This strategy was developed by trial and error over the course of this entire thesis project and settings like this one drive higher convergence in the tallies while keeping computational time minimized. Forced collisions were discovered to be another effective tool to bias particles towards the cells containing the tallies. Those settings, shown below, detail that only the ICRU spheres are prioritized.

```
c Forced Collisions
c      1  2  3  4  5  6  7
FCL:n  0 -1  0 -1 -1  0  0  $1 - 7
c
FCL:p  0 -1  0 -1 -1  0  0  $1 - 7
c
```

Figure 4.8. Screenshot of Forced Collisions settings for ChargerLab50

4.1.2.5 ChargerLab50 Tallies

The tallies used in ChargerLab50 are of the F4 and F6 varieties. Cell 4, the ICRU sphere 1 meter from the source, utilizes F14:N and F16:N for neutrons as well as F24:P and F26:P for the photons. Cell 5, the ICRU sphere behind the wall, uses F34:N, F36:N, F44:P, and F46:P. Cell 2, the ICRU sphere in front of the wall, uses F54:N, F56:N, F64:P, and F66:P. The F4 tallies find the average neutron and photon flux in a cell with an output of particles per square centimeter. The F6 tallies give the average neutron and photon energy deposition in a cell with an output of MeV per gram. The F4 tallies were multiplied by ICRP 74 flux to dose conversion coefficients to yield results in Sieverts per particle. The flux to dose conversions available for the F6 tally were not used by this point in the simulations as it was found that F4 was more effective for the needs of the thesis; F6 still proved its worth on energy deposition when analyzing output files so it was retained as another available data point.

4.1.3 ChargerLab50 Null Case

The final phases of analysis and interpretation of results leading up to this iteration yielded the usefulness of a null case for the model. To this end, ChargerLab50Null was created to produce an attenuation reference point in dose measurements. The only difference between this and the other version is the substitution of air for concrete in Cell 3, essentially removing the wall without disruptive changes to the model geometry. The results of the null case runs were compared against those of the nominal case and this became a reliable method to accurately and quickly determine the attenuation across the concrete wall. Another and more exhaustive method to plot attenuation with respect to

shield depth was developed and used extensively in the MCNP test cases, however for end-to-end attenuation the null case method is just as effective and much faster.

4.2 Z-Pinch Spacecraft

The process to create a model for a hypothetical spacecraft was based upon lessons learned from the modeling of the Charger-1 facility. This allowed for a rapid development of model iterations with the design loop closing rather quickly in less than a semester's time. Key to this was the parallel effort on the neutron verification test case as it had been decided early on to use the same multilayer shield cross section for both problems. The first iterations were executed just prior to the summer 2018 computer crash and this model was the first of the new models to be executed post-crash. There were three iterations on the configuration known as ZShip, this ended up in a very similar geometry as ChargerLab50 as far as the tally locations were concerned. Results from simulation runs on the ZShip3 configuration are what was analyzed for this thesis, and this configuration benefited from all of the other prior efforts which led to a much faster design cycle.

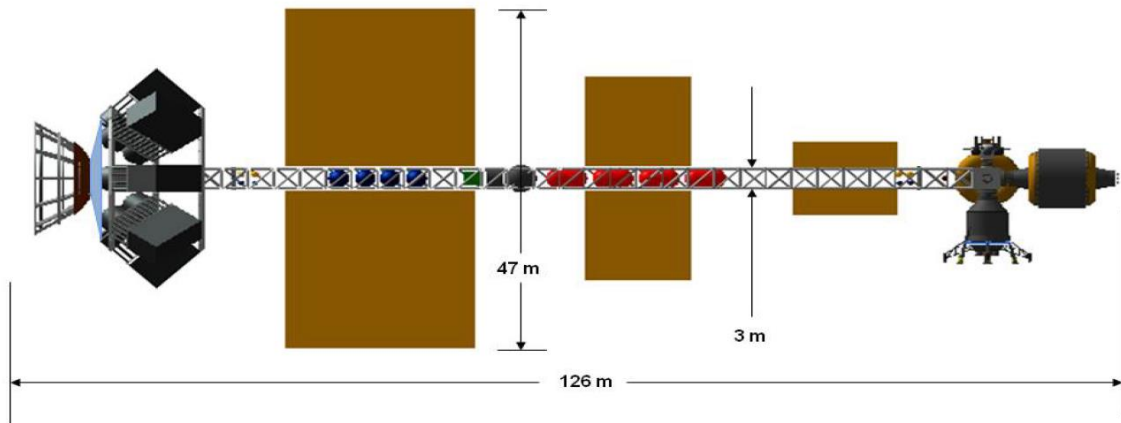


Figure 4.9. Basic dimensions of conceptual z-pinch powered spacecraft [42]

The application of radiation protection techniques to spacecraft are driven by much different requirements than those for a ground-based facility. Since system mass is at a premium, shields by necessity are much thinner and lighter than ground-based shielding and are made of more exotic materials to meet attenuation requirements at minimum weight. Since maximum exposure limits for astronauts are much higher than those for radiation workers, design safety factors can be optimized to reflect that. The environments of interplanetary space outside of the Earth's protective magnetic field greatly increase the risk of exposure from solar charged particles and the flux of Galactic Cosmic Radiation. There are not many comprehensive shielding options available to protect a crew completely from the space radiation environment, but as far as protection from a pulsed fusion propulsion system goes there are good options available.

Since radiation is line-of-sight, there are many built-in features in a spacecraft like shown in Figure 4.9 that lend themselves well for radiation shielding. The plasma being expelled from the propulsion system has the highest predictable neutron and photon flux, and therefore the first and most important shield is located immediately forward of the magnetic nozzle. Due to the aforementioned line-of-sight limitations, this shield need only be of a diameter that is slightly greater than the crew habitat. This creates what is called a shadow shield. Like putting a hand over a light to project a large shadow on a wall, the shield projects its own cone of shadow in the direction of the crew module. The shield for the illustrated Z-pinch concept would need to be a multilayer design, and combining this with a strategy of maximizing distance of the crew module from the rocket exhaust allows for ALARA to be achievable with respect to the propulsion system.

The fidelity of the iterations leading up to ZShip3 has been restricted to the simplest geometries and once again set up like a slab shield problem. The reality is that this makes for a very conservative way to estimate radiation exposure from the propulsion system. In the illustrated concept above, the crew module has an additional measure of protection from the intervening spacecraft hardware. A major feature of this spacecraft design is the fission reactor at the midpoint of the truss that provides startup power for the propulsion system and electricity to the rest of the spacecraft. This is a high density component that by itself could act to be an effective propulsion radiation shield, of course this is before determining the radiation from the reactor itself. The propellant tanks in between the reactor and crew module would also provide a great deal of protection, but would also have a decreasing attenuation capability as propellant is consumed. Just like in the ChargerLab development, an attempt was made early on to make a detailed MCNP model of the full spacecraft, but it was abandoned just as quickly as the complex facility model.

4.2.1 ZShip3 Configuration

The ZShip3 model has boiled down to the essentials of the problem while incorporating features from ChargerLab50. On this model, Cell 8 is the vacuum outside the problem boundary and Cell 7 contains everything else for the problem. Cell 7 is once again a cylinder with a 129.9 cm radius, but with a length shortened to 125.82 meters. Contained in Cell 7 is the fusion plasma source in Cell 1, the adjacent ICRU sphere in Cell 5, and the multilayer shield consisting of Cells 2, 3, and 4. The distance between the radiation source and Cell 6 is 125.5 meters, and only a gap of 50 centimeters separates the beginning of the shield and the radiation source. The only medium for attenuation other

than the shield is distance, for this model is filled with vacuum where there are no other objects.

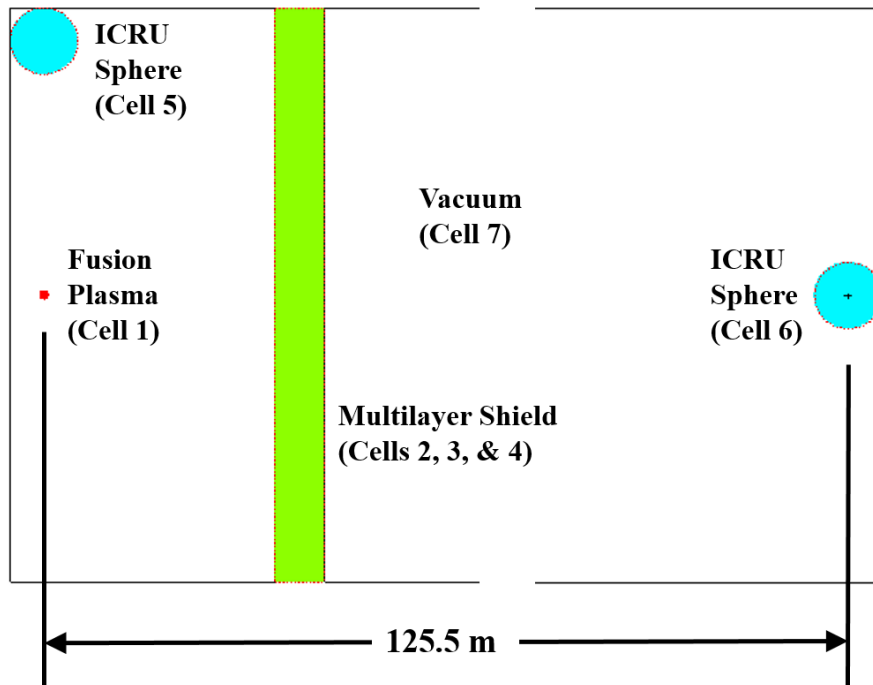


Figure 4.10. ZShip3 Visual Editor layout

The multilayer shield dimensions are derived from the work of Polsgrove and Miernik [8, 42] which in of itself is derived from the work of Emrich on his attenuation tool [68]. This shield configuration is the result of a basic optimization for maximum attenuation while minimizing total shield mass. A multilayer shield takes advantage of low density materials containing hydrogen to absorb fast moving neutrons before passing into a denser boron carbide layer to absorb the slow neutrons. Incoming photons are attenuated through the first layer, but the neutron interactions with the boron carbide layer produce more photons. The third layer consists of a high density metal used to absorb and reflect the photons that were produced in those interactions as well as the few slow neutrons that

have made it through the second layer. In the case of this configuration, that high density metal is tungsten.

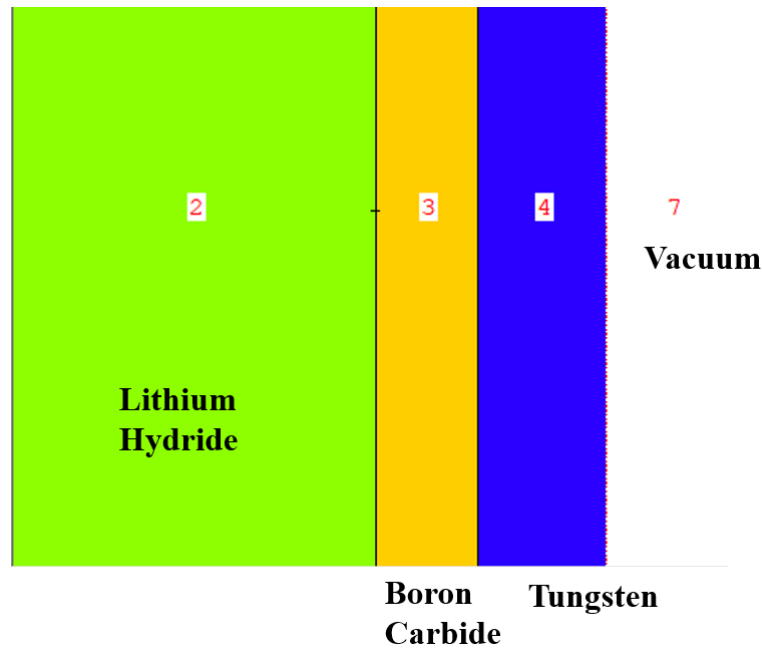


Figure 4.11. ZShip3 Visual Editor zoom on multilayer shield with Cell numbers and material descriptions

Since this shield configuration plays heavily into the analysis of the neutron verification test case problem, there is much more detailed theory and analysis for this shield presented in Appendix B with the contents of the test case. The rest of the input deck for ZShip3 is very similar to ChargerLab50; the source settings are the same, and the tallies are the same configuration with the same flux to dose conversions added. Importance and forced collisions are also in use, with the biggest differences in the importance settings due to the parameters of the problem being different. ZShip3 was also run with a null case where all three shield layers were replaced with vacuum in their respective cells.

CHAPTER 5. PRESENTATION OF DATA

5.1 Analysis of Output Files

The output file from MCNP contains an overwhelming wealth of information pertinent to the simulation run. The general format of the output deck starts with a read back of all of the input cards; if there is an error, many times the first indication may be noted on this input review. Additionally, comments and warnings that appear at the beginning of the run in the command line window are added after each input card that triggered them. If the code is executed without a fatal error and allowed to run to its end, then the first set of data to appear is a table that summarizes the properties for each cell. These include density, volume, mass, and other items depending on the variance reduction method used.

The output file next summarizes the assumptions made for the material data with regards to the various available cross section libraries. Summaries of the physics assumptions as well as exceptions to those assumptions are stated per individual isotope in the material cards. Particle history tables next summarize all of the particles created and lost with a weight and energy assigned to each interaction responsible for the creation or loss. The next set of tables summarize the activity of each type of particle for each cell in the model with tracks entering, population, collisions, and other important statistics presented. If photons are created, a table presents statistics for photons created across a spectrum of energy and cataloged per energy interval.

Each tally is presented with its mean result and relative error as well as the results for each of the ten statistical tests. Other statistics are presented for each tally including variance of variance, shifted center and figure of merit. If the relative error is low enough

and there is enough agreement with statistical tests, confidence intervals are presented. Otherwise a probability density function is plotted for the tally to allow an analyst to be able to extrapolate to better results. The next table summarizes the pass/fail numbers for each tally with respect to the ten statistical tests performed on the results. The final set of tables present the best values available for each tally for a list of NPS particle history numbers concluding with the NPS set for the simulation. These are able to show the trends toward convergence for each tally with relative error, *VOV* and *FOM* tracked along with the tally mean.

There are many more potential datasets that can be presented depending on the settings and assumptions with the MCNP input deck. For example, the output files for KCODE criticality simulations are very large since the successive iterations to narrow down criticality estimates are printed to the output real time during the run. There are many more tricks to using MCNP that have not been covered in this thesis that also affect the final format of an output file. Output files from MCNP simulations provide valuable information and they need to be closely examined to uncover any data trends or missing assumptions. The development of new models is highly dependent on the feedback cycle of examining outputs.

5.1.1 Attenuation Determination from Output

A method was developed for gathering the relevant information needed to be able to find the desired dose at the desired location in the model. Both the ChargerLab50 and ZShip3 configurations operated in Mode N P, therefore photons were produced as a byproduct of neutron interactions in the models. For a given total NPS, each simulation run determined the true amounts of particles produced. In order to normalize the source

assumptions with what could be possible using Charger-1, it was assumed that for the purposes here that one pulse of the z-pinch system would produce 2×10^{28} neutrons per second.

Using data from the output file for each run, the total number of photons produced was divided by the total number of neutrons produced in order to create a ratio to find the number of photons produced per second. With this information in hand, the neutron and photon fluence for each ICRU sphere was determined using spherical area relations; the surface area of the ICRU sphere was divided by that of the sphere created by the radius from the source to the location of the ICRU sphere. This ratio was then used to determine the percentage of particles that the detector would be exposed to. Each ICRU Sphere was given this treatment, and in the case of the one behind the wall in ChargerLab50, the particle rate found at 153 meters was assumed to be that of the null case where the shield material was assumed to be air.

Tally data gathered from the null case, with a special focus on the detector behind the shield, was then tabulated with a focus going toward the relative error for each one. Using this error, an upper and lower uncertainty bound on tally dose was created and tabulated. This same process was then applied to the best set of tally data from the shielded case. This becomes important when considering that the relative error for tallies behind a shield end up being much higher than those for the null case at the same location. This upper and lower bound becomes the basis for a tolerance stack up when considering attenuation calculations.

5.2 ChargerLab50 Results

In order to calculate attenuation, the first item on the agenda is to find the ratio of photons produced per neutron so that both particle production rates can be determined. Each output file provides statistics for the total number of both the neutrons and photons produced in the simulation run. In the case of ChargerLab50, four sets of results were compiled and the photon to neutron ratio was determined for each dataset. These four ratios were then averaged to determine an overall photon to neutron ratio for ChargerLab50. It should be noted that the null case was run at an NPS of 1 billion particle histories while the three shielded cases step up to 3 billion particle histories. The highest NPS on the shielded case was used to drive relative errors behind the shield to levels more comparable to those of the null case.

Table 5.1. NPS and Runtimes for ChargerLab50 Datasets

Output File	NPS	Time [min]
ChargerLab50Null_20181021d	1000000000	180.21
ChargerLab50_20181021c	1000000000	185.05
ChargerLab50_20181021d	2000000000	370.28
ChargerLab50_20181110d	3000000000	357.16

Table 5.2. Particle Statistics for ChargerLab50

Output File	Total Neutrons	Total Photons	Photon to Neutron Ratio	Average Photon to Neutron Ratio
ChargerLab50Null_20181021d	3030252285	29700351	0.0098013	0.0098167
ChargerLab50_20181021c	3030252347	29768650	0.0098238	
ChargerLab50_20181021d	6060475385	59518308	0.0098207	
ChargerLab50_20181110d	9090713795	89280702	0.0098211	

Next in this process is the determination of particle flux at the three different tally locations. The first flux was found at 1 meter from the radiation source using the spherical relations described in the previous section. Given the Z-pinch neutron production rate of 2×10^{28} neutrons per second, the particle fluence at 1 meter is found from relations calculated in Table 5.3. The next particle fluence is found at the ICRU sphere located immediately in front of the concrete wall, the wall being at 152.4 meters from the source and the point of measurement at 1 mm inside the surface of the ICRU sphere. Finally, using the null assumption, the particle fluence is found at the ICRU sphere immediately behind the wall.

Table 5.3. Determination of fluence at 1 meter from the source

Radius	1	[m]
Area of 2 m sphere	12.56637061	[m ²]
Area of ICRU Sphere	0.282743339	[m ²]
Fraction of Radiation Received	0.0225	
Neutron Fluence at ICRU Sphere 1m from Source	4.50E+26	[n/sec]
Photon Fluence at ICRU Sphere 1m from Source	4.42E+24	[p/sec]

Table 5.4. Determination of fluence at location in front of concrete wall

Radius	152.1013	[m]
Area of 152.1013 m sphere	290720.5395	[m ²]
Area of ICRU Sphere	0.282743339	[m ²]
Fraction of Radiation Received	0.000001	
Neutron Fluence at ICRU Sphere, 152.1 m	1.95E+22	[n/sec]
Photon Fluence at ICRU Sphere, 152.1 m	1.91E+20	[p/sec]

Table 5.5. Determination of fluence for null case at location behind shield

Radius	153.0096	[m]
Area of 153 m sphere	294203.0858	[m ²]
Area of ICRU Sphere	0.282743339	[m ²]
Fraction of Radiation Received	0.000000961	
Neutron Fluence at ICRU Sphere, 153m null case	1.92E+22	[n/sec]
Photon Fluence at ICRU Sphere, 153m null case	1.89E+20	[p/sec]

Now that the fluences at the different tally locations have been determined, the next relevant dataset to present is the actual tally results. First, in Table 5.6 the null condition is presented with the dose determined at each tally in an unshielded assumption with only air as the attenuating medium. Next, in Table 5.7 the highest NPS run of ChargerLab50 is presented with the dose determined at each tally in the condition shielded by the concrete wall. In addition to the tally mean in each of these locations, the relative error and the pass/fail scores for the ten statistical tests are also presented.

Table 5.6. Mean tally scores for ChargerLab50Null at 1 billion particle histories

ChargerLab50Null_20181021d						
Par	Tally	Location	Dose	Rel Error	Passed	Missed
			[Sv/particle]			
n	Tally 14	1m from Source	2.45229E-15	0.0005	9	1
n	Tally 34	Behind Wall	3.96611E-20	0.0962	9	1
n	Tally 54	In Front of Wall	4.26925E-20	0.0915	9	1
p	Tally 24	1m from Source	1.37825E-17	0.0007	9	1
p	Tally 44	Behind Wall	2.09608E-22	0.1572	7	3
p	Tally 64	In Front of Wall	2.86757E-22	0.1233	8	2

Table 5.7. Mean tally scores for ChargerLab50 at 3 billion particle histories

ChargerLab50_20181110d						
Par	Tally	Location	Dose	Rel Error	Passed	Missed
			[Sv/particle]			
n	Tally 14	1m from Source	2.45092E-15	0.0003	9	1
n	Tally 34	Behind Wall	9.20503E-22	0.2174	8	2
n	Tally 54	In Front of Wall	5.19049E-20	0.0448	10	0
p	Tally 24	1m from Source	1.37769E-17	0.0004	9	1
p	Tally 44	Behind Wall	8.2968E-23	0.1376	8	2
p	Tally 64	In Front of Wall	7.84753E-22	0.0477	10	0

Using the relative errors from the tally scores, the upper and lower bounds are then found for each tally location. These form the basis for the tolerance stack going forward as the concrete attenuation is determined. This attenuation is determined via division of the tally from the shielded case by the tally from the null condition; the nominal condition is determined by a direct division of the mean tallies and the boundary conditions are found via a slightly more complicated method. To find the lower bound, the lower boundary of the shielded dose is divided by the upper boundary of the null dose. The opposite condition of dividing the upper boundary of the shielded dose by the lower boundary of the null dose leads to the upper bound for the concrete attenuation.

Table 5.8. Concrete attenuation as determined from the stack up of tally tolerance

Description	Lower	Mean	Upper	Units
Neutron Concrete Attenuation	0.01656954	0.02320922	0.03126234	
Photon Concrete Attenuation	0.29498714	0.39582459	0.53427865	
Neutron Fluence at ICRU Sphere Behind Wall, 153m	3.1848E+20	4.461E+20	6.0089E+20	[n/sec]
Photon Fluence at ICRU Sphere Behind Wall, 153m	5.566E+19	7.4687E+19	1.0081E+20	[p/sec]

Now that the concrete attenuation is accounted for, the tallies behind the wall in Table 5.7 can be multiplied by the particle fluence found in Table 5.8 to find the dose rate behind the wall. The other tallies are also multiplied by their respective fluences found in Table 5.3 and Table 5.4 to find the dose rates at their locations. Once again, the lower and upper bounds based upon the uncertainty of the tally relative errors are also taken into account for the calculated dose rates. This is presented in Table 5.9, and these results can then be used to determine the total dose per pulse on the Charger-1 source. The pulse time of the Charger-1 apparatus is assumed to be 100 nanoseconds for the purposes of this analysis, and when multiplied by the dose rates the total dose per pulse is found for each tally and presented in Table 5.10.

Table 5.9. Dose rate range for tallies in ChargerLab50

ChargerLab50_20181110d			Lower	Mean	Upper
Par	Tally	Location	Dose Rate	Dose Rate	Dose Rate
			[Sv/sec]	[Sv/sec]	[Sv/sec]
n	Tally 14	1m from Source	1.10258E+12	1.10291E+12	1.10324E+12
n	Tally 34	Behind Wall	0.229430264	0.410639588	0.67337203
n	Tally 54	In Front of Wall	964.3825297	1009.613201	1054.843873
p	Tally 24	1m from Source	60835503.74	60859847.68	60884191.62
p	Tally 44	Behind Wall	0.00398258	0.006196627	0.009515027
p	Tally 64	In Front of Wall	0.142698784	0.14984646	0.156994136

Table 5.10. Total dose per pulse range for tallies in ChargerLab50

ChargerLab50_20181110d			Lower	Mean	Upper
Par	Tally	Location	Dose Per Pulse	Dose Per Pulse	Dose Per Pulse
			[Sv]	[Sv]	[Sv]
n	Tally 14	1m from Source	110258.3126	110291.4	110324.4874
n	Tally 34	Behind Wall	2.2943E-08	4.1064E-08	6.73372E-08
n	Tally 54	In Front of Wall	9.64383E-05	0.000100961	0.000105484
p	Tally 24	1m from Source	6.083550374	6.085984768	6.088419162
p	Tally 44	Behind Wall	3.98258E-10	6.19663E-10	9.51503E-10
p	Tally 64	In Front of Wall	1.42699E-08	1.49846E-08	1.56994E-08

All of the tally doses can now be combined to find the total dose at each location, following the approach laid out in Equation 58 for the F4 tally. The independent dose measurements from the photons and the neutrons are combined in this step to determine the total ambient equivalent dose. This data is presented in Table 5.11, and with this data the mean total ambient dose per location is then found by adding the upper and lower bounds and then dividing that total by two. The plus or minus tolerance is then found by subtracting the mean from the upper bound or subtracting the lower bound from the mean.

Table 5.11. Total ambient equivalent dose per pulse range for ChargerLab50

ChargerLab50_20181110d	Lower	Nominal	Upper
Location	Dose Per Pulse	Dose Per Pulse	Dose Per Pulse
	[Sv]	[Sv]	[Sv]
1m from Source Total Dose	110264.4	110297.5	110330.6
In Front of Wall Total Dose	0.000096453	0.000100976	0.0001055
Behind Wall Total Dose	0.000000023	0.000000042	0.000000068

Table 5.12. Total ambient equivalent dose per pulse for ChargerLab50

Location	Dose Per Pulse	Tolerance
	[Sv]	[Sv]
1m from Source	110297.5	± 33.1
In Front of Wall	0.000100976	± 0.000004524
Behind Wall	0.000000046	± 0.000000022

With these results, it can now be shown that the radiation dose is significantly attenuated by distance. From the radiation limits discussed in Section 2.5.1, it is plain to see that a person standing unshielded at 1 meter from the source would be exposed to a fatal dose in one pulse of the Charger-1 apparatus initiating D-T fusion. A person standing in front of the concrete wall at 152 meters from the source, assuming no shielding and the only attenuating medium being air, would be exposed to around 0.1 mSv. This unshielded dose is the equivalent of a single chest x-ray or ten days exposure to ground level background radiation [96]. Standing behind the concrete wall, the ambient dose equivalent is four orders of magnitude lower than the dose on the leeward side of the wall. Therefore, from this assessment a conservative conclusion can be reached that the Charger-1 facility is safe for personnel to operate so long as ALARA protocols are adhered to and all personnel are in the shielded location of the control room for the duration of operations.

5.3 Pulsed Fusion Spacecraft Shielding (ZShip3) Results

Using the techniques outlined in the previous section on the ChargerLab50 results, the results for ZShip3 are presented below. For ZShip3, particle production rates were gathered from three different simulation runs with one being the null condition. The null case was run at 1 billion particle histories while two runs of the shielded case were at 1 and 2 billion particle histories respectively. ZShip3 has a unique condition compared to

ChargerLab50 since the medium is vacuum instead of air, this makes photon production much lower than ChargerLab50 since there are no air particles to interact with to create secondary photons. Because of this, only the shielded case was used to determine the average photon production ratio since the only interactions assumed were with the shield materials.

Table 5.13. NPS particle history and Runtimes for ZShip3 Datasets

Output File	NPS	Time
		[min]
ZShip3Null_20181022a	1000000000	121.53
ZShip3_20181022b	1000000000	440.68
ZShip3_20181022c	2000000000	892.72

Table 5.14. Particle Statistics for ZShip3

Output File	Total Neutrons	Total Photons	Photon to Neutron Ratio	Average Photon to Neutron Ratio
ZShip3Null_20181022a	1064244187	32299999	0.030350177	0.05323156
ZShip3_20181022b	1461098689	77785569	0.053237724	
ZShip3_20181022c	2922168804	155533583	0.053225393	

In the configuration of ZShip3, there are two tally locations instead of the three in ChargerLab50. This was decided to be the case since the spacecraft shield is one half meter from the radiation source in ZShip3; since attenuation is normalized with a reading at 1 meter, an ICRU sphere in front of the shield would not be very useful for this problem. Applying the same neutron production rate as that of ChargerLab50, the particle fluence at 1 meter from the source is found from relations found in

Table 5.15. Next, the particle fluence at the astronaut location of 125.371 meters from the source is found for the null condition and presented in Table 5.16. The mean

tallies for the ZShip3Null configuration are presented in Table 5.17, and the mean tallies for the ZShip3 configuration at 2 billion particle histories are presented in Table 5.18. These datasets are of course necessary to determine the attenuation of the multilayer shield and find the fluences at the astronaut location.

Table 5.15. Determination of fluence at 1 meter from the source

Radius	1	[m]
Area of 2 m sphere	12.56637061	[m ²]
Area of ICRU Sphere	0.282743339	[m ²]
Fraction of Radiation Received	0.0225	
Neutron Fluence at ICRU Sphere 1m from Source	4.50E+26	[n/sec]
Photon Fluence at ICRU Sphere 1m from Source	2.40E+25	[p/sec]

Table 5.16. Determination of fluence for null case at location behind shield

Radius	125.371	[m]
Area of 125.371 m sphere	197516.8014	[m ²]
Area of ICRU Sphere	0.282743339	[m ²]
Fraction of Radiation Received	0.0000014	
Neutron Fluence at ICRU Sphere, 125.371m	2.86E+22	[n/sec]
Photon Fluence at ICRU Sphere, 125.371m	1.52E+21	[p/sec]

Table 5.17. Mean tally scores for the ZShip3Null condition at 1 billion particle histories

ZShip3Null_20181022a						
Par	Tally	Location	Dose	Rel Error	Passed	Missed
			[Sv/particle]			
n	Tally 14	1m from Source	2.45229E-15	0.0005	9	1
n	Tally 34	Astronaut, 125.371 m	3.96611E-20	0.0962	9	1
p	Tally 24	1m from Source	1.35863E-17	0.0006	10	0
p	Tally 44	Astronaut, 125.371 m	1.00562E-21	0.0724	9	1

Table 5.18. Mean tally scores for the ZShip3 condition at 2 billion particle histories

ZShip3_20181022c						
Par	Tally	Location	Dose	Rel Error	Passed	Missed
			[Sv/particle]			
n	Tally 14	1m from Source	2.47213E-15	0.0004	10	0
n	Tally 34	Astronaut, 125.371 m	9.54544E-21	0.1009	8	2
p	Tally 24	1m from Source	1.38534E-17	0.0004	10	0
p	Tally 44	Astronaut, 125.371 m	7.53192E-23	0.1437	8	2

Using the relative errors from the tally scores, the upper and lower bounds are once again found for each tally location. The attenuation from the multilayer shield creates its own tolerance stack up just like in ChargerLab50 with upper and lower bounds determined and presented in the next table.

Table 5.19. Multilayer shield attenuation as determined from the stack up of tally tolerance

Description	Lower	Mean	Upper	Units
Neutron Shield Attenuation	0.19740102	0.24067512	0.29316136	
Photon Shield Attenuation	0.05980547	0.07489827	0.09234708	
Neutron Fluence at ICRU Sphere Behind Shield, 125.371m	5.6516E+21	6.8905E+21	8.3932E+21	[n/sec]
Photon Fluence at ICRU Sphere Behind Shield, 125.371m	9.1144E+19	1.1415E+20	1.4074E+20	[p/sec]

With the attenuation of the multilayer shield in hand, the tallies representing the astronaut in Table 5.18 are multiplied by the particle fluence from Table 5.19 to find the shielded dose rate to the astronaut. The dose rate at the location 1 meter from the radiation source is found by multiplying its fluence by the dose rate at its location. This and the dose rate for the astronaut are presented in Table 5.20 along with the upper and lower bounds

for each calculation. The pulse time of the ZShip3 radiation source is assumed to be the same 100 nanoseconds as that of Charger-1 and using this, the dose per pulse is calculated and presented in Table 5.21. Combining the neutron and photon dose values yields the total ambient equivalent dose per pulse range for the two detectors in ZShip3, this is presented in Table 5.22. Finally, in Table 5.23, the total ambient equivalent dose per pulse is presented as the mean value with a tolerance.

Table 5.20. Dose rate range for tallies in ZShip3

ZShip3_20181022c			Lower	Mean	Upper
Par	Tally	Location	Dose Rate	Dose Rate	Dose Rate
			[Sv/sec]	[Sv/sec]	[Sv/sec]
n	Tally 14	1m from Source	1.11201E+12	1.11246E+12	1.1129E+12
n	Tally 34	Astronaut, 125 m	48.50334389	65.77267164	88.20006179
p	Tally 24	1m from Source	331714394.3	331847133.2	331979872
p	Tally 44	Astronaut, 125 m	0.005878413	0.008597358	0.012123514

Table 5.21. Total dose per pulse range for tallies in ZShip3

ZShip3_20181022c			Lower	Mean	Upper
Par	Tally	Location	Dose Per Pulse	Dose Per Pulse	Dose Per Pulse
			[Sv]	[Sv]	[Sv]
n	Tally 14	1m from Source	111201.3517	111245.85	111290.3483
n	Tally 34	Astronaut, 125 m	4.85033E-06	6.57727E-06	8.82001E-06
p	Tally 24	1m from Source	33.17143943	33.18471332	33.1979872
p	Tally 44	Astronaut, 125 m	5.87841E-10	8.59736E-10	1.21235E-09

Table 5.22. Total ambient equivalent dose per pulse range for ZShip3

ZShip3_20181022c	Lower	Nominal	Upper
Location	Dose Per Pulse	Dose Per Pulse	Dose Per Pulse
	[Sv]	[Sv]	[Sv]
1m from Source Total Dose	111234.5231	111279.0347	111323.5463
Shielded Total Dose, 125 m	4.85092E-06	6.57813E-06	8.82122E-06

Table 5.23. Total ambient equivalent dose per pulse for ZShip3

Location	Dose Per Pulse	Tolerance
	[Sv]	[Sv]
1m from Source	111279.03	± 44.51
Shielded Astronaut, 125m	0.000006836	± 0.000001985

The ZShip3 results show a dose per pulse at 1 meter from the source being within the same magnitude as that of the ChargerLab50 configuration. This is to be expected since the source is modeled the same for both cases, with the ZShip3 version having the lower dose due to the vacuum conditions of the model. Since a z-pinch propulsion system can only consistently produce thrust performance through a high pulse rate of implosion events, there is the worry of cumulative dose to the astronaut to consider. Depending on the optimization of the propulsion performance, a space mission with this kind of system would have thousands of pulses for every burn profile. The values for dose determined in the ZShip3 simulation effort show that at between 5000 and 10000 pulses of the system, occupational exposure limits would be reached. Since the space environment is so unforgiving, higher occupational risks from radiation exposure are to be expected anyway.

Both the ZShip3 and ChargerLab50 model configurations are quite conservative for the sake of simulation simplicity. There are major refinements that could be had with

further study and iterations on source properties, deeper detail on other existing hardware not yet modeled and other intervening objects that would further attenuate radiation emitted from the source. The reality is, the astronaut in ZShip3 and the control room occupant in ChargerLab50 would see a lower dose than is found from these particular results. At best, this set of results could be considered the upper bound for exposure to be evaluated in an engineering process. The methods used in these MCNP simulation efforts are a good start on an optimization path, but many new assumptions would need to be considered to drill down to a more accurate representation that really is beyond the scope of this thesis.

CHAPTER 6. DISCUSSION AND CONCLUSIONS

6.1 Discussion of Results

The results of the main analysis performed for this thesis predict that a person pressed against the wall inside the control room closest to the Charger-1 experiment would receive a worst case dose per pulse of 6.8×10^{-8} Sieverts. This is 0.068% of the dose received from a single chest X-ray which was outlined in Chapter 2 to be around 1×10^{-4} Sieverts (0.1 mSv). These results, presented in Section 5.2, also show that a person standing in front of the wall outside the control room would receive a worst case dose roughly equivalent to a chest X-ray. Public exposure limits as shown in Table 2.2 would mean that at continuous exposure, 10 pulses would be enough to reach the annual limit for someone standing in front of the wall. By contrast, occupants of the control room would need over 14,000 exposures to reach the annual limit of 1 mSv for continuous exposure.

All of this of course is based upon the conservative assumptions baked into the simulations in this analysis, the reality that there is more intervening hardware between the control room and the experiment than is modeled and the actual dose will be much less than is presented here. The source was modeled as a point source inside a sphere of plasma in open air; the attenuation from the chamber that contains the plasma is not taken into account nor are the factors of any other intervening equipment such as the rest of the Charger-1 machine or any other potential protective structures. Further work could be done on the ChargerLab models to account for these other attenuating factors, but these conservative initial assumptions will serve the laboratory personnel well to know that they are without a doubt protected while in the control room.

The exercise with the ZShip3 spacecraft is but a first cut of the analysis really needed to see how an astronaut would be protected by a multilayer shield. This is also a very conservative assumption modeling the same source as ChargerLab50 without accounting for intervening spacecraft structures that include propellant tanks, a fission reactor than in of itself would be shielded, and other spacecraft structures. Much more work needs to be done if a shield were to be optimized for a spacecraft to protect crew from radiation from its propulsion system. It was a beneficial exercise to apply what was learned in the ChargerLab process to a spacecraft shield design, but much more work is needed in order to refine this into something useful for future designs. Section 6.4 outlines the path forward for an effort in this vein.

6.2 Safety Recommendations for Charger-1

Moving into implementation of the experiments in the Charger-1 facility, there are a few important factors to consider as the commissioning goes forward. First, it would behoove the organization to appoint a Radiation Safety Officer (RSO) to be the interface with potential regulatory agencies and to ensure that safe practices are implemented in the facility. Knowing the potential for items that will push beyond the original scope of this experiment, especially with PuFF efforts and the potential for the creation of medical isotopes as a side product of the PuFF experiments, getting on top of the regulatory side of this effort will be especially important. Isotopes and the control of them fall under the purview of the NRC. The primary item that should be on the agenda of the RSO would be to develop a radiation safety plan compliant to NRC standards. Since this facility is on US Government property on Redstone Arsenal, the RSO for the base will also need to be

involved in at least reviewing the safety plans as well as the measures being taken to protect personnel.

As long as extreme safety measures are being taken, like access control and sequestration of all operational personnel inside the control room during pulse events, this should be a safe operation. In the early stages of commissioning, it would be beneficial to take measurements of dose at various facility locations during the pulse events. As the experiments gain complexity and power, new measurements should be taken with each step up. This could be accomplished with pocket dosimeters placed possibly at locations that correlate with the ICRU Sphere locations in the ChargerLab model. These can be read and reset in rapid order and the data can be added to a database to catalog readings at the locations of interest. The most accurate readings would be through the use of TLD or OSL badges detailed in Section 2.5.2, with the corresponding monitoring service provided by companies such as Landauer. If need be, personnel could also be added to a monitoring program with these badges in the implementation of an ALARA protocol for experiment operations. Ultimately, this would most likely end up being dictated by the requirements of the Redstone RSO but it is very important to consider this as the facility moves into operation.

6.3 Lessons Learned

MCNP has proved to be an excellent tool for determining attenuation of radiation through different media as well as with the creation of new particles from material interactions. It seems that for most shielding applications, using Monte Carlo methods could be a bit of overkill for the results needed. The various standards organizations for radiation protection have developed rules of thumb and guidelines to streamline the design

process for most industrial and medical installations. Most of these design guides use equations with variables referencing tables of specially-developed energy dependent material constants for attenuation of both photons and neutrons. Examples can be found of this in the main bodies and appendices of NCRP standards written for specific facility installations like particle accelerator facilities [97], medical imaging facilities [98], high energy X-ray and gamma ray radiotherapy facilities [99], as well as more general standards for neutron protection [100].

The values of these special attenuation constants have often been developed through iterative processes using Monte Carlo simulations as well as actual measurements in a radiation environment. This allows for approximations to be applied analytically especially to neutron shielding problems that otherwise would need to be solved numerically. Economic considerations are usually the most important ones in the engineering process, time is equivalent to money and companies who design and build shielding need to watch their bottom lines. Safety factor in a design is always a desirable thing, and the approximations afforded by the standard processes have margin built-in for a conservative design approach. If time and money are less restricted in a design process or the final product is destined for flight hardware with mass restrictions, then the Monte Carlo approach for shielding optimization builds upon its true strengths.

6.4 A Path Forward on Analysis

The usefulness of a Monte Carlo driven design process for radiation protection was proven in this thesis through a main body of research that was focused on running billions of particle histories and hundreds of iterations across thousands of individual output files. The outcome of this ultimately led to the results presented here. Validation of the MCNP

methods used to simulate attenuation of radiation through materials wound up with strong correlation between their results and the textbook examples they were being compared to. The data presented in Chapter 5 as well as the verification and validation approaches for photon problems in Appendix A as well as the neutron problems in Appendix B have unlocked the potential for much deeper uses in design optimization. One approach to consider would be a focus on simulating the z-pinch source in much greater detail, a path already taken in this is shown by the works of Schillo [15].

MCNP has a vast storehouse of material properties as a function of energy level, and depending on the type of fuel source in the fusion event MCNP could be used to predict particle generation. These particles could then be subjected to interactions within different layers of fuel materials to produce secondary particles and even tertiary particles. Results of hundreds of simulations with varying properties such as energy level, density, mass, and volume could be used to create a statistical model to predict the total number and diversity of particles generated by a z-pinch event. It was realized late in the data analysis process that the z-pinch source modeled in ChargerLab50, ZShip3, and the Shield123 runs has an extremely low density consistent with a plasma in the vacuum of space when in reality this would be much closer to that of water. This could alter source emission results considerably. Use of the KCODE criticality function in MCNP6 could also be applied to do a similar approach for the optimization of a PuFF ignition. The potential of Monte Carlo is largely dependent on the sample size of the simulations run. The work presented here utilized up to two laptops at peak times with three or four individual command line windows open executing a series of MCNP simulation runs on each machine. With access

to a computing cluster and automation by software, the true usefulness of the Monte Carlo methods becomes clearer.

During the fall of 2018 when the work on Appendix B was in full swing, data points for the attenuation curves started to emerge with the results of every simulation run. The attenuation curves produced in this initial run showed promise, but with 59 data points these curves needed refinement. In the fall of 2019 as the main body of this thesis was being written, another 54 simulations were executed on this model to add more data points and more refinement. However, the tedious process of manually transferring data from the output files to spreadsheets for further analysis made for some more difficult times in getting those newer data points into the curves. An optimization process could easily be applied to this problem to drill down to the best possible attenuation curves. In order for this to occur, hundreds more simulations would need to be run to smooth the curves with enough data points to be really meaningful. Setting this problem up in a cluster and writing a script to automatically change input parameters for the next step into the shield could rapidly generate data with little user interface in the process. Another script could be written to automate the transfer of output data for analysis.

Manual transfer of particle results and tally values from output files is a tedious process, automation of this would lead to the ability to rapidly optimize a design. Since the volume of data produced in this kind of exercise would be immense, automation would be the best way to make analysis of the data feasible. With these kind of automation tools in hand, an effort to expand the scope of this research would directly benefit from stretching the utility of MCNP simulations. A dissertation intended as a follow-on to this thesis could drive the focus towards optimizations anywhere in a propulsion design that has to deal with

ionizing radiation and particle transfer. The work of this thesis could be expanded upon to flesh out more details in successive iterations of ChargerLab and ZShip with a focus on changing variables such as importance settings, source descriptions, physics assumptions and more. This could lead to the emergence of trends that could be further analyzed to help with increasing model complexity.

The work developed from the verification and validation efforts presented in the appendices is immediately useful for spacecraft shielding analysis. There was only one configuration studied of the multilayer shield in this thesis and the results so far show room for improvement. A trade study for the best performing spacecraft shield configuration with an eye on constraints such as the lowest possible mass could be performed using the automation methods previously described. This could assist in the closure of many future mission designs where vehicle mass is at a premium and the spacecraft operational environment has extreme amounts of fluence much like that of the Juno mission orbiting Jupiter.

With the prospects for future work on nuclear propulsion related activities being better than they have in been decades, there are many other challenges that could be overcome with the help of MCNP. The BURN function of MCNP is an example of a tool that could be handy for tracking fuel depletion in a fission reactor, additionally it is able to determine resultant nucleotides from radioactive decay [101]. During the original literature survey for this thesis, several uses emerged for MCNP in dosimetry, radiography, neutronics, photonics, criticality estimates and reactivity estimates in addition to attenuation calculations. A basic review of some literature sources have found evidence of other efforts to automate analysis using MCNP as an input source. One such example is

the SPOC (Space Propulsion Optimization Code) tool that utilizes a MATLAB environment with inputs from MCNP6 as well as the radiation transport code Serpent to add neutrons and heating from a fission reactor to another thermal and performance tool for optimizing NTR propulsion design. The SPOC package allows for the rapid generation and analysis of multiple NERVA-based NTR core designs [102].

There are undoubtedly many other custom made tools and applications dating back decades for this kind of effort locked away in the proprietary recesses of various labs, universities and corporations in the radiation business. The path of developing the analysis as well as the conveyance of the fundamentals involved with radiation protection in this thesis has led to an application for MCNP that would benefit greatly from further study and refinement. The level of detail that could be reached is up to a future analyst to determine and Appendix C provides examples of the input decks used in this analysis as reference points should someone wish to continue this journey. The sky is not the limit to the possibilities at hand as we forge another link in the chain to the stars.

REFERENCES

- [1] Griffin, M., French, J., *Space Vehicle Design*, Second Edition, American Institute of Aeronautics and Astronautics, 2004
- [2] Cassibry, J., Cortez, R., Stanic, M., Seidler, W., Adams, R., Statham, G., Fabinski, “The Case and Development Path for Fusion Propulsion”, *Journal of Spacecraft and Rockets*, Vol. 52, Issue 2, pg 595-612, 2015
- [3] Finseth, J., “ROVER Nuclear Rocket Engine Program Overview of ROVER Engine Tests Final Report”, NASA Marshall Space Flight Center, NASA-CR-189270, 1991
- [4] Moekel, W., “Comparison of Advanced Propulsion Concepts for Deep Space Exploration”, *Journal of Spacecraft and Rockets*, Vol. 9, Issue 12, pp. 863-868, 1972
- [5] Jahn, R., *Physics of Electric Propulsion*, McGraw Hill, ISBN 67-26883, 1968
- [6] Mason, L., “A Power Conversion Concept for the Jupiter Icy moons Orbiter”, NASA Glenn Research Center, NASA/TM-2003-212596, AIAA-2003-6007, 2003
- [7] Drake, B., ed., “Human Exploration of Mars Design Reference Architecture 5.0”, National Aeronautics and Space Administration, NASA-SP-2009-566, 2009
- [8] Miernik, J., Statham, G., Fabisinski, L., Maples, C., Adams, R., Polsgrove, T., Fincher, S., Cassibry, J., Cortex, R., Turner, M., “Fusion Propulsion Z-Pinch Engine Concept”, NASA Technical Reports Server, 2011
- [9] Atzeni, S., Meyer-Ter-Vehn, J., *The Physics of Inertial Fusion – Beam Plasma Interaction, Hydrodynamics, Hot Dense Matter*, Oxford Science Publications, Oxford University Press, ISBN 978-0-19-856264-1, 2004

- [10] Heirbaut, J., “How to Line a Thermonuclear Reactor”, <https://www.sciencemag.org/news/2012/08/how-line-thermonuclear-reactor>, 2012, Retrieved 3/6/2020
- [11] Hagler, M., Kristiansen, M., *An Introduction to Controlled Thermonuclear Fusion*, D.C. Heath and Company, ISBN 0-669-99119-8, 1977
- [12] Teller, E., Ed., *Fusion, Volume 1, Part A: Magnetic Confinement*, Academic Press, Inc., ISBN 0-12-685201-4, 1981
- [13] Bethe, H., “Energy Production in Stars”, *Physical Review*, 55, 1939
- [14] Kammash, T., Ed., *Fusion Energy in Space Propulsion*, Volume 167 *Progress in Astronautics and Aeronautics*, American Institute of Aeronautics and Astronautics, 1995
- [15] Schillo, K., “Three Dimensional Modeling of Fusion Yield in Plasma Jet-Driven Magneto-Inertial Fusion”, PhD Dissertation, The University of Alabama in Huntsville, 2019
- [16] Urey, H., Brickwedde, F., Murphy G., “A Hydrogen Isotope of Mass 2”, *Physical Review*, 39, 1932
- [17] Kaufman, S., Libby, W., “The Natural Distribution of Tritium”, *Physical Review*, 93, 1954
- [18] Zerriffi, H., “Tritium: The environmental, health, budgetary, and strategic effects of the Department of Energy’s decision to produce tritium.”, Institute for Energy and Environmental Research, 1996
- [19] Cortez, R., “Initial Design Process for a Pulsed Thermonuclear Fusion Reaction Engine”, Master’s Thesis, The University of Alabama in Huntsville, 2011

- [20] Doshi, B., et al., "Design and manufacture of the ITER cryostat," 2013 IEEE 25th Symposium on Fusion Engineering (SOFE), pp. 1-6., San Francisco, CA, 2013
- [21] "MIT and newly formed company launch novel approach to fusion power", <http://news.mit.edu/2018/mit-newly-formed-company-launch-novel-approach-fusion-power-0309>, Retrieved on 3/5/2020
- [22] Lindl, J., et al., "The physics basis for ignition using indirect-drive targets on the National Ignition Facility", *Physics of Plasmas*, Vol. 11, p. 339, American Institute of Physics, 2004
- [23] Miley, G., *Fusion Energy Conversion*, American Nuclear Society, ISBN 978-0894480089, 1976
- [24] Lindemuth, I., "The Case for Magnetized Target Fusion (MTF) a.k.a. Magneto-Inertial Fusion (MIF)", National Academy of Sciences Committee on the Prospects for Inertial Confinement Fusion Energy Systems, 2011
- [25] Adams, R., Cassibry, J., Bradley, D., Fabinsky, L., Statham, G., "Pulsed Fission-Fusion (PuFF) – Phase I Report", NASA Innovative Advanced Concepts, 2014
- [26] Schultze, N., "Fusion Energy for Space Missions in the 21st Century", NASA-TM-4298, 1991
- [27] McGuire, T., et al., "Lockheed Martin Compact Fusion Reactor Concept, Confinement Model and T4B Experiment", Lockheed Martin Corporation, 2016
- [28] Squire, J., et al., "Experimental Research Progress Toward the VASIMR Engine", 28th International Electric Propulsion Conference, 2003
- [29] Jarboe, T., et al., "Spheromak Fusion Propulsion for Future Solar System Exploration", *Journal of Propulsion and Power*, Vol. 21, No. 2, 2005

[30] Roth, J., "Effects of Applied DC Radial Electric Fields on Particle Transport in a Bumpy Torus Plasma," IEEE Trans. on Plasma Sci., PS-6, 158., 28., 1978

[31] Berry, L, et al., "ELMO Bumpy Torus", Oak Ridge National Laboratory, ORNL/TM-6743, 1979

[32] Teller, E., Ed., *Fusion, Volume 1, Part B: Magnetic Confinement*, Academic Press, Inc., ISBN 0-12-685241-3, 1981

[33] "The first plasma: the Wendelstein 7-X fusion device is now in operation", https://www.ipp.mpg.de/3984226/12_15, Max Planck Institute for Plasma Physics, 2015, Retrieved 3/5/2020

[34] "HSX – Helically Symmetric Experiment", <https://hsx.wisc.edu/>, Retrieved 3/5/2020

[35] "Large Helical Device Project", <https://www-lhd.nifs.ac.jp/pub/>, Retrieved 3/5/2020

[36] Clery, D., "Fusion "Breakthrough" at NIF? Uh, Not Really ...", <https://www.sciencemag.org/news/2013/10/fusion-breakthrough-nif-uh-not-really>, October 10, 2013, Retrieved 3/13/2020

[37] Bussard, R., "Some Physics Considerations of Magnetic Inertial Electrostatic Confinement: A New Concept for Spherical Converging Flow Fusion", *Fusion Technology*, Volume 19, March 1991

[38] Bussard, R., "Inertial-Electrostatic-Fusion Propulsion Spectrum: Air-Breathing to Interstellar Flight", *Journal of Propulsion and Power*, Volume 11, No. 2, //March-April 1995, pg. 365 – 372

[39] Ventura, T., “Robert Bussard on IEC Fusion Power and The Polywell Reactor”, <https://medium.com/discourse/robert-bussard-on-iec-fusion-power-the-polywell-reactor-be4a59dc7318>, 2019, Retrieved 3/6/2020

[40] Polsgrove, T., Fincher, S., Adams, R., Cassibry, J., Cortez, R., Turner, M., Maples, C., Miernik, J., Statham, G., Fabisinski, L., Santarius, J., Percy, T., “Design of Z-pinch and Dense Plasma Focus Powered Vehicles,” AIAA-2011-962, 2011.

[41] Lindemuth, I., Siemon, R., “The fundamental parameter space of controlled thermonuclear fusion” *American Journal of Physics* 77, 407, 2009

[42] Polsgrove, T., Adams, R., Fabisinski, L., Fincher, S., Maples, C., Miernik, J., Percy, T., Statham, G., Turner, M., Cassibry, J., Cortez, R., Santarius, J., “Z-Pinch Pulsed Plasma Propulsion Technology Development – Final Report”, Advanced Concepts Office (ED04), NASA Marshall Space Flight Center, 2010

[43] Adams, R., Alexander, R., Chapman, J., Fincher, S., Hopkins, R., Philips, A., Polsgrove, T., Litchford, R., Patton, B., Statham, G., White, P., Thio, Y., “Conceptual Design of In-Space Vehicles for Human Exploration of the Outer Planets”, NASA TP-2003-212691, 2003

[44] Cuneo, M., et al., "Magnetically Driven Implosions for Inertial Confinement Fusion at Sandia National Laboratories," *IEEE Transactions on Plasma Science*, vol. 40, no. 12, pp. 3222-3245, December 2012.

[45] Kirkpatrick, R., Lindemuth, I., et al., "Generation and Compression of a Target Plasma for Magnetized Target Fusion," Los Alamos National Laboratory, Los Alamos, NM, 1998.

[46] Munson, K., Shumlak, U., Nelson, B., "Extreme ultraviolet light production from a ZaP Flow Z-Pinch xenon plasma," Journal of Micro Nanolithography, MEMS, and MOEMS , vol. 7, no. 1, p. 013003, January 2008.

[47] Shumlak, U., et al., "Advanced Space Propulsion Based on the Flow-Stabilized Z-Pinch Fusion Concept", American Institute of Aeronautics and Astronautics, AIAA-2006-4805, 2006

[48] Freeland, R., Lamontagne, M., "Firefly Icarus: An Unmanned Interstellar Probe Using Z-Pinch Fusion Propulsion", Journal of the British Interplanetary Society, Vol. 68, pp. 68-80, 2015

[49] Sze, H., Banister, J., et al., "Progress in Double-Shell Gas Puff Z-Pinches", American Institute of Physics, 2002

[50] Taylor, B., Cassibry, J., Adams, R., et al., "An Overview of the Charger-1 Pulsed Power Facility", IEEE Transactions on Plasma Science, Vol. 46, No. 11, pp. 3986 – 3992, November 2018

[51] Ware, K., Bell, D., Gullickson, R., and Vitkovitsky, I., "Evolving Approaches to Pulsed X-Ray Sources," IEEE Transactions on Plasma Science, Vol. 30, No. 5, October 2002, pp. 1733-1741.

[52] Adams, R., Cassibry, J., Cortez, R., "Charger-1: A Pulsed Fusion Propulsion Testbed", NASA Technical Reports Server, 20120016902, 2012

[53] Battistoni, G., et al., "Overview of the FLUKA code", Annals of Nuclear Energy, Vol. 82, August 2015, pp. 10-18

[54] Agostinelli, S., et al., "G EANT-4 – a simulation toolkit", Nuclear Inst. and Methods in Physics Research, A, Volume 506, Issue 3, July 2003, p. 250-303.

[55] Chinaka, E., “Radiation Shielding Analysis and Optimisation for the Mineral-PET Kimberlite Sorting Facility using the Monte Carlo Calculation Code MCNPX”, Master’s Thesis, University of Johannesburg, Johannesburg, South Africa, 2014.

[56] Lukhele, F., “Radiation Shielding Calculations by Means of MCNPX”, Master’s Thesis, University of Zululand, Mangeze, South Africa, 2006

[57] Meyerian, A., “Monte-Carlo simulations in respect of radiation protection”, Master’s Thesis, University of Munster, Munster, 2012

[58] Davis, A., “Radiation Shielding of Fusion Systems”, Doctor of Philosophy Dissertation, The University of Birmingham, U.K., 2010

[59] Spackman, D., “Design and Analysis of Radiation Shielding Eyewear”, Master’s Thesis, Oregon State University, Corvallis, Oregon, 2013

[60] Dickson, E., “Experimental Shielding Evaluation of the Radiation Protection Provided by Residential Structures”, Doctor of Philosophy Dissertation, Oregon State University, Corvallis, Oregon, 2013

[61] Asbury, S., “Multi-Grid Genetic Algorithms for Optimal Radiation Shield Design”, Doctor of Philosophy Dissertation, The University of Michigan, Ann Arbor, Michigan, 2012

[62] Kowash, B., “Parameter Study for Optimizing Mass of a Space Nuclear Power System Radiation Shield”, Master’s Thesis, Air Force Institute of Technology, Wright-Patterson Air Force Base, Ohio, 2002

[63] Dugal, C., “Application of Monte Carlo to Linac Bunker Shielding Design”, Master’s Thesis, Carleton University, Ottawa, Ontario, Canada, 2006

- [64] Khatchadourian, R., “Monte Carlo Simulations for Neutron Shielding in Radiotherapy Bunkers”, Master’s Thesis, McGill University, Montreal, Quebec, 2013
- [65] Shultis, J., Faw, R., “An MCNP Primer”, Technical Report, Department of Mechanical and Nuclear Engineering, Kansas State University, 2011
- [66] Chilton, A.B., Shultis, J.K., and Faw, R.E., *Principles of Radiation Shielding*, 1st Edition, Prentice Hall, ISBN 0-13-709907-X, 1984
- [67] Cacuci, D., Ed., Shultis, J., Faw R., *Handbook of Nuclear Engineering, Chapter 11 – Radiation Shielding and Radiological Protection*, Springer Science and Business Media, 2010
- [68] Emrich, W., *Principles of Nuclear Rocket Propulsion*, Butterworth-Heinemann, ISBN 9780128044742, 2016
- [69] “Conversion Coefficients for use in Radiological Protection against External Radiation”, Annals of the ICRP Publication 74, International Commission on Radiological Protection, 1996
- [70] “Radiation Quantities and Units”, Report 19, International Commission on Radiation Units and Measurements, Washington DC, 1971
- [71] Reilly, D., Ensslin, N., Smith, H., Kreiner, S., “Passive nondestructive assay of nuclear materials.”, NUREG/CR-5550, U.S. Nuclear Regulatory Commission, 1991
- [72] Sublette, C., “Nuclear Weapons Frequently Asked Questions”, <http://nuclearweaponarchive.org/Nwfaq/Nfaq4-1.html>, Retrieved 3/8/2020
- [73] “Standards for Protection Against Radiation”, United States Code of Federal Regulations, 10 CFR Part 20

[74] Choppin, G., Liljenzin, J., Eckberg, C., *Radiochemistry and Nuclear Chemistry*, 4th Edition, 2013

[75] “Basic Radiation Protection and Radiobiology”, <https://radiologykey.com/basic-radiation-protection-and-radiobiology-2/>, Retrieved 9/22/2019

[76] Hubbell, J., Seltzer, S., “X-Ray Mass Attenuation Coefficients”, <https://www.nist.gov/pml/x-ray-mass-attenuation-coefficients>, Radiation Physics Division, PML, NIST, 1996, Retrieved 3/10/2020

[77] “Data for Use in Protection Against External Radiation”. Annals of the ICRP, Publication 51, International Commission on Radiological Protection, vol 17, no 2/3. Pergamon Press, Oxford, 1987

[78] "Average Energy Required to Produce an Ion Pair", Report 31, International Commission on Radiation Units and Measurements, Washington DC, 1979

[79] Valentin, J., “The 2007 Recommendations of the International Commission on Radiation Protection”, Annals of the ICRP Publication 103, 2007

[80] “Phantoms and Computational Models in Therapy, Diagnosis and Protection”, Report 48, International Commission on Radiation Units and Measurements, Washington DC, 1992

[81] Eckerman, K., et al., “Compendium of Dose Coefficients based on ICRP Publication 60”, Annals of the ICRP Publication 119, International Commission on Radiological Protection, 2012

[82] “Radiation Monitoring for Protection of the Public after Major Releases of Radionuclides to the Environment”, Report 92, International Commission on Radiation Units and Measurements, Washington DC, 2015

[83] “Recommendations of the ICRP”, Annals of the ICRP Publication 26, International Commission on Radiological Protection, 1977

[84] “Ionizing Radiation Exposure of the Population of United States”, NCRP Report 93, National Council on Radiation Protection and Measurements, 1987

[85] Johnson, A., et al., “Spaceflight Radiation Health Program at the Lyndon B. Johnson Space Center”, National Aeronautics and Space Administration, NASA-TM-104782, 1993

[86] Khan, F., “The Physics of Radiation Therapy”, Lippincott Williams & Wilkins, ISBN-10 0781730651, 2003

[87] Stabin, M., “Radiation Protection and Dosimetry: An Introduction to Health Physics”, Springer, ISBN 978-1441923912, 2010

[88] Shavers, M., et al., “Implementation of ALARA radiation protection on the ISS through polyethylene shielding augmentation of the Service Module Crew Quarters”, *Advanced Space Research*, Vol. 34, No. 6, 2004, pp. 1333-7

[89] Holmes-Siedle, A., Adams, L., *Handbook of Radiation Effects*, 2nd Edition, Oxford University Press, ISBN 978-0198507338, 2002

[90] Cook, J., “Juno Armored Up to Go to Jupiter”, https://www.nasa.gov/mission_pages/juno/news/juno20100712.html, Retrieved 3/9/2020

[91] Emrich, W., *Rocket Propulsion Using Nuclear Fission*, Mathematica Viewer, 2015

[92] X-5 Monte Carlo Team, "MCNP – A General Monte Carlo N-Particle Transport Code, Version 5, Volume I: Overview and Theory", LA-UR-03-1987, Los Alamos National Laboratory, 2008

[93] X-5 Monte Carlo Team, "MCNP – A General Monte Carlo N-Particle Transport Code, Version 5, Volume II: User's Guide LA-CP-03-0245, Los Alamos National Laboratory, 2008

[94] Pelowitz, D. (ed.), "MCNP6 User's Manual", Version 1.0 May 2013 Manual Rev. 0, Los Alamos National Laboratory, 2013

[95] Pelowitz, D. (ed.), "MCNPXTM User's Manual", Version 2.7.0, LA-CP-11-00438, Los Alamos National Laboratory, 2011

[96] "Radiation Dose to Adults From Common Imaging Examinations", <https://www.acr.org/-/media/ACR/Files/Radiology-Safety/Radiation-Safety/Dose-Reference-Card.pdf>, American College of Radiology, Retrieved 3/9/2020

[97] "Radiation Protection for Particle Accelerator Facilities", NCRP Report 144, National Council on Radiation Protection and Measurements, 2005

[98] "Structural Shielding Design for Medical X-Ray Imaging Facilities", NCRP Report 147, National Council on Radiation Protection and Measurements, 2005

[99] "Structural Shielding Design and Evaluation for Megavoltage X- and Gamma-Ray Radiotherapy Facilities", NCRP Report 151, National Council on Radiation Protection and Measurements, 2005

[100] "Protection Against Neutron Radiation", NCRP Report 38, National Council on Radiation Protection and Measurements, 1971

[101] Fensin, M., et al., “Monte Carlo Burnup Interactive Tutorial”,
https://mcnp.lanl.gov/pdf_files/la-ur-09-2051.pdf, Los Alamos National Laboratory, 2009,
Retrieved 3/9/2020

[102] Eades, M., “¹³⁵Xe in LEU Cermet Nuclear Thermal Propulsion System”,
PhD Dissertation, The Ohio State University, 2016

[103] Hubbell, J., Seltzer, S., “X-Ray Mass Attenuation Coefficients – Tissue, Soft,
4 Component”,
<https://physics.nist.gov/PhysRefData/XrayMassCoef/ComTab/tissue4.html>, Radiation
Physics Division, PML, NIST, 1996, Retrieved 3/10/2020

APPENDIX A: PHOTON VERIFICATION PROBLEM

The methods and tools used for the analysis of the ChargerLab and ZShip models require validation with respect to known methods for calculating the attenuation of photons. An intensive effort was embarked upon in the spring semester of 2018 to create an MCNP simulation of a photon attenuation problem found in a textbook. This ultimately was chosen from the work of Emrich [91], having been deemed relevant due to its NTR propulsion applications. This problem is outlined below.

An NTR-based human spaceflight mission to Mars has to consider the mass of shielding as a major part of its design, and to minimize this they could be supplemented by the attenuation provided by the liquid hydrogen fuel tanks. These tanks would add an extra layer of protection for the crew with regards to the gamma radiation emanating from the propulsion system's nuclear reactor. This vehicle is represented by the schematic of Figure A.1, and the most basic parts of the spacecraft design are considered for attenuation calculations.

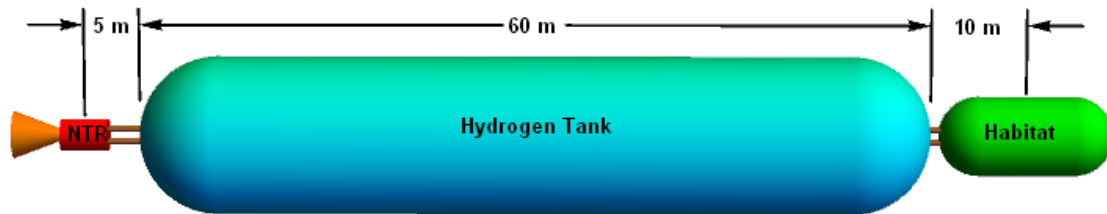


Figure A.1. NTR-based spacecraft diagram [91]

As the NTR engine operates, the depletion of the liquid hydrogen causes the liquid level in the tank to decrease at a rate of 2.5 cm/sec. For the reactor, the 6 MeV gamma ray power produced is 300 MW and the volume of the core is assumed to be 100,000 cm³. From these given conditions, the whole body dose by prompt fission gamma rays to an

astronaut located at the center of the habitat after completion of engine burn can be found. Given the rate of hydrogen depletion, a plot of the gamma ray dose received by the astronaut as a function of time can also be found. Another calculation to be done is in finding the dose that the astronaut would have received assuming that no hydrogen was available for shielding.

The following simplifying assumptions are to be made: First, assume that the astronaut has a mass of 75 kg with an effective cross sectional area of 8000 cm². Next, the hydrogen tank is assumed to be fully depleted after the engine burn and that this hydrogen is the only radiation shielding available for the crew. For the sake of simplicity in analysis, the reactor core is assumed to be a sphere of uranium with an effective density of 10 g/cm³ and that the reactor has a constant power density. No other spacecraft materials are accounted for in this analysis such as tanks, structures, engine hardware and crew cabins. Since the reactor and astronaut are a non-trivial distance apart, as well as the reactor size being small relative to the spacecraft, the reactor is treated as a point source in this analysis.

In this analysis, the 6 MeV gamma ray flux to the astronaut can be modeled using a differential form of the gamma ray attenuation expression in Equation A.1.

$$d\phi_{\gamma f}(R) = e^{-\mu_r T} [Ae^{-\alpha\mu_s Q} + (1 - A)e^{-\beta\mu_s Q}] \frac{e^{-\mu_s Q}}{4\pi R^2} ds = e^{-\mu_r T} G_\gamma(\mu_s Q) ds \quad (\text{A.1})$$

Differentiated, this becomes

$$\frac{dD}{dt} = S [Ae^{-\alpha\mu_s z} + (1 - A)e^{-\beta\mu_s z}] \frac{e^{-\mu_s z}}{4\pi R^2} \quad (\text{A.2})$$

where D is the dose resulting from 6 MeV prompt fission gamma rays, z is the instantaneous level of hydrogen in the propellant tank, and S is the gamma ray source intensity.

The propellant level in the tank as a function of time can be determined as

$$z = 6000 - 2.5t \quad (\text{A.3})$$

The time needed to drain the propellant tank is then computed from Equation A.2,

$$0 = 6000 - 2.5t_0 \quad \Rightarrow \quad t_0 = \frac{6000}{2.5} = 2400 \text{ sec} \quad (\text{A.4})$$

where t_0 is the time required to drain the propellant tank.

Using Equations A.2 and A.3, the differential gamma ray energy flux to the astronaut is then written as

$$\frac{dD}{dt} = S \left[A e^{-\alpha \mu_s (6000 - 2.5t)} + (1 - A) e^{-\beta \mu_s (6000 - 2.5t)} \right] \frac{e^{-\mu_s (6000 - 2.5t)}}{4\pi R^2} \quad (\text{A.5})$$

Integrating Equation A.5 over the time needed to drain the hydrogen tank finds an expression for the total 6 MeV gamma ray energy received by the astronaut via the engine burn that can be determined such that

$$\begin{aligned} D &= \frac{S}{4\pi R^2} \int_0^t \left[A e^{-\alpha \mu_s (6000 - 2.5t)} \right. \\ &\quad \left. + (1 - A) e^{-\beta \mu_s (6000 - 2.5t)} \right] e^{-\mu_s (6000 - 2.5t)} dt \\ &= S_a \left[\frac{A}{1 + \alpha} (e^{2.5t(1+\alpha)\mu_s} - 1) e^{-6000(1+\alpha)\mu_s} \right. \\ &\quad \left. + \frac{1 - A}{1 + \beta} (e^{2.5t(1+\beta)\mu_s} - 1) e^{-6000(1+\beta)\mu_s} \right] \end{aligned} \quad (\text{A.6})$$

where $S_a = \frac{0.0318S}{\mu_s R^2}$, which is the gamma ray surface source intensity.

Using Figure A.2, the specific mass attenuation coefficient for liquid hydrogen at 6 MeV can be found. This chart was derived from tables of data provided by NIST [76].

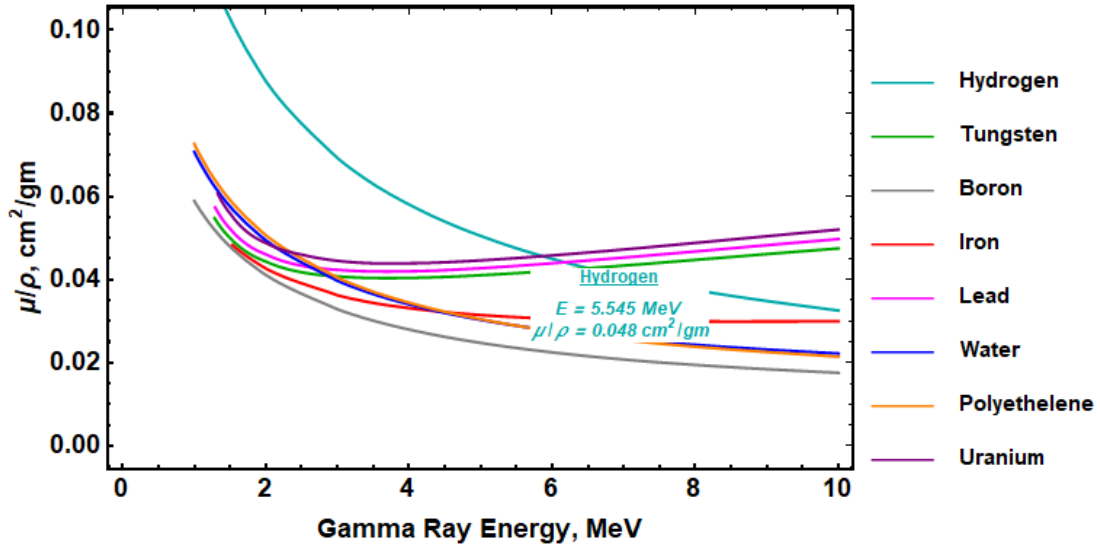


Figure A.2. Gamma ray mass attenuation coefficients [91]

$$\frac{\mu_s}{\rho} = 0.045 \text{ cm}^2/\text{g}$$

$$\rho_{LH_2} = 0.07 \text{ g}/\text{cm}^3$$

(A.7)

$$\mu_s = \rho \frac{\mu_s}{\rho} = (0.07 \text{ g}/\text{cm}^3) (0.045 \text{ cm}^2/\text{g}) = 0.00315 \text{ cm}^{-1}$$

The Taylor gamma ray buildup factors for liquid hydrogen are found as

$$A = 6.82, \alpha = -0.016, \beta = 0.043 \quad (\text{A.8})$$

Using Figure A.2, the specific mass attenuation coefficient for uranium at 6 MeV comes out to be

$$\frac{\mu_r}{\rho} = 0.046 \text{ cm}^2/\text{g}$$

$$\rho_U = 10 \text{ g}/\text{cm}^3 \quad (\text{A.9})$$

$$\mu_r = \rho \frac{\mu_r}{\rho} = (10 \text{ g}/\text{cm}^3) (0.046 \text{ cm}^2/\text{g}) = 0.46 \text{ cm}^{-1}$$

The gamma radiation emitted by the reactor has a source term that can be determined by taking into account the fact that gamma radiation is both created and absorbed within the reactor. Since the reactor is assumed to be spherical with a constant power density, the source term can be determined by

$$S = \frac{PN_{\gamma f}(E)}{\frac{4}{3}\pi R^3} \int_0^R 4\pi r^2 e^{-\mu_r r} dr$$

$$= \frac{3PN_{\gamma f}(E)\{2 - e^{-\mu_r R}[2 + \mu_r R(2 + \mu_r R)]\}}{(\mu_r R)^3} \quad (\text{A.10})$$

Where the radius of the reactor is determined by

$$R = \left(\frac{3}{4\pi}V_{Rx}\right)^{\frac{1}{3}} = \left(\frac{3}{4\pi}(100,000 \text{ cm}^3)\right)^{\frac{1}{3}} = 28.8 \text{ cm} \quad (\text{A.11})$$

With the reactor power being

$$P = 300 \text{ MW} = 300 \times 10^6 \text{ W} \quad (\text{A.12})$$

Figure A.3 allows for the energy distribution of fission produced gamma rays to be found as shown in Equation A.13 below.

$$N_{\gamma f}(6) = 7.2e^{-1.09E} = 7.2e^{-1.09(6)} = 0.0104003 \quad (\text{A.13})$$

Using the results from Equation A.13 combined with Equation A.10, the gamma ray source intensity can be determined (as shown in Equation A.14).

$$S = \frac{3PN_{\gamma f}(E)\{2 - e^{-\mu_r R}[2 + \mu_r R(2 + \mu_r R)]\}}{(\mu_r R)^3}$$

$$= \frac{(3)(300 \times 10^6 \text{ W})(0.0104003)\{2 - e^{-(0.46)(28.8 \text{ cm})}[2 + (0.46)(28.8 \text{ cm})(2 + (0.46)(28.8 \text{ cm}))]\}}{((0.46)(28.8 \text{ cm}))^3} \quad (\text{A.14})$$

$$= 8047.88 \text{ W} \left(1 \times 10^7 \frac{\text{erg}}{\text{W sec}}\right) = 8.05 \times 10^{10} \frac{\text{erg}}{\text{sec}}$$

$$\begin{aligned}
D &= \left(14447 \frac{\text{erg}}{\text{cm}^2}\right) \left[\frac{6.82}{1 - 0.016} \left(e^{2.5t(1-0.016)(0.00315)} \right. \right. \\
&\quad \left. \left. - 1 \right) e^{-6000(1-0.016)(0.00315)} \right. \\
&\quad \left. + \frac{1 - 6.82}{1 + 0.043} \left(e^{2.5t(1+0.043)(0.00315)} \right. \right. \\
&\quad \left. \left. - 1 \right) e^{-6000(1+0.043)(0.00315)} \right] \tag{A.16} \\
&= 0.000840 e^{0.00775t} - 0.000222 e^{0.00821t} - 0.000618 \\
D &= 19515 \frac{\text{erg}}{\text{cm}^2} \text{ at } t = t_0 = 2400 \text{ sec}
\end{aligned}$$

When taking astronaut mass and cross sectional area into account as well as assuming an RBE of one, the dose is calculated to be

$$\begin{aligned}
Dose &= \left(D \frac{\text{erg}}{\text{cm}^2} \right) \left(\frac{8000 \text{ cm}^2}{75,000 \text{ g}} \right) \left(\frac{1 \text{ RAD g}}{100 \text{ erg}} \right) \left(1 \frac{\text{REM}}{\text{RAD}} \right) = 0.001067D \\
&= 20.9 \text{ REM} \tag{A.17}
\end{aligned}$$

The dose to the astronaut as a function of time may be determined by plotting Equation A.17 using Equation A.16 such that

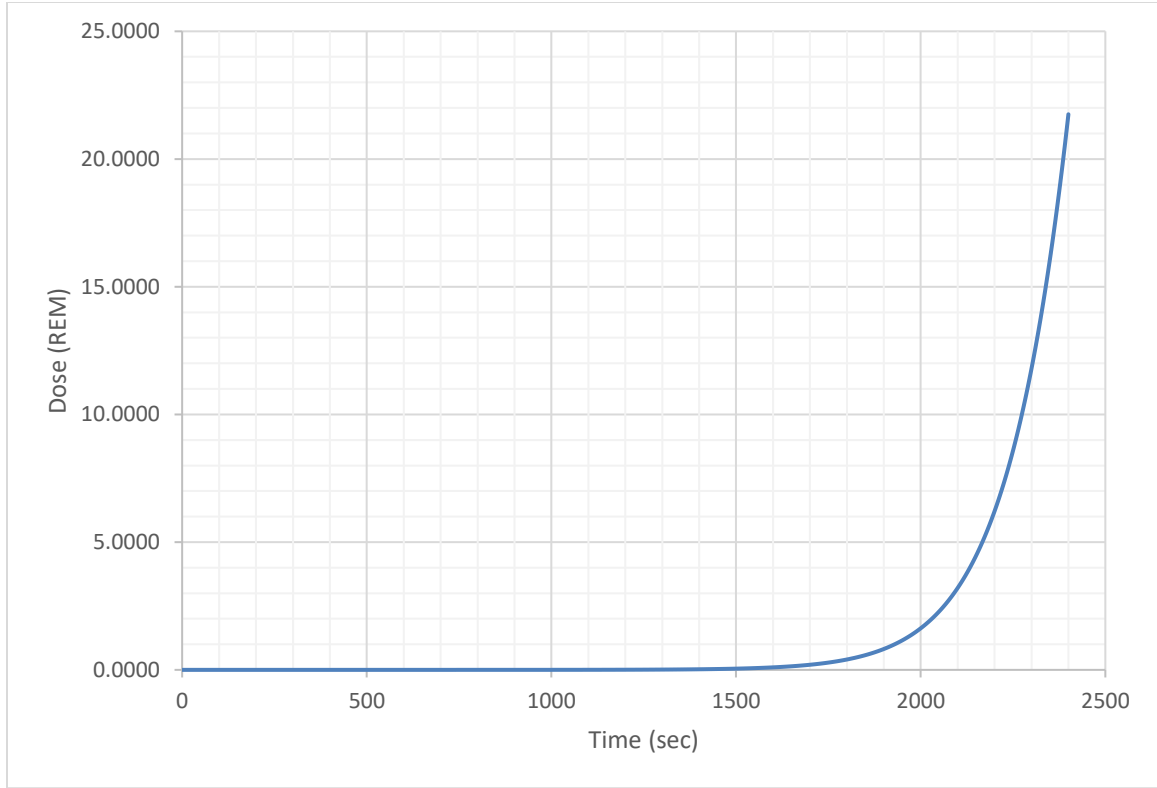


Figure A.4. Dose to the astronaut as a function of burn time

In order for the unshielded dose to the astronaut to be considered in the event of no liquid hydrogen being available for that shielding task, it is necessary to observe that the only attenuation of the gamma radiation comes from geometric spreading since the only medium is vacuum. Knowing this, Equation A.6 can be modified such that

$$\begin{aligned}
 D &= \frac{S}{4\pi R^2} \int_0^t [Ae^{-\alpha_0(6000-2.5t)} + (1-A)e^{-\beta_0(6000-2.5t)}] e^{-0(6000-2.5t)} dt \\
 &= \frac{S}{4\pi R^2} \int_0^t [1] dt = \frac{St}{4\pi R^2}
 \end{aligned} \tag{A.18}$$

and substituting numerical values from the problem statement into Equation A.18 yields

$$\begin{aligned}
 D &= \frac{St}{4\pi R^2} = \frac{\left(8.05 \times 10^{10} \frac{\text{erg}}{\text{sec}}\right) t}{4\pi(7500 \text{ cm})^2} = 113.9t \frac{\text{erg}}{\text{cm}^2} = 273300 \frac{\text{erg}}{\text{cm}^2} \\
 &\quad \text{at } t = t_0 = 2400 \text{ sec}
 \end{aligned} \tag{A.19}$$

Using Equation A.17 to convert the unshielded gamma radiation from Equation A.19 to a biological equivalent dose to the astronaut yields

$$Dose = 0.001067D = 292 \text{ REM} \quad (\text{A.20})$$

The unshielded dose to the astronaut is over an order of magnitude higher than the dose shielded by the depleting liquid hydrogen level. This difference speaks well to the ability for a material such as liquid hydrogen to attenuate gamma ray photons. The methods used in this problem to find the total dose are relatively simple, as attenuation calculations with photons are straightforward and easy to implement. Since this approach is straightforward, it follows that an approach to modeling and simulation of this problem in MCNP should be also.

For the majority of the semester in the spring of 2018, the task was undertaken to replicate the textbook problem using the methods available in MCNP. This effort became the proving ground for the learning curve of MCNP and the methods used were ultimately less efficient than what was accomplished in ChargerLab, ZShip and the Shield123 iterations. If it were not for the toil of the photon verification effort, the efficiency of the later models would not have been arrived at. The development of the Emrich13-1 family of simulations, named for the Problem 13.1 in the textbook [91], went through several phases with multiple iterations for each phase. The first phases of the model development were concerned with what was to be done about the time dependent dose variable with respect to the changing liquid hydrogen level. Also in this time period, the physics assumptions and variance reduction techniques were gradually improved through trial and error. The second major phase of the model development concerned the reactor model and the problems inherent in the simplified assumptions in the earlier hand calculations. The

third phase of this effort incorporated the lessons learned from the initial work to make a final set of data points to plot and share to compare with the hand calculations.

In the early part of the model development, many paths were taken in the process to begin optimization of the tallies and the source assumptions. The approach that was decided on with regards to modeling the propellant level drainage was to create snapshots in time to represent the varying liquid level. A series of simulation conditions were created to represent the liquid level and various time steps, and this was set up in such a way that each time step of the engine burn could be represented by a single simulation. This initial process was spent over the course of 87 individual simulation runs averaging 97 minutes each. Within this bulk of data gathering, 11 iterations were performed as the process for variance reduction, tally efficiency and other items were ironed out. At the conclusion of this phase, it was determined that exact replication of the original problem was not feasible due to some limitations in MCNP with regards to simplifications made for the hand calculations.

The initial configuration of the Emrich13-1 model consisted of a spherical problem boundary with a radius of 4000 cm (Cell 5), outside of which was the vacuum of Cell 1 where particles were killed from the simulations. The liquid hydrogen tank was represented by Cell 3, a cylinder of propellant with an initial length of 6000 cm; Surface 3 became the liquid level and its location with respect to Surface 2 would be varied to be at the correct location to represent the depleted liquid level at each time step. Cell 4 represented the astronaut in the crew cabin and was modeled as a disc made from ICRU four component tissue to match the assumptions of the original problem. The reactor, represented by Cell 2, was made from uranium and was assumed to match the density of

10 g/cm³ from the original problem. Interestingly, the assumption made by Emrich on this density neglects the fact that elemental uranium is actually 18.2 g/cm³; this shows that these assumptions were attempting to account for a lower density of a reactor made from more than just uranium. The reactor, the astronaut and the liquid hydrogen are the only materials in the model that photons can interact with, the rest of the model is vacuum.

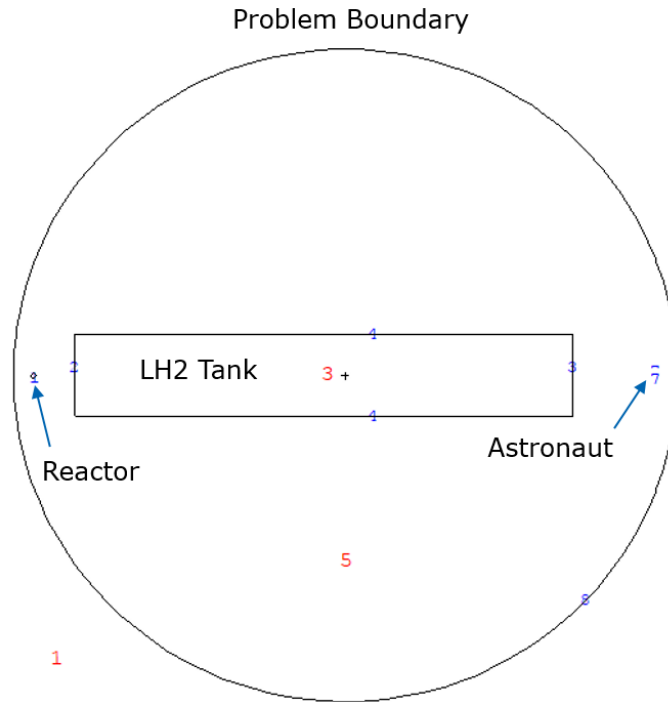


Figure A.5. Initial configuration of Emrich13-1 model

The initial iterations found that not enough photons were reaching the tallies to drive relative errors down to usable numbers. This led to an intensive series of runs with the liquid hydrogen tank being empty (represented as vacuum in Cell 3) to tweak settings on physics assumptions and other tricks to drive particles toward the astronaut. After several more trial runs it was determined that too much attenuation was occurring in the uranium of the reactor itself; MCNP sent warnings that this cell was set as a conductor and this high-Z material attenuated too well to emit as much radiation as the original problem.

This was not an issue in the original problem since the material properties used were derived from the NIST tables for attenuation coefficients at the 6 MeV energy level. The ability to use this assumption is the hinge point on being able to solve this analytically. What was needed on the MCNP side was a relaxation of the density of the uranium and a blended material assumption that could be developed based upon knowing the other materials of the reactor like the moderators and reactor vessel.

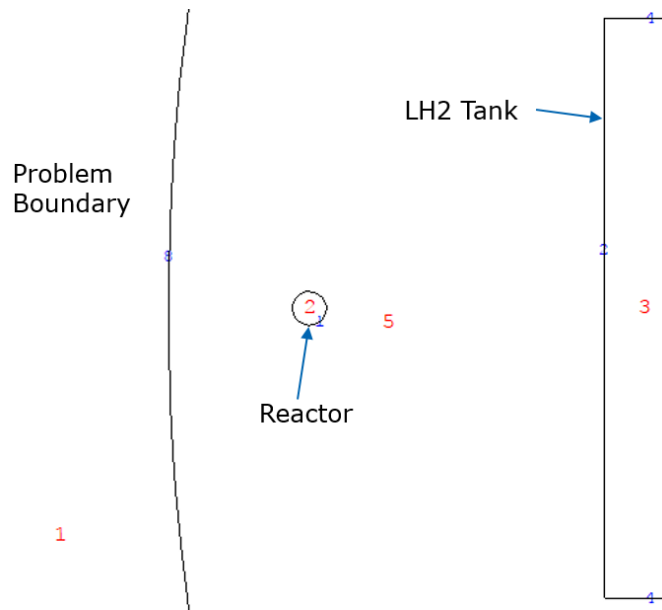


Figure A.6. Zoom in on reactor side of Emrich13-1 model

This started the second phase of model development where it was decided that the highest priority was to determine the attenuation of the uranium sphere in the original problem. To do this, the reactor sphere in the original problem was treated analytically by substituting the uranium properties in Equation A.14 with those of the ICRU Four Component Tissue as found in the NIST tables at 6 MeV (Equation A.21) [103]. This led to a gamma ray source intensity based upon a reactor composed of ICRU Four Component Tissue that could be compared to the source intensity of a uranium reactor as found in

Equation A.14. Dividing the results of Equation A.22 by the results of Equation A.14 yields a 213.134 attenuation factor.

$$\frac{\mu_{r,I}}{\rho} = 0.02739 \text{ cm}^2/\text{g}$$

$$\rho_I = 1 \text{ g}/\text{cm}^3 \quad (\text{A.21})$$

$$\mu_{r,I} = \rho \frac{\mu_{r,I}}{\rho} = (1 \text{ g}/\text{cm}^3) (0.02739 \text{ cm}^2/\text{g}) = 0.02739 \text{ cm}^{-1}$$

$$S = \frac{3PN_{\gamma f}(E) \{2 - e^{-\mu_{r,I}R} [2 + \mu_{r,I}R (2 + \mu_{r,I}R)]\}}{(\mu_{r,I}R)^3}$$

$$= \frac{(3)(300 \times 10^6 \text{ W})(0.0104003) \{2 - e^{-(\mu_{r,I})(28.8 \text{ cm})} [2 + (\mu_{r,I})(28.8 \text{ cm}) (2 + (\mu_{r,I})(28.8 \text{ cm}))]\}}{((\mu_{r,I})(28.8 \text{ cm}))^3} \quad (\text{A.22})$$

$$= 1747903.03 \text{ W} \left(1 \times 10^7 \frac{\text{erg}}{\text{W sec}}\right) = 1.7479 \times 10^{13} \frac{\text{erg}}{\text{sec}}$$

In addition to finding this attenuation, a new blended material assumption was found for the reactor model in MCNP. This material was found from an example problem in the MCNP5 User's Manual [92, 93] that modeled a reactor with distinct fuel rods and control rods. The materials for both were combined to make a blended assumption for the MCNP reactor sphere to be made from 49% uranium-238, 1% uranium-235, 2% carbon, 1% oxygen, 1% sodium, and 1% copper. Using this information and the attenuation calculated analytically, a series of EmrichReactor model runs was conducted. A baseline to compare to for attenuation was developed made from ICRU Four Component Tissue instead of the blended reactor assumption. Several iterations were attempted with variations in source assumptions as well as reactor densities to narrow down the best fit to match the attenuation found analytically. Along the way in this process, Forced Collisions

was discovered and first implemented to drive convergence in relative errors and cut computation times roughly in half over prior simulations. After 70 simulation runs comparing ICRU Four Component Tissue, elemental uranium and two blended assumptions with a variety of densities, the attenuation from the ICRU tissue was matched with the blended assumption identified above having a density of $6.87387969 \text{ g/cm}^3$.

With this data and assumption in hand, a final iteration was conceived to conduct a step-wise series of simulations to measure the dose to the astronaut at each time step throughout the engine burn. This iteration, known as Emrich13-1e, contained four tallies to measure dose to the astronaut and to the liquid hydrogen column. Tally 12 on Surface 7 measured the particle flux on the leeward surface of the astronaut, Tally 14 measured the particle flux to the whole astronaut in Cell 4, Tally 16 measured the energy deposition in Cell 4, and Tally 26 measured the energy deposition in the liquid hydrogen. Initially, it was considered to use flux-to-dose conversion coefficients to find the dose at each time step in RAD/particle, but in order to find the actual dose a particle flux per second would need to be known. This data point would rely on assumptions the author was not prepared to make. Instead, a curve was generated using the Tally 14 readings of photon/cm^2 as a function of time.

As shown in Figure A.7, the shape of the curve matches very closely to the shape of the curve in Figure A.4. The biggest difference is in the magnitude of the units on the y-axis, but the general shape of both curves are the same between the two. This shows a strong correlation for the method deployed by MCNP and the analytical method covered in the original problem. Another iteration could be performed to make these curves exactly match, but this would involve the use of flux-to-dose conversion coefficients and

assumptions for time dependent particle flux from the source. This could end up being another intensive matching exercise to arrive at the correct assumption on the particle flux per unit time. Unfortunately, the Emrich13-1e data cannot be mined further since all raw output files and input files were lost in a computer crash in the summer of 2018. All of the processed data survived, but a new iteration would have to be done from scratch. There are plenty of notes to rebuild from, but this level of detail was decided to be enough on this appendix.

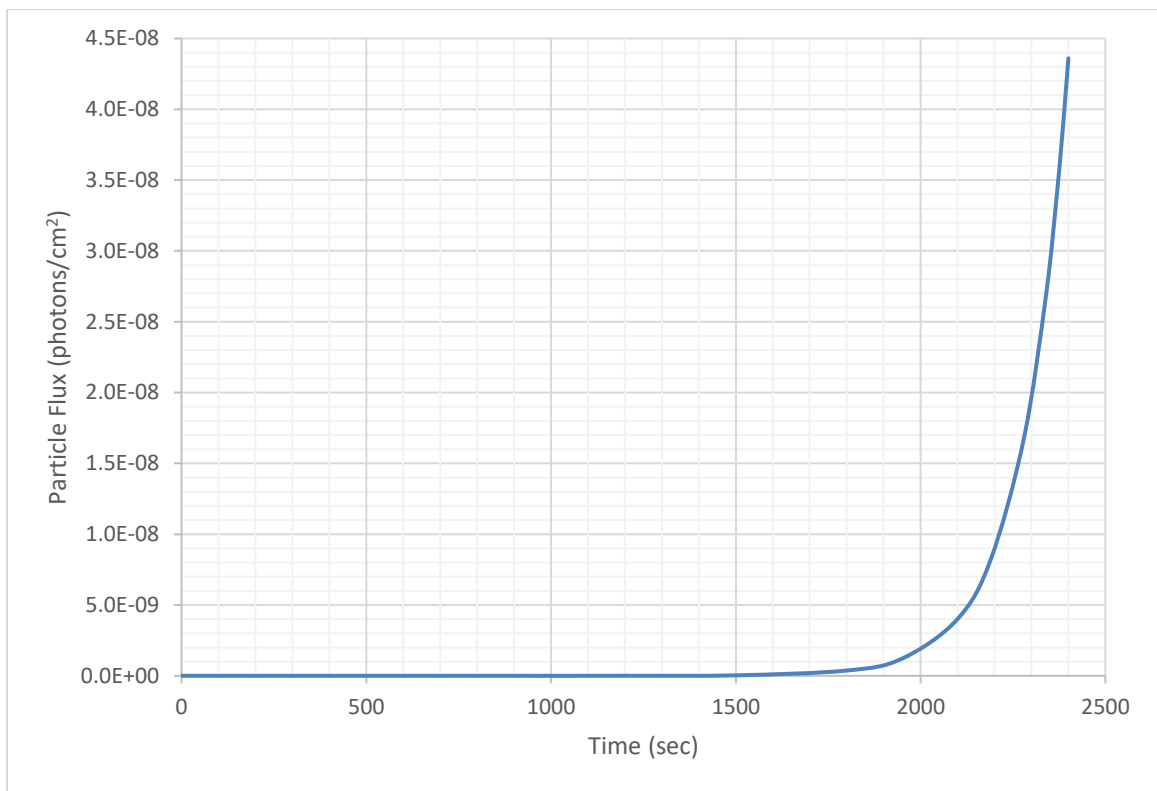


Figure A.7. Particle flux to astronaut as a function of burn time

Table A.1. Burn time with simulation input and output conditions

Burn Time	Surface 3		Cell 4	
T	py	File Name	Tally 14	Relative Error
[sec]	[cm]		[photons/cm ²]	
2400	500	Emrich13-1e_Empty_20180417b	4.35977E-08	0.0061
2397.6	506	Emrich13-1e_001_20180418a	4.27895E-08	0.0064
2395.2	512	Emrich13-1_002_20180418a	4.19958E-08	0.0064
2392.8	518	Emrich13-1e_003_20180418a	4.12167E-08	0.0064
2390.4	524	Emrich13-1e_004_20180418a	4.04204E-08	0.0064
2388	530	Emrich13-1e_005_20180418a	3.96035E-08	0.0064
2385.6	536	Emrich13-1e_006_20180418a	3.88650E-08	0.0064
2380.8	548	Emrich13-1_008_20180418a	3.74071E-08	0.0064
2370	575	Emrich13-1e_012_20180418a	3.43108E-08	0.0064
2340	650	Emrich13-1e_025_20180418a	2.69762E-08	0.0064
2280	800	Emrich13-1e_050_20180417a	1.68145E-08	0.0064
2190	1025	Emrich13-1e_087_20180418b	8.22061E-09	0.0064
2100	1250	Emrich13-1_125_20180417a	4.00880E-09	0.0065
1950	1625	Emrich13-1e_187_20180418a	1.21727E-09	0.0065
1800	2000	Emrich13-1e_250_20180417a	3.72879E-10	0.0081
1500	2750	Emrich13-1_375_20180417a	3.41210E-11	0.0064
1200	3500	Emrich13-1e_500_20180417a	3.15289E-12	0.0064
900	4250	Emrich13-1e_625_20180417a	2.91290E-13	0.0064
600	5000	Emrich13-1_750_20180417a	2.69210E-14	0.0064
300	5750	Emrich13-1e_875_20180417a	2.48726E-15	0.0064
156	6110	Emrich13-1e_935_20180418a	7.92836E-16	0.0064
12	6470	Emrich13-1e_995_20180417a	2.52737E-16	0.0064
0	6500	Emrich13-1_Full_20180417b	2.29785E-16	0.0064

APPENDIX B: NEUTRON VERIFICATION PROBLEM

The scope of this thesis is contingent upon the assumption that the modeling and simulation in MCNP is valid with regards to the actual physics involved in the problem. This is true for all of the particles involved in the calculations. This appendix is focused on the neutron side of the MCNP simulations; in order to verify that the attenuation results are indeed valid, an established standard will be needed to compare results to. Unlike the photon verification, there are no straight forward ways to account for neutron attenuation that are precise without the use of statistical tools. The interaction of neutrons with matter is covered on a basic level in Chapter 2, and a basic concept for this is known as the cross section. The microscopic cross sections, σ , are described in Section 2.3. When dealing with neutron interactions for shielding, it is more useful to discuss this in terms of the macroscopic cross section, Σ . On a basic level, this is related to the microscopic cross section via the atomic density of the material in question.

$$\Sigma = N\sigma \tag{B.1}$$

In this thesis, a spacecraft is modeled with a multilayer shield to moderate the photon and neutron flux from the propulsion system. In actual flight design approaches, a shield like this would be optimized for maximum attenuation while minimizing total shield mass. Fast neutron cross sections are low for the most part, and in the case of the multilayer shield, these are slowed down to thermal energies by the use of scattering interactions off of a hydrogen rich material such as what would be used in the first layer. The boron rich material in turn attenuates the slower neutrons. In a simplified form, the fast neutron flux is assumed to decay exponentially such that

$$\phi^1(z) = \phi_0^1 e^{-(\Sigma_s^{1 \rightarrow 2} + \Sigma_c^1)z} \quad (\text{B.2})$$

The thermal neutron flux will behave according to diffusion theory, with neutron scattering from the fast group in Equation B.2 being the source term for the thermal energy group such that

$$D^2 \frac{d^2}{dz^2} \phi^2 - \Sigma_c^2 \phi^2 + \phi_0^1 e^{-(\Sigma_s^{1 \rightarrow 2} + \Sigma_c^1)z} = 0 \quad (\text{B.3})$$

Solving for the differential equation as expressed by Equation B.3,

$$\begin{aligned} \phi^2(z) = & \left(\phi_0^2 - \frac{\phi_0^1 (\Sigma_c^1 + \Sigma_s^{1 \rightarrow 2})}{D^2 (\Sigma_c^1 + \Sigma_s^{1 \rightarrow 2})^2 - \Sigma_c^2} \right) e^{-z \sqrt{\frac{\Sigma_c^2}{D^2}}} \\ & - \frac{\phi_0^1 (\Sigma_c^1 + \Sigma_s^{1 \rightarrow 2})}{D^2 (\Sigma_c^1 + \Sigma_s^{1 \rightarrow 2})^2 - \Sigma_c^2} e^{-(\Sigma_c^1 + \Sigma_s^{1 \rightarrow 2})z} \end{aligned} \quad (\text{B.4})$$

where ϕ_0^1 is the fast flux at reactor/shield interface ($z=0$) and ϕ_0^2 is the thermal flux at reactor/shield interface ($z=0$). Therefore, from Equations B.2 and B.4

$$\phi^1 \sum_{j=1}^i h_j = \phi_{0,i}^1 e^{h_i(-(\Sigma_c^1 + \Sigma_s^{1 \rightarrow 2}))} = \phi_{0,i+1}^1 \quad (\text{B.5})$$

and

$$\begin{aligned} \phi^2 \sum_{j=1}^i h_j = & \left(\phi_{0,i}^2 - \frac{\phi_{0,i}^1 (\Sigma_c^1 + \Sigma_s^{1 \rightarrow 2})}{D^2 (\Sigma_c^1 + \Sigma_s^{1 \rightarrow 2})^2 - \Sigma_c^2} \right) e^{-z \sqrt{\frac{\Sigma_c^2}{D^2}}} \\ & - \frac{\phi_{0,i}^1 (\Sigma_c^1 + \Sigma_s^{1 \rightarrow 2})}{D^2 (\Sigma_c^1 + \Sigma_s^{1 \rightarrow 2})^2 - \Sigma_c^2} e^{-(\Sigma_c^1 + \Sigma_s^{1 \rightarrow 2})z} = \phi_{0,i+1}^2 \end{aligned} \quad (\text{B.6})$$

where $\phi_{0,i}^1$ is the fast flux at the beginning of material region i and $\phi_{0,i}^2$ is the thermal flux at the beginning of material region i . The above equations are sufficient to gather approximations for neutron attenuation, but they are not rigorously correct due to the use

of diffusion theory. Transport theory, such as that used in MCNP, will yield more numerically accurate results [68].

A Mathematica tool has been developed to use the above approximations to create relative attenuation curves through the different materials of a multilayer shield. This tool has its limitations, but it is representative of a slab shield model with a cross sectional area equivalent to a 1 cm² core cut through the entire thickness of the shield. The plotting function is influenced by input parameters that are set up on a sliding scale for shield layer thicknesses, gamma ray energy, ratio of fast neutron flux to thermal neutron flux as well as the ratio of photons produced by neutron interactions [68]. The work done by Polsgrove et al made use of this tool in preliminary sizing for a shield on a z-pinch propulsion system [42]. The configuration and dimensions of each layer in that work form the basis for the analysis in this thesis on the ZShip3 simulations as detailed in Chapters 4 and 5. Figure B.1 details the published screenshot of the attenuation tool in that paper.

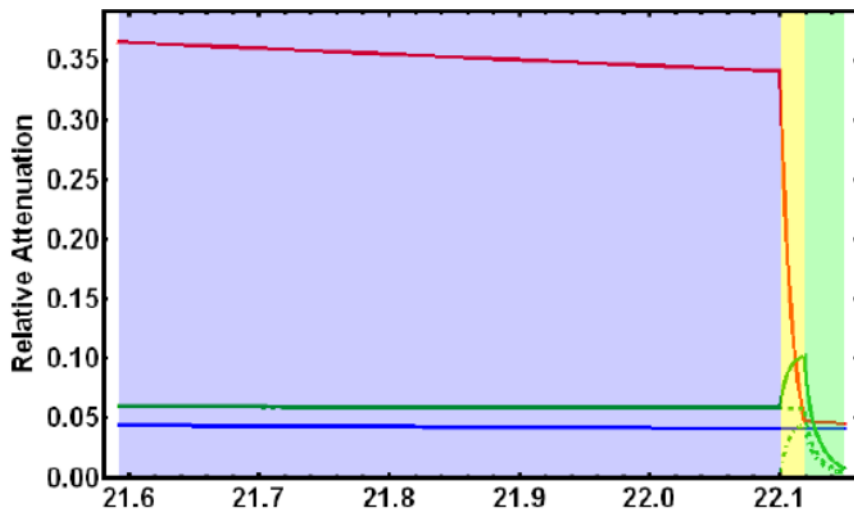


Figure B.1. Screenshot of Mathematica tool results in NASA study [42]

In this diagram the blue line indicates the fast neutrons, the red line indicates the thermal neutrons and the green line indicates the photons. The y-axis shows the attenuation at each point in the x-axis relative to the shield entrance at $x = 0$ cm. The lavender region on this image represents the lithium hydride layer, the yellow region is the boron carbide layer and the green region is the tungsten layer. For the sake of simplicity, the lithium hydride layer will be known as Shield 1, the boron carbide as Shield 2 and the tungsten as Shield 3.

Table B.1. Configuration and dimensions for each shield layer

Layer	Material	Thickness (cm)
Shield 1	Lithium Hydride	22.0
Shield 2	Boron Carbide	0.02
Shield 3	Tungsten	0.025

The ZShip3 model was subjected to multiple simulation runs in order to find dose at the crew cabin, the results of which are covered earlier in this thesis. It was decided to use this same model as the basis neutron verification, and an effort was made to make a model in MCNP that exactly replicates the conditions of the Mathematica tool's model. In parallel, the shield dimensions were entered into the Mathematica tool in an attempt to match the attenuation curves from Figure B.1. The results of this are shown in Figure B.2. In order to match the relative attenuation curves generated by the tool in MCNP, it was decided that a series of step-wise simulations would need to be run in MCNP.

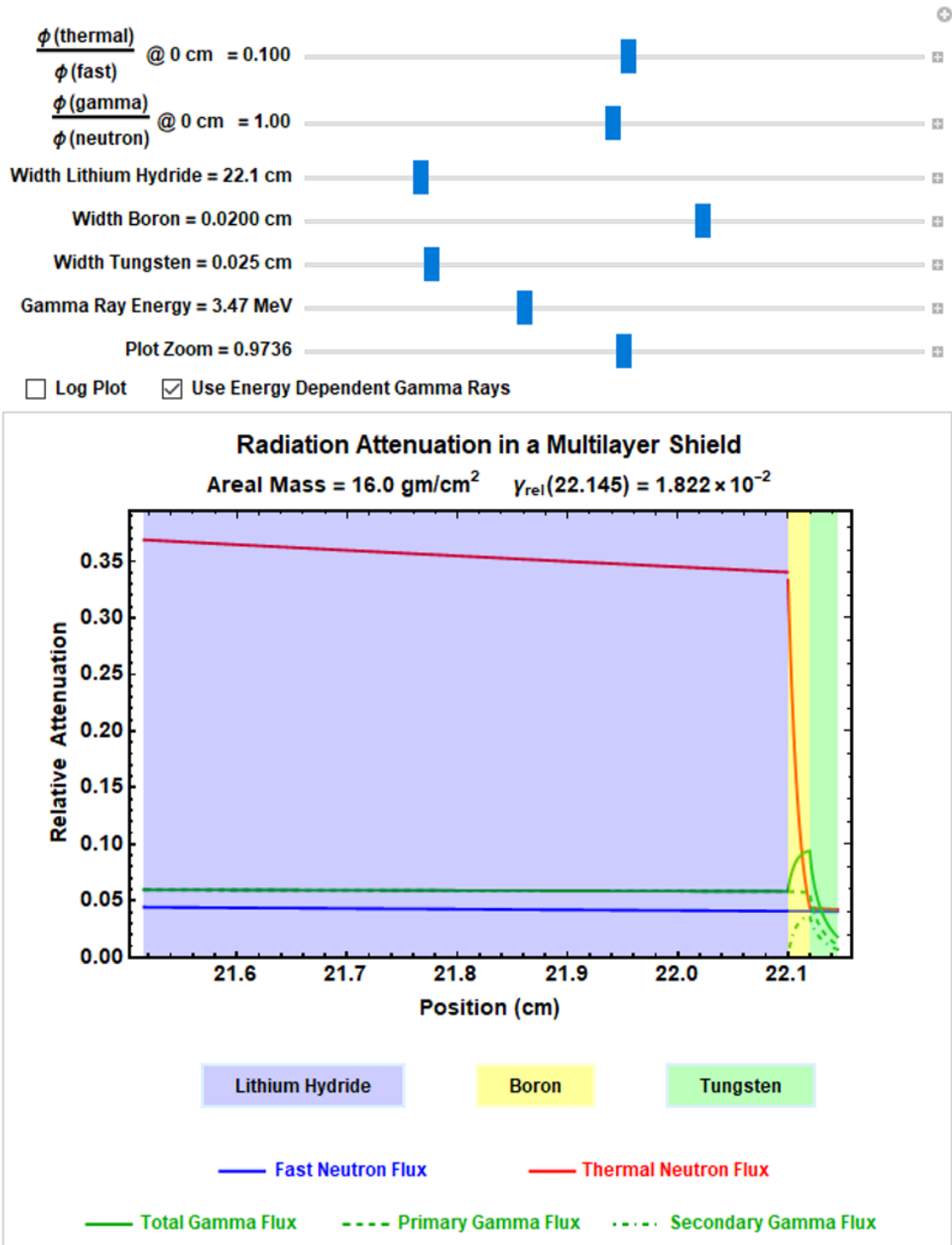


Figure B.2. Screenshot of Mathematica tool with inputs set to match Figure B.1

The relative attenuation curves across the shield layers are not difficult for a tool like Mathematica to generate using relatively simple governing equations, but using MCNP to generate this kind of curve is not so easy. The approach that was made to solving this is the same as the one used in the photon verification modeling and simulation. Each data point on the attenuation curve is the result of an MCNP simulation that is set up to measure the attenuation at a given distance from the shield entrance.

Three basic models were developed for these simulations and these were known as Shield1, Shield12, and Shield123. Each of these models have the same basic geometries, but they also have their own special configurations depending on the distance along the axis from the shield entrance the simulation condition is for. Starting at 50 cm on the model y-axis, the Shield 1 entrance is the reference point for all attenuation and the surface for this in the MCNP model is always Surface 4 and is also considered point 0 on the thickness of the shield. In all of the model configurations, Surface 5 is the Shield 1 to Shield 2 interface, Surface 6 is the Shield 2 to Shield 3 interface, and Surface 7 is the Shield 3 exit.

From 0 cm at the Shield 1 entrance to 22 cm at the Shield 2 interface, all simulations are run using the Shield1 configuration. From 22 cm at the Shield 2 interface to 22.02 cm at the Shield 3 interface, all simulations are run using the Shield12 configuration. From 22.02 cm at the Shield 3 interface to 22.025 cm at the Shield 3 exit, all simulations are run using the Shield123 configuration. In each configuration, the radiation source is modeled as a point isotropic source of neutrons with an energy of 14.1 MeV radiating in all directions. This point is 100 cm from the Shield 1 entrance, and this distance was chosen as a simple 1 meter reference point for inverse square calculations. The physics assumption for all of these configurations is MODE N P, which means that the particles being tracked

are neutrons emitted from the source as well as photons resulting from the neutron interactions in the model.

Each configuration contains seven surfaces and six cells, and the model geometry is that of a narrow cylinder cutting a cross section equal to an area of 1 cm^2 from the source location to the shield and through each layer of the shield. This means that all of the particle tracking happens inside of a 0.5642 cm radius cylinder that is 123.02 cm long. This also mimics the configuration of the multilayer shield in the Mathematica tool. Any particle that goes outside of this cylinder is killed and is no longer tracked. Attenuation is found through measurements taken at tally regions all throughout the model. Each of these are F2 tallies which measure the average particle flux across a surface with units of particles/ cm^2 .

Surface 4 has the F32:N and F42:P tallies assigned to it for neutrons and photons, respectively. Surface 5 has the F52:N and F62:P tallies, Surface 6 has the F72:N and F82:P tallies and Surface 7 has the F92:N and F102:P tallies. To keep the models from getting too complicated and to maintain consistency, a decision was made to have a migrating surface in each model configuration to tally flux at points throughout the shield layers. The Shield1 configuration, shown in Table B.2, has a migrating Surface 5 with Shields 2 and 3 set as vacuum instead of their actual shielding materials. The Shield12 configuration, shown in Table B.3, has a migrating Surface 6 with the Shield 3 material set as vacuum. The Shield123 configuration, shown in Table B.4, moves Surface 7 and all three shield materials are set as their intended materials.

Table B.2. Shield1 configuration

Layer	Material	Start y	Finish y	MCNP Cell
Source Cell	Vacuum	-51	-49	Cell 1
Source Location	Vacuum	-50	-50	Cell 1
99 cm gap	Vacuum	-49	50	Cell 5
Shield 1	Lithium Hydride	50	72	Cell 2
Shield 2	Vacuum	72	72.02	Cell 3
Shield 3	Vacuum	72.02	72.025	Cell 4

Table B.3. Shield12 configuration

Layer	Material	Start y	Finish y	MCNP Cell
Source Cell	Vacuum	-51	-49	Cell 1
Source Location	Vacuum	-50	-50	Cell 1
99 cm gap	Vacuum	-49	50	Cell 5
Shield 1	Lithium Hydride	50	72	Cell 2
Shield 2	Boron Carbide	72	72.02	Cell 3
Shield 3	Vacuum	72.02	72.025	Cell 4

Table B.4. Shield123 configuration

Layer	Material	Start y	Finish y	MCNP Cell
Source Cell	Vacuum	-51	-49	Cell 1
Source Location	Vacuum	-50	-50	Cell 1
99 cm gap	Vacuum	-49	50	Cell 5
Shield 1	Lithium Hydride	50	72	Cell 2
Shield 2	Boron Carbide	72	72.02	Cell 3
Shield 3	Tungsten	72.02	72.025	Cell 4

The migrating surfaces create a shield segment from Shield 1 entry to the point that the measurement is being taken. This forms the basis for each simulation becoming a data point for an attenuation curve to be drawn from. The approach that was taken initially was to set up equally spaced intervals from 0 to 100% of each shield layer thickness, but then

fidelity was increased by running simulations at many other intervals in between. Figure B.3 provides an illustration of the migrating surfaces and how attenuation was determined at each interval step.

An example of this in the Shield1 configuration has simulations that were run with Surface 5 located at 25%, 50%, 75% and 100% of Shield 1 thickness. This created output files with filenames containing the following format for the aforementioned intervals: Shield1_025, Shield1_050, Shield1_075 and Shield1_Full for the 100% configuration. Surface 5 was placed at 5.5 cm into the shield at 25% thickness, 11 cm into the shield at 50% thickness, 16.5 cm into the shield at 75% thickness and 22 cm into the shield at 100% thickness.

The Shield12 configuration was the same approach, but attenuation was measured at Surface 6 placed at percentage thicknesses into Shield 2. The attenuation measured in the Shield12 configuration accounts for the full thickness of Shield 1 in addition to the percentage thickness of Shield 2. The Shield123 configuration does this as well, but the attenuation of the full Shield 1 and Shield 2 are taken into account in addition to the percentage thickness of Shield 3 as measured at Surface 7. Ultimately, the relative attenuation curves were determined through the execution of 59 of these simulations for the initial cut at this problem.

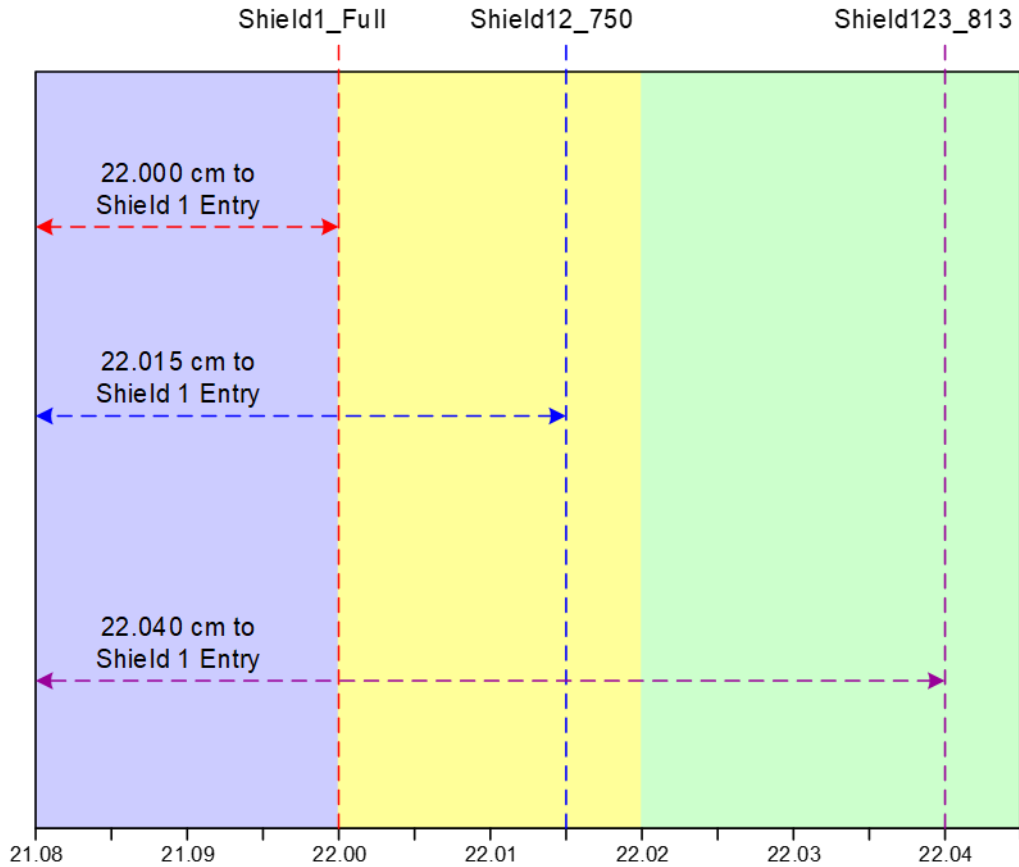


Figure B.3. Illustration of measurement intervals determining attenuation at points through the shield

With these simulations, depending on the particle being tallied as well as its location with the requisite material properties at that location, relative error of the tallies could be rather high. In order to drive the relative errors down into acceptable and easily explainable intervals, each simulation was run with 2 billion particle histories. Depending on the configuration and CPU load at the time, these simulations ran anywhere from 76 minutes to 261 minutes with an average run time of around 145 minutes across all 59 simulations for the initial cut at this problem.

The methodical gathering of data points in the initial cut went through 27 simulations in the Shield1 configuration, 16 simulations in the Shield12 configuration and

16 simulations in the Shield123 configuration. In order to generate a finer mesh at points where a plot would be zoomed in, like in Figure B.2, much tighter intervals were run in the Shield1 configuration in the last 2.5% of the Shield 1 thickness. Between 21.978 cm and 22.0 cm, six evenly spaced simulations were executed covering 99.91% through 99.96% of the shield thickness. Since Shield 2 and 3 are so much thinner in relation to Shield 1, this was deemed appropriate for accurate plotting.

The following is the result of 2 billion particle histories from the output file known as “Shield1_500_a_20181106a”. This simulation placed Surface 5 halfway through the Shield 1 lithium hydride material at 11 cm from the shield entry of Surface 4. As far as this model is concerned, the only material is the lithium hydride and every other cell is vacuum including the cells standing in for Shields 2 and 3. The neutron flux tallies in this case both have very small relative errors, but the photon flux tallies have relative errors much higher. This is due to the small amount of photons that were produced by neutron collisions, the ratio of photons per neutrons being on the order 1.6×10^{-6} .

Table B.5. Neutron flux tallies at Surfaces 4 and 5 in the Shield1_500 configuration

Shield 1 Entry		F32:N		Shield 1/2 Interface		F52:N	
Surface 4		Statistical Tests		Surface 5		Statistical Tests	
Tally 32	Relative Error	Passed	Missed	Tally 52	Relative Error	Passed	Missed
[n/cm ²]				[n/cm ²]			
5.37987E-06	0.0079	9	1	8.19868E-07	0.0099	8	2

Table B.6. Photon flux tallies at Surfaces 4 and 5 in the Shield1_500 configuration

Shield 1 Entry		F42:P		Shield 1/2 Interface		F62:P	
Surface 4		Statistical Tests		Surface 5		Statistical Tests	
Tally 42	Relative Error	Passed	Missed	Tally 62	Relative Error	Passed	Missed
[p/cm2]				[p/cm2]			
5.61347E-09	0.2126	7	3	6.43203E-10	0.3176	7	3

The following is the result of 2 billion particle histories from the output file known as “Shield12_750_a_20181029a”. In this simulation, Surface 6 is placed three-quarters of the way through the boron carbide material of Shield 2 at a distance of 22.015 cm from the shield entry of Surface 4. In this model, Shield 1 and Shield 2 both have their requisite materials and every other cell is vacuum. Again, the neutron flux tallies have very acceptable relative errors while the photon flux tally at Surface 6 is considered to be garbage data. The ratio of photons produced per neutron collision in this configuration is 7.65×10^{-7} .

Table B.7. Neutron flux tallies at Surfaces 4 and 6 in the Shield12_750 configuration

Shield 1 Entry		F32:N		Shield 2/3 Interface		F72:N	
Surface 4		Statistical Tests		Surface 6		Statistical Tests	
Tally 32	Relative Error	Passed	Missed	Tally 72	Relative Error	Passed	Missed
[n/cm2]				[n/cm2]			
5.37679E-06	0.0079	10	0	7.18958E-08	0.0327	9	1

Table B.8. Photon flux tallies at Surfaces 4 and 6 in the Shield12_750 configuration

Shield 1 Entry		F42:P		Shield 2/3 Interface		F82:P	
Surface 4		Statistical Tests		Surface 6		Statistical Tests	
Tally 42	Relative Error	Passed	Missed	Tally 82	Relative Error	Passed	Missed
[p/cm2]				[p/cm2]			
3.90417E-09	0.1613	7	3	8.42775E-11	1	7	3

The following is the result of 2 billion particle histories from the output file known as “Shield123_500_a_20181028a”. In this simulation, Surface 7 is placed halfway through the tungsten material of Shield 3 at a distance of 22.0325 cm from the shield entry of Surface 4. In this model, all three shields have their requisite materials with all other cells being vacuum. The neutron flux tallies in this simulation all have very low relative errors while the photon flux tallies have very high relative errors. The ratio of photons produced per neutron collision in this configuration is 6.91×10^{-7} .

Table B.9. Neutron flux tallies at Surfaces 4 and 7 in the Shield123_500 configuration

Shield 1 Entry		F32:N		Shield 3 Exit		F92:N	
Surface 4		Statistical Tests		Surface 7		Statistical Tests	
Tally 32	Relative Error	Passed	Missed	Tally 92	Relative Error	Passed	Missed
[n/cm2]				[n/cm2]			
5.37563E-06	0.0079	8	2	7.12902E-08	0.0365	9	1

Table B.10. Photon flux tallies at Surfaces 4 and 7 in the Shield123_500 configuration

Shield 1 Entry		F42:P		Shield 3 Exit		F102:P	
Surface 4		Statistical Tests		Surface 7		Statistical Tests	
Tally 42	Relative Error	Passed	Missed	Tally 102	Relative Error	Passed	Missed
[p/cm2]				[p/cm2]			
3.85625E-09	0.1607	7	3	5.74041E-10	0.5934	5	5

For each interval of shield thickness, the particle flux tallies provide intensities accurate to within their respective relative errors. In each case, the Shield 1 Entry is the reference point as Tally 32 for neutrons and Tally 42 for photons. This is 100 cm from the radiation source and is set as point zero for the shield thickness. Depending on the model configuration, tallies throughout the shield thickness are measured from different surfaces. Attenuation at the interval is found by dividing the appropriate model tally by the reference tally for photons and neutrons. Since the scope of this problem concerns neutrons more than photons and the relative errors of the photon tallies are all in the questionable to unusable categories, only neutron attenuation will be plotted. Attenuations for both particle sets were calculated, but the extremely low number of photons causes the accuracy of their plots to be questionable.

The tolerance stackup due to relative error on the tallies needs to be taken into account when the attenuation is calculated. For each tally the upper and lower bounds of the attenuation tolerance were found. For each interval, the upper and lower bounds of the particle flux for each tally were calculated. The lower and upper bounds for the attenuation in each interval were found by dividing the lower bound of the shield depth tally by the upper bound of the shield entry tally for the lower bound of attenuation. The upper

attenuation bound for each interval was found by dividing the upper bound of the shield depth tally by the lower bound of the shield entry tally. The following example illustrates this process for “Shield1_500_a_20181106a”.

Table B.11. Tally values for Shield1_500_a_20181106a

Tally 32	Relative Error	Tally 52	Relative Error
[neutrons/cm ²]		[neutrons/cm ²]	
5.37987E-06	0.0079	8.19868E-07	0.0099
Tally 42	Relative Error	Tally 62	Relative Error
[photons/cm ²]		[photons/cm ²]	
5.61347E-09	0.2126	6.43203E-10	0.3176

Taking the median tally values shown in Table B.11, the Relative Attenuation can be found for both the neutrons and the photons.

Table B.12. Relative attenuations found from median tally values

Shield 1 Neutron Relative Attenuation	Shield 1 Photon Relative Attenuation
0.152395504	0.114582068

The upper and lower bounds of the tallies are found through the following relations:

$$T_L = T - (T\bar{R}) \quad (\text{B.7})$$

$$T_L = T - (T\bar{R}) \quad (\text{B.8})$$

with T_L = the lower tally bound, T_U = the upper tally bound, T = the median tally value, and \bar{R} = the relative error of the tally. Using the above equations, the following table shows the upper and lower bounds of the tallies for both the photons and the neutrons.

Table B.13. Upper and lower bounds for tally values in Shield1_500_a_20181106a

Tally 32		Tally 52	
Lower	Upper	Lower	Upper
[neutrons/cm ²]	[neutrons/cm ²]	[neutrons/cm ²]	[neutrons/cm ²]
5.33737E-06	5.42237E-06	8.11751E-07	8.27985E-07
Tally 42		Tally 62	
Lower	Upper	Lower	Upper
[photons/cm ²]	[photons/cm ²]	[photons/cm ²]	[photons/cm ²]
4.42005E-09	6.80689E-09	4.38922E-10	8.47484E-10

Now that the upper and lower tally values have been established, the upper and lower bounds for attenuation can be found.

Table B.14. Upper and lower bounds of attenuation Shield1_500_a_20181106a

Surface 5/4 Neutron Attenuation		Surface 5/4 Photon Attenuation	
Lower	Upper	Lower	Upper
0.149704126	0.155129744	0.064481942	0.191736516

Each simulation result is subjected to the above analysis and tabulated. These results become the data points for the plots of relative attenuation as a function of shield depth.

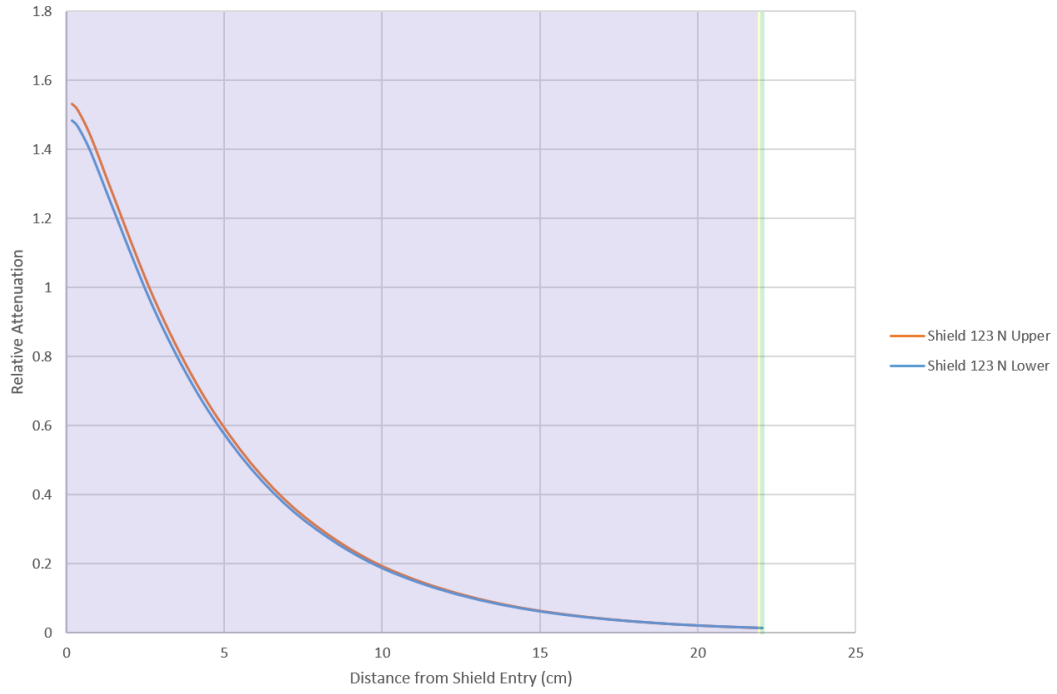


Figure B.4. Neutron attenuation through multilayer shield upper and lower bounds

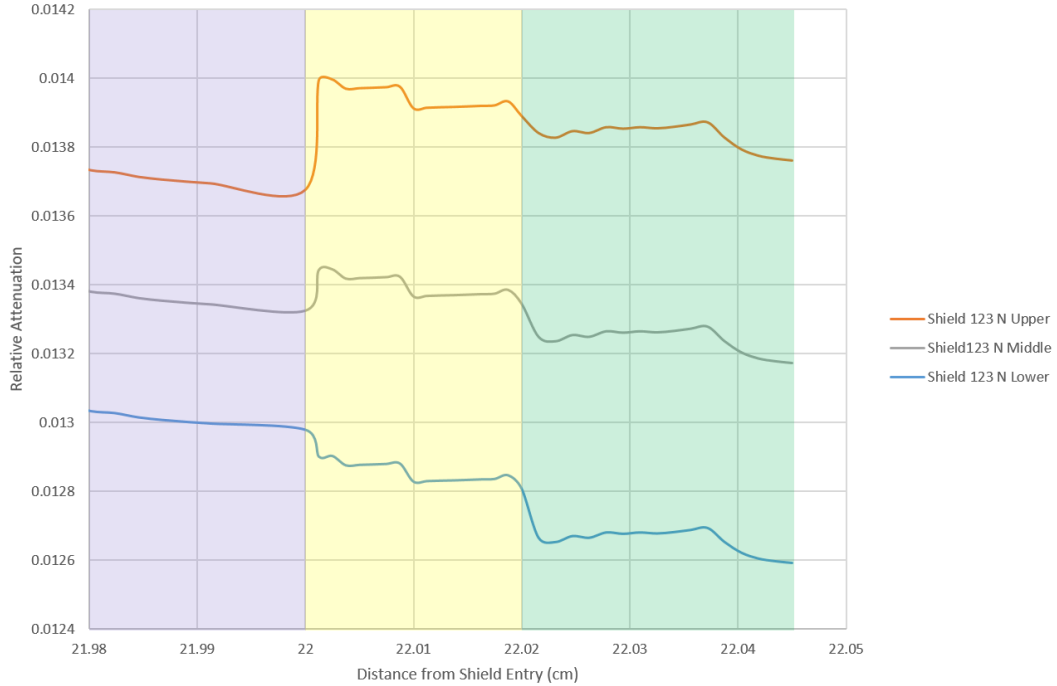


Figure B.5. Neutron attenuation detail on Shield 1 - Shield 2- Shield 3 interface region

The attenuation curves generated from the MCNP data runs show a smooth regression from around a 1.5 relative attenuation at shield entry down to around 0.013 at shield exit. Figure B.5 shows the attenuation upper and lower bounds as well as the mean in the region that joins all three shield layers. With these curves in hand, an attempt was made to match them using the Mathematica tool. Figure B.6 shows the extent to which the tool was used in order to generate the closest possible match. The blue curve of the fast neutron flux shows a similar shape but slightly different magnitude to the neutron attenuation illustrated in Figure B.4.

The MCNP attenuation starts at around 1.5 while the Mathematica attenuation starts at 1.0 for the fast neutron flux. A trend that has been noted with the Mathematica tool is that in this configuration, if the ratio of thermal to fast neutrons is maximized at 0.800, the fast neutron relative attenuation starts at around 0.55 at shield entry. The minimum thermal to fast neutron ratio on this tool is 0.010, and in this case the relative attenuation starts at 1. The ratio of gammas produced by neutron interactions has the lowest extent in the tool at 0.1, but the MCNP results yield an average ratio of 1×10^{-6} . If the Mathematica tool had lower limits in both of these ratios, one has to wonder if the starting relative attenuation change again and trend towards values more consistent with the MCNP results.

In comparing Figure B.5 to the Mathematica results zoomed in on the three shield region in Figure B.7, there is a closer agreement in relative attenuation between the two graphs. The fast neutron flux attenuation in the Mathematica tool is around 0.04 and trending upward ever so slightly in Shield 2 and 3. The MCNP results show a downward trend across all three shields punctuated by a slight upward trend in Shield 2 before trending downward in Shield 3 in the median and upper limits of attenuation. It is notable that on

the upper attenuation limit in Figure B.5, the relative attenuation is slightly higher at the Shield 3 exit than at $x = 21.98$ in Shield 1. This is similar to Figure B.7, but with the magnitude at around 0.014 instead of a 0.4 relative attenuation.

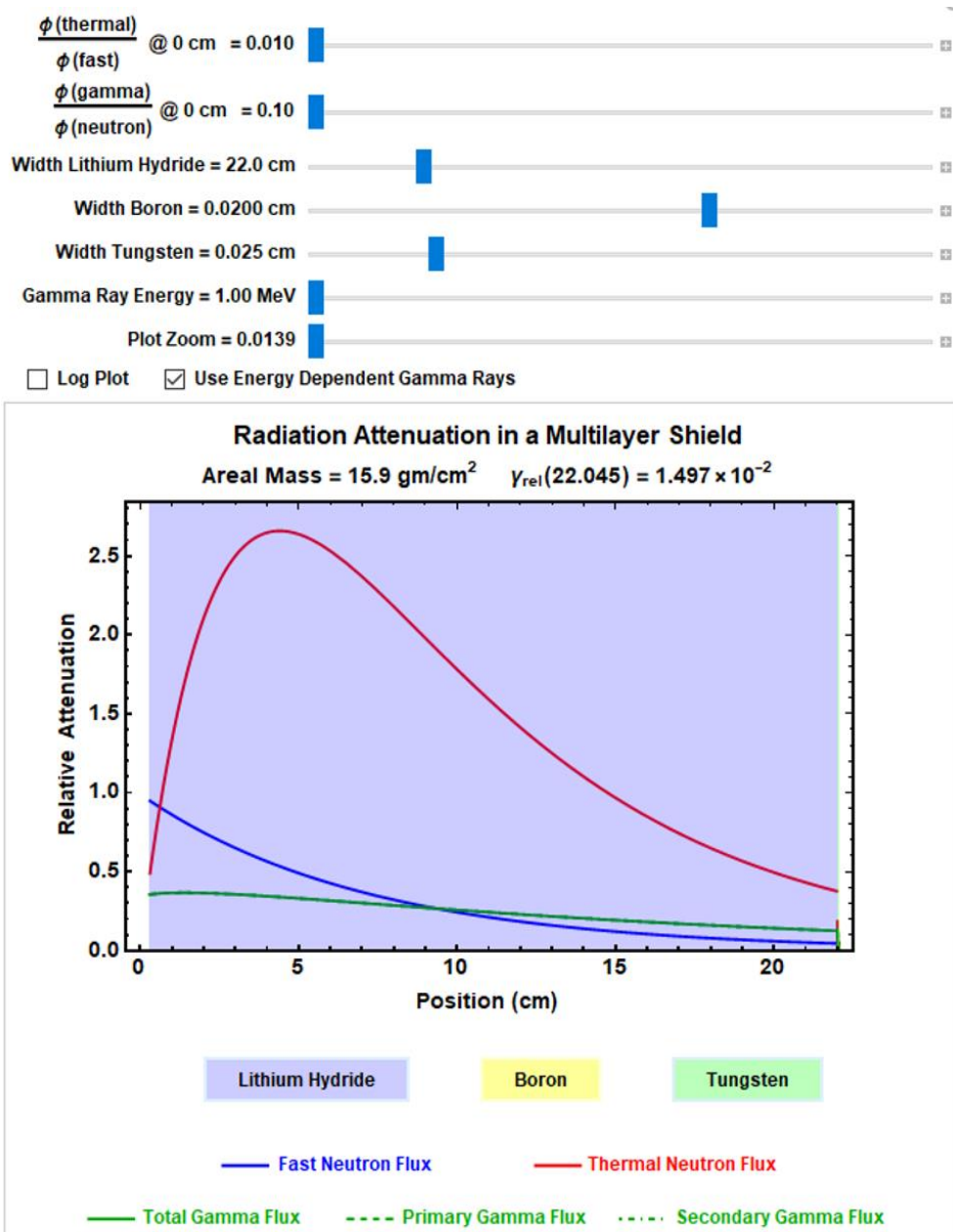


Figure B.6. Mathematica tool closest match to MCNP curves

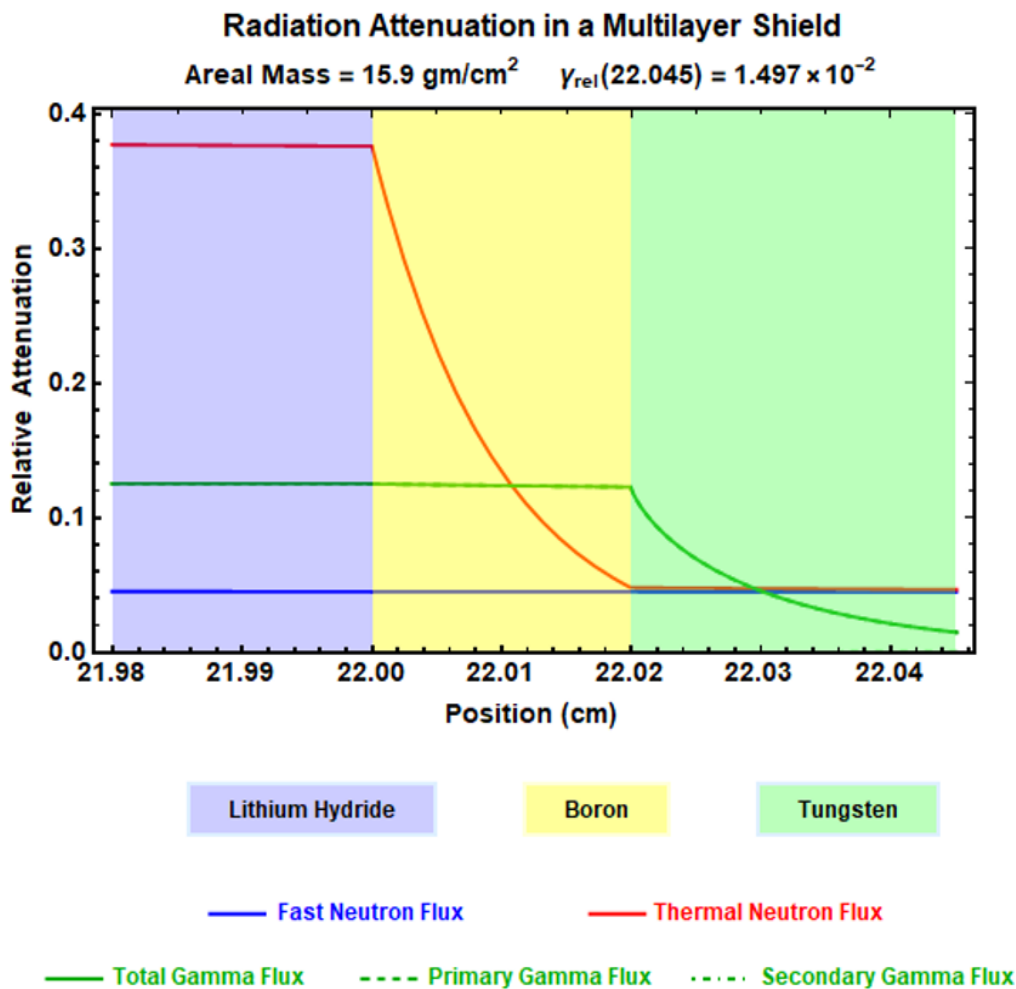


Figure B.7. Zoom in on the Shield 1 - Shield 2 - Shield 3 region on the Mathematica tool

It seems counter-intuitive that attenuation relative to shield entry should be anything other than 1 at shield entry. In fact, in the initial cut of the MCNP runs, there is a gap in the first 0.017 cm of shield thickness since the first data point is 8% through the thickness of Shield 1. This gap can lead one to wonder if additional simulations were run to close that gap and capture data points in the first 7% of shield thickness if the behavior of the relative attenuation would change. In spite of the differences in magnitude though, it is noteworthy to consider that the shapes of the curves are very similar between the MCNP results and the fast neutron curve in the Mathematica tool.

When considering the fact that the governing equations in the Mathematica tool generate approximations, an interesting case study can be made comparing the difference that intense Monte Carlo simulations for each data point can make. Much more time could be spent running additional simulations to generate a finer mesh in data points available to be plotted, and this would seem to allow for more accurate representations of relative attenuation. Kicking particle histories higher and accepting longer run times would also yield more accurate results, if these particle histories were made large enough the relative errors of the photon results would be driven down as well. 59 total data points seems like a small amount when the circumstances of their generation are not taken into account. To this end, another series of simulations were run in a second cut that occurred well over a year after the initial cut was performed. This was attempt to close the gaps that were identified and further explore the potential for this technique that has been developed to find relative attenuation.

The additional simulations that were run led to a new total of 116 data points to be plotted. The distribution between the different shield layers then became 52 data points for Shield 1, 32 data points for Shield 2, and 32 data points for Shield 3. A heavy focus was on the gap between the shield entry and the first data point of the initial cut as well as a more intense look at the transition zones in the shield interface regions. This led to a smoothing of lines in the curves and a new wrinkle in the relative attenuation in the initial gap after shield entry as well as new details in the shield interface regions.

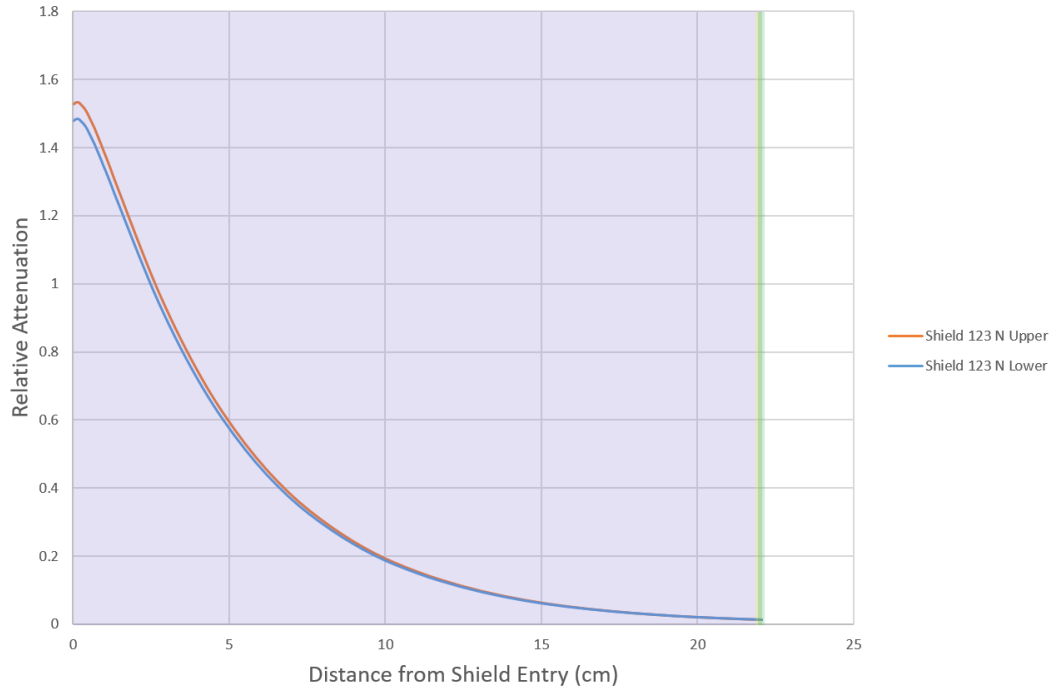


Figure B.8. Upper and lower bound neutron attenuation curves from second cut

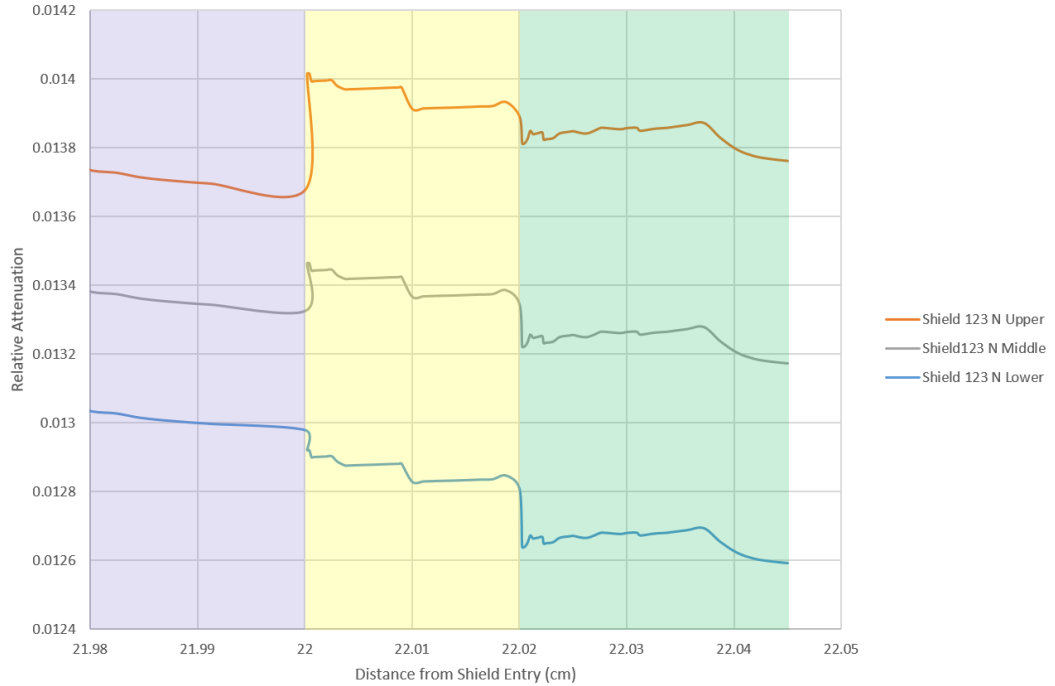


Figure B.9. Shield interface region neutron attenuation from second cut

The additional detail in these plots demonstrates the challenges of relying on plots with limited data points, for when additional data points are added some parts of these curves can change drastically. In Figure B.8, the gap was filled in the first seven percent of the thickness of Shield 1 when compared to the previous version. The immediate detail that pops out is the relative attenuation starting lower than initially shown and having a peak before beginning the regressive tail-off the further into the shield thickness. This plot is hardly conclusive since there is still a gap between shield entry and the first data point. An exercise could be done to zoom into finer and finer detail to see exactly where the relative attenuation really begins.

When zooming into the interface regions between the three shield layers as shown in Figure B.9, the additional data points drastically change the shape of each curve at the interfaces as a finer mesh was created across all three layers. One thing that readily becomes apparent is that the transitions become more abrupt in attenuation at each interface the finer the mesh becomes. The magnitudes do not change at these transitions, but the actual transitions start to resemble cliffs instead of slopes. When compared to the curves generated in the Mathematica tool in the same transition zone, these jumps in magnitude are not as apparent. This might also be due to a lower resolution on the plot in that tool. It appears that in general, there is strong agreement between MCNP and the Mathematica tool when it comes to the general shape of attenuation curves. Magnitudes seem to be different, and it would be an interesting exercise to attempt to increase the fidelity of secondary photon production to see how the curves are affected with MCNP results. Otherwise, the Mathematica tool itself may need some tweaking as the photon production ratios found in MCNP are orders of magnitude smaller than is available on the slider in the

Mathematica tool. How would the plots appear in this tool if the option were given to drive this ratio down to the level that is being found by MCNP in the Mode NP physics assumption? Further work is needed, especially with the MCNP side in driving down relative errors on the photon tallies. There are limitations on the Mathematica side of this since there is a narrow range of energy levels and particle ratios that are able to yield accurate approximations for this attenuation.

After initial review of the data presented in this appendix, an error was found by Emrich with a typo in the tungsten attenuation coefficient correlation used by the Mathematica tool. A revision was made to this calculator and as a check against previous results, the plot from Figures B.6 and B.7 was replicated using the newest version of the tool. Shown in Figures B.10 and B.11, these new curves have shapes almost identical to the original ones until they get into the transition region of the tungsten layer. In the zoomed plot at the transition zone, the neutron attenuation curves are largely unchanged from the previous version. The photon attenuation however has changed significantly; instead of a rapid drop off in attenuation starting with the beginning of the tungsten layer, the slope of the curve steepens and declines much less drastically. This seems to be reasonable since the attenuation coefficients for the photons are much more accurate in correlation than they are for the neutrons. A conclusion can be reached that this new iteration of the Mathematica calculator is more accurate than the previous one now that the typo has been fixed. Further study to go hand in hand with new MCNP runs could improve this tool as well, especially if the MCNP runs were to be constrained to the calculator's limits.

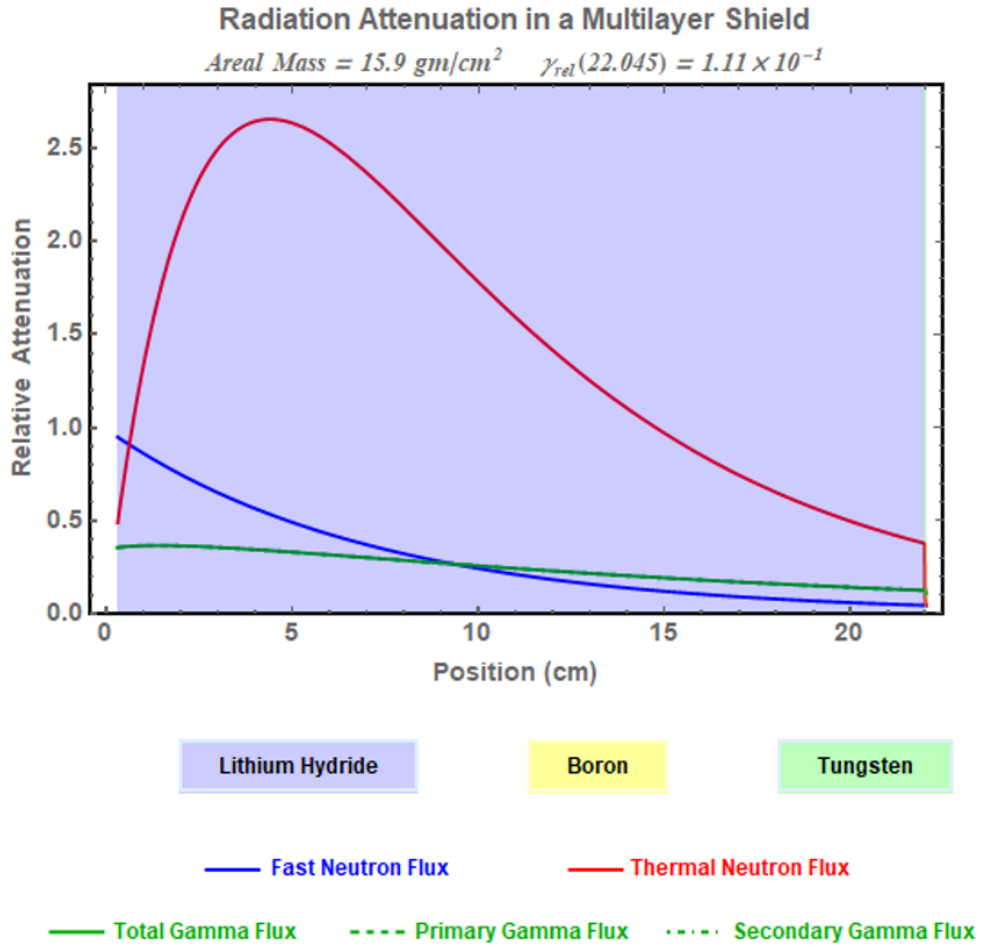


Figure B.10. Revised Mathematica tool closest match to MCNP curves

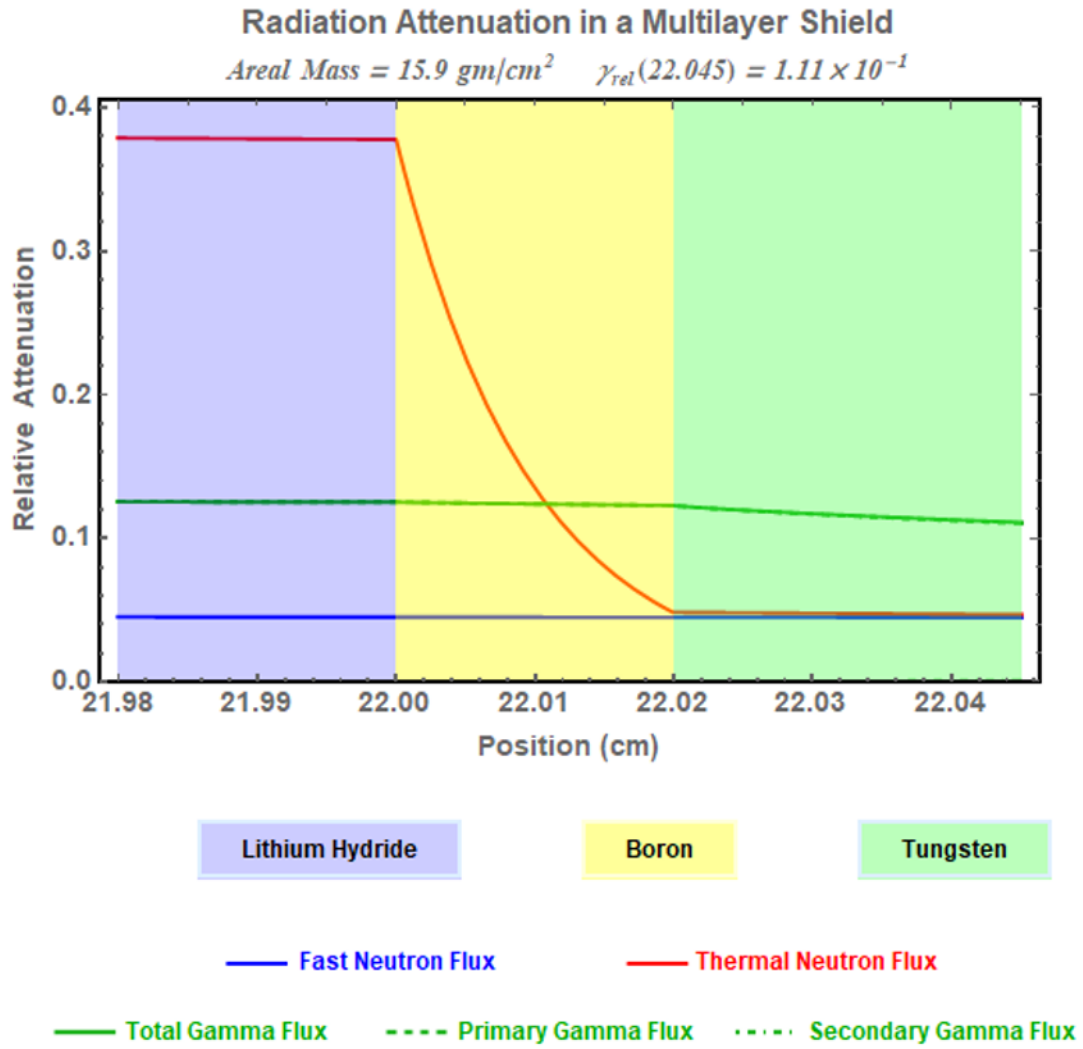


Figure B.11. Zoom in on the Shield 1 - Shield 2 - Shield 3 region on the revised Mathematica tool

Table B.15. Data points gathered from MCNP simulations for Appendix B

Surface Location			File Name	Combined Attenuation	
5	6	7		Lower	Upper
[cm]	[cm]	[cm]			
0.0220	22.02	22.045	Shield1_001_a_20191118a	1.4799746	1.527489569
0.0440	22.02	22.045	Shield1_002_a_20191118a	1.482575631	1.530174107
0.0660	22.02	22.045	Shield1_003_a_20191118a	1.483845771	1.531485024
0.0880	22.02	22.045	Shield1_004_a_20191118a	1.484478527	1.532138095
0.1100	22.02	22.045	Shield1_005_a_20191118a	1.485165885	1.532847521
0.1320	22.02	22.045	Shield1_006_a_20191119a	1.485249789	1.532934119
0.1540	22.02	22.045	Shield1_007_a_20191119a	1.485043886	1.532721605
0.1719	22.02	22.045	Shield1_008_a_20181107a	1.484522975	1.53218397
0.1870	22.02	22.045	Shield1_0085_a_20191119a	1.483595973	1.531227207
0.1980	22.02	22.045	Shield1_009_a_20191120a	1.482997434	1.530609452
0.2200	22.02	22.045	Shield1_010_a_20191120a	1.481055533	1.528605205
0.3300	22.02	22.045	Shield1_015_a_20191120a	1.470555394	1.517767956
0.3438	22.02	22.045	Shield1_016_a_20181107a	1.468964832	1.516126329
0.4400	22.02	22.045	Shield1_020_a_20191120a	1.455555399	1.502286383
0.6600	22.02	22.045	Shield1_030_a_20191121a	1.414717091	1.460429025
0.6875	22.02	22.045	Shield1_031_a_20181107a	1.409330063	1.454867933
0.8800	22.02	22.045	Shield1_040_a_20191121a	1.367025046	1.411195969
0.9900	22.02	22.045	Shield1_045_a_20191121a	1.341737234	1.385091064
1.0316	22.02	22.045	Shield1_047_a_20181107a	1.333014127	1.376086098
1.2100	22.02	22.045	Shield1_055_a_20191122a	1.29159958	1.333333377
1.3750	22.02	22.045	Shield1_063_a_20181029a	1.251880939	1.292331358
2.7500	22.02	22.045	Shield1_125_a_20181029a	0.941616808	0.972430982
4.1250	22.02	22.045	Shield1_188_a_20181029a	0.697102791	0.720203349
5.5000	22.02	22.045	Shield1_250_a_20181029a	0.513382042	0.530606686
6.8750	22.02	22.045	Shield1_313_a_20181029a	0.376173305	0.388949976
8.2500	22.02	22.045	Shield1_375_a_20181029a	0.277192361	0.286779188
9.6250	22.02	22.045	Shield1_438_a_20181029a	0.20261702	0.209750447
11.0000	22.02	22.045	Shield1_500_a_20181106a	0.149704126	0.155129744
12.3750	22.02	22.045	Shield1_563_a_20181029a	0.110249715	0.11435973
13.7500	22.02	22.045	Shield1_625_a_20181029a	0.080783912	0.083879314
15.1250	22.02	22.045	Shield1_688_a_20181029a	0.05916724	0.061471231
16.5000	22.02	22.045	Shield1_750_a_20181101b	0.043775396	0.045552859
17.8750	22.02	22.045	Shield1_813_a_20181029a	0.032220935	0.033596375
19.2500	22.02	22.045	Shield1_875_a_20181029a	0.023673329	0.024743214
20.6250	22.02	22.045	Shield1_938_a_20181029a	0.017563524	0.018427191
21.9560	22.02	22.045	Shield1_998_a_20191122a	0.013110341	0.013812937

21.9582	22.02	22.045	Shield1_9981_a_20191122a	0.013105689	0.013808036
21.9604	22.02	22.045	Shield1_9982_a_20191122a	0.013100517	0.013805348
21.9626	22.02	22.045	Shield1_9983_a_20191123a	0.013095865	0.013800446
21.9648	22.02	22.045	Shield1_9984_a_20191123a	0.01309029	0.013794571
21.9670	22.02	22.045	Shield1_9985_a_20191123a	0.013085656	0.013789688
21.9692	22.02	22.045	Shield1_9986_a_20191123a	0.013081004	0.013784786
21.9714	22.02	22.045	Shield1_9987_a_20191123a	0.013076371	0.013779903
21.9736	22.02	22.045	Shield1_9988_a_20191123a	0.013071737	0.01377502
21.9780	22.02	22.045	Shield1_999_a_20181108a	0.013051591	0.013753791
21.9802	22.02	22.045	Shield1_9991_a_20181107a	0.01303217	0.013733324
21.9824	22.02	22.045	Shield1_9992_a_20181107a	0.013026613	0.013727469
21.9846	22.02	22.045	Shield1_9993_a_20181108a	0.013014124	0.013714308
21.9868	22.02	22.045	Shield1_9994_a_20181108a	0.013006685	0.013706468
21.9890	22.02	22.045	Shield1_9995_a_20181108a	0.013001128	0.013700612
21.9912	22.02	22.045	Shield1_9996_a_20181108a	0.012996512	0.013695748
22.0000	22.02	22.045	Shield1_Full_a_20181029a	0.012978376	0.013676636
22	22.00020	22.045	Shield12_010_a_20191118a	0.012919955	0.014015963
22	22.00040	22.045	Shield12_020_a_20191118a	0.01292024	0.014016272
22	22.00060	22.045	Shield12_030_a_20191118a	0.012899698	0.013993987
22	22.00080	22.045	Shield12_040_a_20191118a	0.012900001	0.013994316
22	22.00100	22.045	Shield12_050_a_20191118a	0.012900287	0.013994626
22	22.00120	22.045	Shield12_060_a_20191119a	0.012900572	0.013994936
22	22.00125	22.045	Shield12_063_a_20181028a	0.012900644	0.013995013
22	22.00140	22.045	Shield12_070_a_20191119a	0.012900858	0.013995246
22	22.00170	22.045	Shield12_085_a_20191119a	0.012901233	0.013995652
22	22.00180	22.045	Shield12_090_a_20191120a	0.012901375	0.013995807
22	22.00200	22.045	Shield12_100_a_20191120a	0.012901661	0.013996117
22	22.00250	22.045	Shield12_125_a_20181028a	0.012902375	0.013996891
22	22.00300	22.045	Shield12_150_a_20191120a	0.012886937	0.013980143
22	22.00375	22.045	Shield12_188_a_20181028a	0.012875129	0.013970131
22	22.00400	22.045	Shield12_200_a_20191120a	0.012875325	0.013970344
22	22.00500	22.045	Shield12_250_a_20181029a	0.012876431	0.013971544
22	22.00600	22.045	Shield12_300_a_20191121a	0.012877484	0.013972687
22	22.00625	22.045	Shield12_313_a_20181028a	0.012877681	0.0139729
22	22.00750	22.045	Shield12_375_a_20181029a	0.01287918	0.013974526
22	22.00800	22.045	Shield12_400_a_20191121a	0.012879786	0.013975185
22	22.00875	22.045	Shield12_438_a_20181028a	0.012880393	0.013975843
22	22.00900	22.045	Shield12_450_a_20191121a	0.012880697	0.013976172
22	22.01000	22.045	Shield12_500_a_20181029a	0.012827831	0.013913238
22	22.01100	22.045	Shield12_550_a_20200122a	0.012829116	0.013914632
22	22.01125	22.045	Shield12_563_a_20181028a	0.012829437	0.01391498

22	22.01250	22.045	Shield12_625_a_20181028a	0.012830686	0.013916335
22	22.01375	22.045	Shield12_688_a_20181028a	0.012831543	0.013917264
22	22.01500	22.045	Shield12_750_a_20181029a	0.012832882	0.013918716
22	22.01625	22.045	Shield12_813_a_20181028a	0.012834381	0.013920342
22	22.01750	22.045	Shield12_875_a_20181028a	0.012835684	0.013921755
22	22.01875	22.045	Shield12_938_a_20181106a	0.012846322	0.013933294
22	22.02	22.045	Shield12_Full_a_20181028a	0.01280725	0.013890916
22	22.02	22.02025	Shield123_010_a_20191118a	0.01263842	0.013812502
22	22.02	22.02050	Shield123_020_a_20191118a	0.012639771	0.013813979
22	22.02	22.02075	Shield123_030_a_20191118a	0.012651206	0.013826476
22	22.02	22.02100	Shield123_040_a_20191118a	0.012672048	0.013849254
22	22.02	22.02125	Shield123_050_a_20191119a	0.012663441	0.013839848
22	22.02	22.02150	Shield123_060_a_20191119a	0.012664721	0.013841247
22	22.02	22.02156	Shield123_063_a_20181028a	0.012665041	0.013841597
22	22.02	22.02175	Shield123_070_a_20191119a	0.012666037	0.013842685
22	22.02	22.02213	Shield123_085_a_20191119a	0.012667744	0.013844551
22	22.02	22.02225	Shield123_090_a_20191120a	0.012648592	0.013823619
22	22.02	22.02250	Shield123_100_a_20191120a	0.012649872	0.013825018
22	22.02	22.02313	Shield123_125_a_20181028a	0.012652619	0.01382802
22	22.02	22.02375	Shield123_150_a_20191120a	0.012665575	0.01384218
22	22.02	22.02469	Shield123_188_a_20181028a	0.012669922	0.01384693
22	22.02	22.02500	Shield123_200_a_20191120a	0.012671149	0.013848271
22	22.02	22.02625	Shield123_250_a_20181028a	0.01266512	0.013841683
22	22.02	22.02750	Shield123_300_a_20191121a	0.012679507	0.013857406
22	22.02	22.02781	Shield123_313_a_20181028a	0.012680431	0.013858416
22	22.02	22.02938	Shield123_375_a_20181028a	0.012676572	0.013854199
22	22.02	22.03000	Shield123_400_a_20191121a	0.012679507	0.013857406
22	22.02	22.03094	Shield123_438_a_20181028a	0.012680431	0.013858416
22	22.02	22.03125	Shield123_450_a_20191121a	0.012672287	0.013849515
22	22.02	22.03250	Shield123_500_a_20181028a	0.012677533	0.013855249
22	22.02	22.03375	Shield123_550_a_20191122a	0.012680218	0.013858183
22	22.02	22.03406	Shield123_563_a_20181027a	0.012681427	0.013859505
22	22.02	22.03563	Shield123_625_a_20181027a	0.012687669	0.013866326
22	22.02	22.03719	Shield123_688_a_20181027b	0.012693448	0.013872643
22	22.02	22.03875	Shield123_750_a_20181027a	0.012652903	0.013828331
22	22.02	22.04031	Shield123_813_a_20181027b	0.012621712	0.013794242
22	22.02	22.04188	Shield123_875_a_20181027b	0.0126048	0.013775759
22	22.02	22.04344	Shield123_938_a_20181027b	0.012597047	0.013767286
22	22.02	22.04500	Shield123_Full_a_20181027c	0.012592068	0.013761844

APPENDIX C: EXAMPLE INPUT DECKS

Input Deck: ChargerLab50

Simplified Version of ChargerLab50

c mcnp6 i=ChargerLab50.txt o=ChargerLab50_20181110d.txt

```
c ***** Block 1: Cells *****
  1      4      -1e-6      -1      $D-T, D-D Primary Reaction
  2      2      -1.0      -9      $ICRU Sphere in front of wall
  3      1      -2.35      4 -5 -3      $concrete wall
  4      2      -1.0      -7      $ICRU Sphere 1m from source
  5      2      -1.0      -8      $ICRU Sphere behind wall
  6      3 -1.20484E-3 #1 #2 #3 #4 #5 2 -6 -3 $air
  7      0      0      #6      $problem boundary
```

```
c ***** Block 2: Surface Cards *****
  1      sy -7620 2
  2      py -7635
  3      cy 129.9
  4      py 7620
  5      py 7680.96
  6      py 7710.96
  7      s 0 -7620 114.9 15
  8      sy 7695.96 15
  9      s 0 7605 -30 15
```

```
c ***** Block 3: Data Cards *****
mode n p
```

c *****

```
c Concrete, density = 2.35g/cm^3
m1 1001.70c -0.005558 $concrete (ordinary with ENDF-VI)
    8016.70c -0.498076 11023.70c -0.017101 12024.70c -0.001999
    12025.70c -0.000264 12026.70c -0.000302 13027.70c -0.045746
    14028.70c -0.289486 14029.70c -0.015181 14030.70c -0.010425
    16032.70c -0.001216 16033.70c -1e-005 16034.70c -5.7e-005
    19039.70c -0.01788 19040.70c -2e-006 19041.70c -0.001357
    20040.70c -0.08019 20042.70c -0.000562 20043.70c -0.00012
    20044.70c -0.00188 20046.70c -4e-006 20048.70c -0.000186
    26054.70c -0.000707 26056.70c -0.01139 26057.70c -0.000265
    26058.70c -3.6e-005
```

c *****

```
c ICRU Soft Tissue, Four Component, density = 1.00 g/cm^3
```

```
m2 1001.70c -0.101172 $tissue,
    6000.70c -0.111000
    7014.70c -0.026000 8016.70c -0.761828
```

c *****

```
c ICRP Air, density = 1.20484E-3 g/cm^3
```

```
m3 7014.70c -0.755636 $air (US S. Atm at sea level)
    8016.70c -0.231475 18000.35c -0.012889
```

c *****

```
c D-T, D-D Plasma density = 1e-6 g/cm^3
```

```
m4 1002.70c -0.250000 $Deuterium Tritium
    1003.70c -0.250000 2003.70c -0.250000 2004.70c -0.250000
```

c *****

```
c Importance
```

```
c      1      2      3      4      5      6      7
IMP:n 1      8      4      5      9      3      0      $1 - 7
```

```
c
IMP:p 1      8      4      5      9      3      0      $1 - 7
```

c *****

```

c --- Point Isotropic Source, 14.1 MeV Neutrons
c   Particles in all directions
C
SDEF POS=0 -7620 0 CEL=1 PAR=1 ERG=d1
SP1 -4 -14.1 -1
phys:p 100 0 0 0 0
phys:n 100 50
NPS 3000000000
c *****
c Forced Collisions
c   1   2   3   4   5   6   7
FCL:n 0 -1  0 -1 -1  0  0      $1 - 7
c
FCL:p 0 -1  0 -1 -1  0  0      $1 - 7
c
c *****
F14:N   4 $ Average Neutron Flux in Cell 4, 1m from source
F24:P   4 $ Average Photon Flux in Cell 4, 1m from source
c multiply neutron fluence by conversion coefficient
de14 log 1E-9 1E-8 2.53E-8 1E-7 2E-7 5E-7 1E-6 2E-6
        5E-6 1E-5 2E-5 5E-5 1E-4 2E-4 5E-4 1E-3 2E-3
        5E-3 0.01 0.02 0.03 0.05 0.07 0.1 0.15 0.2
        0.3 0.5 0.7 0.9 1 1.2 2 3 4 5 6 7 8 9 10 12
        14 15 16 18 20 30 50 75 100 125 150 175 201
df14 log 6.6E-12 9E-12 1.06E-11 1.29E-11 1.35E-11 1.36E-11
        1.33E-11 1.29E-11 1.2E-11 1.13E-11 1.06E-11
        9.9E-12 9.4E-12 8.9E-12 8.3E-12 7.9E-12 7.7E-12
        8E-12 1.05E-11 1.66E-11 2.37E-11 4.11E-11 6E-11
        8.8E-11 1.32E-10 1.7E-10 2.33E-10 3.22E-10
        3.75E-10 4E-10 4.16E-10 4.25E-10 4.2E-10 4.12E-10
        4.08E-10 4.05E-10 4E-10 4.05E-10 4.09E-10 4.2E-10
        4.4E-10 4.8E-10 5.2E-10 5.4E-10 5.55E-10 5.7E-10
        6E-10 5.15E-10 4E-10 3.3E-10 2.85E-10 2.6E-10
        2.45E-10 2.5E-10 2.6E-10
c multiply photon fluence by conversion coefficient
de24 log 0.01 0.015 0.02 0.03 0.04 0.05 0.06 0.08 0.1 0.15
        0.2 0.3 0.4 0.5 0.6 0.8 1 1.5 2 3 4 5 6 8 10
df24 log 6.1E-14 8.3E-13 1.05E-12 8.1E-13 6.4E-13
        5.5E-13 5.1E-13 5.3E-13 6.1E-13 8.9E-13
        1.2E-12 1.8E-12 2.38E-12 2.93E-12 3.44E-12
        4.38E-12 5.2E-12 6.9E-12 8.6E-12 1.11E-11
        1.34E-11 1.55E-11 1.76E-11 2.16E-11 2.56E-11
c calculate neutron kerma for cell 6
F16:N   4 $ Neutron Energy Deposition in Cell 4, 1m from source
c calculate photon kerma for cell 6
F26:P   4 $ Photon Energy Deposition in Cell 4, 1m from source
c multiply neutron kerma by Q
F34:N   5 $ Average Neutron Flux in Cell 5, Behind wall
F44:P   5 $ Average Photon Flux in Cell 5, Behind wall
c multiply neutron fluence by conversion coefficient
de34 log 1E-9 1E-8 2.53E-8 1E-7 2E-7 5E-7 1E-6 2E-6
        5E-6 1E-5 2E-5 5E-5 1E-4 2E-4 5E-4 1E-3 2E-3
        5E-3 0.01 0.02 0.03 0.05 0.07 0.1 0.15 0.2
        0.3 0.5 0.7 0.9 1 1.2 2 3 4 5 6 7 8 9 10 12
        14 15 16 18 20 30 50 75 100 125 150 175 201
df34 log 6.6E-12 9E-12 1.06E-11 1.29E-11 1.35E-11 1.36E-11
        1.33E-11 1.29E-11 1.2E-11 1.13E-11 1.06E-11
        9.9E-12 9.4E-12 8.9E-12 8.3E-12 7.9E-12 7.7E-12
        8E-12 1.05E-11 1.66E-11 2.37E-11 4.11E-11 6E-11
        8.8E-11 1.32E-10 1.7E-10 2.33E-10 3.22E-10
        3.75E-10 4E-10 4.16E-10 4.25E-10 4.2E-10 4.12E-10
        4.08E-10 4.05E-10 4E-10 4.05E-10 4.09E-10 4.2E-10
        4.4E-10 4.8E-10 5.2E-10 5.4E-10 5.55E-10 5.7E-10
        6E-10 5.15E-10 4E-10 3.3E-10 2.85E-10 2.6E-10

```

```

                2.45E-10 2.5E-10 2.6E-10
c multiply photon fluence by conversion coefficient
de44 log 0.01 0.015 0.02 0.03 0.04 0.05 0.06 0.08 0.1 0.15
        0.2 0.3 0.4 0.5 0.6 0.8 1 1.5 2 3 4 5 6 8 10
df44 log 6.1E-14 8.3E-13 1.05E-12 8.1E-13 6.4E-13
        5.5E-13 5.1E-13 5.3E-13 6.1E-13 8.9E-13
        1.2E-12 1.8E-12 2.38E-12 2.93E-12 3.44E-12
        4.38E-12 5.2E-12 6.9E-12 8.6E-12 1.11E-11
        1.34E-11 1.55E-11 1.76E-11 2.16E-11 2.56E-11
c calculate neutron kerma for cell 5
F36:N    5 $ Neutron Energy Deposition in Cell 5, Behind wall
c calculate photon kerma for cell 5
F46:P    5 $ Photon Energy Deposition in Cell 5, Behind wall
c multiply neutron kerma by Q
F54:N    2 $ Average Neutron Flux in Cell 2, In Front of wall
F64:P    2 $ Average Photon Flux in Cell 2, In Front of wall
c multiply neutron fluence by conversion coefficient
de54 log 1E-9 1E-8 2.53E-8 1E-7 2E-7 5E-7 1E-6 2E-6
        5E-6 1E-5 2E-5 5E-5 1E-4 2E-4 5E-4 1E-3 2E-3
        5E-3 0.01 0.02 0.03 0.05 0.07 0.1 0.15 0.2
        0.3 0.5 0.7 0.9 1 1.2 2 3 4 5 6 7 8 9 10 12
        14 15 16 18 20 30 50 75 100 125 150 175 201
df54 log 6.6E-12 9E-12 1.06E-11 1.29E-11 1.35E-11 1.36E-11
        1.33E-11 1.29E-11 1.2E-11 1.13E-11 1.06E-11
        9.9E-12 9.4E-12 8.9E-12 8.3E-12 7.9E-12 7.7E-12
        8E-12 1.05E-11 1.66E-11 2.37E-11 4.11E-11 6E-11
        8.8E-11 1.32E-10 1.7E-10 2.33E-10 3.22E-10
        3.75E-10 4E-10 4.16E-10 4.25E-10 4.2E-10 4.12E-10
        4.08E-10 4.05E-10 4E-10 4.05E-10 4.09E-10 4.2E-10
        4.4E-10 4.8E-10 5.2E-10 5.4E-10 5.55E-10 5.7E-10
        6E-10 5.15E-10 4E-10 3.3E-10 2.85E-10 2.6E-10
        2.45E-10 2.5E-10 2.6E-10
c multiply photon fluence by conversion coefficient
de64 log 0.01 0.015 0.02 0.03 0.04 0.05 0.06 0.08 0.1 0.15
        0.2 0.3 0.4 0.5 0.6 0.8 1 1.5 2 3 4 5 6 8 10
df64 log 6.1E-14 8.3E-13 1.05E-12 8.1E-13 6.4E-13
        5.5E-13 5.1E-13 5.3E-13 6.1E-13 8.9E-13
        1.2E-12 1.8E-12 2.38E-12 2.93E-12 3.44E-12
        4.38E-12 5.2E-12 6.9E-12 8.6E-12 1.11E-11
        1.34E-11 1.55E-11 1.76E-11 2.16E-11 2.56E-11
c calculate neutron kerma for cell 8
F56:N    2 $ Neutron Energy Deposition in Cell 2, In Front of wall
c calculate photon kerma for cell 8
F66:P    2 $ Photon Energy Deposition in Cell 2, In Front of wall
c multiply neutron kerma by Q

```


Input Deck: ZShip3

zship3 20181022

```
c ***** Block 1: Cells *****
  1   1  -1e-6   -1          $D-T, D-D Primary Reaction
  2   2  -0.78   3 -4 -2     $Li-H Layer
  3   3  -2.52   4 -5 -2     $B4C Layer
  4   4  -19.3   5 -6 -2     $W Layer
  5   5  -1.0    -8          $ICRU Sphere 1m from Source
  6   5  -1.0    -9          $ICRU Sphere at 125m
  7   0          #1 #2 #3 #4 #5 #6 10 -7 -2 $Vacuum
  8   0          #7          $Problem Boundary

c ***** Block 2: Surface Cards *****
  1   sy -52 2
  2   cy 129.9
  3   py 50
  4   py 72
  5   py 72.02
  6   py 72.045
  7   py 12515
  8   s 0 -52 114.9 15
  9   sy 12500 15
 10  py -67

c ***** Block 3: Data Cards *****
mode n p
c
c *****
c D-T, D-D Plasma density = 1e-6 g/cm^3
m1  1002.70c  -0.250000 $Deuterium Tritium
     1003.70c  -0.250000 2003.70c  -0.250000 2004.70c  -0.250000
c *****
m2  3006.70c  -0.0325 $Lithium Hydride, 0.78 g/cm^3
     3007.70c  -0.4675 1001.70c  -0.5000
c *****
m3  5010.70c  -0.144242 $Boron Carbide, 2.52 g/cm^3
     5011.70c  -0.638368 6000.70c  -0.21739
c *****
m4  74182.70c -0.260586 $Tungsten, 19.3 g/cm^3
     74183.70c -0.142269 74184.70c -0.307531 74186.70c -0.289615
c *****
c ICRU Soft Tissue, Four Component, density = 1.00 g/cm^3
m5  1001.70c  -0.101172 $tissue,
     6000.70c  -0.111000
     7014.70c  -0.026000 8016.70c  -0.761828
c *****
c Importance
c   1  2  3  4  5  6  7  8
IMP:n 1  3  3  3  8  9  4  0  $1 - 8
c
IMP:p 1  3  3  3  8  9  4  0  $1 - 8
c
c *****
c --- Point Isotropic Source, 14.1 MeV Neutrons
c   Particles in all directions
c
sdef erg=14.1 par=1 cel=1 pos=0 -52 0
phys:p 100 0 0 0 0
phys:n 100 50
NPS 100000
c *****
c Forced Collisions
c   1  2  3  4  5  6  7  8
```

```

FCL:n 0 0 0 0 -1 -1 0 0 $1 - 8
C
FCL:p 0 0 0 0 -1 -1 0 0 $1 - 8
C
C *****
F14:N 5 $ Average Neutron Flux in Cell 5, 1m from source
F24:P 5 $ Average Photon Flux in Cell 5, 1m from source
c multiply neutron fluence by conversion coefficient
de14 log 1E-9 1E-8 2.53E-8 1E-7 2E-7 5E-7 1E-6 2E-6
        5E-6 1E-5 2E-5 5E-5 1E-4 2E-4 5E-4 1E-3 2E-3
        5E-3 0.01 0.02 0.03 0.05 0.07 0.1 0.15 0.2
        0.3 0.5 0.7 0.9 1 1.2 2 3 4 5 6 7 8 9 10 12
        14 15 16 18 20 30 50 75 100 125 150 175 201
df14 log 6.6E-12 9E-12 1.06E-11 1.29E-11 1.35E-11 1.36E-11
        1.33E-11 1.29E-11 1.2E-11 1.13E-11 1.06E-11
        9.9E-12 9.4E-12 8.9E-12 8.3E-12 7.9E-12 7.7E-12
        8E-12 1.05E-11 1.66E-11 2.37E-11 4.11E-11 6E-11
        8.8E-11 1.32E-10 1.7E-10 2.33E-10 3.22E-10
        3.75E-10 4E-10 4.16E-10 4.25E-10 4.2E-10 4.12E-10
        4.08E-10 4.05E-10 4E-10 4.05E-10 4.09E-10 4.2E-10
        4.4E-10 4.8E-10 5.2E-10 5.4E-10 5.55E-10 5.7E-10
        6E-10 5.15E-10 4E-10 3.3E-10 2.85E-10 2.6E-10
        2.45E-10 2.5E-10 2.6E-10
c multiply photon fluence by conversion coefficient
de24 log 0.01 0.015 0.02 0.03 0.04 0.05 0.06 0.08 0.1 0.15
        0.2 0.3 0.4 0.5 0.6 0.8 1 1.5 2 3 4 5 6 8 10
df24 log 6.1E-14 8.3E-13 1.05E-12 8.1E-13 6.4E-13
        5.5E-13 5.1E-13 5.3E-13 6.1E-13 8.9E-13
        1.2E-12 1.8E-12 2.38E-12 2.93E-12 3.44E-12
        4.38E-12 5.2E-12 6.9E-12 8.6E-12 1.11E-11
        1.34E-11 1.55E-11 1.76E-11 2.16E-11 2.56E-11
c calculate neutron kerma for cell 6
F16:N 5 $ Neutron Energy Deposition in Cell 5, 1m from source
c calculate photon kerma for cell 6
F26:P 5 $ Photon Energy Deposition in Cell 5, 1m from source
F34:N 6 $ Average Neutron Flux in Cell 6, 126m from source
F44:P 6 $ Average Photon Flux in Cell 6, 126m from source
c multiply neutron fluence by conversion coefficient
de34 log 1E-9 1E-8 2.53E-8 1E-7 2E-7 5E-7 1E-6 2E-6
        5E-6 1E-5 2E-5 5E-5 1E-4 2E-4 5E-4 1E-3 2E-3
        5E-3 0.01 0.02 0.03 0.05 0.07 0.1 0.15 0.2
        0.3 0.5 0.7 0.9 1 1.2 2 3 4 5 6 7 8 9 10 12
        14 15 16 18 20 30 50 75 100 125 150 175 201
df34 log 6.6E-12 9E-12 1.06E-11 1.29E-11 1.35E-11 1.36E-11
        1.33E-11 1.29E-11 1.2E-11 1.13E-11 1.06E-11
        9.9E-12 9.4E-12 8.9E-12 8.3E-12 7.9E-12 7.7E-12
        8E-12 1.05E-11 1.66E-11 2.37E-11 4.11E-11 6E-11
        8.8E-11 1.32E-10 1.7E-10 2.33E-10 3.22E-10
        3.75E-10 4E-10 4.16E-10 4.25E-10 4.2E-10 4.12E-10
        4.08E-10 4.05E-10 4E-10 4.05E-10 4.09E-10 4.2E-10
        4.4E-10 4.8E-10 5.2E-10 5.4E-10 5.55E-10 5.7E-10
        6E-10 5.15E-10 4E-10 3.3E-10 2.85E-10 2.6E-10
        2.45E-10 2.5E-10 2.6E-10
c multiply photon fluence by conversion coefficient
de44 log 0.01 0.015 0.02 0.03 0.04 0.05 0.06 0.08 0.1 0.15
        0.2 0.3 0.4 0.5 0.6 0.8 1 1.5 2 3 4 5 6 8 10
df44 log 6.1E-14 8.3E-13 1.05E-12 8.1E-13 6.4E-13
        5.5E-13 5.1E-13 5.3E-13 6.1E-13 8.9E-13
        1.2E-12 1.8E-12 2.38E-12 2.93E-12 3.44E-12
        4.38E-12 5.2E-12 6.9E-12 8.6E-12 1.11E-11
        1.34E-11 1.55E-11 1.76E-11 2.16E-11 2.56E-11
c calculate neutron kerma for cell 6
F36:N 6 $ Neutron Energy Deposition in Cell 6, 126m from source
F46:P 6 $ Photon Energy Deposition in Cell 6, 126m from source

```

Input Deck: Emrich13-1e_Full

```

Problem 13.1 from "Rocket Propulsion Using Nuclear Fission" by Bill Emrich
C *****
C GEOMETRY:      X point source of reactor, 6 MeV photons
C               A astronaut receiving dose
C   ^  z-axis
C   |
C   |
C   |<-5m->|<-----60m----->|<----10m---->|
C   |
C   X-----[                LH2 Tank                ]-----[ Astronaut ]--> y-axis
C
C Nuclear Thermal Rocket with Liquid Hydrogen Propellant
C No shielding assumed but the propellant
C Assume Reactor is point source and a sphere of LEU
C Assume power density is constant in reactor
C Reactor is 300 MW with Core Volume of 100000 cm^3
C Fuel depletion rate 2.5 cm/sec
C Astronaut assumed to have cross sectional area of 8000 cm^2
C Astronaut assumed to have 75 kg mass
C
C ***** Block 1: Cells *****
C
C   1      0      5
C   2      1  -6.873879  -1
C   3      2  -0.07085    2 -3 -4
C   4      3    -1        6 -7 -8
C   5      0            #2 #3 #4 -5
C
C   $problem boundary
C   $reactor
C   $Full LH2 Tank
C   $Astronaut (ICRU Disc)
C   $vacuum around ship
C
C ***** Block 2: Surface Cards *****
C
C   1      so 28.8
C   2      py 500
C   3      py 6500
C   4      cy 500
C   5      sy 3760.6 4000
C   6      py 7500
C   7      py 7509.375
C   8      cy 50.463
C
C ***** Block 3: Data Cards *****
mode p
C
C *****
C Blended Reactor Mass (50% fuel/50% moderator), density = 6.873879 g/cm^3
m1      92235      -0.490000 92238      -0.010000 6000      -0.200000
        8016        -0.100000 11023      -0.100000 29000      -0.100000
C *****
C Liquid Hydrogen, density = 0.07085 g/cm^3
m2      1000      -1      $LH2
C *****
C From Dugal (2006)
C ICRU Soft Tissue, Four Component, density = 1.00 g/cm^3
m3      1000      -0.101172 6000      -0.111000
        7000      -0.026000 8000      -0.761828
C *****
C Importance
C   1      2      3      4      5
IMP:p  0      5      8      9      3      $1 - 5
C *****
C --- 6 MeV spontaneous fission gamma photon energy reactor, point source
C
SDEF  POS 0 0 0  PAR=2  ERG=6
phys:p 10 0 0 0 0
NPS 250000000

```

```
C *****
C Forced Collisions
C   1   2   3   4   5
FCL:p 0   0  -1  -1   0      $1 - 5
C *****
F12:P  7 $ Tally on Surface 7 Astronaut Surface
F14:P  4 $ Tally on Cell 4 Astronaut Dose
F16:P  4 $ Photon Energy Deposition in Cell 4
F26:P  3 $ Photon Energy Deposition in Cell 3 LH2 Column
```

Input Deck: Shield1_Full_a

```
Shield1_Full_a
c mcnp6 i=Shield1_Full_a.txt o=Shield1_Full_a_20181029a.txt
c ***** Block 1: Cells *****
  1      0      1 -2 -3
  2      2    -0.78    4 -5 -3    $Li-H Layer, Shield 1
  3      0      5 -6 -3    $B4C Layer, Shield 2
  4      0      6 -7 -3    $W Layer, Shield 3
  5      0      #1 #2 #3 #4 1 -7 -3    $Vacuum
  6      0      #5    $Problem Boundary

c ***** Block 2: Surface Cards *****
  1      py -51
  2      py -49
  3      cy 0.5642
  4      py 50
  5      py 72
  6      py 72.02
  7      py 72.045

c ***** Block 3: Data Cards *****
mode n p
phys:n 100 50
phys:p
c
c *****
m2      3006.70c      -0.0325    $Lithium Hydride, 0.78 g/cm^3
      3007.70c      -0.4675    1001.70c      -0.5000
c *****
c m3      5010.70c      -0.144242    $Boron Carbide, 2.52 g/cm^3
c      5011.70c      -0.638368    6000.70c      -0.21739
c *****
c m4      74182.70c      -0.260586    $Tungsten, 19.3 g/cm^3
c      74183.70c      -0.142269    74184.70c      -0.307531    74186.70c      -0.289615
c *****
c Importance
c      1      2      3      4      5      6
IMP:n 1      9      4      3      2      0      $1 - 6
c
IMP:p 1      9      4      3      2      0      $1 - 6
c
c *****
c --- Point Isotropic Source, 14.1 MeV Neutrons
c      Particles in all directions
c
sdef erg=14.1 par=1 cel=1 pos=0 -50 0
NPS 200000000
c *****
c Forced Collisions
c      1      2      3      4      5      6
FCL:n 0      -1      0      0      0      0      $1 - 6
c
FCL:p 0      -1      0      0      0      0      $1 - 6
c
c *****
F12:N 2 $ Average Neutron Flux Surface 2, Reactor Exit
F14:N 1 $ Average Neutron Flux in Cell 1, Reactor Dose
F32:N 4 $ Average Neutron Flux Surface 4, Shield 1 Entry
F34:N 2 $ Average Neutron Flux in Cell 2, Shield 1 Dose
F52:N 5 $ Average Neutron Flux Surface 5, Shield 1/2 Interface
F54:N 3 $ Average Neutron Flux in Cell 3, Shield 2 Dose
F72:N 6 $ Average Neutron Flux Surface 6, Shield 2/3 Interface
F74:N 4 $ Average Neutron Flux in Cell 4, Shield 3 Dose
```

F92:N 7 \$ Average Neutron Flux Surface 7, Shield 3 Exit
F22:P 2 \$ Average Photon Flux Surface 2, Reactor Exit
F24:P 1 \$ Average Photon Flux in Cell 1, Reactor Dose
F42:P 4 \$ Average Photon Flux Surface 4, Shield 1 Entry
F44:P 2 \$ Average Photon Flux in Cell 2, Shield 1 Dose
F62:P 5 \$ Average Photon Flux Surface 5, Shield 1/2 Interface
F64:P 3 \$ Average Photon Flux in Cell 3, Shield 2 Dose
F82:P 6 \$ Average Photon Flux Surface 6, Shield 2/3 Interface
F84:P 4 \$ Average Photon Flux in Cell 4, Shield 3 Dose
F102:P 7 \$ Average Photon Flux Surface 7, Shield 3 Exit

Input Deck: Shield12_Full_a

```
Shield12_Full_a
c mcnp6 i=Shield12_Full_a.txt o=Shield12_Full_a_20181028a.txt
c ***** Block 1: Cells *****
  1      0      1 -2 -3
  2      2      4 -5 -3      $Li-H Layer, Shield 1
  3      3     -2.52     5 -6 -3      $B4C Layer, Shield 2
  4      0      6 -7 -3      $W Layer, Shield 3
  5      0      #1 #2 #3 #4 1 -7 -3      $Vacuum
  6      0      #5      $Problem Boundary

c ***** Block 2: Surface Cards *****
  1      py -51
  2      py -49
  3      cy 0.5642
  4      py 50
  5      py 72
  6      py 72.02
  7      py 72.045

c ***** Block 3: Data Cards *****
mode n p
phys:n 100 50
phys:p
c
c *****
m2      3006.70c      -0.0325      $Lithium Hydride, 0.78 g/cm^3
      3007.70c      -0.4675      1001.70c      -0.5000
c *****
m3      5010.70c      -0.144242      $Boron Carbide, 2.52 g/cm^3
      5011.70c      -0.638368      6000.70c      -0.21739
c *****
c m4      74182.70c      -0.260586      $Tungsten, 19.3 g/cm^3
c      74183.70c      -0.142269      74184.70c      -0.307531      74186.70c      -0.289615
c *****
c Importance
c      1      2      3      4      5      6
IMP:n 1      8      9      4      2      0      $1 - 6
c
IMP:p 1      8      9      4      2      0      $1 - 6
c
c *****
c --- Point Isotropic Source, 14.1 MeV Neutrons
c      Particles in all directions
c
sdef erg=14.1 par=1 cel=1 pos=0 -50 0
NPS 200000000
c *****
c Forced Collisions
c      1      2      3      4      5      6
FCL:n 0      0      -1      0      0      0      $1 - 6
c
FCL:p 0      0      -1      0      0      0      $1 - 6
c
c *****
F12:N      2      $ Average Neutron Flux Surface 2, Reactor Exit
F14:N      1      $ Average Neutron Flux in Cell 1, Reactor Dose
F32:N      4      $ Average Neutron Flux Surface 4, Shield 1 Entry
F34:N      2      $ Average Neutron Flux in Cell 2, Shield 1 Dose
F52:N      5      $ Average Neutron Flux Surface 5, Shield 1/2 Interface
F54:N      3      $ Average Neutron Flux in Cell 3, Shield 2 Dose
F72:N      6      $ Average Neutron Flux Surface 6, Shield 2/3 Interface
F74:N      4      $ Average Neutron Flux in Cell 4, Shield 3 Dose
```

F92:N 7 \$ Average Neutron Flux Surface 7, Shield 3 Exit
F22:P 2 \$ Average Photon Flux Surface 2, Reactor Exit
F24:P 1 \$ Average Photon Flux in Cell 1, Reactor Dose
F42:P 4 \$ Average Photon Flux Surface 4, Shield 1 Entry
F44:P 2 \$ Average Photon Flux in Cell 2, Shield 1 Dose
F62:P 5 \$ Average Photon Flux Surface 5, Shield 1/2 Interface
F64:P 3 \$ Average Photon Flux in Cell 3, Shield 2 Dose
F82:P 6 \$ Average Photon Flux Surface 6, Shield 2/3 Interface
F84:P 4 \$ Average Photon Flux in Cell 4, Shield 3 Dose
F102:P 7 \$ Average Photon Flux Surface 7, Shield 3 Exit

Input Deck: Shield123_Full_a

```
Shield123_Full_a
c mcnp6 i=Shield123_Full_a.txt o=Shield123_Full_a_20181027a.txt
c ***** Block 1: Cells *****
  1      0      1 -2 -3
  2      2     -0.78    4 -5 -3      $Li-H Layer, Shield 1
  3      3     -2.52    5 -6 -3      $B4C Layer, Shield 2
  4      4    -19.3     6 -7 -3      $W Layer, Shield 3
  5      0          #1 #2 #3 #4 1 -7 -3 $Vacuum
  6      0          #5                      $Problem Boundary

c ***** Block 2: Surface Cards *****
  1      py -51
  2      py -49
  3      cy 0.5642
  4      py 50
  5      py 72
  6      py 72.02
  7      py 72.045

c ***** Block 3: Data Cards *****
mode n p
c
c *****
m2      3006.70c      -0.0325 $Lithium Hydride, 0.78 g/cm^3
      3007.70c      -0.4675 1001.70c      -0.5000
c *****
m3      5010.70c      -0.144242 $Boron Carbide, 2.52 g/cm^3
      5011.70c      -0.638368 6000.70c      -0.21739
c *****
m4      74182.70c     -0.260586 $Tungsten, 19.3 g/cm^3
      74183.70c     -0.142269 74184.70c     -0.307531 74186.70c     -0.289615
c *****
c Importance
c      1  2  3  4  5  6
IMP:n  1  7  8  9  2  0      $1 - 6
c
IMP:p  1  7  8  9  2  0      $1 - 6
c
c *****
c --- Point Isotropic Source, 14.1 MeV Neutrons
c      Particles in all directions
c
sdef erg=14.1 par=1 cel=1 pos=0 -50 0
phys:n 100 50
phys:p
NPS 2000000000
c *****
c Forced Collisions
c      1  2  3  4  5  6
FCL:n  0  0  0 -1  0  0      $1 - 6
c
FCL:p  0  0  0 -1  0  0      $1 - 6
c
c *****
F12:N   2 $ Average Neutron Flux Surface 2, Reactor Exit
F14:N   1 $ Average Neutron Flux in Cell 1, Reactor Dose
F32:N   4 $ Average Neutron Flux Surface 4, Shield 1 Entry
F34:N   2 $ Average Neutron Flux in Cell 2, Shield 1 Dose
F52:N   5 $ Average Neutron Flux Surface 5, Shield 1/2 Interface
F54:N   3 $ Average Neutron Flux in Cell 3, Shield 2 Dose
F72:N   6 $ Average Neutron Flux Surface 6, Shield 2/3 Interface
F74:N   4 $ Average Neutron Flux in Cell 4, Shield 3 Dose
```

F92:N 7 \$ Average Neutron Flux Surface 7, Shield 3 Exit
F22:P 2 \$ Average Photon Flux Surface 2, Reactor Exit
F24:P 1 \$ Average Photon Flux in Cell 1, Reactor Dose
F42:P 4 \$ Average Photon Flux Surface 4, Shield 1 Entry
F44:P 2 \$ Average Photon Flux in Cell 2, Shield 1 Dose
F62:P 5 \$ Average Photon Flux Surface 5, Shield 1/2 Interface
F64:P 3 \$ Average Photon Flux in Cell 3, Shield 2 Dose
F82:P 6 \$ Average Photon Flux Surface 6, Shield 2/3 Interface
F84:P 4 \$ Average Photon Flux in Cell 4, Shield 3 Dose
F102:P 7 \$ Average Photon Flux Surface 7, Shield 3 Exit